Association of Metallurgical Engineers of Serbia
Faculty of Technology and Metallurgy, University of Belgrade
Serbian Foundrymen's Society
Metallurgical Academic Network of SEE Countries
Institute for Technology of Nuclear and Other Mineral Raw Materials
Institute of Chemistry, Technology and Metallurgy
Vinca Institute of Nuclear Sciences
Lola institute

MME SEE 2015

Metallurgical & Materials Engineering Congress of South-East Europe

PROCEEDINGS AND BOOK OF ABSTRACTS

Editor:

Marija Korać

June 3-5, 2015
Belgrade, Serbia

Editor:

Dr Marija Korać
Faculty of Technology and Metallurgy, University of Belgrade

Technical editor:

Department of Printing Engineering
Faculty of Technology and Metallurgy, University of Belgrade

Published by:

Association of Metallurgical Engineers of Serbia (AMES)

Circulation:

150 copies

Printed by:

Department of Printing Engineering Faculty of Technology and Metallurgy
Karnegijeva 4, POB 35-03
11 120 Belgrade, Serbia
Tel: +381 11 3370 492

ISBN 978-86-87183-27-8

Supported by:

The Ministry of Education, Science and Technological Development
Republic of Serbia

International Scientific Committee

- *Željko Kamberović, Serbia, Chairman*
- Đorđe Janaćković, Serbia
- Mirjam Jan Blažić, Slovenia
- Zijah Burzić, Serbia
- Sveto Cvetkovski, Macedonia
- Vladan Ćosović, Serbia
- Martin Debelak, Slovenia
- Kemal Delijić, Montenegro
- Aleksandar Dimitrov, Macedonia
- Mile Djurdjevic, Austria
- Natalija Dolić, Croatia
- Bernd Friedrich, Germany
- Vladimir Genevski, Bulgaria
- Marija Korać, Serbia
- Vladimir Krstić, Canada
- Milan T. Jovanović, Serbia
- Nikola Majinski, Serbia
- Vesna Maksimović, Serbia
- Srećko Manasijević, Serbia
- Boštjan Markoli, Slovenia
- Srđan Marković, Serbia
- Jožef Medved, Slovenia
- Sulejman Muhamedagić, Bosnia and Herzegovina
- Primož Mrvar, Slovenia
- Dimitrios Panias, Greece
- Miljana Popović, Serbia
- Nenad Radović, Serbia
- Karlo Raić, Serbia
- Endre Romhanji, Serbia
- Rebeka Rudolf, Slovenia
- Miroslav Sokić, Serbia
- Jasna Stajić-Trošić, Serbia
- Srećko Stopić, Germany
- Nada Štrbac, Serbia
- Nadežda Talijan, Serbia
- Tatjana Volkov-Husović, Serbia
- Zdenka Zovko-Brodarac, Croatia
- Rossitza Paunova, Bulgaria

PREFACE

Metallurgical & Materials Engineering Congress of South-East Europe (MME-SEE 15) is a meeting of scientists, professionals and specialties working not only in the field of processing of metals and materials, but also those engaged in research related to the production, structure and property relationship and applications of modern materials.

Time has shown a strong need for interdisciplinary research in metallurgical and materials engineering. Therefore, in order to cover all research fields, Congress represents fusion of following scientific events: Balkan Conference of Metallurgy, Processing and Structure of Materials, Light metals and Composite materials and International Foundrymen Conference. Regional significance is supported by South East Europe Associations of Metallurgical Engineers, Balkan Union of Metallurgists and Chambers of Commerce of SEE Countries, and organized by Association of Metallurgical Engineers of Serbia, Serbian Foundrymen's Society and Metallurgical Academic Network of SEE Countries

The Congress brings together a wide range of related topics and presents the views from both academia and industry. Future of metal industry in South-East European countries, geology and minerals potentials for metallurgy production, new industrial achievements, developments and trends in extractive metallurgy, ferrous and nonferrous metals production, metal forming, casting, powder metallurgy, new and advanced materials, coating, galvanizing, corrosion and protection of materials, process control and modeling, recycling and waste minimization, nanotechnology, sustainable development, solvothermal synthesis, physical metallurgy and structure of materials, welding, environmental protection and education are all covered in the Proceedings.

The Scientific Committee hopes that the Congress will help to improve the knowledge on the symbiotic topics as processing and materials properties.

The Editor would like to thank the Scientific Committee, and the Secretariat - CONGREXPO d.o.o. and all those who helped in making the Congress a success.

The Congress is organized jointly by the Association of Metallurgical Engineers of Serbia, Faculty of Technology and Metallurgy, University of Belgrade, Serbian Foundrymen's Society, Metallurgical Academic Network of SEE Countries, Institute for Technology of Nuclear and Other Mineral Raw Materials, Institute of Chemistry, Technology and Metallurgy, Vinca Institute of Nuclear Sciences and Lola institute

Special thanks are due to the Ministry of Education, Science and Technological Development of the Republic of Serbia for the financial support of the Congress,

Editor

Content

Plenary lectures

CHALLENGES AND OPPORTUNITIES FOR ALUMINUM BASED MATERIALS – RESEARCH AND INDUSTRIAL PERSPECTIVES IN EU AND SEE STATES

Kemal Delijić

Faculty of Metallurgy and Technology, University of Montenegro, Podgorica
kemal@ac.me

Abstract

The paper analyzed challenges and opportunities for aluminum based materials in the context of the research, industrial perspectives and aluminum market, and describes some industry's economics, strategic importance and close links to many downstream industrial sectors such as transport, construction, engineering and packaging. The European aluminum industry represents the whole value chain, from alumina and primary production to semi-finished, end-use products and recycling. The demand for aluminum products in Europe is predicted to continue to grow with encouraging perspectives in all key markets. A strategic value chain for Europe can be illustrated through €36.8 billion annual turnover, 255,000 direct jobs and over 1 million indirect jobs within Europe and 16% of total global aluminum production. An analysis of the research opportunities for Al based materials in the light of “Agenda for Action” developed by European Aluminum Association in relation to the "Metallurgy Europe", program in the field of metals research and manufacturing, selected as a new Eureka Cluster is also presented.

Keywords: Al industry, Al-based materials, EU perspectives

Overview of the Aluminum Industry

Aluminum is one of the most important metals used by modern societies, and aluminum industry is the largest non-ferrous metal industry in the world economy. Since its industrial production, demand for aluminum has been continuously increasing to around 53 million tonnes in 2014 and its application has extended to variety of economic sectors. Aluminum is the third most abundant element in the earth’s crust and the most abundant metallic element, and it never occurs as a free element in nature. Smelting of Al, as an industrial activity, is the youngest and largest activity of the non-ferrous metal industry, as it began only about a century ago. Aluminum is a material with a wide range of applications, e.g. transport vehicles, construction, packaging industry, electronic production, household appliances, etc., and consequently the economic activities of these industrial sectors determine the overall demand for aluminum [1]. Today, the EU aluminum industry directly represents a workforce of about 255,000 people and its annual turnover is about 36.8 billion Euros.

Global flow of Aluminum

Aluminum's combination of properties results in its use in a wide variety of products, many of which are indispensable to modern life. Aluminum's strength, light weight, and workability have led to increased use in transportation systems (light vehicles, railcars and aircraft), as efforts to reduce fuel consumption have increased. Aluminum's excellent thermal properties and resistance to corrosion have led to its use in air conditioning, refrigeration, and heat-exchange systems. Finally, its malleability has allowed it to be rolled and formed into very thin sheets used in a variety of packaging [2, 3]. A generalized model of the entire life cycle, or flow, of aluminum, as an example for 2010 year, is presented in Figure 1.

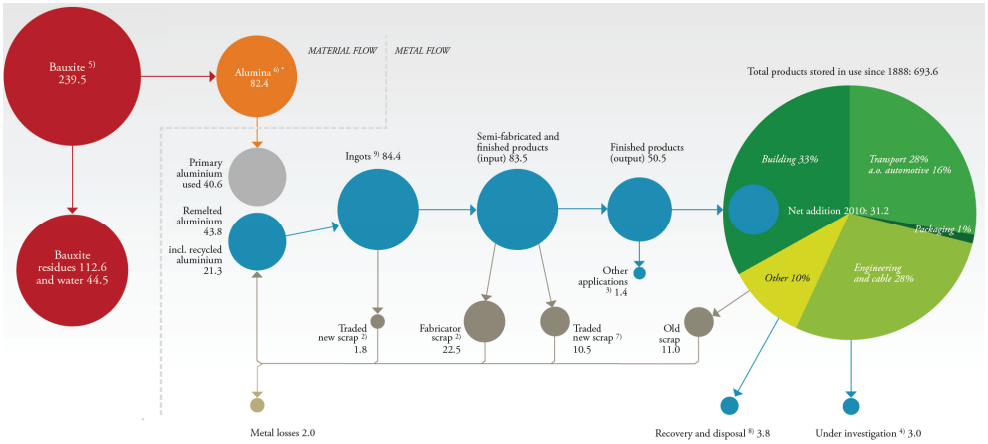

Fig. 1. Material flow balance for aluminum - Global aluminum flows in 2010. Taking into account the finished products entering into use (50.5 million metric tons) and the old scrap recovered for recycling (11 million metric tons), the global recycled content for aluminum is about 22 percent [5].

Production and consumption

The aluminum industry comprises three main production streams:

- Primary production is the creation through electrolysis of aluminum from the raw material *alumina*;
- Semi-fabrication of flat rolled products (plate sheets, foil), extruded products (profiles) and castings.
- Secondary raw material production is the re-melting or refining from processed or used aluminum scrap.

Primary aluminum production begins with the mining of bauxite, which is processed first into alumina and subsequently into aluminum metal. The processing of bauxite to alumina involves initial chemical processing, and the main waste from this process is the "red mud," usually disposed of in a landfill. The electrolysis of alumina to produce aluminum involves the use of aluminum fluoride, carbon anodes, and large amounts of electricity. Primary aluminum production is electricity intensive process and consumes majority of the energy used in this

sector. Furthermore, the most significant waste products from the production of aluminum from alumina are air emissions, including two kinds of perfluorocarbon (PFC) gases and carbon dioxide (CO_2) from the production of anodes and electricity. Therefore energy price and GHGs reduction policy has great influence on the technology evolution and the economy of the aluminum industry and production.

Based upon available data [6] over 228 million metric tons (Mt) of bauxite was produced in 2014. Australia, China, and Brazil are some of the most dominant countries in bauxite mine production, generating 81 million, 47 million, and 32.5 million metric tons of bauxite, respectively, in 2014, as shown in Figure 2. Six countries each produced more than 10 Mt of bauxite (Australia, 81 Mt; China, 47 Mt; Brazil, 32.5 Mt; Guinea, 19.3 Mt; Jamaica, India, 19 Mt and, Jamaica, 13.9 Mt) and together accounted for 91 percent of global production. The distribution of bauxite production reflects the geologic history and climatic factors that favor the formation of bauxite as well as economic factors, such as the cost of production at individual sites.

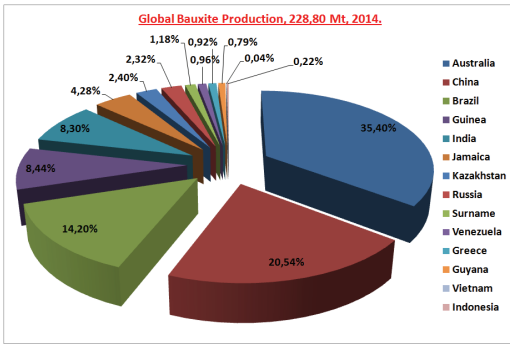

Fig. 2. Global bauxite production, 2014 (top world producers).

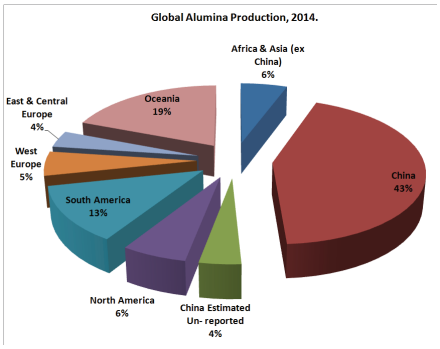

Fig. 3. Global alumina production, 2014 (top world producers).

Known bauxite reserves are around 29 billion metric tons. At the current rate of extraction, these reserves will last more than 100 years. However, it is estimated that the total resources are in the order of 55 billion to 75 billion metric tons when undiscovered bauxite resources are included, located in South America (33%), Africa (27%), Asia (17%), Oceania (13%) and elsewhere (10%). This would extend the time perspective to 250 - 340 years. In recent years, prospecting has increased the reserves more rapidly than the rate of extraction: from 1995 to 2011, 2.7 billon metric tons were extracted, but the reserves increased from 23 billion metric tons to 29 billion metric tons [6-9].

The capacity of bauxite mines worldwide is increased to 228.8 million metric tons (Mt) by 2014, from 183 Mt in 2006, or by 25 percent, or almost 3.2 percent per year. According to some global Al-flow predictions [2, 4], aluminum consumption in 2025 is likely to increase by more than 2.5 times, to 120 Mt compared with 45.3 Mt in 2006, which represents a predicted growth rate of 4.1 percent per year. Most of the increased consumption will take place in countries that consumed only modest

amounts of aluminum. China, which consumed about 6.6 kilograms per capita in 2006, is expected to consume almost 30 kilograms per capita in 2025. Russia, Brazil, and India also are expected to increase their aluminum consumption significantly. Consumption in high-income countries is not expected to change significantly on a per capita basis, but total consumption may change modestly owing to changes in population. To meet the projected consumption of 120 Mt of aluminum, the world would need to produce about 570 Mt of bauxite and about 230 Mt of alumina.

Global alumina production in 2014 was 108.5 Mt; of this amount, 51.3 Mt (47.31%) was produced in China; 20.8 Mt in Oceania; 20,2 Mt in the Americas, 9.9 Mt in West-East-Central Europe, and 6,1 Mt in Africa&Asia (ex China), as illustrated in Figure 3. China, South America and Oceania produced ~80 percent of global alumina production [9]. Not all alumina is used to produce aluminum; about 10 percent of alumina is used to produce refractory and other chemical products.

Global production of primary aluminum in 2014 was about 53 Mt, and 27.5 Mt (52%) of this amount was produced in China. The Americas produced 6.1 Mt (11.5%) of primary aluminum;, West-East-Central Europe 7.2 Mt (13.7%), Asia (ex China) 2.43 Mt, and Oceania 2 Mt. Nine countries produced at least 1 Mt of primary aluminum (China, Russia, Canada, USA, Australia, Brazil, Norway, India and UAE) [11]. These eight countries accounted for more than 80 percent of global primary aluminum production. Five of the six leading producers of primary aluminum were also among the six leading producers of alumina.

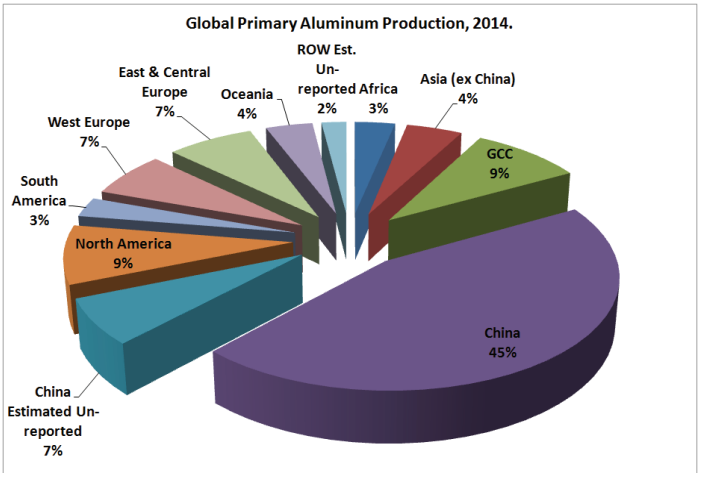

Fig. 4. Global primary aluminum production, 2014 (top world producers).

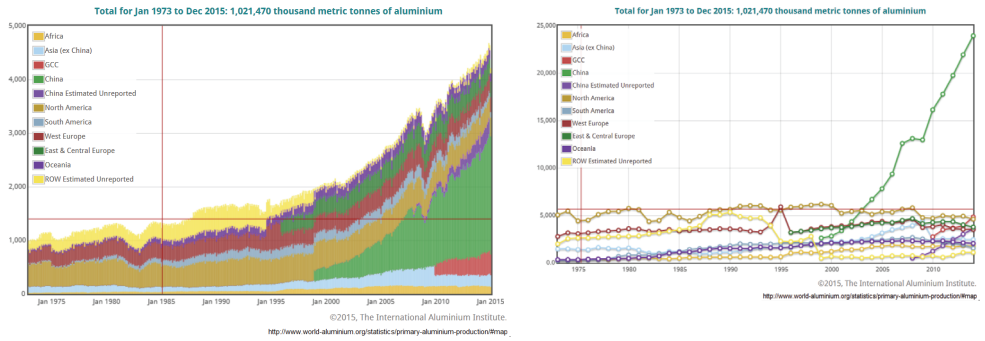

Fig. 5. Total production of aluminum 1974-2015 [10].

Canada, which does not produce bauxite and is not one of the six leading producers of alumina, was usually the third ranked producer of primary aluminum. Abundant hydroelectricity led to the location of aluminum smelters in Canada. Aluminum smelting is energy intensive, and changes in the price and availability of energy result in the location of new smelters in areas with cheap and available energy. The availability of abundant supplies of natural gas has led to the development of significant aluminum smelters in Bahrain and the United Arab Emirates in recent years. New aluminum smelters are being built in Iceland, such as the Fjardaal smelter, because of the availability of abundant electricity generated from hydropower and geothermal power.

Of the secondary aluminum output, the Americas produces about 4.46 Mt; Asia, 3.6 Mt; and Europe and Eurasia, 3.8 Mt. Production of secondary aluminum in Africa and the Middle East is negligible. Based upon USGS data, the six leading producers of secondary aluminum accounts for about 80 percent of global production of secondary aluminum (USA, China, Japan, Germany, Italy, and Mexico) [2, 4].

The comparison of the consumption of aluminum by end-use category in high-income and low-to middle-income countries show that the leading use of aluminum in many high-income countries is to produce goods in the *transportation sector*, and in low-to middle-income countries, aluminum is used mainly in the production of electrical systems and by the construction industry. Differences in the end uses of aluminum by income have important implications for the recovery of post-consumer scrap because the in-service life of electrical systems and construction uses is much longer than that of many transportation uses [2, 4].

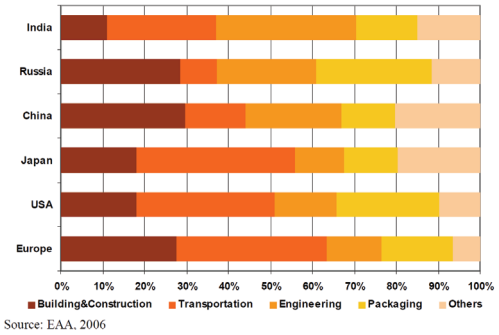

Fig. 6. Aluminum sectoral consumption in different world regions.

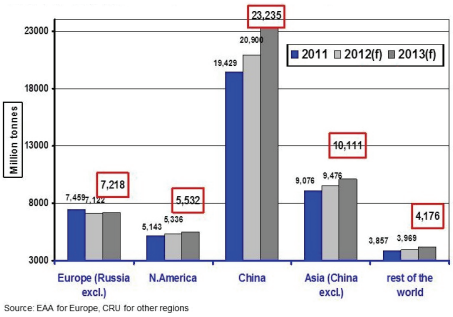

Fig. 7. Primary aluminum consumption 2011-2013.

Some analysis of aluminum consumption per capita versus the GDP per capita, made for 20 most populous countries, suggests that, in general, countries with a GDP per capita of less than $5,000 consume less than 5 kg of aluminum per capita; countries with a GDP per capita between $5,000 and $15,000 consume between 5 and 10 kg of aluminum per capita; and countries with per capita incomes of greater than $25,000 consume between 15 and 35 kg of aluminum per capita [2, 4]. According to forecasts made on the basis of the world population increasing, GDP per capita, aluminum consumption per capita and aluminum consumption for the 40 most populous countries (based on the average of the past decade), and assuming that aluminum production is equal to aluminum consumption, the world aluminum consumption is estimated to be 120 Mt in 2025. This represents a forecast of growth rate of 4.1 percent per year. Most of the increases are estimated to occur in low- and middle-income countries. Consumption in high-income countries is not expected to rise significantly on a per capita basis, but total consumption may increase modestly owing to population increases.

EU aluminum industry in facts

Within the wider European area, aluminum production was about one tenth of world production. Norway (29.5% of EU35 production) and Iceland (17.4%) were the largest producers of aluminum in this region, followed by Germany (8.5%), France (7.5%) and Spain (7.1%) [12-14].

EU27 produces 1.15% of world bauxite and EU33 produces 2% of world bauxite. Greece is ranked 1st in EU27 with 85% also 1st in EU33 with 58%, and 12th in the world with 1%. The map in the Figure 8 gives an overview of the localization of the European smelters (2010 data) and their relative capacity of production [14, 15].

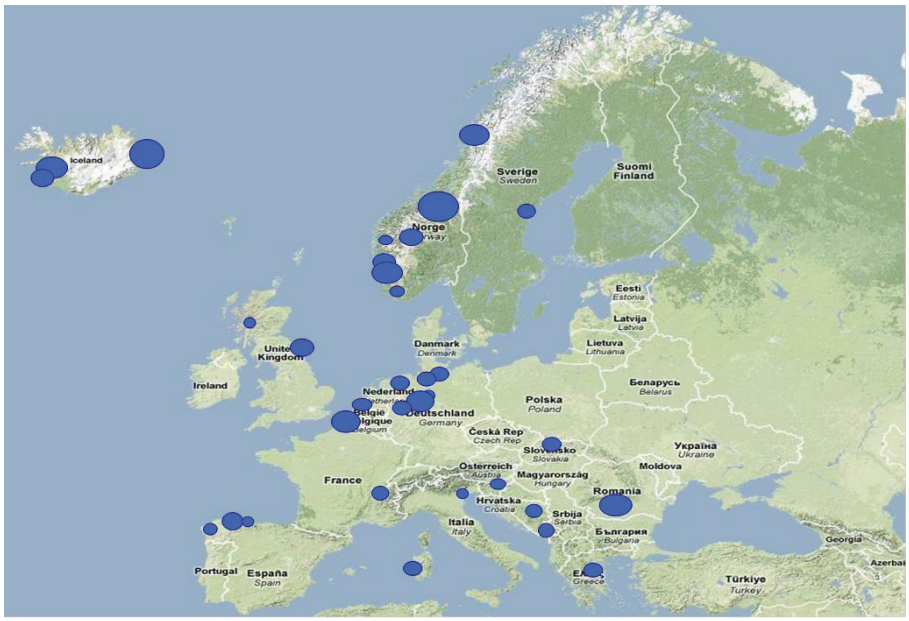

Fig. 8. European map of smelters by capacity of production – 2010 data [15].

Six European countries (from EU35) products bauxite to materially significant level (Greece, France, Hungary, Bosnia and Herzegovina, Montenegro, Turkey), and in 2012 their share in world production was 1.1%. Greece has produced 66.3% of the total produced 2.74 million tonnes of bauxite in 2012 at the level of EU35, Figure 9. Eight European countries (from EU35) reported the production of alumina in 2012 and their share in world production of alumina was 3.5%. In terms of SEE countries Greece is the largest producer of alumina (Figure 10).

Sixteen European countries (from EU35) reported the production of primary aluminum in 2012 and their share in world production of alumina was 10.9%, and in terms of SEE countries, Romania was the largest producer of alumina (Figure 11). Its share in EU35 production was 4.6%.

The main end-use markets for aluminum products in Europe as reported by the European Aluminium Association are shown in Figure 12. Building and transport are main end-use markets, each with around one third of the total. The remainder goes into applications such as electrical and mechanical engineering, office equipment, domestic appliances, lighting, chemistry and pharmaceuticals.

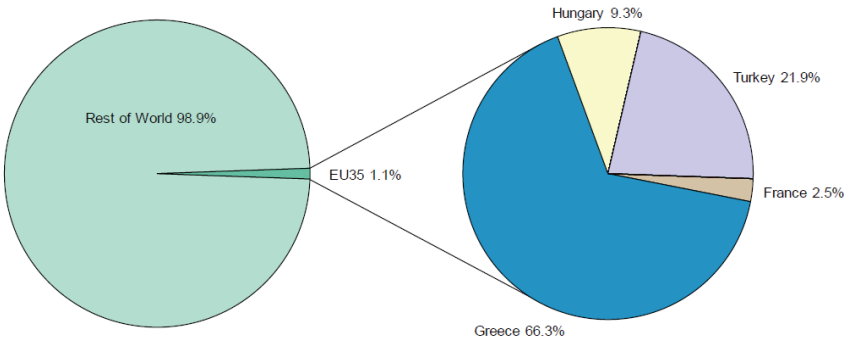

Fig. 9. EU 35 - Production of bauxite in 2012 [16].

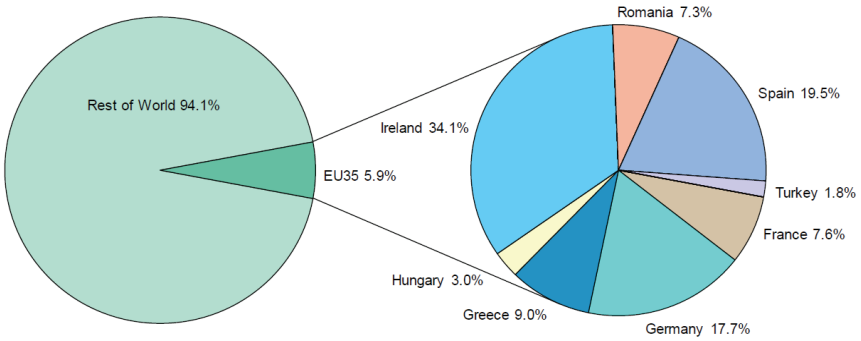

Fig. 10. EU 35 - Production of Alumina in 2012 [16].

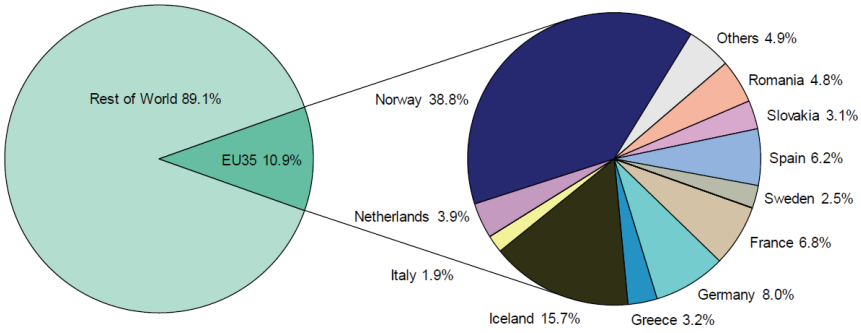

Fig. 11. EU 35 - Production of primary aluminum in 2012 [16].

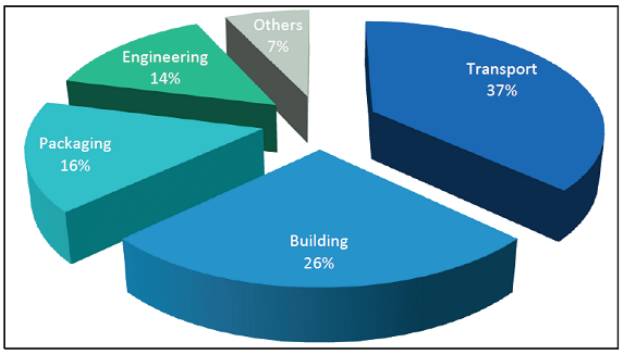

Source: European Aluminium Association

Fig. 12. The main end-use markets for aluminum products in Europe.

The aluminum industry is a key sector for Europe, and that strategic value chain can be illustrated through €36.8 billion annual turnover, and with estimated 255,000 people employed mostly in downstream activities (rolling, extrusion, castings, foil, wire rod, finishing, etc.). Considering indirect services and the fabrication of aluminum for end-user industries, the whole aluminum value chain provides employment for more than one million people in Europe [17]. EU aluminum industry accounts for 16% of total global aluminum production, half of which comes from recycling.

The recycling rate in Europe ranges from 63% (beverage cans) to more than 90% (building, automotive, transportation). Historically, more than 50% of the aluminum currently produced in the EU countries originates from recycled raw materials [13, 17]. European industry is the world leader in recycling with a recycling chain that is well established in Europe and the majority of aluminum in Europe actually produced from scrap [19].

The amount of aluminum used per car produced in Europe was almost tripled between 1990 and 2012. Weight savings presently achieved lead to an average annual fuel saving of 65 litres per car. A key target on the EU sustainability agenda is to decrease the average CO_2 emissions from cars and light-commercial vehicles. Some data of European Environment Agency suggests that the mass of European vehicles is increasing, hence it is more necessary than ever to introduce lightweight materials and techniques. Al-based materials allow for significantly reduced vehicle mass, thereby saving up to 50% over competing materials in many applications. Al-based materials represents a weight reduction potential that can be exploited immediately to reduce average emissions from future cars by 3-4 g CO_2/km, thereby improving the sustainability and safety of cars for future generation [20]. Aluminum is also essential for resource efficiency in buildings. Intelligent facades incorporating aluminum systems can decrease energy consumption by up to 50%. The aluminum beverage can is the world's most recycled container because it is easily collected, crushed, and recycled. In Europe, two-thirds of aluminum beverage cans were recycled in 2010, representing at least 24 billion cans, three times as many than 20 years ago [20].

In 2012, the EAA outlined its Roadmap to sustainable growth until 2050 [22]. It found that based on the Commission's long-term targets (92% reduction of emissions from the power sector) and the sector's commitment in terms of direct emissions (70%) a massive 79% reduction in emissions could be achieved by 2050. The retention of the industry in Europe offers the biggest potential in emissions' reductions whilst safeguarding skills and employment, as shown in Figure 13 [23].

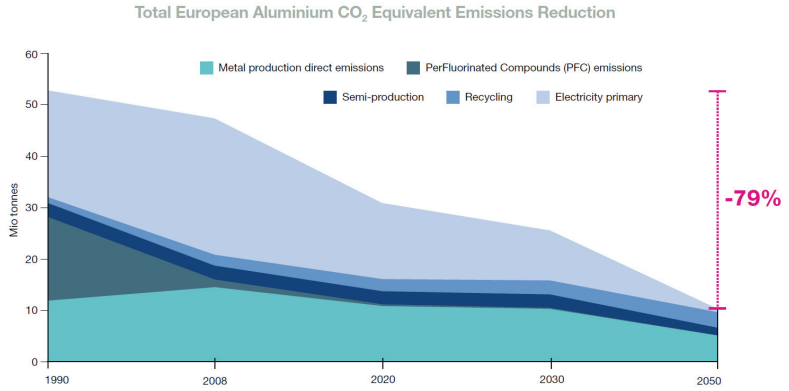

Fig. 13. Total European Aluminum CO_2 Equivalent Emission Reduction [22].

The global aluminum sector has witnessed year-on-year growth in demand for many years. Demand in Europe is also constantly on the increase, which differentiates it from other industrial sectors because the consumption of aluminum products is directly linked to wealth and increased economic activity and increase in using Al-based materials as a substitute to different competing materials, especially in the automotive and packaging sector.

Although European aluminum production grew since 1997 to mid-2008, this industry was strongly affected by the economic downturn and experienced significant volume reductions for all its sectors in 2009. Alumina production fell by more than 30%, primary production by 20%, and rolling and extrusion by 18% and 22% respectively. Several smelters have closed or reduced production all over Europe and others are under serious threat. The EU-27 share of primary production has globally decreased from 11% worldwide in 2004 to 6% in 2011 and may further decrease in the coming years if disinvestment trends are not reversed. Also, the semi-fabrication segments have not recovered pre-crisis levels, and it is significant to mention a growing scrap leakage. Since 2002, the EU has become a net exporter of approximately 1 Mt of scrap annually. Recyclable material is a key input of production, and this high level of exportation can considerably hinder the industry's world leadership [23].

As a consequence of these trends the risk of dependency on imports affects entire industry chain and many downstream facilities and SMEs. When demand is growing and the industry can cope with it and grow further, when the level of skills and innovation is high such as in Europe's plants, then de-industrialization is simply unacceptable [23].

Since the 2008 crisis, 11 smelters closed or curtailed out of 24 facilities, causing the reduction of EU27 primary Al-production for 36%. These trends caused the EU import dependency in 2013 of about 51%, and, again, it is significant to note the 22% of scrap export each year. During these years, the total number of employees has decreased by 16%, 29% for metal supply (primary and recycling segments) and 11% for semi-fabrication sectors respectively. Primary production of unwrought aluminum is electro-intensive, with 30% - 40% of production costs relating to the price of energy (incl. raw materials). Energy costs are particularly high in Europe when compared with global prices. Between 2005 and 2012 the European industry experienced a 38% rise in electricity prices compared with minus 4% in the US and 16% in Japan [24]. A significant part of the increase in energy prices is attributable to EU regulation or to national implementation of EU adopted targets. High energy prices and decreased availability of some alloying elements and scrap are putting strong pressure on aluminum sector.

In March 2010, the European Commission launched its growth strategy for the coming decade. In particular, the EU aims to encourage a growth which is smart (i.e. fostering knowledge, innovation, education and digital society), sustainable (i.e. making our production more resource efficient while boosting our competitiveness) and inclusive (i.e. raising participation in the labour market, the acquisition of skills and the fight against poverty). To do so, aluminum industry needs to remain competitive and be submitted to the same rules than its competitors. Even in the digital age and in the era of knowledge and services, manufacturing industries remain an essential foundation of the economy. Apart from providing a substantial part of employment and economic output, manufacturing industries are also fundamental to the provision of the infrastructure and equipment through which knowledge is developed and transferred, services are invented and provided. Industry supplies the essential hardware on which the whole software of the digital economy operates. Early 2013 the European Commission launched a Fitness Check on the legislative environment within which the aluminum industry operates, and Centre for European Policy Studies analyzed the cumulative costs impact attributable in energy, climate change, environment, competition, trade, and products policies. The study surveyed 46 plants accounting for more than 60% of EU production capacity, focusing on 8 policy areas and 52 legislative and non-legislative policies. The study concluded that the cumulative costs of EU regulation constituted more than one third of the competitive gap between Europe and the Middle East (the lowest cost producers) in 2012, but also emphasized the importance of the EU's aluminum industry [22, 26]. The following conclusions are emphasized in this study:

- It is possible to produce aluminum at competitive level in the EU, but cumulative regulatory costs are high;
- Electricity is one of the key factors affecting the competitiveness of the EU primary aluminum industry, as it represents over a third of total production costs. Consequently, EU and MS policies affecting the energy price have the greatest impact. 45% come from the increase in energy prices due to the effects of the ETS. EU environmental regulations are responsible for 13% of the burden;

- Primary aluminum producers that buy electricity in the current market are at risk of not being competitive since today's electricity prices would reduce their margins to an unsustainable level without an improvement in the power market conditions or without EU or national policy addressing these issues, more producers might be at risk of closing down;
- World demand is increasing and secondary production, i.e. recycling, is not able to satisfy demand. A high share of existing aluminum will not be available for recycling for decades as it is currently in long term use, for example in buildings and vehicles;
- Primary production is often connected to the specialized, high-tech use of aluminum downstream (e.g. in the mechanical industry). By losing it there is the risk of losing the whole value-chain [22, 26].

Research Perspectives

To compete today with America and Asia and to maintain its patent priority on metal-based products, Europe must increase its efforts to make metallurgical discoveries and develop innovation in its products and production capabilities. In that sense there is the necessity of reinforcing Europe's strategic industrial strength in metals and strengthening the "metallurgical infrastructure" in Europe consisting of academic, industrial and governmental organizations [25, 30].

The ongoing supply position of raw materials, including “critical materials”, insufficient support for the entire knowledge-chain from basic research in metallurgy to industrial applications in Europe, needs of reduction of the cost and shortening of the development cycle for a new product development are recognized as some of the main risks in this area. These areas, defined as "risk", suggest some directions for action, mainly in the field of working on innovative sustainable and bankable metallurgical processes to produce raw materials from lower grade and more complex resources, substitutes applications and recycling, with more effective knowledge transfer to industry, new material development, improvement of existing materials by incremental research, and materials’ processing. There is also a need for better fit between academic scientific results and industrial needs and effective knowledge transfer, followed by innovation in development of processes oriented toward the design of new and multifunctional materials [25, 30].

Europe is very prominent in the field of metallurgy – not only in academic research and invention, but also in industrial alloy production, down-stream processing, end-user applications and recycling. In order to maintain the high standard of living in Europe, it is essential to keep investing in the next generation of metallic products. This will help us aim for the future and tackle some of the societal challenges related to energy, renewable, climate change reduction, health care and job security. Many national studies have recently been carried out in Europe. They have all concluded that metallurgy, as a fundamental and applied research topic, is suffering from low levels of public investment and student enrolment. More must be done to promote R&D in this field in Europe [25-27]. Furthermore, given the huge added-value of metal products, totaling 1.3 trillion Euros per annum, Europe must increase and coordinate its efforts across the

entire materials value chain – from material discovery, alloy design, processing, optimization, to scale-up and in-service deployment, and in that sense Materials Science and Engineering Expert Committee recommended the creation of the "Metallurgy Europe" research and development programme, based on substantial and sustained contributions from the EC (Horizon 2020), national funding agencies, EU industry, EIRO forum partners and academia [26, 27].

This research programme has identified 17 future material requirements and 50 cross-sectoral metallurgical R&D topics, to be funded during the 2012–2022 time period. From selected future requirements for metals, alloys and metal matrix composites, following can be linked to the R&D activities with the Al-based materials: accelerated synthesis, discovery and insertion of new alloys into real applications; higher *specific* mechanical performance for lightweight structural alloys; new lightweight and damage-resistant material architectures, in particular for transportation; improved understanding and control of degradation, corrosion and irradiation phenomena; special physical or multifunctional properties; more predictive, physically-based simulation of properties and processing behavior of metal products; advanced material and defect characterization using microscopy (photons, electrons, ions), X-rays, neutrons, positrons or sonic methods; novel metal processing including improved alloy production, metal forming, near-net-shape and additive manufacturing, powder processes, HIP-ing, heat treatment, surface treatment, corrosion protection, joining techniques and recycling; lifetime performance assessment, including time-dependent micro-structural evolution and multi-parameter optimization of performance; resource-efficiency and more widely available or lower cost constituent elements; better environmental performance, REACH compliance, recyclability and sustainability, tracked by ISO-guided life-cycle analyses [26-30].

Fifty research topics have been identified as having high strategic and technical value for European industry in the coming decades. These topics are categorized according to (i) material discovery, (ii) novel design, metal processing and optimization, and (iii) fundamental understanding of metallurgy, and following list topics represents a strong interest for aluminum based materials:

- ***Materials discovery***: high-throughput synthesis and combinatorial screening technology to accelerate the discovery and implementation of new high-performance alloys and other next-generation materials; metal–matrix composites (MMCs), employing both micro and nano-scale reinforces, for a variety of lightweight structural components (Mg, Al, Ti) and thermal (Cu, Al) materials, core-shell precipitation-hardened alloys (e.g. Al–Li–Sc, Al–Mg–Sc, other), and associated heat treatment protocols, for high-specific strength components; non-consumable corrosion-resistant inert anodes of use in metal oxide electrolysis (Al, Fe, Ti, etc.); novel nanocrystalline metal hydrides (e.g. Mg, Al or Li-based) with very fast ab- and desorption kinetics, for hydrogen storage [25, 30];
- ***Novel design, metal processing and optimization:*** ultra-lightweight and cellular architectures, including metal foams, hollow spheres, etc; bulk nanostructured Al and Cu alloys for advanced electrical conductors with

high strength and electrical conductivity; fine-grained Ti or Al alloys for superplastic forming (SPF), for transport structures; new metallurgical methods for powder production and powder metallurgy, including for example new atomization, cold spraying, spray forming and coating techniques; metallurgy of surfaces and interfaces in order to design parts with improved corrosion, wear and fatigue properties, as well as novel interfaces with polymers for gluing [25, 30];

- ***Fundamental understanding of metallurgy:*** computational alloy design aided by electronic and atomistic modeling (DFT, MD, kMC), microstructural and micro-mechanical simulation, genetic algorithms, data mining and neural networks; predictive computer modeling of degradation phenomena, such as oxidation, corrosion, stress corrosion cracking, fatigue, creep, wear, radiation damage, liquid metal embrittlement and hydrogen embrittlement; fundamental studies of nucleation, modeling solid–liquid interface free energies and the discovery of novel grain refiners, for the purposes of producing very fine-grained equiaxed cast microstructures; deep understanding of fracture and damage mechanics of newly developed alloys, composites and material architectures; alloy behavior and fracture mechanics, in particular at cold and cryogenic temperatures, for Arctic, offshore and space applications [25, 30];

Some of the "champion topics" [30] in the areas of research, development and innovation of Al-based materials, according to the consensus by the EU experts, which are most important to address in the upcoming programmes to ensure that Europe retains a strong competitive position are listed in order of priority:

- 2000, 5000, 6000, 7000 alloys with improved strength, formability, corrosion resistance (of parent metals and welds);
- development of novel aluminum compound metal/metal and/or metallic/non-metallic structures (sandwich structures);
- development of new environmental friendly technologies for joining similar and dissimilar materials;
- extended use of aluminum compound metal structure with increased fire resistance;
- defect based metallurgy;
- intermetallics;
- powder processing and metallurgy [30].

Transport sector represents [30] one of the main driving forces in the field of metallurgy in Europe, in view of energy efficiency, light weighting, safety and recycling. Many studies have addressed the use of improved materials ranging from High Strength Steel, Aluminum, Sandwich Structure, aiming to reduce the weight, and typical selected challenges in improving energy efficiency by the use of Al-based materials are:

- Extend the use and qualities of 5xxx to 6xxx alloy grades;

- Modify alloys and heat treatment procedures to achieve more efficient age hardening;
- Improve mechanical properties, e.g. by small grain size (sub-100nm microstructures);
- Move to higher strength weldable alloys such as 7xxx series;
- Improve mechanical properties of joints when welded;
- Improve fatigue life and corrosion performances;
- Extended design concepts by use of specialty extrusions;
- Assess 5xxx Al-Mg alloys with high balanced Mg content (improved strength and formability including control of corrosion resistance);
- Improve protection technologies to insulate aluminum to prevent the galvanic action;
- Improve welding characteristics with similar / dissimilar material (incl. steel);
- Higher temperature capability of aluminum, beyond 250°C (300°C);
- Al-Li alloys (2098, etc) to broaden the supply base;
- Al-Mg-Sc alloy systems for weldability [30].

Education and Skills in European Metallurgy

There is a strong experts' and stakeholders' view that European industry needs more highly skilled people in metallurgy. Shortage of the qualified graduates/engineers in metallurgy and metal processing in general is a major concern. The advancement of engineers' skills is essential for the ensuring technological development and the enhancement of European innovation in the area of metallurgy, and it can be achieved through the upgrading of existing education programs and by the development of new programmes addressing research and innovation, designed for future needs. In general there is a need for an improved focus on metallurgical education and increase of the attractiveness of metallurgy as career stressing particularly systemic understanding and translate new research methods to metallurgy. Education on conventional metallurgy should be promoted with the use of case studies highlighted [30].

Summary

Metallurgy concerns the materials science and the technology of metals, the processing, product building and industrial exploitation of metals. It is the core activity underpinning primary metals production, alloying and processing, production and material flow. These activities account for 46% of the total manufacturing value and 11% of the total gross domestic product (GDP) in the EU [30, 31].

European countries are very prominent in metallurgical academic research, industrial alloy production, down-stream processing, end-user applications and recycling. In order to maintain the high standard of living in Europe, it is essential to keep investing in the next generation of metallic products.

The European aluminum industry represents the whole value chain, from alumina and primary production to semi-finished, end-use products and recycling. The demand for aluminum products in Europe is predicted to continue to grow with

encouraging perspectives in all key markets. A strategic value chain for Europe can be illustrated through €36.8 billion annual turnover, 255,000 direct jobs and over 1 million indirect jobs within Europe and 16% of total global aluminum production.

The comparison of the consumption of aluminum by end-use category in high-income and low- to middle-income countries show that the leading use of aluminum in many high-income countries is to produce goods in the *transportation sector*, and in low- to middle-income countries, aluminum is used mainly in the production of electrical systems and by the construction industry.

The world aluminum consumption is estimated to be 120 Mt in 2025. This represents a forecast of growth rate of 4.1 percent per year. Most of the increases are estimated to occur in low- and middle-income countries. Consumption in high-income countries is not expected to rise significantly on a per capita basis, but total consumption may increase modestly owing to population increases.

Aluminum industry in European countries needs to remain competitive and be submitted to the same rules than its competitors. Even in the digital age and in the era of knowledge and services, manufacturing industries remain an essential foundation of the economy, so there is the necessity of reinforcing Europe's strategic industrial strength in metals and strengthening the "metallurgical infrastructure" in Europe consisting of academic, industrial and governmental organizations.

There is also a need for better fit between academic scientific results and industrial needs and effective knowledge transfer, followed by innovation in development of processes oriented toward the design of new and multifunctional materials.

Many national studies have recently been carried out in Europe, concluding that metallurgy, as a fundamental and applied research topic, are suffering from low levels of public investment and student enrolment. There is a strong experts' and stakeholders' view that European industry needs more highly skilled people in the field of metallurgy.

References

[1] Zheng Luo, Antonio Soria, "Prospective Study of the World Aluminium Industry", EC Joint Research Centre, Institute for Prospective Technological Studies, http://ipts.jrc.ec.europa.eu, JRC40221, EUR 22951 EN, ISBN 978-92-79-07357-1, ISSN 1018-5593, DOI 10.2791/36024

[2] Menzie, W.D., Barry, JJ, Bleiwas, D.I., Bray, E.L., Goonan, T.G., and Matos, Grecia, 2010, "The global flow of aluminum from 2006 through 2025": http://pubs.usgs.gov/of/2010/1256/pdf/ofr2010-1256.pdf U.S. Geological Survey Open-File Report 2010–1256

[3] Subodh Das and Weimin Yin "Trends in the Global Aluminum Fabrication Industry", JOM, 2007, pp.83-87

[4] "Sustainable Materials Management - Materials Case Study 2: Aluminium", OECD Environment Directorate, http://www.oecd.org/environment/waste/46194971.pdf, OECD, 2010.

[5] "Aluminium, Environment and Society" International Aluminium Institute IAI and Svein Richard Brandtzg, Hydro Norway, 2012. www.hydro.com
[6] World bauxite mine production, http://www.statista.com/statistics/264964 /production-of-bauxite/
[7] U.S. Geological Survey, Mineral Commodity Summaries, January 2012
[8] U.S. Geological Survey, 2012, Aluminum [Advance Release], August 2013 [Revised November 2013],
[9] U.S. Geological Survey, 2014, Mineral commodity summaries 2014: U.S. Geological Survey, 196 ISBN 978–1–4113–3765–7, http://www.usgs.gov/ pubprod, U.S. Geological Survey, Mineral Commodity Summaries, January 2015
[10] http://www.world-aluminium.org/statistics/alumina-production/
[11] USGS Minerals Yearbook 2013, volume I, Commodity Report
[12] EC *DG Enterprise and Industry* "Report On Critical Raw Materials For The Eu Non-Critical Raw Materials Profiles" http://ec.europa.eu/enterprise/ policies/ raw-materials/files/docs/crm-non-critical-material-profiles_en.pdf
[13] "The state of aluminium production in Europe", European Commision, http://europa.eu/rapid/press-release_MEMO-13-954_en.htm, Last update: 12-02-2015
[14] "Aluminum use in Europe, Country Profile 2007-2010", http://www.alueurope.eu/aluminium-use-in-europe-by-country/
[15] European Aluminum Association "Environmental Profile Report for the European Aluminium Industry", Life Cycle Inventory data for aluminium production and transformation processes in Europe, April 2013-Data for the year 2010
[16] European Mineral Statistics 2008-12, World Mineral Statistics database, British Geological Survey 2014, Keyworth, Nottingham
[17] "Sustainability of the European Aluminum Industry 2010" European Aluminium Association http://www.alueurope.eu/pdf/2010_Sustainability_ of_the_European_aluminium_industry.pdf
[18] European Aluminium Association: http://www.alueurope.eu/key-topics/ recycling/
[19] "Assessment of Cumulative Cost Impact for the Steel and Aluminium Industry: Final Report Aluminium" Centre for European Policy Studies (2013), p. 20
[20] "Aluminium in Cars: Unlocking the Lightweight Potential", EAA (2013)
[21] "Two out of three aluminium beverage cans can be recycled in Europe", EAA (2012)
[22] "An aluminium 2050 roadmap to a low-carbon Europe: Lightening the Load", EAA (2012) http://www.alueurope.eu/wp-content/uploads/2012/03/03_An-aluminium-2050-roadmap-to-a-low-carbon-Europe.pdf
[23] “Agenda for Action-Towards A Competitive And Sustainable Aluminium Industry In Europe", http://www.alueurope.eu/wp-content/uploads/ 2011/08/EAA-Agenda-for-Action-20131127.pdf
[24] International Energy Agency, energy prices and taxes (derived from DECC, 2013)
[25] "Metallurgy Europe – A Renaissance Programme for 2012-2022", Science

Position Paper, European Science Foundation, MatSEEC, Pg. 5, www.esf.org/matseec, Printing: Ireg – Strasbourg June 2012 ISBN: 978-2-918428-74-9

[26] *"Europe 2020 Strategy – Towards a Resource-Efficient Europe"*, EC, Brussels, 26th January 2011, COM (2011) 21

[27] *"Materials for Key Enabling Technologies"*, EMRS and ESF MatSEEC Document, Strasbourg, June 2011 IREG – Strasbourg, ISBN: 978-2-918428-43-5

[28] *"Computational Techniques, Methods and Materials Design"*, ESF MatSEEC Science Position Paper, March 2011.

[29] *"EU Raw Materials Critical List"*, EC, Brussels, 17th June 2010, MEMO/10/263

[30] "Metallurgy made in and for Europe The Perspective of Producers and End-Users, Directorate-General for Research and Innovation", Luxembourg: Publications Office of the European Union, 2014 ISBN 978-92-79-43310-8 doi 10.2777/11914 European Union, 2014.

[31] "Prospects for the Global Metal Industry" International Metalworkers' Federation(IMF), Geneva, September 2000.

FUTURE PROSPECTS OF STEEL

Marjan Mačkošek

Štore steel d.o.o., Železarska cesta 3, 3220 Štore, Slovenia
marjan.mackosek@store-steel.si

Abstract

Presented paper deals with future prospect of steel industry in the world. Production and consumption of steel in the world is growing, and is more pronounced in the field of special steels. Half of the world's steel production came from China. For steel industry future there are two concepts: one which gives priorities to large integrated ironworks and a new one, favoring micro steel mills which are market niche players or are supplying certain local areas. Slovenian steelworks is successfully transformed in industry which is today a modern, efficient, successful business and a big exporter.
Keywords: steel, production, consumption, forecast

World steelworks

The world production of materials and metals, presented in Table 1, clearly shows that steel is a material of the past, present and future. Depending on availability it can not be replaced with any other materials or metals.

Table 1. Global materials and metals production, U.S. Geological survey, 2015

materials	mio ton
cement	4.180
steel	**1.650**
lime	350
salt	269
gypsum	160
sulphur	72
soda ash	52

metals	mio ton
steel	**1.650**
aluminum	49,3
copper	18,7
zinc	13,3
silver	0,026
gold	0,0028
platinum	0,00016

From the data of the global steel production (Figure 1) it can be seen that the production and consumption of steel in the world is growing. Meanwhile, the European steel market is a mature market where growth will be moderate, more pronounced in the field of special steels.

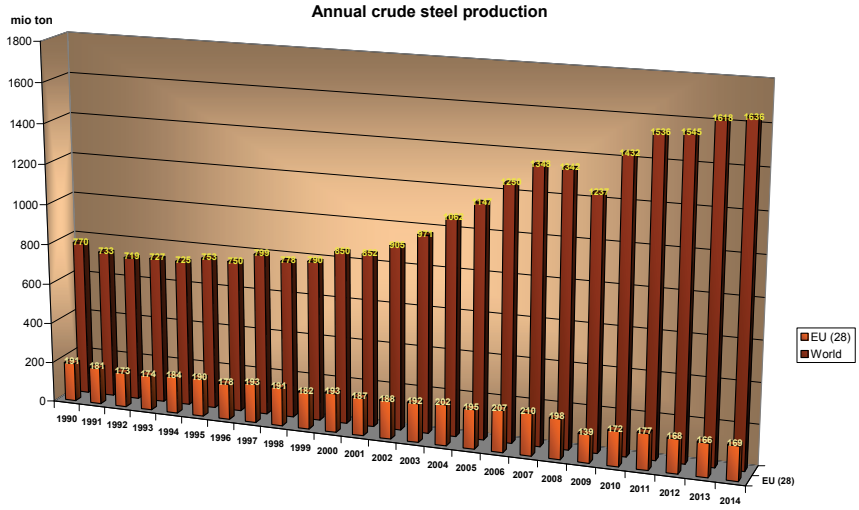

Fig. 1. Annual crude steel production, Worldsteel.org, 2015

In 2014 half of the world's steel production came from China, while in countries members of European Union only 10%. In Figure 2 distribution of steel production in 2015 is presented.

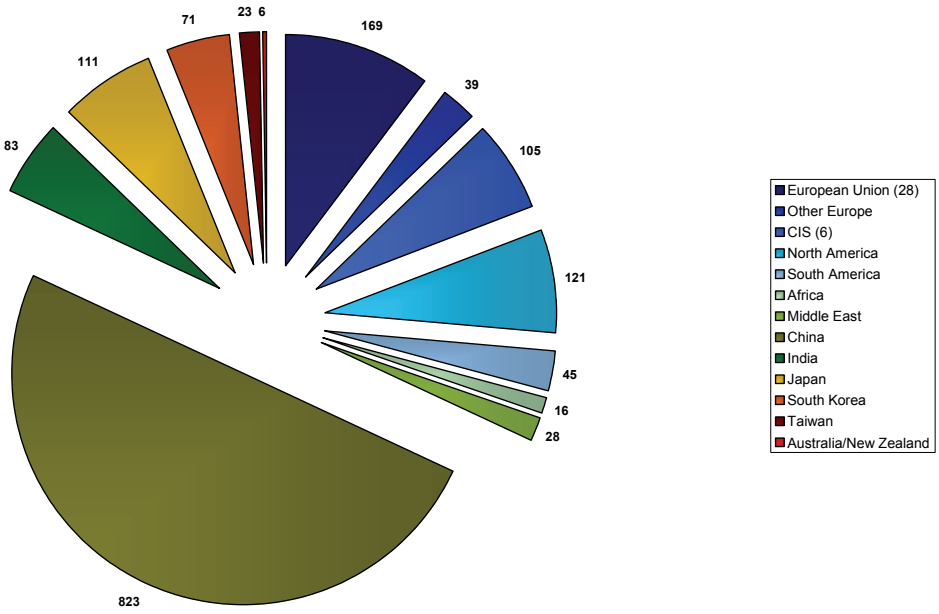

Fig. 2. Regional and countries steel production 2015, Worldsteel.org, 2015

According to the steel consumption per capita, presented in Table 2., it has the highest potential in fast developing economies, where construction steel will dominate due to urbanization and building of infrastructure. In the developed economies, the steel consumption per capita has stabilized at around 300 kg.

Table 2. Advanced and fast developing economies (BRIC) – Comparison with world average 2014, http://data.worldbank.org, World steel in figures 2014, Worldsteel

	GDP EUR per capita	urban ratio % of population	Steel use kg per capita
World	9.942	53	225
United States	49.704	81	300
Japan	36.202	92	516
European Union	33.208	74	274
Russian Federation	13.692	74	301
Brazil	10.503	85	132
China	6.379	53	515
India	1.405	32	58

Due to population growth in the world, world steel production over the next 15 years will grow according to the National Intelligence Council (Table 3 & Figure 3). In the year 2030 there will be 8.3 billion people on Earth, of which 60% will live in urban areas. If the consumption per capita will be at the same level as today, we would need 1,867 million tons of steel annually. In the case of consumption of 300 kg steel per capita, as much as 2.490 million tones will be needed.

Table 3. Steel consumption development, National Intelligence Council, Global trends 2030: Alternative Worlds

	2015	2030
Population	7.000.000.000	8.300.000.000
Urban population	3.500.000.000	4.900.000.000
Steel use 225 kg per capita	1.575.000.000	1.867.500.000
Steel use 300 kg per capita		2.490.000.000

Forecast of estimated infrastructure spending for period 2013-2030 presented in Figure 4, confirms that the construction of all types of infrastructure requires large quantities of all types of steel.

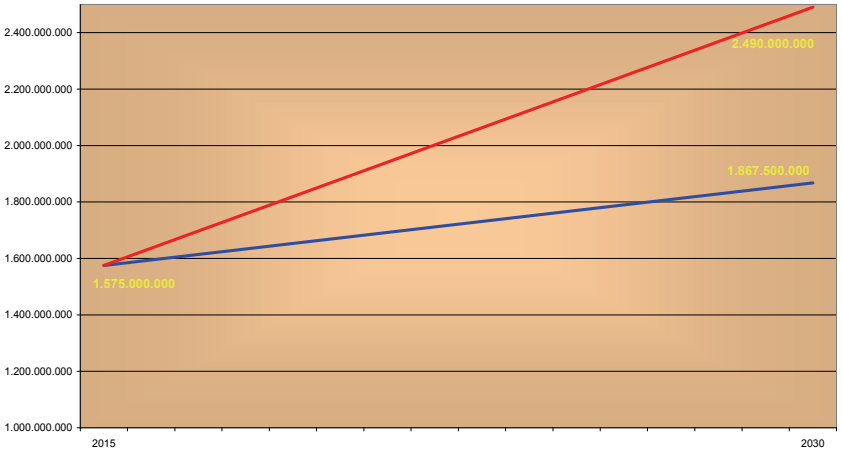

Fig. 3. Steel consumption development (tonnes), National Intelligence Council, Global trends 2030: Alternative Worlds

Despite attempts for large concentrations of producers (it was quite intense in China, which has 6 of the 10 largest companies), with the exception of Arcelor Mittal, no group has increased production to more than 50 million tonnes. Thus, in business with steel there is still room for a multitude of small independent producers, which are mostly locally oriented. Top 20 of steel producers in the world are presented in Figure 5, with their production capacities.

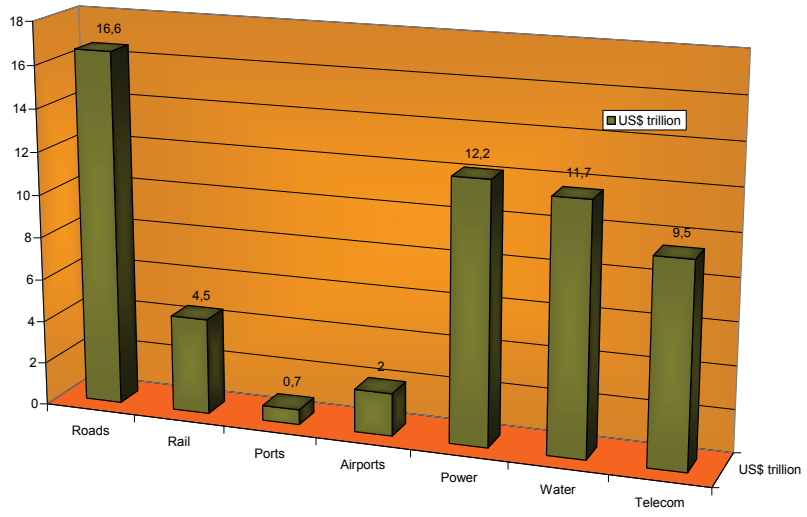

Fig. 4. Estimated infrastructure spending 2013-2030 (US$ trillion), McKinsey global institute, 2013

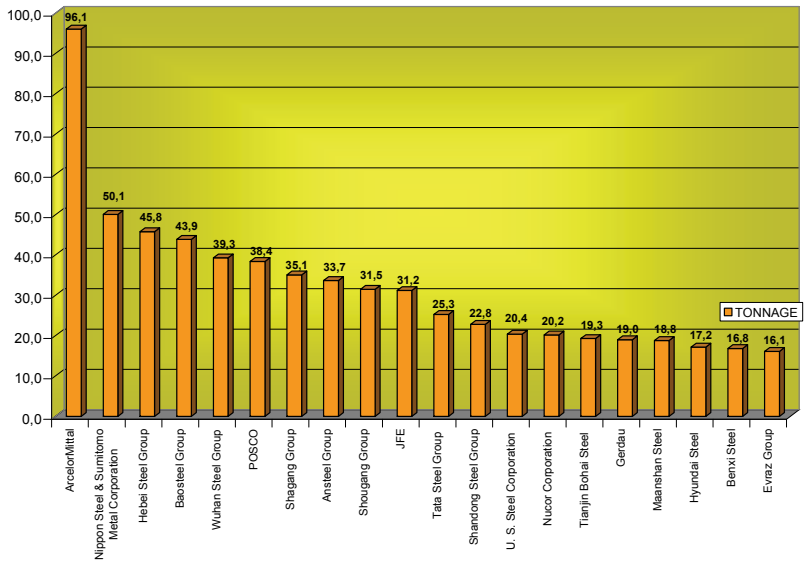

Fig. 5. Top 20 steel producers, Worlsteel.org

There are two concepts, a previous one, which gives priorities to large integrated ironworks and a new one, favoring micro steel mills which are market niche players or are supplying certain local areas.

The successful concept of the micro steelworks was developed by NUCOR from the USA, where 90 companies produce more than 20 million tons of steel.

Fig. 6. Nucor-location map, http://www.nucor.com/

The concept of micro steel works has enabled the development of technologies for processes using much less space than is required for the integrated ironworks.

For example, Nucor thin-strip casting needs 60 m length, while conventional slab casting needs 500 – 800 meter length, as presented in Figure 7.

Fig. 7. Length difference between Nucor thin-strip casting and conventional slab casting, http://www.nucor.com/

Slovenia Steelworks

In the period after 1990, Slovenian steelworkers have successfully transformed the steel industry which is today a modern, efficient, successful business and a big exporter.

Figure 8 shows Slovenian crude steel production for period 1992 – 2014, and Figure 9 Slovenian economy export rates for 2014.

The concept of efficiency is based on four strategic directions:

1. Manufacturing in the mini steel mills,
2. To be a niche manufacturer,
3. Automated production,
4. Smart specialization;

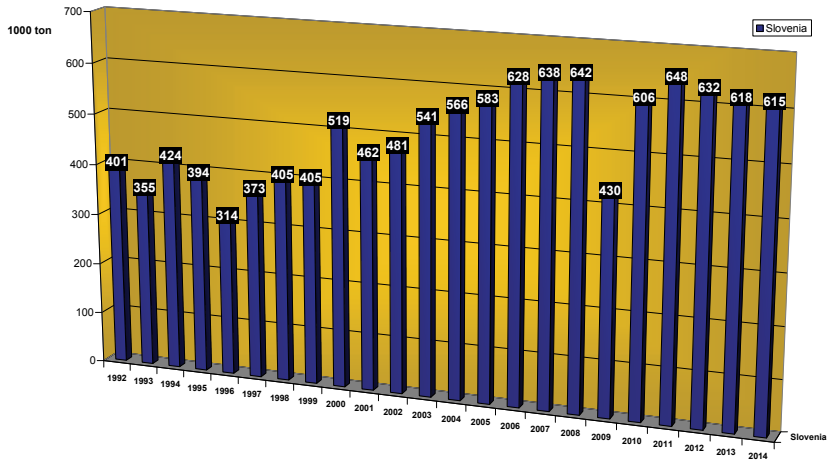

Fig. 8. Slovenian crude steel production 1992 – 2014, Worldsteel.org

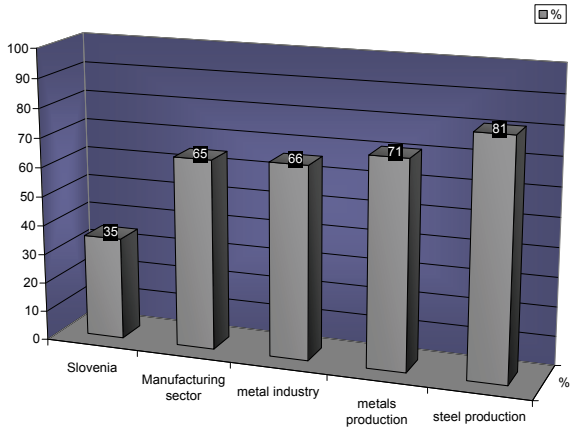

Fig. 9. Slovenian economy export rates, Slovenian Chamber of Commerce, 2014

Niche products Slovenian steelworks are:

- Acroni - stainless quarto plate,
- Metal - tool steel,
- Store Steel - steel for automotive industry;

The concept of efficiency, niche products and main Slovenian steelworks are presented in Figure 10.

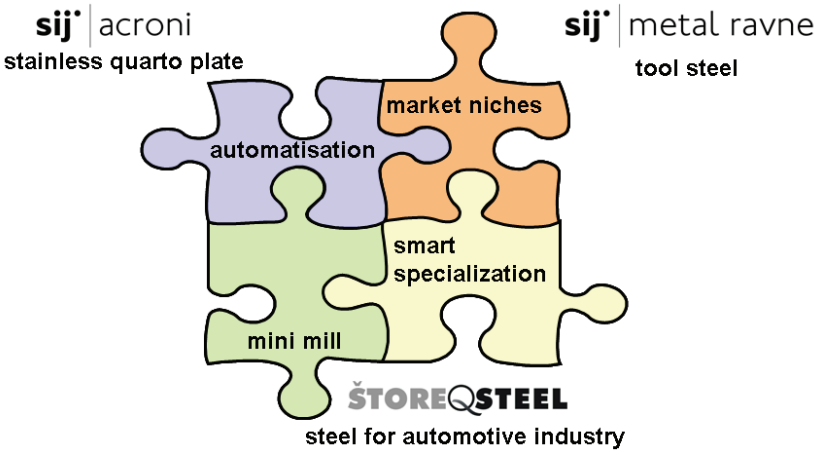

Fig.10. Slovenian steel producers

In Slovenia a Strategic Council for metallurgy was formed, which besides the steelworkers also includes other metals producers, universities and research institutes (Figure 11).

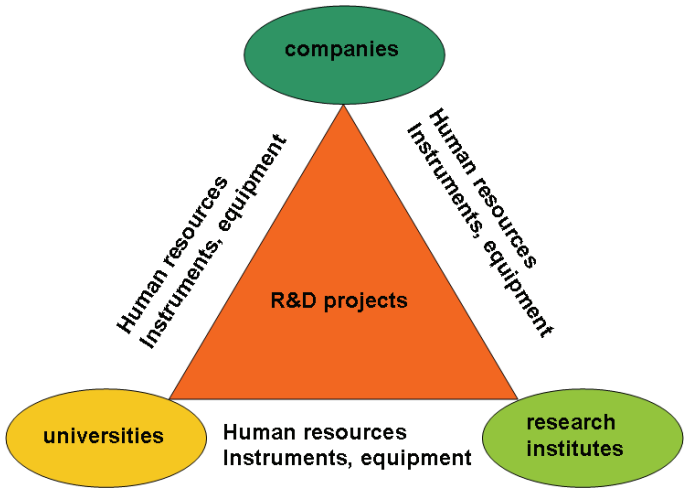

Fig. 11. Concept of Strategic Slovenian council of metallurgy

Concluding remarks

Strategic Council for metallurgy has created Strategy of Metallurgy development in Slovenia 2015 – 2025. Primary R&D areas of metallurgy in Slovenia are:

1. Recycling of metallic materials and metallurgical waste with the aspect of sustainable production and environment.
2. Advanced metallic materials for complex applications.

3. Design of metallic materials and complex products by casting and transformation.
4. The composite and gradient metal based materials.
5. Special metals and alloys for use in specific advanced areas (medicine, dentistry, electronics, magnets, optics, telecommunications, energy, etc.).
6. The modeling and simulation of metallurgical processes.

In the European development programme Horizon 2020, a European programme Metallurgy Europe has been prepared – a Renaissance program for period 2012-2022, where metallurgy due to the strategic importance of metallic materials in all areas has been ranked in the priority areas of development.

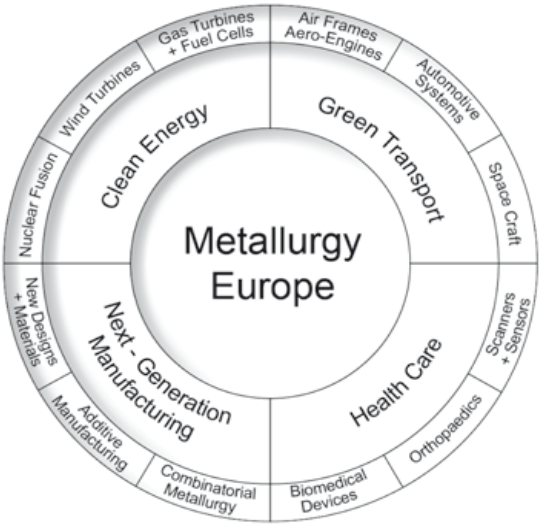

Fig. 12. Concept of Metallurgy Europe, Eurekanetwork.org

The strategic importance of metallurgy for economic efficiency has been recognized by the Slovenian government, which includes Slovenian metallurgy in the European development projects.

NEMAK SOLUTIONS FOR HIGHLY LOADED CYLINDER HEADS

M. B. Djurdjevic[1], B. Stauder[1], M. Rafetzeder[2], F.J. Feikus[2] and J. Gontarev[1]

[1]*Nemak Linz GmbH, Linz, Austria*
[2]*Nemak Europe GmbH, Frankfurt a. M., Germany*

Abstract

Nemak is a global automotive supplier with 35 manufacturing facilities located in 14 different countries in North and South America, Europe, and Asia employing over 20,000 people worldwide, Nemak is ready to meet the demands of the automotive industry around the world. In order to satisfy growing demands of the customers Nemak is working on R&D projects to process-, material-, and product innovations. Recently achieved results of two of R&D projects are presented in more detail.

Key words: cylinder head, high performance engine, AlCu7MnZr alloy, NemaCoat ® enamel coating

Introduction

Nemak started operations in 1979 (figure 1) and is currently the worldwide leading supplier of Aluminium cylinder head and block castings for passenger car engines. The company presently employs more than 20000 people in 35 plants worldwide (figure 2).

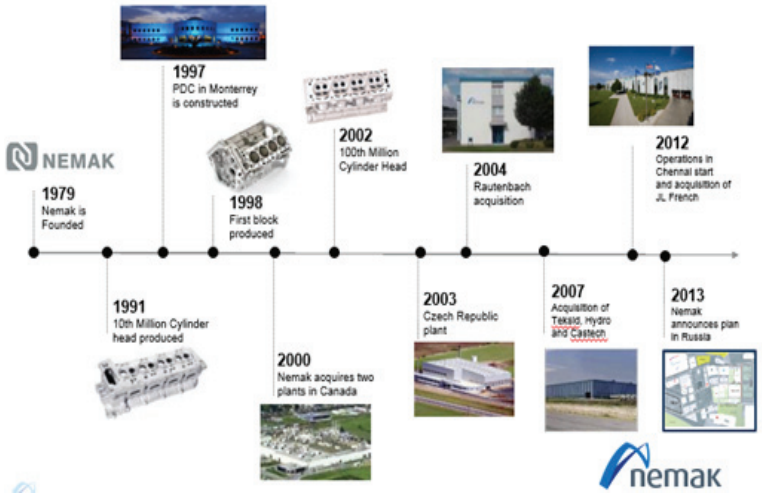

Fig. 1. Nemak's growth history

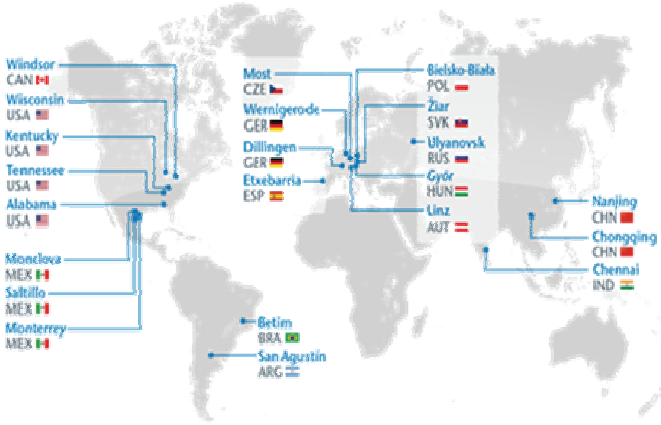

Fig. 2. Plant locations in the world

Figure 3 shows Nemak's high-tech aluminum components (cylinder heads and engine blocks) as well as structural and transmission parts produced for most of the car producers worldwide. Talent development, continuous investment in research, technological innovation, and a sustained growth are the stepping-stones behind Nemak's global leadership in its segment.

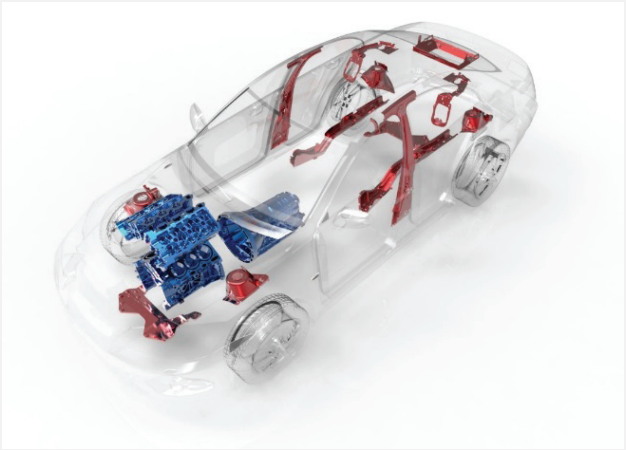

Fig. 3. Al-castings for power train, transmission and car body

Research & Development at Nemak

Strong investment into R&D is one of the key success factors for Nemak in order to achieve and maintain a strong position as a leading supplier of aluminum cast components for the automotive industry. As a part of Nemak's R&D, the Nemak Linz R&D team is currently working on various R&D projects. Two of these projects are highlighted as follows.

New Nemak Alloy for High Performance Engines

Due to constantly increasing demands on the power density of the engines, increasing thermal and mechanical loads have to be carried by the standard aluminum alloys (family of Al-Si and Al-Si-Cu alloys) that are now reaching their limits. New generations of engines require new aluminum alloys that will be able to sustain the highest demands of mechanical properties especially at elevated temperatures (>250 °C). Two groups of casting alloys can be recognized that may provide better mechanical properties at elevated temperatures. The first one is based on the attempt to improve the mechanical properties of already applied AlSi and AlSiCu series of hypoeutectic and eutectic alloys by adding elements such as Ti, Zr, V, Cr, etc. to improve both intermediate and elevated temperature properties of engine parts. According to past findings these alloys provide adequate tensile and yield strength at temperatures closely up to 250°C but have insufficient durability to be considered for further applications. The second group are AlCu alloys, which were in the focus of Nemak's R&D work. The newly developed AlCu alloy [1], offers significant potential to be used in future engines due to the excellent mechanical properties at elevated temperatures.

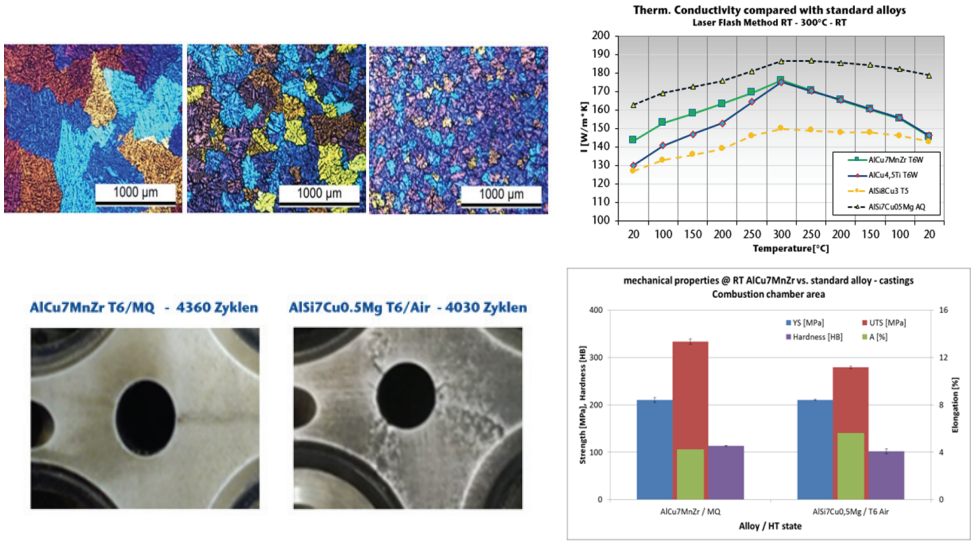

Fig. 4. Achieved metallurgical (grain size), thermo-physical (thermal conductivity) and (thermo-) mechanical properties of the new alloy AlCu7MnZr.

Figure 4, illustrates some metallurgical, physical and mechanical properties of the alloy, which have been further improved through the following processes: melt treatment, heat treatment and alloying element additions. Melt treatment was carried out to improve the integrity of as cast parts (lower tendency to hot tearing formation). With proper T6 heat treatment which comprises solution heat treatment, quenching and artificial aging, it has been achieved the best compromise between strength and ductility. Through addition of alloying elements (Zr, V, …) it has been improved the mechanical properties of AlCu alloys in as cast and/or age-hardening

conditions. Achieved results related to mechanical properties at room temperature and other quality control assessments of produced cylinder heads have confirmed Nemak expectation that the AlCu7MnZr alloy has significant potential to be used in automotive industry in particular for the production of cylinder heads. Further investigations on corrosion behavior will support the results obtained so far to establish a new high performance AlCu7MnZr alloy for highest demands in the automotive industry.

Thermal insulation of cylinder head - exhaust system to improve engine performance

Beside demands on the higher engine power, automotive producers are facing with some additional demand concerning elevated exhaust temperature and heat input into the coolant in order to avoid damage for local engine components caused by the local hot gas stream. In cooperation with company Kühn Email, Nemak Linz GmbH developed an insulating coating for complex exhaust channels that meets the high requirements in terms of thermal stability [2]. Inorganic, non-metallic, amorphous material provided with functional additives is a basic of coating. According to Figure 6 (a), NemaCoat® consists of two sections: (i) the base coating ensures a perfect connection to the aluminum, while (ii) the deck coating is then the "functional layer" to the flow channel, which can be separately adjusted based on the needs. As figure 6 (b) shows, conducted trials on the hot gas test cell have achieved a reduction of heat transfer by 16%.

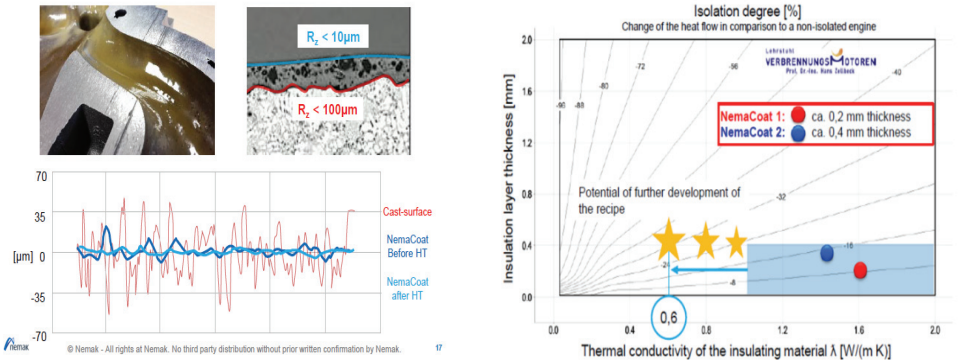

(a) (b)

Fig. 5. (a) Surface smoothing after application of NemaCoat®
(b) Change of the heat flow into cooling system in comparison to a non-insulated exhaust gas manifold

The development work in the establishment of the NemaCoat® led to a production-ready process for producing an insulating layer on cast aluminum surfaces. Theoretical calculations of the motor potential and verification on a hot gas test confirmed the efficiency potential. Investigation of the coating structure confirmed under all load conditions a very high layer durability. This was verified by hot and cold thermal shock tests and engine test meanwhile.

Conclusions

Nemak's leading position in manufacturing complex, high-tech aluminum components for the global automotive industry is based on establishing excellence on four key pillars: People, Systems, Core Processes and Innovation. The demonstrated R&D portfolio thus is further strengthening this leading supplier position. This article illustrated some of Nemak R&D activities and their importance to satisfy growing demands of automotive industries. Driven by the synergy of the high performance Rotacast® process and the availability of the innovations with high professional employees, Nemak will continue to be a leading supplier and partner for the automotive industry in the future.

Literature

[1] L. Kniewallner, M. Rafetzeder, B. Stauder, M. Djurdjevic, F. J. Feikus, "Entwicklung und Anwendung einer AlCu-basierten Hochleistungsgusslegierung für Zylinderköpfe", VDI Berichte 2254, Gießtechnik im Motorenbau, Magdeburg, 10.-11.2.2015, pp. 115 - 132.

[2] R. Gosch, F.J. Feikus, B. Stauder, J. Gontarev, M. Rafetzeder, "Thermisch isolierte Gaskanäle in Zylinderköpfen zur Verbesserung des Motorverhaltens", VDI Berichte 2254, Gießtechnik im Motorenbau, Magdeburg, 10.-11.2.2015, pp.47 - 58.

PHYSICAL-METALLURGICAL ASPECT OF FORMATION OF CORE–SHELL AND HOLLOW NANOSPHERES

S. Šturm[1], K. Žužek Rožman[1], B. Markoli[2], E. Sarantopoulou[3], Z. Kollia[3], A. C. Cefalas[3] and S. Kobe[1]

[1]Department for Nanostructured Materials, Jozef Stefan Institute, 1000 Ljubljana, Slovenia
[2]Department of Materials and Metallurgy, Faculty of Natural Sciences and Engineering,University of Ljubljana, 1000 Ljubljana, Slovenia
[3]National Hellenic Research Foundation, 11635 Athens, Greece
E-mail: bostjan.markoli@omm.ntf.uni-lj.si

Abstract

Nanotechnology literally means any technology on a nanoscale that has applications in real world. Nanotechnology encompasses the production and application of physical, chemical, and biological systems at scales ranging from individual atoms or molecules to submicron dimensions, as well as the integration of the resulting nanostructures into larger systems. Nanotechnology is likely to have a profound impact on our economy and society in the early 21st century, comparable to that of semiconductor technology, information technology, or cellular and molecular biology. Science and technology research in nanotechnology promises breakthroughs in areas such as materials and manufacturing, nanoelectronics, medicine and healthcare, energy, biotechnology, information technology, and national security[1].

Our research efforts were focused, on fabrication of hollow nanospheres produced via PLA in nitrogen ambient gas based on Al-O, Co-Pt and Sm-Fe(Ta)-N system, which could be technologically relevant in biomedical, magnetic and catalytic applications. The structure and composition of core-shell and hollow nanospheres were characterized by scanning/transmission electron microscopy (STEM/TEM), energy-dispersive x-ray spectroscopy (EDXS) and electron energy-loss spectroscopy (EELS). Combined STEM-EELS technique was applied to calculate nitrogen density and pressure inside the voids within individual nanospheres, providing data for reconstructing formation mechanism of core-shell and hollow nanospheres. Obtained results confirm the idea of generalized formation mechanism of core-shell and hollow nanospheres, where the spheres are nucleated at relatively high pressure and temperature in the plasma plume. Hollow spheres are afterwards formed by a combined mechanism of gas intake, gas condensation within the saturated liquid sphere and melt-solidification phenomena. The proposed formation mechanism opens the possibilities for the fabrication of metallic hollow nanospheres in various material systems [2,3].

Introduction

The discovery of novel materials, processes, and phenomena at the nanoscale and the development of new experimental and theoretical techniques for research provide fresh opportunities for the development of innovative nanosystems and nanostructured materials. The properties of materials at the nanoscale can be very different from those at a larger scale. When the dimensions of a material are reduced from large size, the properties remain the same at first, then small changes occur, until finally, dramatic changes in properties occur when the size drops below 100 nm. If only one length of a three-dimensional nanostructure is of nanodimensions, the structure is reffered to as a quantum well. When two sides are of nanometer length, we can consider the matrial to be a quantum wire. Finally, quantum dot has all three dimensions in the nano range [1].

Materials can be nanostructured for new properties and novel performance, which paved new ways in science and technology with the advent of Micro- and nanosystems. This includes micro/nanoelectrical systems (MEMS/NEMS) and MEMS/NEMS for biological and medical applications that are reffered to as bioMEMS/bioNEMS or medMEMS/medNEMS [1].

Applications of MEMS/NEMS range from industrial, consumer, defense, and biomedical field resulting in construction of MEMS accelerometers, piezoresistive pressure sensors, disposable blood pressure sensors, thermal inkjet printheads, micromirror arrays, optical cross-sections in telecommunications, chemical/biosensors, picosatellites, fuel cells, hydraulic and pneumatic consumers etc. [1].

Our research efforts were focused on fabrication of hollow and core-shell nanospheres that could see applications in medical field. This is mainly due to their unique properties and the fact that it is possible to control the properties over the shell to some extent. A large number of reported synthesis procedures are based on using prefabricated nanostructured materials as templates, which are subsequently followed by various chemical transformations, such as diffusion, oxidation, ion exchange and galvanic replacement, resulting in the formation of hollow structures [4–7]. As an example, the synthesis of hollow nanostructures from their solid counterparts can be achieved using the Kirkendall effect, where the voids are created by the accumulation of vacancies resulting from different ion mobilities. Based on the Kirkendall effect, different binary metal–oxide or metal–sulfide nanospheres can be formed via a two-step synthesis that involves the formation of a metal particle, which is then followed by subsequent oxidation processing [8,9].

We have chosen three different systems, Al-O, Sm-Fe(Ta)-N, and Co–Pt as very promising system scovering areas of magnetism, and catalysis, with the possibility to fine tune the physical properties by adjusting both the composition and the morphology of nanoparticles [10–12]. In our studies we have demonstrated that by applying PLA in an ambient nitrogen gas the gas-filled hollow or core-shell like nanospheres can be successfully produced, where the composition of the particles is controlled by the target composition. By means of various techniques of transmission electron microscopy we aimed to characterize both structure and composition of synthesised nanospheres as well as to determine the nitrogen

pressure inside the individual voids in the case of hollow nanospheres. We then further employed the experimental data for reconstruction of the formation mechanism of nanospheres, and suggestions towards the general formation mechanism for gas-filled nanospheres in other metallic systems have been made.

Materials and methods

The PLA apparatus consisted of a molecular fluorine laser at 157 nm and a stainless steel vacuum chamber, placed in a computerized X–Y–Z–h micro-translation stage, schematically shown in Fig. 1.

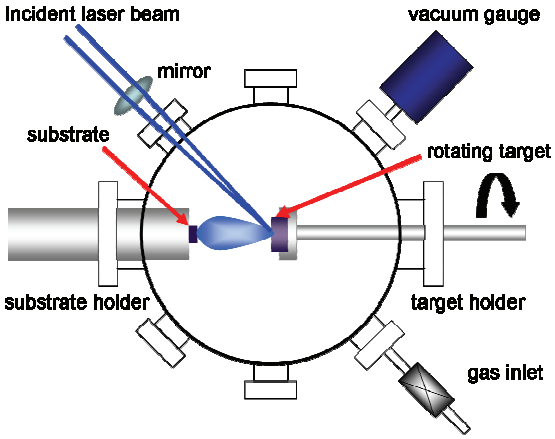

Fig. 1. Schematic set up of the applied PLA apparatus

Each time a freshly polished alloy target with the composition Al99.99, Co48Pt52 and Sm13.8Fe82.2Ta4.0 was positioned perpendicular to the laser beam and focused with a high-quality CaF_2 lens through a 5 mm aperture in a compact geometry. The distance between the target and the substrate was fixed at 1 cm. The deposition parameters were 30 mJ, a 3–5 J cm^{-2} fluence (~600 lm laser spot size on the target) at 15 Hz. The nanoparticles were deposited in high-purity nitrogen at 0.1 MPa. The nanoparticles were deposited directly on a lacy-carbon copper grid. The latter deposition procedure allowed a direct investigation of the obtained product by the use of transmission electron microscopy (TEM).

For the detailed structural and compositional investigations of hollow nanospheres a field-emission (scanning) transmission electron microscope TEM/STEM (JEM-2010F) operated at 200 keV (Cs = 0.48 mm) equipped with a high-angle annular dark-field (HAADF) detector, energy-dispersive X-ray spectroscopy (EDXS), (LINK ISIS EDS 300) and electron energy-loss spectroscopy (EELS) (Gatan PEELS 766) was applied. The probe size in the STEM was 2 nm, while the HAADF collection angle was set between 60 and 160 mrad. The EELS spectra were background-subtracted, and corrected for the dark current and the channel-to-channel gain variation of the photodiode detector. The full width at half maximum (FWHM) of the zero-loss line was 1.2 eV. Prior to the quantification of the EELS spectra the effect of the plural scattering was removed by applying the Fourier-ratio deconvolution method [13]. The number density of the nitrogen atoms

in the voids of the nanospheres was determined by a modified procedure initially proposed for measuring the density of He atoms in nanometre-sized bubbles in steels using a combined STEM–EELS technique [14,15]. The following equation gives the number density of nitrogen atoms (nN) in the void: nN =IN/(σNIZLd) IN and IZL are the intensities measured from the N–K ionization edge and the zero-loss peak, respectively. The corresponding intensities were integrated over an energy window (ΔE) of 8 eV. The intensity of the N–K edge was measured starting from the ionization edge onset. σN is the angle-integrated hydrogenic cross-section for the nitrogen K-shell ionization, calculated for the experimental collection angles. d represents the measured diameter of the void. This equation assumes that the void diameter is significantly larger than the electron beam and the measurement was performed in the central region of the void, providing localized information on an individual void. The error values related to the accuracy in the determination of the cross-section, the N–K signal and the void diameter were estimated to be ~10%. The total error of the calculated density, applying standard error-propagation relations, amounts to 17%.

Results and discussion

Crystal structure and composition analysis of nanospheres deposited on a Si-Ta substrate

Using HRTEM we could establish that spherical droplets or nanospheres with diameters between 10 and 100 nm were generated during the deposition. The nanocrystalline layer was composed mainly of iron and samarium with a high concentration of oxygen and trace amounts of tantalum and nitrogen. Spherical droplets, which were the focus of these investigations, were found either isolated, in the form of necklaces-like structures, or agglomerated. The majority of the observed spheres deposited on the Si substrate were amorphous, which was verified by the corresponding selected-area diffraction pattern (SAED) analysis. All the analyzed amorphous spheres were oxidized, rich in iron and samarium, with the amounts of tantalum being of the order of a few atomic per cent.

Besides amorphous spheres, core–shell structured spheres were occasionally observed, which are characterized by a crystalline central part and an outer amorphous rim. The crystalline region of the sphere was confirmed by the presence of lattice fringes, which are observed in the enlarged section of the central part of the sphere. We then additionally executed the fast Fourier transform (FFT), which was calculated from the related section of the HRTEM image, reveals discrete reflection points, proving the periodic structure of the inner sphere region.

The corresponding chemical composition of the amorphous and core–shell spheres, neglecting the presence of oxygen, was $Sm_{46}Fe_{51}Ta_3$ and $Sm_{27}Fe_{71}Ta_2$, respectively. When including the recorded concentration of oxygen the obtained composition was substantially modified to $Sm_{20}Fe_{22}Ta_1O_{57}$ and $Sm_{15}Fe_{39}Ta_1O_{45}$, respectively. Although the compositions from the central part of the amorphous sphere might represent the overall composition of a sphere, this might not be the case for the spheres composed of the amorphous shell and the crystal core. In fact, the EDXS spectra that were acquired from the core regions of several spheres

were consistently showing higher concentrations of iron compared to the measurements performed in the region of the amorphous shell.

By dividing the nanospheres into the amorphous surface and crystalline core segment and taking into account the atomic fractions of Fe, Am, Ta and O in the analyzed volume we could get the correct concentration values. So, the final composition of the crystalline core yields the composition $Fe_{90.3}N_{9.7}$.

The analysis of nanospheres deposited directly on a lacey-carbon copper grid

The direct ablation of the target on a lacey-carbon copper grid produced comparable final products to those produced when the material was deposited on a Si–Ta substrate. The spheres were mainly homogeneous, amorphous and oxidized. Beside these, spheres with a darker spherical contrast in theircentral regions were, in addition, regularly observed. According to thickness measurements and HAADF–STEM image analysis the dark round contrast can only be attributed to the formation of voids. It was estimated that 15% of all the analyzed spheres were hollow. The average composition, obtained from the solid bulk regions of such spheres, neglecting the oxygen concentration, was $Sm_{31.5\pm4.9}Fe_{67.8\pm5.1}Ta_{0.7\pm0.8}$. The large standard deviation of tantalum is due to the low measured concentration, approaching the detection limits. Nitrogen, on the other hand, was only measured in all cases, only in the void, and not in the bulk regions or within the amorphous homogeneous spheres.

Based on results gained by various methods we could propose the model for the formation of the core–shell nanospheres and the hollow nanospheres. Our assumptions are founded on phase relations and equilibria known from the binary Sm–Ta, Fe–Sm, Fe–Ta, Fe–N, Fe–O, Sm–N, Sm–O, Ta–N and Ta–O diagrams, since the ternary Fe–Sm–Ta and quaternary Fe–Sm–Ta–N–(O) diagrams are not known. The nanospheres are most likely to be formed from the melt, which means they are molten when leaving the surface of the target. In parallel the atomization of the target is in progress, which results in the deposition of material that is a few nanometer in size, in which the examined nanospheres are embedded. All the examined nanospheres and the nanocrystalline deposits were found to be oxygen rich (approx. 50 at. %). The different average chemical compositions of the deposited spheres are believed to be due to the marked inhomogeneity of the Fe–Sm–Ta target. Looking at the average chemical composition of the nanospheres it was found that when the initial Fe/Sm ratio was close to 1:1 the nanospheres were compositionally homogeneous with an amorphous structure. The average composition of these spheres corresponded to $Sm_{46}Fe_{51}Ta_3$. If the initial composition of the droplet had a higher Fe/Sm ratio, i.e., close to two, complex nanospheres were formed. They have either a core–shell ($Sm_{27}Fe_{71}Ta_2$) or a hollow ($Sm_{32}Fe_{67}Ta_1$) structure. Since the diffusivities of oxygen and nitrogen are a few orders of magnitude higher in a molten mixture of Fe–Sm–Ta than in solid oxides or an iron-rich solid solution it is believed that the molten droplets are enriched with nitrogen and oxygen as soon as they are formed and during the flight time. The presence of oxygen in this system is considered as an impurity that originates from the N_2 gas source. The solidification process of the molten droplets enriched with nitrogen and oxygen, due to the high cooling rates, starts immediately after the deposition on the substrate. In the first step, the liquid-phase

separation and the directional cooling from the outer parts of the droplet into the interior results in the formation of a solid, amorphous Sm–Ta–O-rich shell, which was observed in both cases, i.e., for the core–shell and hollow spheres. Sm and Ta have a high affinity for O_2 and are prone to form Sm_2O_3 and Ta_2O_5 (the G is much lower, by approx. 1500 kJ, than for Fe_xO_y [16]) which in turn are susceptible to form amorphous structures if the cooling rates are high [17]. On the other hand, iron has a high affinity for nitrogen, forming an interstitial solid solution (the max. solubility of N_2 in iron is 10.3 at. %) [18]. During the cooling and solidification of the Sm–Ta–O-rich outer rim, the melt in the inner part of the sphere is continuously enriched with iron and dissolved nitrogen. At the same time, the solid oxide rim prevents any significant outwards diffusion of nitrogen, forcing it to stay in the Fe-rich melt, which is entrapped in the sphere.

The amount of dissolved nitrogen in the remaining melt is believed to be the determining parameter for the core–shell or hollow nanosphere formation. If the melt contains more than an equilibrium amount of nitrogen determined by the phase diagram it is very likely that the melt solidification will result in a hollow nanosphere. On the other hand, if the amount of nitrogen is such that it can be incorporated into the solid Fe, the formation of core–shell structures is more likely to happen.

Crystal structure and composition analysis of CoPt nanospheres

CoPt-based nanospheres were produced by a direct ablation of the CoPt target on a lacy-carbon copper grid. Crystal structure of CoPt-based nansopheres was determined by comparing the experimental and calculated SAED patterns. The experimental and corresponding rotational averaged SAED pattern matches with the calculated diffraction pattern, based on the Co50Pt50 face-centred cubic (fcc) phase with a cell parameter a = 0.384 nm [19]. A representative nanobeam electron-diffraction (NBED) pattern, acquired from individual spheres, proves that they are single crystalline. Some spheres contained planar defects, i.e. stacking faults or twins. They are most probably caused by internal stresses due to the high cooling rates and are typical for metals with the fcc structure [20].

Although a distinct difference in contrast between inner and outer regions of nanospheres was established no significant changes in the crystal structure and/or crystal orientation could be determined. It turned out that the compositional difference between the central region and the adjacent shell region, i.e. $Co_{CENTRAL}/Co_{SHELL}$ at.% ratio, was 1.05 and responsible for the contrast differences. The exact compositions of the central and the shell regions were $Co_{57}Pt_{43}$ and $Co_{54}Pt_{46}$, respectively. However, such small compositional differences cannot explain the almost 30% drop in the intensity measured from the intensity profile. Most likely reason for that is the presence of the voids within the nanospheres themselves. Eventhough the analysed sphere's diameter ranged between 24 and 41 nm, with a mean value and standard deviation of 34 ± 5 nm, no significant correlation could be found between their sizes and the composition.

Crystal structure and composition analysis of CoPt nanospheres

Pure Al target was PLA processed and produced nanospheres with predominantly amorphous structure. It was established that nitrogen was restricted to the inner region of the nanospheres although the solubility of nitrogen in molten aluminium is negligent. Outer regions of Al-based nanospheres were composed of Al_2O_3 in amorphous form due to relative high cooling rates preventing the formation of pure crystalline structure. This very outer layer of amorphous Al_2O_3 was also a very effective barrier preventing the dissolved nitrogen to escape form the inner regions during the solidification of nanospheres.

Characterization of nitrogen in voids by EELS

The light-element concentrations, N and O in this case, were measured using EELS. This analysis confirmed that the N signal is associated only with the voids, while no signal could be measured in the shell region. Moreover, the presence of oxygen could not be detected, which indicates that the nanospheres remained in the un-oxidized state. Following these results, the nanospheres with the indicated spherical dark contrast, which was regularly observed in HAADF-STEM images, can be defined as hollow spheres filled with gas or as nanospheres with gas bubbles.

Determination of nitrogen pressure in voids

The diameters of the measured voids ranged between 15 nm and 19 nm, with a mean value and relatively narrow standard deviation of 16 ± 2 nm. The diameters of the corresponding spheres ranged between 24 nm and 45 nm, with a mean value and a higher standard deviation of 35 ± 8 nm. The resulting calculated number density of nitrogen atoms obtained from six measured spheres was between 1 and 2 nm^{-3}, with an average value of n = 1.58 ± 0.4 nm^{-3}. The pressure in the void was estimated from the values of the nitrogen density and the related void volume by using a suitable equation of state. To calculate the pressure in the void accurately, with respect to the given density and the temperature range, a standard correction of an ideal gas law using a virial expansion was applied. The resulting calculated average pressure in the voids near the ambient temperature (300 K) was 1.9 ± 0.3 MPa. Assuming that the voids filled with gas were formed while the spheres were still in the liquid phase the equilibrium pressure needs to be recalculated for a given temperature range. According to the literature data [21], the boiling temperature for the Co–Pt alloy at ambient pressure is ~3000 K. The corresponding pressure of the nitrogen in the voids at this temperature would increase to a value of 34.3 ± 9 MPa.

The gas-filled hollow spheres presented in this study were most probably formed via a nucleation-and-growth process. The condensation of such particles starts already within the ablated vapour, with vapour species undergoing enough collisions with the background gas for them to nucleate and grow. Consequently, these particles would exhibit a homogenous composition enriched with the more volatile component, due to preferential ablation, which would be size-independent. On the other hand, the particles that are expelled from the melt would be enriched with the less volatile component, since they experience a loss of the more volatile

component on their path towards the substrate [22]. This consequently leads to deposits in which the composition depends upon the particle size [23]. For the Co–Pt system, the corresponding vaporization enthalpies (ΔH_{vap}) of the Co and Pt are 377 and 469 kJ mol^{-1}, respectively. According to this, we can expect that the plume will be enriched with Co, which results in Co-rich nanoparticles, as was already observed by Trelenberg et al. [24]. This is also in agreement with our findings where Co-rich nanospheres, with an average composition of $Co_{55\pm3}Pt_{45\pm3}$, were deposited from the Co-deficient target ($Co_{48}Pt_{52}$), confirming that they have been formed directly from the vapour phase, via the already described evaporation–condensation mechanism.

It was reported that the background gas influences the plasma kinetics and, consequently, the formation of the nanoparticles. Observations like plume splitting and plasma deceleration were related to the appearance of the shock wave and a contact front, where the shock wave is caused by the sudden impact of the expanding plasma with the background gas, resulting in a propagating perturbation with the contact front establishing the border between this perturbed gas and the plasma [25,26]. The heterogeneous nucleation and growth of the nanoparticles within the plume is bound to this narrow shock-wave region of the highly compressed, supersaturated vapour mixture, which is composed of the ablated vapour and the background gas, with large temperature and density gradients as well as pressure differences [27]. The vapour pressure and the temperature just behind the plasma front can be estimated using the general laws of the conservation of mass, momentum and energy [28]. The estimated vapour pressures of the Co–Pt plasma expanding into the nitrogen gas at 0.1 MPa would be in the range of ~100 MPa to several GPa, while the vapour temperatures would range between ~10^3 and 10^4 K [27,28]. Immediately after the condensed particles are ejected from the high-pressure and high-temperature plasma region, the particle nucleation and growth are heavily suppressed as a result of the rapid drop in pressure and temperature [27]. As a result the dissolved nitrogen in the molten sphere will start to condense and form an initial nitrogen bubble. The amount of dissolved nitrogen in the Co–Pt at the boiling point and ambient pressure was estimated using Sievert's law for liquid metals. The calculated amount of dissolved nitrogen in a liquid Co–Pt sphere for given temperature and pressure conditions is ~14 at.%. It is worth mentioning that the solubility of nitrogen in a molten sphere at a higher pressure and temperature would be even greater. For comparison, the nitrogen solubility in solid Co at 1873 K and ambient pressure is only 0.3 at.%, while in Pt it can be considered as negligible [28]. This is not a surprising result if we consider that prior to the condensation of the Co–Pt–N particles, the temperature and pressure in the plume can briefly reach well over 10^4 K and several GPa, respectively, which is enough to supersaturate the Co–Pt with nitrogen. The properties of the condensed nanoparticles, such as the composition, the crystal structure and the morphology, are largely dependent on the interplay between the thermodynamics of the two-phase region, i.e. the liquid–vapour, the rules of solidification for the multi-component system and the kinetic constraints during rapid cooling. Namely, the time scale of these processes is in the range of tenths of a second, which is based on the fact that all the examined nanospheres

had a crystalline structure. This implies that the cooling rates must have been in the range from 10^2 to 10^3 K s^{-1} or less. Had they been higher than this, the spheres would be in an amorphous state [29].

The nitrogen bubble pressure (P) within the molten Co–Pt sphere is equilibrated over the surface tension (γ) of the Co–Pt liquid following the relation $P = 2\gamma/r$, where *r* stands for the radius of the nitrogen bubble. The calculated nitrogen pressure in bubbles with an experimentally measured diameter of 32 ± 1.6 nm would yield a value of ~2 ×10^2 MPa. The fact that the measured pressure in the voids was one order of magnitude lower suggests that the cooling rates were such that it gave the nitrogen sufficient time to partially diffuse from the nanosphere. As the temperature of the molten sphere is dropping due to cooling (primarily through conduction), the permeability of Co–Pt to nitrogen is also dropping exponentially, while the interdiffusion of Co and Pt is severely hindered. For instance, the interdiffusion coefficient for Co and Pt is $D_{1537\ K} \cong 4\times10^{-11}$ cm^2 s^{-1}, while the diffusion coefficient for nitrogen at the same temperature is much higher, with $D_{1537\ K} \cong 0.9$ cm^2 s^{-1}. Moreover, the preferential diffusion of nitrogen towards the centre of the sphere is promoted by the fact that the solubility of nitrogen in the solid (0.3 at.%) is much lower than in the liquid (14 at.%). This is in accordance with our results, as the nitrogen signal was only measured in the void, while no nitrogen was detected in the rim of the sphere. The arrangement of the Co–Pt spheres in string-type structures is due to the magnetic dipole–dipole interaction between the particles. Depending on the particle volume, the magnetization can be fixed within an individual particle if the volume exceeds a certain critical volume [30]. For Co–Pt with a fcc crystal structure the calculated critical diameter equals ~15 nm, which means that the particles produced in our study are ferromagnetic. They are most probably in a single-domain state, since the calculated critical diameter of the single-domain particle for the Co–Pt fcc crystal structure equals ~30 nm [31]. Moreover, spontaneous magnetic fields with a magnetic flux density in the range of kilogauss were already observed in laser-produced plasma due to the large temperature gradients, which generate thermoelectric currents [32]. Such magnetically induced self-assembly, which originates from the magnetostatic interactions, can yield unique structures from strings to necklaces, as observed in our study. According to the obtained results we propose the formation mechanism for gas-filled hollow metallic nanospheres, which can be generalized for other metallic systems. At first, the condensation of the spheres starts from the supersaturated mixture of ablated species and ambient gas at a relatively high pressure and temperature. The melt needs to be acceptable for gas intake, as this provides a molten sphere with the highest concentration of dissolved nitrogen. Then, the metallic system in relation to the background nitrogen gas should be selected so that the high solubility differences between the melt and the corresponding solid are achieved. Finally, the outwards diffusion of nitrogen through the sphere's solid rim, for example, by providing high cooling rates, should be suppressed.

Conclusions

The obtained results support the idea that gas-filled hollow spheres could be fabricated in various complex metallic systems by applying PLA in the presence of a background gas, taking into consideration that in relation to the background gas high solubility differences between the melt and corresponding solids are achieved. The core–shell spheres were composed of a crystalline $Fe_{90}N_{10}$ core with a Sm–Ta–O rich amorphous rim. The hollow spheres containing N_2 gas were formed from an Fe-rich melt supersaturated with nitrogen. We believe that the determining parameter for the formation of either a core–shell or a hollow nanosphere is the amount of dissolved nitrogen in the initial molten droplet. The presented results confirm that nitrogen-filled Co–Pt spheres can be fabricated successfully. The spheres were formed by condensation from the plume in a region of high pressure and temperature. We believe that the nitrogen bubble within the liquid nanosphere was initially formed due to the abrupt drop of pressure and temperature in the nitrogen-saturated liquid sphere. Subsequently, the nitrogen could diffuse from the interior of the sphere outwards. However, due to the fast solidification and the formation of the solid rim the outward diffusion of nitrogen is heavily suppressed, preventing the N_2 gas from escaping the sphere.

Reference

[1] Bhushan B 2010 Springer Handbook of Nanotechnology (Springer-Verlag Berlin Heidelberg)
[2] Sturm S, Zuzek Rozman K, Markoli B, Sarantopoulou E, Kollia Z, Cefalas A C and Kobe S 2010 Nanotechnology 21 485603
[3] Sturm S, Rozman K Z, Markoli B, Antonakakis B E, Sarantopoulou E, Kollia Z, Cefalas A C, Kobe S 2013 Acta Materialia 61 7924
[4] Vasquez Y, Henkes A E, Chris Bauer J, Schaak R E. 2008 J. Solid State Chem. 181 1509
[5] Zhang Q, Wang W, Goebl J, Yin Y. 2009 Nano Today 4 494
[6] Jones M R, Osberg K D, MacFarlane RJ, Langille M R, Mirkin C A 2011 Chem. Rev. 111 3736
[7] [Moon G D, Ko S, Min Y, Zeng J, Xia Y, Jeong U. 2011 Nano Today 6 186
[8] Yin Y, Rioux RM, Erdonmez CK, Hughes S, Somorjal GA, Alivisatos AP 2004 Science 304 711
[9] Ibánez M, Fan J, Li W, Cadavid D, Nafria R, Carrete A, et al. 2011 Chem. Mater. 23 3095
[10] Chen G, Xia D, Nie Z, Wang Z, Wang L, Zhang L, et al. 2007Chem. Mater. 19 1840
[11] Vasquez Y, Sra AK, Schaak RE. 2005 J. Am. Chem. Soc. 127 12504
[12] Sun Q, Wang S, Wang R. 2012 J. Phys. Chem. C 116 5352
[13] Egerton RF. Electron energy loss spectroscopy 2nd ed. New York: Plenum; 1996.
[14] [Walsh CA, Yuan J, Brown LM. 2000 Philos. Mag. A 80 1507
[15] Fréchard S, Walls M, Kociak M, Chevalier JP, Henry J, Gorse D. 2009 J. Nucl. Mater. 393 102
[16] Gale W F and Totemeier T C 2004 Smithells Metals Reference Book 8th edn

(Amsterdam: Elsevier)
[17] Fahlman B D 2003 Materials Chemistry (The Netherlands: Springer)
[18] Massalski T B, Okamoto H, Subramanian P R and Kacprzak L 1990 Binary Alloys Phase Diagrams vol 2 (Metals Park, OH: ASM)
[19] Burditt M F 1993 Ductile Iron Handbook (Des Plains: American Foundrymen's Society)
[20] Kobe S, Zuzek K, Sarantopoulou E, Kollia Z and Cefalas A C 2005 Appl. Surf. Sci. 248 349
[21] Zuzek K, McGuiness P J and Kobe S 1999 J. Alloys Compounds 289 213
[22] Egerton R F 1996 Electron Energy Loss Spectroscopy 2nd edn (New York: Plenum)
[23] Trasobares S, Stéphan O, Colliex C, Hug G, Hsu W K, Kroto H W and Walton D R M 2001 Eur. Phys. J. B 22 117
[24] Ahn C C, Krivanek O L, Burgner R P, Disco M M and Swann P R 1993 EELS Atlas (Arizona: A Joint Project of Arizona State University HREM Facility and Gatan)
[25] [Horn I, Günther D. 2003 Appl. Surf. Sci. 207 144
[26] De Posada E, Arronte M A, Ponce L, Rodríguez E, Flores T, Lunney J G. 2011 J. Phys.: Conf. Ser. 274 012078
[27] Sharma A K, Thareja R K. 2005 Appl. Surf. Sci. 243 68
[28] Zel'dovich Y B, Raizer Y P. In: Hayes W D, Probstein R F, editors. 2002 Physics of shock waves and high-temperature hydrodynamic phenomena (New York: Dover)
[29] Gaskell D R. 2003 Introduction to the thermodynamics of materials 4th ed. (New York: Taylor & Francis)
[30] Yu M, Liu Y, Sellmyer D J. 2000 J. Appl. Phys. 87 6959
[31] Cullity B D, Graham C D. 2008 Introduction to magnetic materials 2nd ed. Hoboken (NJ: Wiley-IEEE Press)
[32] Li C K, Séguin F H, Frenje J A, Rygg J R, Petrasso R D, Town R P J, et al. 2006 Phys. Rev. Lett. 97 135003

Oral presentations

RESEARCH PRIORITIES IN THE DEVELOPMENT OF FUTURE GENERATIONS OF WROUGHT ALUMINIUM ALLOYS

Varužan Kevorkijan

Impol R in R d.o.o., varuzan.kevorkijan@impol.si

Abstract

This work presents our current understanding of the influences of various trace elements and impurities, as well as the changes in the chemical composition of the alloys, on their particular properties, including the possible impact of developments on the global aluminium industry and the competitiveness of wrought aluminium alloys in comparison with high-strength steels.
Keywords: Wrought Aluminium Alloys, Standard Alloys, Recycling Friendly Alloys, Performance to Cost Index, Research Properities

Introduction

To be competitive with advanced, high-strength steels and other engineered materials, wrought aluminium alloys need to offer the customer a better performance-to-cost index. Therefore, the purpose of this paper is to review the latest efforts in the development and redesign of wrought aluminium alloys with which producers are planning to improve their competitiveness on the global market. In general, the performance-to-cost index of wrought aluminium alloys can be increased either by improving their mechanical properties or reducing their cost of production. An additional improvement in the performance-to-cost index of wrought aluminium alloys is possible by replacing standard alloys, and their limited recyclability, with the so-called “recycling-friendly” alloys, designed to maximise the performance-to-cost index.

Strategies for improving the Performance-to-Cost Index of wrought aluminium alloys

Among the commercial attributes of wrought aluminium alloys, the performance-to-cost index represents one of the most important and critical [1]. The reasons for this are as follows: (i) The high cost of primary aluminium, new industrial scrap and pure alloying elements, (ii) The deficit in the properties of wrought aluminium alloys in comparison with some leading competitive materials (e.g., high-strength steels), (iii) The deficit in the sustainability of primary aluminium, caused by the large amount of energy consumed by all of the processes associated with its production.

In order to improve the performance-to-cost index of wrought aluminium alloys it is necessary to enhance the alloy’s properties (especially the tensile strength), while at the same time minimizing the costs [2].

To ensure the enhancement of the alloy’s properties, new strengthening procedures should be developed and implemented to achieve higher strength, while a significant reduction in the production costs might only result from further

improvements in the recyclability of wrought alloys. As will be discussed, any further improvements in the strengthening of wrought aluminium alloys are questionable. As a result, a more promising route to enhancing the performance-to-cost index is to reduce the production costs. However, improvements to the recyclability of wrought aluminium alloys with standard compositions (with a maximum amount of the so-called trace elements of 1500 ppm and 500 ppm of each) mostly depend on the ability of the global aluminium industrial community to develop a fast and cost-effective technology for the automatic separation of old, post-consumed and municipal scrap into single alloys with a well-defined chemical composition [3]. In parallel with scrap separation, it will be necessary to develop and implement several computer-assisted blending and processing procedures, or, in other words, a kind of “digitalisation” of scrap yards [2].

These procedures are currently at a fundamental, early stage of industrial development, which means that their introduction to regular production will require several decades. In addition, one should note that the cost of high-quality automatic separation would significantly influence the successful commercialization of industrial separation technology for low-grade scrap. To achieve higher recyclability, and, as a result, a more significant reduction in production costs, several new strategies for improving the performance-to-cost index of wrought aluminium alloys are based on the development of the new, so-called “recycling-friendly” alloys [4]. Moreover, some of them are looking at replacing the existing standards, formulated on the purity of primary aluminium (achieved by electrolysis) with new standards, formulated on the purity of scrap, achieved by scrap sorting. One of the aims of the new standards is the possible unification of wrought aluminium alloys into just a few grades, with a proper combination of properties, as illustrated in Fig. 1.

It is clear that the main motivation for these efforts is an improvement in the recyclability of wrought aluminium alloys. However, before completing the development of new alloy compositions and the formulation of new standards, it will be necessary to attain a fundamental understanding of the complex influence of the larger amount of trace elements on the properties of wrought aluminium alloys and, in addition, all the consequences that non-standard alloy compositions will have on the global aluminium pool. The properties of wrought aluminium alloys are the result of a complex interaction between the chemical composition and the microstructural features obtained during the solidification, thermal treatments and deformation processing [5]. Thus, with constant processing parameters, the properties are a consequence of the chemical composition of the alloy, and, vice-versa, the tolerance limits for the concentration intervals of the alloying elements depend on the required properties.

On the other hand, cost reduction mostly depends on the technological possibilities of replacing as many of the expensive raw materials (the primary aluminium and the alloying elements) as possible with scrap. The extent of such a replacement depends on the ability of the production technology to preserve the standard composition and quality of the alloy or, to put it another way, to meet the customer’s requirements by offering scrap-intensive alloys. In other words, the difficulty in recycling wrought aluminium alloys is the problem of achieving the standard tolerances, or more generally, the ability of an alloy to absorb elements

not normally present in its composition [1]. This is the starting point for designing the so-called “recycling-friendly” wrought aluminium alloys.

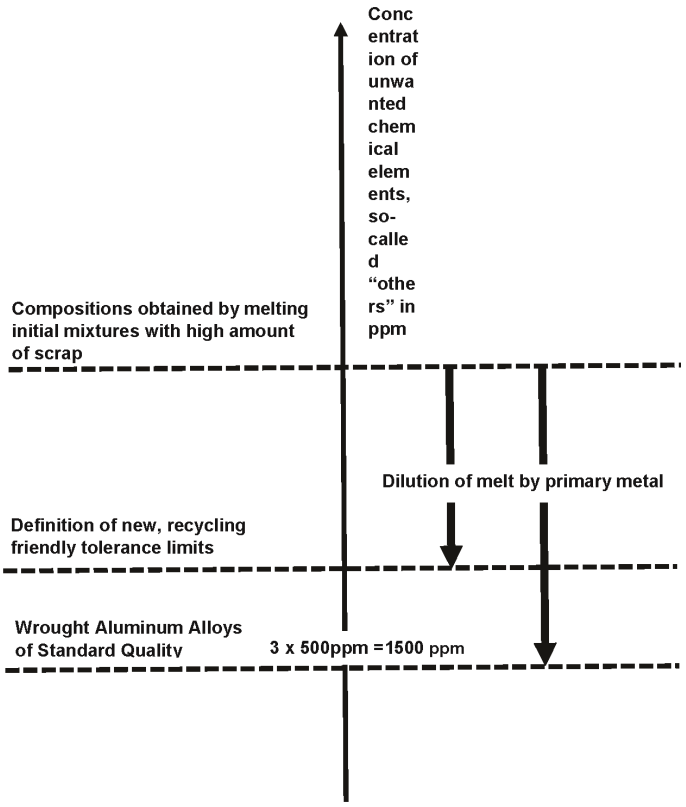

Fig.1. Comparison of the concentration level of unwanted chemical elements in standard and so-called “recycling-friendly” wrought aluminium alloys.

Development of standard wrought aluminium alloys with better mechanical properties

By applying the existing strengthening procedures (cold deformation and alloying), it is possible to fabricate wrought aluminium alloys with a maximum tensile strength of about 550 MPa. Considering the cost of these alloys with respect to their mechanical properties and, particularly, with the cost and performance of new generations of steel, it is evident that such a strengthening level cannot ensure the attractive performance-to-cost index of wrought alloys on a long-term basis. In other words, in order to create wrought aluminium alloys with higher tensile strengths (e.g., up to 700 MPa), it will be necessary to develop new, more effective strengthening strategies.

It is well known that the strengthening of a wrought aluminium alloy depends on the size differences between the solute atoms of the alloying elements and the aluminium, and that it can be improved by cold deformation and alloying. As a

result of alloying the strength increases by solid-solution hardening, dispersion hardening and precipitation hardening (age-hardening). Hardening, annealing and aging are well implemented in the current production of wrought aluminium alloys. The problem is that these methods have only limited potential for strength improvement. The result is wrought aluminium alloys with a deficit in terms of performance (particularly the tensile strength). The significant difference in the actual strength of commercial alloys and their theoretical strength [5] is due to the presence of lattice defects, mainly dislocations. Therefore, all future, advanced strengthening mechanisms (including these involving in-situ-formed, nano-sized particles or precipitates) will focus on limiting the movement of dislocations.

Development of cost-effective standard wrought aluminium alloys

A prerequisite for the successful recycling of wrought aluminium alloys with a standard composition is an ability to mix the standard chemical composition of the alloy using various grades of old scrap (waste or end-of-life products).

In order to achieve such a mixing procedure for the industrial level and environment, it is necessary to organize the scrapyard so that it consists of different material streams, each with a proper and well-controlled chemical composition. In addition, it is necessary to develop a methodology for mixing the proper combination of material streams, which is essential for achieving the required alloy composition – standard alloys or the alternative, so-called "recycling-friendly" alloys [2].

A breakthrough in the recycling of post-consumed scrap for the production of wrought alloys of standard composition with an improved performance-to-cost index will be achieved only by developing and implementing a fully automatic, highly adaptable and cost-effective sorting technology. Even in this case, the cost of sorting as well as the quality-to-cost ratio of the recycled wrought alloys will remain very important issues with respect to increasing their market share, especially in demanding segments. The problem is that the current generations of automatic, aluminium-scrap sorting lines are not yet capable of dividing the incoming scrap into scrap streams based on sorts and concentrations of minor and trace elements. However, results obtained from the laboratory suggest that some of these technologies might, in the near future, fulfil industrial requirements for the accurate sorting of wrought aluminium scrap into scrap streams with concentration tolerance limits that are close enough to achieve a standard composition for the pre-melting mixture. Nevertheless, for the industrial application of the automatic sorting of incoming wrought aluminium scrap it will be necessary to achieve high-precision and cost-effective sorting in real time (usually less than 10 ms), which is still in the development stage.

Possibilities for the development of "recycling-friendly" wrought aluminium alloys

An extensive experimental investigation of the influence of changes in the chemical composition of wrought aluminium alloys on their properties might result, in forthcoming decades, in so-called alternative compositions of wrought aluminium alloys. In contrast to standard compositions, alternative compositions typically have

broader compositional tolerance limits, for at least some of alloying elements and impurities, making their blending from scrap streams much easier and more cost-effective. The expectation is that such alternative compositions of wrought aluminium alloys, if properly formulated and processed, could also provide a sufficient quality level and mix of properties for the end-user [6].

Plenty of chemical elements are present in wrought aluminium alloys. Based on their concentrations in an alloy composition, the alloying elements are divided into: (i) major, (ii) minor and (iii) trace and unwanted elements. The major alloying elements (Zn, Cu, Mn, Mg, Si and Fe) are those involved in the alloy's designation (AlFeSi, AlMg, AlSi, AlMn, AlMgSi, AlCu, AlCuMg, AlZnMg and AlZnMgCu). Their addition to aluminium results in the creation of basic alloy properties and a combination of them within different alloy series. In contrast to that, minor alloying elements (Ti, B, Zr, Cr, V, Sc, Ni, Sn, Bi, Sb etc.) only indirectly affected the specific alloy's properties. Regarding unwanted and trace elements, they are particularly important because their presence, even at very small concentrations, could have a tremendous effect on the solidification and microstructure development, as well as on further processing steps – strengthening mechanisms, thermal treatments and formability. The trace and unwanted elements are either initially present in the raw materials (primary aluminium and pure alloying elements) or introduced by contamination at various stages of the entire production process. The mechanism by which the major and minor alloying elements create the alloy properties are solid-solution strengthening, strain hardening, precipitation or age hardening, etc. The influence of minor alloying elements involves grain refining or heat treatment [5].

Regarding the future commercialisation of "recycling-friendly" alloys, it is important to note that the production and distribution of wrought aluminium alloys with alternative compositions will cause a significant accumulation of unwanted elements and impurities and, hence, change the chemical composition of the existing wrought aluminium material pool. In other words, besides standard alloys with a content of "others" of less than 0.15%, there will be more and more new alloys with alternative compositions in which the content of "others" will be higher than 0.15% [7]. In principle, there are three possibilities for managing this influence: (i) to create alternative compositions with a concentration of others (minor and trace elements) below 0.15%, as in standard alloys, (ii) to accept a higher amount of others in both standard alloys and alloys with alternative compositions as a new standard, or (iii) to produce, fabricate and recycle standard and alternative compositions, keeping each of the groups in its own, separate pool.

Before the final implementation of "recycling-friendly" alloys it will also be necessary to quantify and understand the main differences in the quality of primary aluminium as a virgin metal obtained by electrolysis and recycled aluminium alloy obtained by melting from scrap. The principal difference is in the fact that the primary aluminium is a material with a clear "material-processing history", solidified only once, whereas the "processing history" of recycled aluminium is usually unknown. Hence, the main quantitative measurable differences in as-cast, wrought aluminium alloys produced (i) once from primary aluminium and (ii) secondly from scrap is in the amount of unwanted and trace elements as well as in the grain morphology – the grain size and the dendrite arm spacing (DAS).

The main long-term R&D challenges in the field of the development of new, “recycling-friendly” wrought aluminium alloys are: (i) the unification of wrought aluminium alloys, and (ii) the development of universal alloy compositions that are “recycling friendly”. It is a very demanding development process to formulate the new international standards for wrought aluminium alloys with larger compositional tolerance limits. In addition to that, the new standards should enable the replacement of up to 80% of the electrolytic grades of primary aluminium with recycled metal, at the same time ensuring the required combination of alloy properties and increased competitiveness [8].

Conclusion

As demonstrated, the future generations of wrought aluminium alloys should combine enhanced mechanical properties and cost effectiveness. However, efforts focused on the optimisation of the performance-to-cost ratio of wrought aluminium alloys are limited by the existing methods for increasing the strength and the high cost of the primary aluminium. Therefore, the real technological breakthrough is in a major revision of the international standards, resulting in the development of completely new grades of wrought aluminium alloys.

References

[1] V. Kevorkijan, *Metall. Mater. Eng*., 16(2), pp. 103-114, 2010.
[2] V. Kevorkijan et al., *Light Metals 2015*, ed. M. Hyland, TMS, pp. 237-242, 2015.
[3] V. Kevorkijan, *JOM*, 62(8), pp. 37-42, 2010.
[4] S. K. Das, *Light Metals 2006*, ed. T. J. Galloway, pp. 911-916, 2006.
[5] M. Tiryakioğlu and J. T. Staley, *Handbook of Aluminium, Vol. 1*, ed. G. E. Totten, D. S. MacKenzie,CRC Press, Taylor & Francis Group, pp. 81-209, 2003.
[6] V. Kevorkijan, *Metall. Mater. Eng*., 19(3), pp. 249-257, 2013.
[7] C. Koffler, *Sustainability*, 5, pp. 4546-4560, 2013.
[8] V. Kevorkijan, *Metall. Mater. Eng.,* 47(1), pp. 13-23, 2013.

PHYSICAL SIMULATION OF SOLIDIFICATION: FROM PREDICTING CAST MICROSTRUCTURES TO HIGH-THROUGHPUT SCREENING OF SOLIDIFICATION-MICROSTRUCTURE RELATIONSHIPS

S. Milenkovic, M. Rahimian, I. Sabirov

IMDEA Materials Institute, C/ Eric Kandel 2, 28906, Getafe, Madrid, Spain
srdjan.milenkovic@imdea.org

Abstract

The first part of the study describes physical simulation as a tool for predicting microstructure and hardness of investment castings of complex shape parts. The tool combines a thermal model for predicting local cooling rate during solidification at each point of a casting and melting/solidification experiments in thermo-mechanical simulator under controlled cooling rates. This concept is applied to investment casting of complex shape nozzle guide vanes from Mar-M247 Ni-based superalloy. The second part introduces a novel tool for high-throughput screening of the solidification-microstructure relationships. It consists of an experiment with a constant cooling rate and variable temperature gradient, yielding a range of solidification rates. Corresponding spread of microstructures along the sample obtained in a single experiment was confirmed by adequate changes in the grain size, as well as the secondary dendrite arm spacing.
Keywords: Investment casting, physical simulation, high-throughput methods, solidification, microstructure

Introduction

Recent progresses in science and technology have created a new opportunity for researchers to mimic the large scale industrial processes in laboratory by high capability physical simulator machines. Physical simulation of metallurgical processes is often employed for development of novel manufacturing routes. Physical simulation involves the exact reproduction of the thermal and mechanical processes in the laboratory that the material has to undergo in the full scale fabrication process. In the first part of this paper physical simulation as a tool for predicting microstructure and hardness of investment castings of complex shape parts is described, whereas in the second part a novel tool for high-throughput screening of the solidification-microstructure relationships based on physical simulation is introduced.

Physical simulation of investment casting

Investment casting process, known as a lost wax casting or precision casting, is a well established process for production of near net-shape components. Due to excellent surface finish and dimensional accuracy, this process is especially useful for casting of complex shape with thin elements [1]. This manufacturing technique has been widely used for fabrication of various parts Development of investment casting routes for the complex shape parts is usually carried out via a 'trial and error' approach or, in other words, via experimental casting trials. The casting parameters are varied until good quality castings are produced. However, this strategy is very expensive and time consuming [2]. Modelling of investment casting is another approach to determine the optimum casting parameters [3]. Simulation of casting is reliable when the accurate data of materials are known at processing conditions, and boundary conditions are defined precisely. However, precise prediction of local phase composition, second phase precipitates, segregations, etc. is out of capabilities of the current casting simulation tools, whereas these microstructural features significantly affect the local mechanical and functional properties in the castings from Ni-based superalloys.

Physical simulation of metallurgical processes is often employed for development of novel manufacturing routes. There is a body of research where physical simulation of continuous casting was successfully performed. This metallurgical process is characterized by complex three-dimensional heat flow which is determined by the melt temperature, the temperature of the walls of the caster, the geometry and thickness of the slab, and the velocity of the slab. Similarly, the investment casting process is also characterized by complex three-dimensional heat flow determined by numerous casting parameters including melt temperature, temperature of ceramic mould, casting shape, thermo-physical properties of ceramic mould and metal, etc. Thus, significant variations of local cooling rate during solidification of complex shape part can be expected in its different sections. In the first part of the present work, the physical simulation of investment casting of complex shape parts was applied to the investment casting process of nozzle guide vanes (NGV) from Mar-M247 Ni-based superalloy.

High-throughput screening of solidification microstructure relationships

The classical one-at-a-time research methodology to develop new materials limits technological progress, particularly nowadays when engineering design tools have radically reduced the time necessary to optimize new products. New strategies based on combinatorial materials science (CMS) and high-throughput (HT) techniques have been recently introduced to speed up materials innovation. Thin films with discrete composition libraries or continuous composition gradients (spreads) are currently used to study composition–structure–property relationships of complex functional materials in one shot. In contrast, HT methods involving bulk materials are rather scarce and bulk diffusion couples have been just used in metallurgy for the evaluation of diffusion coefficients or the determination of phase diagrams.

A majority of manufacturing processes involve melting and solidification. Nevertheless, the effect of solidification processing variables on the microstructure is still being determined following the one-alloy-at-a-time strategy, and new alloy development remains a very long and costly process. To overcome these limitations, the second part of this paper introduces a novel HT methodology for establishing solidification-microstructure relationships of metallic alloys.

Experimental procedure

Physical simulation of investment casting

Physical simulation of investment casting begins with calculation of the local cooling rates during solidification using the ProCast based thermal model. Mould filling during investment casting was modeled using the three-dimensional finite element solver ProCast (a trademark of ESI group) by solving the conservation of mass, momentum and heat flow equations [4]. The detailed description of the thermal model and thermo-physical parameters applied in modelling of investment casting of NGV from Mar-M247 Ni-based superalloys can be found in the very recent manuscript by Torroba et al. [5], where the model was validated against experimental temperature measurements during casting trials.

The outcomes from modelling, namely cooling rates, served as input parameters for the melting/solidification experiments in the thermo-mechanical simulator GLEEBLE 3800. The melting/solidification experiments were carried out in argon atmosphere The samples were heated up to temperature and then cooled at two different cooling rates of 0.25 and 1 ºC/s, which were calculated by thermal model for some defined sections of NGV. The microstructure of the mid-section area under welded thermocouple of the Gleeble samples was carefully analyzed. The standard metallographic techniques were used for preparation of specimens with mirror-like surface. The surface was etched using chemical solution containing 25g $FeCl_3$, 60 ml HCl, and 25 ml H_2O to reveal grain boundaries and dendritic microstructure. The optical microscope OLYMPUS BX51 was employed to study grain and dendritic structure. Analysis of carbide particles was done in scanning electron microscope (SEM) EVO MA 15 operating at 18 kV. Microhardness was measured using SHIMADZU HMV-2 microhardness tester using the 300 g load for 15 s. At least ten measurements were done on each selected area. Finally, experimental casting trials were successfully carried out for validation of the tool.

The experimental procedure for high-throuput methodology involved the same experiments in a Gleeble 3800, with only difference that in this case there were 4 thermocouples welded to the samples.

Results and discussion

Physical simulation of investment casting

This section describes the microstructure of the Gleeble samples compared with the microstructure of the NGV samples. Secondary dendrite arm spacing, grain structure, phase composition and morphology of carbides were analyzed, since these are the main microstructural features determining properties of Ni-

based superalloys. Fig. 1 shows dendritic microstructure of Mar-M247 Ni-based superalloy in the Gleeble samples and in the NGV samples. It is seen that morphology of dendritic structure in the Gleeble samples (Fig. 1a,c) is very similar to that of the NGV samples (Fig. 1b,d) at both cooling rates. The results of SDAS measurements listed in Table 1 shows a very good accordance of SDAS in the Gleeble samples and in the as-cast NGV samples for both cooling rates. The SDAS-values decrease with increasing cooling rate which agrees well with the results reported earlier by Zhang et al. [6] and many other research groups. According to Kurz and Fisher [7], the SDAS is determined by the local solidification time because the diffusion coefficient of the solute is significantly larger in the liquid than in the solid. The local solidification time decreases with increasing cooling rate resulting in finer SDAS.

Fig. 2 demonstrates grain structure of the Gleeble samples (Fig. 2a,c) and NGV samples (Fig. 2c,d) at cooling rates of 0.25ºC/s (Fig. 2a,b) and 1ºC/s (Fig. 2c,d). It is seen that physical simulation can reproduce well the grain structure of the as-cast NGV at both cooling rates. The average grain sizes in the specimens after physical simulation and in the NGV are in a good accordance and tend to decrease with increasing cooling rate. Comparing the microstructures, it can be also observed that the morphology of the grains is identical too. This observation is confirmed by comparing the average aspect ratios of the grains (Table 1). The values of average aspect ratio of 2.10 and 2.36 obtained in the Gleeble samples for the cooling rates of 0.25 and 1 ºC/s match perfectly with the values of 2.19 and 2.44 in the as-cast NGV samples.

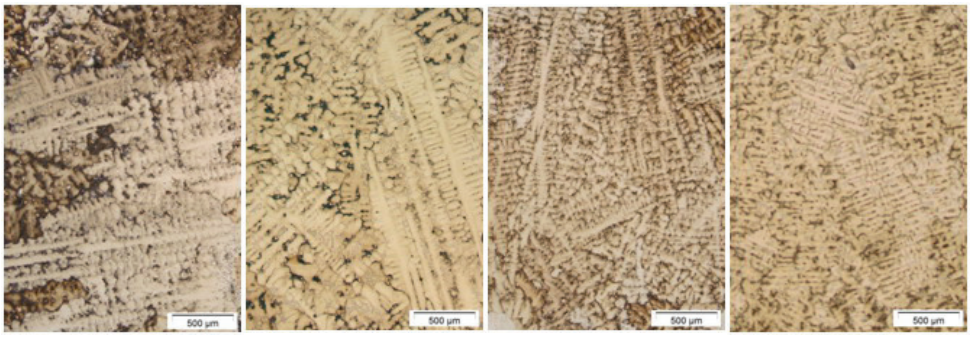

a) *b)* *c)* *d)*

Fig. 1. Dendritic microstructure of a) Gleeble sample at 0.25 ^{0}C/s, b) NGV sample at 0.25 ^{0}C/s; c) Gleeble sample at 1 ^{0}C/s d) NGV sample at1 ^{0}C/s.

Table 1. Results of microstructural characterization and microhardness measurements of the Gleeble and NGV samples.

Processing			***Gleeble samples***		***NGV samples***	
Cooling rate (°C/s)			**0.25**	**1**	**0.25**	**1**
Phase composition	**Carbide**	size (μm)	8±2	4±2	7±3	4±2
		vol. fraction (%)	1.1	1.8	1.2	1.7
		spacing **λ** (μm)	23±4	9±1	18±2	9±1
	γ/γ´ eutectic	vol. fraction (%)	10.4	3.4	10.2	3.2
		size (μm)	44±9	24±5	41±8	23±6
SDAS		(μm)	70±12	35±8	66±13	39±9
Grain structure		grain size (μm)	1279±347	1050±284	1264±693	1018±437
		aspect ratio	2.1	2.36	2.19	2.44
Microhardness		(HV)	382±20	408±15	381±16	415±7

As it is well known, the morphology, size and volume fraction of carbide particles can strongly affect mechanical strength and creep resistance of Ni-based superalloys [8]. Table 1 depicts the match of carbides in the Gleeble samples and in the as-cast NGV samples. The reduction of cooling rate results in reduction of average carbide size and inter-particle spacing in the as-cast NGV, and this is also well captured in physical simulation. Volume fraction of carbide particles in the as-cast NGV samples tends to increase from 1.2 % to 1.70% with increasing cooling rate that is also reproduced by physical simulation, where it increases from 1.1 % to 1.8 % (Table 1). It can be rationalized based on reduction of time for diffusion of alloying elements (in other words, carbide growth time) with increasing cooling rate. Smaller SDAS at higher cooling rates results in reduction of carbide inter-particle spacing, since according to He et al. [9], interdendritic areas are preferred location for segregation of carbide forming elements and carbide formation in the Ni-based superalloys. Formation of larger number of carbide nuclei together with the smaller interdendritic area could be the reason for increasing carbide volume fraction with increasing cooling rate.

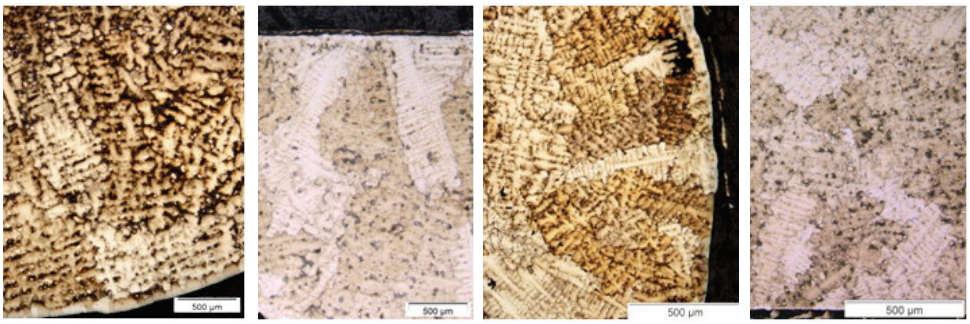

a) *b)* *c)* *d)*

Fig. 2. Grain structure of a) Gleeble sample at 0.25ºC/s, b) NGV sample at 0.25 ºC/s c) Gleeble sample at 1 ºC/s and d) NGV sample at 1ºC/s

In the Ni-based superalloys, γ/γ´eutectic is a non-equilibrium solidification micro constituent caused by segregation of eutectic forming elements such as Ti and Al in interdendritic areas during solidification process [10]. Formation of γ/γ´eutectic pools is controlled by chemical composition of the alloy and cooling rate during alloy solidification. The results of their quantitative analysis are listed in Table 1. It is seen that physical simulation (Gleeble samples) can very well predict morphology, size and volume fraction of γ/γ´ eutectic pools in the as-cast NGV at both cooling rates. Their average size decreases from 41±8 µm to 23±6 µm with increasing cooling rate in the as-cast NGV, that matches well with the outcomes of physical simulation (Gleeble samples), where it drops from 44±9 µm to 24±5 µm (Table 1). Similar trend is shown involume fraction of γ/γ´ eutectic. Gleeble samples predict its reduction from 10.4 % to 3.4 % with increasing cooling rate, which is in a very good accordance with the results for the as-cast NGV, 10.2 % and 3.2 %, respectively (Table 1). As demonstrated by Liu et al. [11], higher cooling rates result in dendrite refinement leading to lower amount of segregations and smaller eutectic pools. Finally, the results of microhardness measurements on all studied specimens are also listed in Table 1. A very good agreement between microhardness data measured on the as-cast NGV and on specimens after physical simulation can be noted. It is seen that the average microhardness values increase with increasing cooling rate from 381 HV to 415 HV and from 382 HV to 408 HV in the as-cast NGV and Gleeble samples, respectively. This result can be expected since microhardness is governed by microstructural features which were very well reproduced in physical simulation. Reduction of SDAS with increasing cooling rate improves strength, as was shown by Milenkovic et al. [12]. Finer carbides, higher carbide volume fraction and lower inter-particle spacing in the specimens cooled at higher cooling rate also result in contribution to higher particle strengthening. It should be noted that grain size effect on strength of the material cannot be analyzed in this case, since grains (having size > 1 mm) are much larger than the diameter of plastic zone in microhardness testing (~100 µm).

High-throughput screening of solidification microstructure relationships

The temperature-time plots for different cooling rates are presented in Fig. 3a. They show that the cooling rate was very well controlled at cooling rate of 0.25 ºC/s with all thermocouples displayed consistent values. At the cooling rate of 10 ºC/s some instability appeared, but this did not affect the average cooling rate. So, the experimental average cooling rates matched the set ones. This indicates that the casting process with precisely controlled cooling rates can be successfully reproduced in the Gleeble thermomechanical simulator. The same data were used to plot the temperature variation along the axis of the sample, as shown in Fig. 3b. It was assumed that the distribution is symmetrical around the midsection. The data were then fitted using polynomial regression. It can be clearly seen that in both samples temperature distribution varies with the distance from the midsection. In the case of cooling rate of 0.25ºC/s, the variation in temperature is much lower with the minimum of 1275ºC at the distance of 12 mm. On the other hand, sample cooled at 10ºC/s showed a significantly higher range of the temperature deviation.

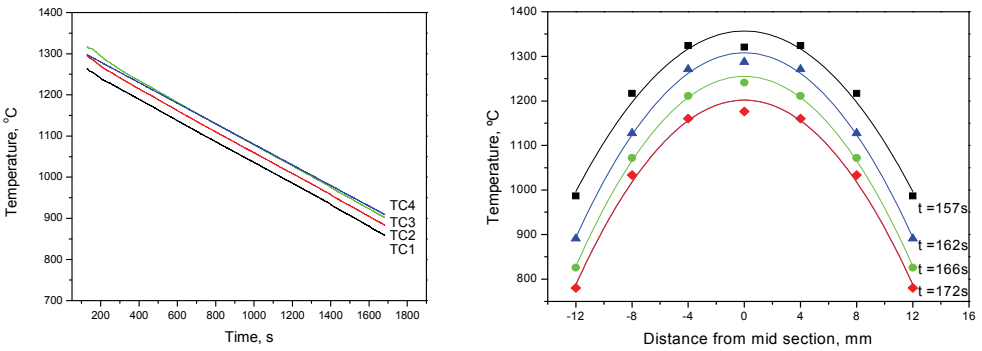

Fig. 3. a) Cooling curves recorded by four thermocouples during the melting/solidification experiment; b) Temperature distribution along the sample axes.

In the next step, the obtained function of temperature distribution enabled to determine temperature gradient at each distance from the midsection of the ingot by simply differentiating it. Results depicted in Fig. 4 clearly show that the temperature gradient increases linearly from the midsection of the sample toward the cooling extremities. It may be observed that the central part of the sample solidified at very low temperature gradients <1ºC/mm, whereas the parts at the end of the melting zone, at the distance of 8 mm from the midsection were subjected to the temperature gradient as high as 40K/mm.

Fig. 4 also shows the microstructures at the midsection, 4 and 8 mm from the midsection of the samples. The microstructure of the sample cooled at 10ºC/s exhibited a remarkable refinement of microstructure when approaching the midsection. These observations were supported by the measurements of the SDAS and grain size (Fig. 4). Both the dendrite spacing and the grain size increase with the distance from the midsection. Secondary dendrite arm spacing is key

microstructural feature of castings since it influences many of the important mechanical properties. According to the theory of crystal growth [7], it is inversely proportional to the growth rate. As the solidification velocity increases, the microstructural length scales (primary and secondary dendrite arm spacings) decrease. Thus the variation in dendrite arm spacing clearly indicate that different part of the sample solidified at different rates, con-firming thus assumptions made upon temperature gradients variation.

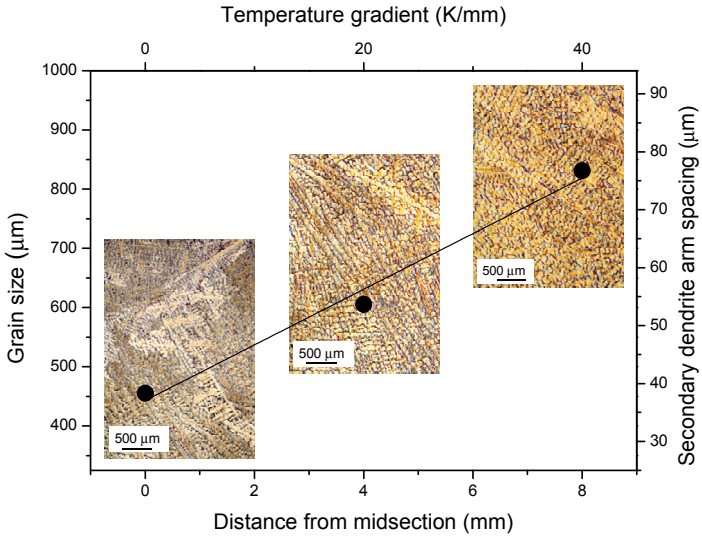

Fig. 4. Temperature gradient, microstructure, grain size and secondary dendrite arm spacing vs. distance from the midsection

All information presented so far point out that in a single sample subjected to a constant cooling rate, but varying temperature gradient, a range of solidification rates were obtained, which yielded a spread of microstructures. Hence, it can be stated that presented methodology fulfils all the requirements to be classified as a high-throughput method for establishing the solidification-microstructure relationship. For the first time, a spread of microstructures corresponding to a range well controlled solidification rates was produced in a single melting/solidification experiment.

Summary

In the first part of the paper it has been demonstrated how to perform physical simulation of investment casting of complex shape parts by combining thermal modelling with melting/solidification under controlled cooling rate in thermo-mechanical simulator. First, the local cooling rates during solidification at each point of cast were predicted via thermal modelling and subsequently, melting/solidification experiments were carried out under controlled cooling rates determined by thermal model. Physical simulation of investment casting of nozzle guide vanes (NGV) from MAR-M247 Ni-based superalloy was performed for selected areas of NGV. It is demonstrated that physical simulation predicts well the

local secondary dendrite arm spacing (SDAS), grain structure, phase composition, morphology of carbide particles and microhardness. Physical simulation of investment casting has numerous advantages over standard trial-and-error approach for development of new investment casting process. It leads to higher efficiency of experimental work and to reduction of material's amount required for development of the new investment casting process, as well as it improves quality of the final product.

In the second part, a novel high-throughput method for establishing the solidification-microstructure relationships has been presented. It involves a physical simulation of melting/solidification experiment with a constant cooling rate and variable temperature gradient. A demonstration of its effectiveness has been performed on state-of-the-art Ni-based superalloy IN718. In a single sample cooled at 10 ºC/s a range of temperature gradients from 1 -40 K/mm and solidification rates from 0.25 -10 mm/s was produced. A corresponding spread of microstructures obtained was confirmed by adequate changes in the grain size, as well as, secondary dendrite arm spacing. The presented method has a lot of advantageous features that makes it unique and promises a great future. First of all, it may be applied to virtually all metallic materials. Also, it is quite simple and not time consuming. In addition, it can be used for microstructure screening and optimizing of all relevant solidification processes, from directional solidification, over investment casting to rapid solidification. Furthermore, it can be used for the optimization of a specific process. Finally, it is suitable for both laboratory and industrial environment.

Acknowledgments

This investigation was carried out in frame of the VANCAST project (EU, FP7, ERA-NET MATERA+). SM and IS acknowledge gratefully the Spanish Ministry of Economy and Competitiveness for financial support through the Ramon y Cajal fellowships.

References

[1] Pattnaik S, Karunakar DB, Jha PK. J Mater Proc Tech 2012;212:2332-48.
[2] Mandziej ST. Mater Tehnol. 2010;44:105-19.
[3] [Hamilton RW, See D, Butler S, Lee PD. Mater Sci Eng A 2003;343:290-300.
[4] Gasko KL, Janowski GM, Pletka BJ. Mater Sci Eng A 1988;104:1-8.
[5] A.J. Torroba OK, L. Calba, L. Maestro, E. Carreno-Morelli, M. Rahimian, S. Milenkovic, I. Sabirov, J. LLorca. Integr Mater Manuf Innov 2014 (in press).
[6] Zhang Y., Huang B., Li J., Metall Mater Trans A 2013;44:1641-1644.
[7] Kurz W, Fisher DJ. Fundamentals of Solidification. Fourth revised edition ed. Aedermannsdorf, Switzerland: Trans Tech Publications; 1998.
[8] Szczotok A, Rodak K. Mater Sci Eng 2012;35:012006.
[9] He LZ, Zheng Q, Sun XF, Hou GC, Hu ZQ. J. Mater Sci 2005;40:2959-64.
[10] Seo SM, Lee JH, Yoo YS, Jo CY, Miyahara H, Ogi K. Metall Mater Trans A 2011;42:3150-9.
[11] Liu C, Shen J, Zhang J, Lou L. J Mater Sci Tech 2010;26:306-10.
[12] Milenkovic S, Rahimian M, Sabirov I. Metall Mater Trans B 2014;45:482-8.

MICROSTRUCTURE AND MECHANICAL PROPERTIES OF Al-ALLOYS WITH QUASICRYSTALS

I. Naglič[1], K. Delijić[2], Z. Samardžija[3], F. Bikić[4], B. Leskovar[1], B. Markoli[1]

[1]*University of Ljubljana, Faculty of Natural Science and Engineering, Slovenia*
[2]*University of Montenegro, Faculty of Metallurgy and Technology, Montenegro*
[3]*Institute Jožef Stefan, Department of Nanostrctured Materials, Slovenia*
[4]*University of Zenica, Faculty of Metallurgy and Materials Science, Bosnia and Herzegovina*

Abstract

Aluminium alloys with primary icosahedral quasicrystals (iQCs) were prepared in this work. Alloys of Al-Mn-Cu-Mg-Si with different content of manganese were prepared in chamber furnace and cast into a copper mould with 5 mm diameter. Light microscopy (LM) was used for the characterization of microstructure and evaluation of possible presence of QCs based on their morphology. Mechanical properties of prepared alloys were also determined in as-cast condition. Microstructure of fractured sample revealed that decohesion of primary phase was not observed.

Keywords: aluminium, quasicrystals, microstructure, mechanical properties

Introduction

Quasicrystals (QCs) were discovered by Shechtman et al. [1] in 1982 and this discovery created revolution in crystallography. QCs were first discovered in Al-Mn alloy system by rapid cooling of such alloy melts. Diffraction pattern of icosahedral QCs (iQCs) indicated icosahedral symmetry, which is forbidden in traditional crystallography, and nonperiodic array of diffraction peaks [2]. These first discovered QCs were thermodynamically metastable which means that they decompose into a crystalline phase on heating. Soon after discovery of QCs, stable QCs were also discovered [3-5]. Several practical applications of QCs are already known [6,7]. One of the characteristics of iQCs is their high symmetry. High symmetry ensures that there are many possible orientations for planar matching with another phase and quasiperiodicity ensures an epitaxy at the interface with periodic planes of many possible spacings [11]. These properties of iQCs make them good candidates for reinforcing phase in metallic matrix materials.

In this work we prepared aluminium alloys which contained an in-situ formed primary iQCs. We also characterized their microstructure and mechanical properties.

Experimental

Alloys from Al-Mn-Cu-Mg-Si alloy system were prepared in a chamber furnace from pure elements. Melting and casting was performed at 880 °C. Alloys were cast into a copper mould (copper block with dimensions 100x100x120mm)

with castings diameter of 5 and 15 mm. Estimated cooling rate in 5 mm diameter casting was found to be approximately 500 K/s. Bulk chemical composition of as-cast samples, presented in Table 1, were determined by XRF (X-ray fluorescence) analyser Thermo Scientific Niton XL3t GOLDD+.

Table 1: Bulk composition of alloys determined by XRF

		Al	Mn	Cu	Mg	Si
BI01A-2	wt.%	87,62	5,48	3,26	2,59	1,05
	at.%	91,67	2,81	1,45	3,01	1,06
BI01-2	wt.%	84,25	6,52	3,10	4,52	1,61
	at.%	88,37	3,36	1,38	5,26	1,63
BI02-2	wt.%	82,94	8,81	3,35	3,52	1,37
	at.%	88,31	4,61	1,52	4,17	1,40
BI03-2	wt.%	77,21	10,03	3,90	6,89	1,97
	at.%	82,72	5,28	1,77	8,20	2,03

Castings with 5 mm diameter were used for characterization of microstructure and mechanical properties in as-cast condition. Light microscopy (LM) was used for characterization of microstructure and evaluation of possible presence of QCs based on morphology. Samples for LM were mounted, grind and polished. Final polishing was performed by SiO_2 suspension and followed by etching in NaOH solution. Samples for compression testing with 5 mm in diameter were approximately 10 mm long. Universal uniaxial loading machine FPZ 100/1, VEb Thüringen Industriewerk was used for determining compressive strength, compressive yield strength and compressive fracture strain in an as-cast condition. Compression testing results presented in this work are an average value of two tested samples prepared from the same casting.

Results and discussion

Microstructure of alloys in the edge and central region of casting with diameter of 5 mm is presented in Figure 1. Primary phases present in these alloys predominately shows dendritic morphology. These dendrites often shows five branches which indicates that these primary phases are iQCs. Besides iQCs, decagonal quasicrystals (dQCs) are also probably present in sample BI03-2 with highest content of manganese as it is presented in Figure 1 g and 1h. dQCs are suspected to be present in both edge and central region of the casting. Morphology of primary dQCs is also distinctive and it shows dendritic morphology with 10 branches present in ideal case. Appearance of dQCs in sample BI01-3 is consistent with observation that metastable dQCs appears in the cases of smaller cooling rate and higher manganese content [8-10].

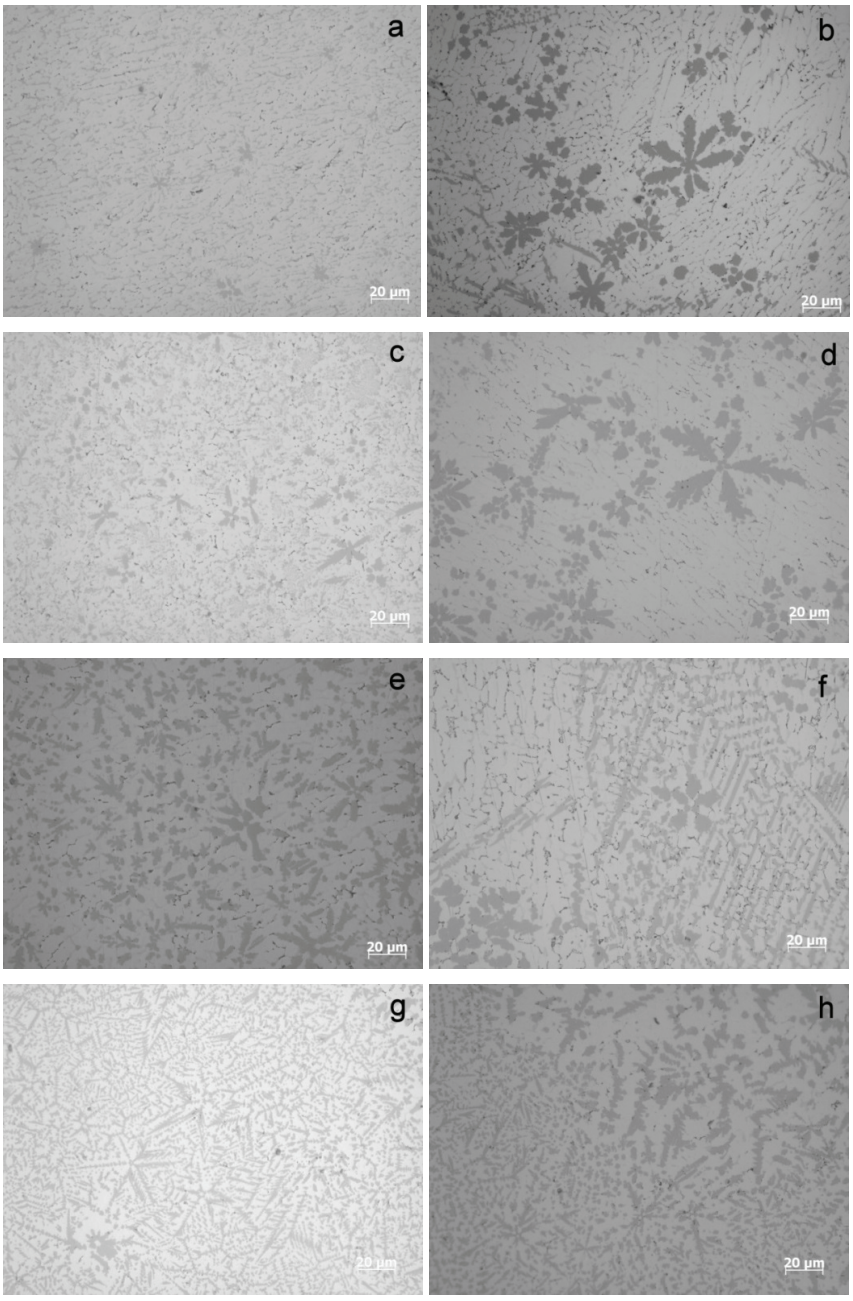

Fig. 1. LM images of edge (a, c, e, g) and central (b, d, f, h) regions of as-cast alloys BI01A-2 (a, b), BI01-2 (c, d), BI02-2 (e, f) and BI03-2 (g, h).

Compressive strength, compressive yield strength and compressive fracture strain are presented in Table 2. Largest compressive strength and compressive fracture strain was found in the case of a sample BI01A-2. On the other hand largest compressive yield strength was found for a sample BI03-2 which shows lowest value for compressive strength and compressive fracture strain. The trend of increase in compressive yield strength and decrease of compressive strength and fracture strain correspond well to the increased content of manganese, copper and magnesium in our alloys. Increased manganese content increases the amount of primary iQCs phase.

Table 2. Compression test results

Sample	Compressive yield strength (MPa)	Compressive strength (MPa)	Compressive fracture strain (%)
BI01A-2	330	776	19,7
BI01-2	326	762	16,1
BI02-2	391	678	11,9
BI03-2	430	645	7,7

Mechanical properties of these alloys are comparable to those in age-hardenable aluminium alloys and discontinuously reinforced metal matrix composites [12, 13]. These results seem promising for further development of such alloys.

It was already mentioned that iQCs possesses high symmetry which ensures that there are many possible orientations for matching with another possibly crystalline phase. Quasiperiodicy ensures an epitaxy with periodic planes of many possible spacing [8]. Since the interface between reinforcing phase and matrix is particularly important for the mechanical properties of such materials, it is interesting to evaluate this. Microstructure of test specimen BI01-2 after compression testing near the shear crack is presented in Figure 2.

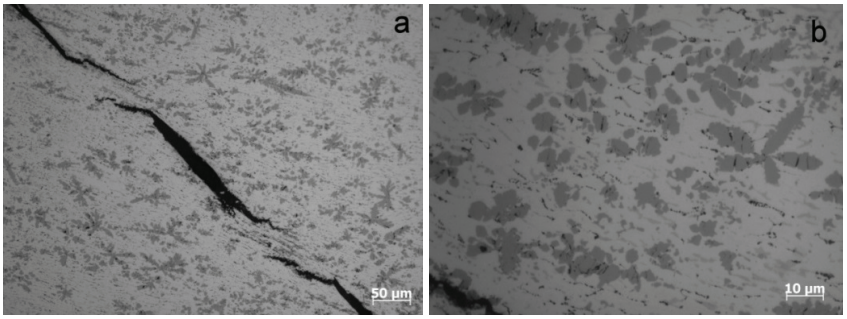

Fig. 2. LM microscopy images of fractured sample BI01-2 near the shear crack after compression testing: macro view of shear crack (a) and detailed view of cracks in dendritic iQCs.

Microstructure of fractured sample BI01-2 shows that aluminium matrix is highly deformed near the shear crack. Several iQCs branches are also cracked particularly those which are close to the shear crack. Decohesion of primary iQCs phase was not observed despite severe deformation of aluminium matrix and cracking of primary iQCs phase.

Conclusions

Four alloys were prepared which all predominately contain primary iQCs. Compressive testing reveals that compressive yield strength increases while compressive strength and compressive fracture strain decreases with increasing content of manganese (increasing amount of primary iQCs) and copper and magnesium. Compressive yield strength ranges between 326 and 430 MPa while compressive fracture strain was between 19,7 and 7,7 %. Several iQCs branches close to the shear crack have cracked while decohesion of primary iQCs phase was not observed.

Acknowledgements

This work was realized through the financial support of bilateral project SLO-MNE BI-ME/14-15-012.

References

[1] D. Shechtman, I. Blech, D. Gratias and J- W. Cahn, Physical Review Letters, 53 (1984) 1951-1954
[2] A. P. Tsai, Sci.Tecnol.Adv.Mater. 9 (2008) 013008, 1-20
[3] A. P. Tsai, A. Inoue and T. Masumoto, Jpn. J. Appl. Phys., 26 (1987) 1505-1507
[4] A. P. Tsai, A. Inoue and T. Masumoto, Jpn. J. Appl. Phys., 27 (1988) 1587-1590
[5] C. A. Guryan, A. I. Goldman, P. W. Stephens, K. Hiraga, A. P. Tsai, A. Inoue, and T. Masumoto., Phys. Rev. Lett. 62 (1989) 2409-2412
[6] J.-M. Dubois, Chem. Soc. Rev., 41 (2012) 6760–6777
[7] Y. K. Vekilov and M. A. Chernikov, Physics-Uspekhi, 53 (2010) 537-560
[8] L. Bendersky, Phys. Rev. Lett. 55 (1985) 1461-1463
[9] R. J. Schafer and L. Bendersky, Scripta Metallurgica, 20 (1986) 745-750
[10] N. Thangaraj, G. N. Subbanna, S. Ranganathan and K. Chattopadhyay, Journal of Microscopy, 146 (1987) 287-302
[11] A. Singh and A. P. Tsai, J. Phys.: Condens. Matter., 20 (2008) 314002 (12pp)
[12] ASM International Handbook Committee, ASM handbook, Volume 2, Properties and Selection: Nonferrous Alloys and Special-Purpose Materials, 1990

IMPACTS OF LIME QUALITY ON ALUMINA PRODUCTION USING THE BAYER PROCESS

Céline DEWAGHE[1], Elise DI MARINO[1], Razvan TULIGA[1], Pavel HANZL[2]

Carmeuse Research and Technology, Boulevard de Lauzelle 65, B-1348 Louvain-la-Neuve, Belgium elise.dimarino@carmeuse.com
Celine.Dewaghe@carmeuse.com
Carmeuse Europe, Mokra 356, 664 04 Mokra, Czech Republic,
pavel.hanzl@carmeuse.cz

Abstract

Lime is an indispensable chemical for 4 basic steps in alumina extraction from bauxite using the Bayer process. Each of these steps requires a specific set of lime quality parameters. Lime functionalities for each step and critical quality parameters are reviewed and listed. Different lime types were tested and customised in operation size at two big South European alumina producers. Experience from these application trials is discussed to prove the theoretical assumptions in the industrial size.

Introduction

The Bayer process, although invented by K.J. Bayer in 1888, remains the most efficient one to produce aluminium from bauxitic ores. The process is based on alkali leaching and purification of alumina as the source material for aluminium reduction in a smelting process. Caustic is the main reagent in the Bayer process while several further chemicals are applied. Lime is the main auxiliary chemical used for this process. The lime industry performs customised product development to produce and supply the Bayer installations with the best fitting products having specific usage properties.

Lime application and functionalities in the Bayer process

In most industrial installations, lime is used in the following steps of the Bayer process:

- Digestion process
- Causticising
- Sodium aluminate liquor “polish filtration”

The basic process flow with main lime input points is shown at Fig 1

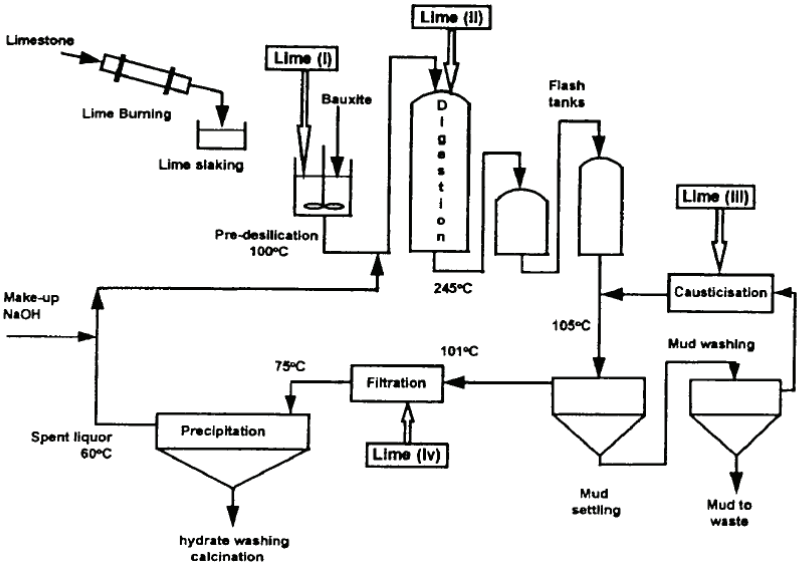

Fig. 1. Schematic diagram of Bayer process [1]

More details on each steps and main lime functionalities are described in the following parts.

Lime preparation step

Lime for the Bayer process is used mainly in a form of calcium hydroxide slurry, technically called as Milk-of-Lime (MOL). MOL is prepared by dispersing calcium hydroxide ($Ca(OH)_2$) or by quicklime slaking (i.e. wet hydration of CaO. Depending on the given application step, slaking is performed either with water or with spent liquor at a range of temperatures.

Typical lime slakers are designed either as continuous (more frequent) or batchwise. The schemes of these two basic types are shown at Fig 2 and 3. Both installation types provide comparable MOL quality but differ in volume output or further practical parameters.

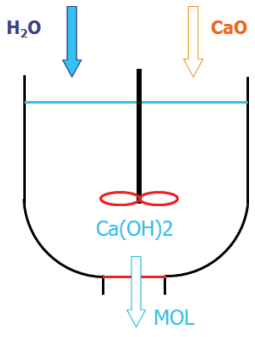

Fig. 2. Schematic representation of batchwise process for MOL preparation

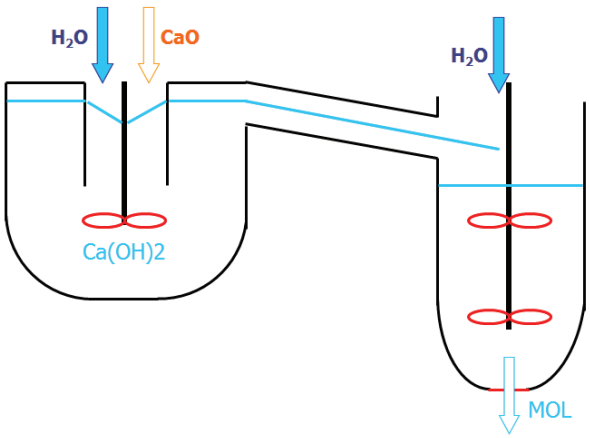

Fig. 3. Schematic representation of continuous process for MOL preparation

The common lime parameters for MOL preparation units in most of the Bayer installations are the following:

- Grain size

Theoretically there are no limits on quicklime granulation except the effects of grits (see further). The incoming lump lime in coarse granulation is crushed to a typical size of 0-20 or 0-40mm.

- Chemical purity – residual carbonate content

The residual calcium carbonate reduces the total yield of MOL from a given lime volume; the carbonate in a form of grit needs to be removed from the MOL slaker.

- Reactivity with water

The reactivity, expressed as a temperature increase in time for a given water/lime ratio (at standardized initial temperature), is a critical parameter for any lime slaking unit. Besides technical and safety impacts (e.g. moisture release, slaked slurry movement / stability in the reaction vessel or drum), inappropriate reactivity may cause increase of viscosity which may cause conveying issue, and significant variation of particle size of the lime slurry.To some extent, the impact of reactivity can be compensated by the slaking water or alkali liquor temperature.

The common MOL parameters required, regardless the production unit type and the application sites, are the following:

- Dry matter content (directly linked with density)
- Viscosity
- Settling rate
- Fineness

Digestion process

In the digestion step, the key of the Bayer process, all Al_2O_3 in the bauxite must be extracted.

Aluminium hydroxide is treated with NaOH at temperature and pressure,

which vary depending on type of ore and economic factors, to give a solution of sodium tetrahydroxoaluminate.

$Al(OH)_3 + NaOH \rightarrow Na^+ + Al(OH)_4^-$

The second important reaction in digestion is desilication, which consumes high amount of Na(OH).

$Al_2O_3.2SiO_2.2H_2O + 6\ NaOH \rightarrow 2NaAlO_2 + 2Na_2SiO_3 + 5H_2O$ [2]

The first purpose of lime addition is to initiate given minerals dissolution at high temperature and pH.

$Ca(OH)_2$ catalyses the diaspore (alpha-AlO(OH) dissolution which allows a reduction of digestion temperature.

$$Ca(OH)_2 + AlOOH \xleftrightarrow{H_2O+OH^-} CaO.Al(OH)_3 \xleftrightarrow{} Ca(OH)_2 + Al(OH)_4^-$$ [1]

Other purposes of lime addition during digestion are the following:

- It catalyses the conversion of Goethite (alpha-FeO(OH)) into Hematite (alpha-Fe2O3).
- Very low SiO_2 concentrations can be achieved if an excess of CaO is charged. A less soluble desilication compound (cancrinite) is formed. [2]
- The addition of $Ca(OH)_2$ captures phosphate by forming insoluble compound following the reaction: $5Ca(OH)_2 + 3\ Na_3PO_4 \rightarrow Ca_5(PO_4)_3OH + 9NaOH$
- It removes carbonate in forming insoluble compounds
- It minimises the effect of sodium titanates on aluminium extraction. The reaction between NaOH and Ti compounds in bauxite can lead to the formation of sodium titanates. Their formation is undesirable since they form a gelatinous film over the aluminium compound, which would lower the extraction efficiency. This happens even at high temperature (290°C) that normally favours complete extraction. The direct reaction of CaO and TiO_2 may eliminate the formation of sodium titanates and associated problems. [1]

In this step, lime can be added as dry product or as MOL in the ball milling step, or as MOL in the digestion step itself.

In digestion step, typically 2 to 3 % of CaO is added at dry bauxite ore. Higher CaO than 5 % of dry bauxite weight results in the formation of Tri Calcite aluminate (TCA) in the red mud, with a consequent decrease in the alumina extraction and therefore the lime dosage needs to be adjusted precisely. [1]

The critical lime and MOL parameters are the following:

- Active CaO content
- Reactivity with water

- Purity

Impurities and trace elements that can affect the digestion process are carbonate and silica.

Causticising

Na_2CO_3 present in the Bayer liquors may be removed by reaction of CaO or $Ca(OH)_2$ to $CaCO_3$ according to the following chemical reaction :

$Ca(OH)_2$ (or CaO) + Na_2CO_3 <-> $CaCO_3$ + 2NaOH [1]

$3CaO.Al_2O_3.6H2O + 3\ Na_2CO_3$ <-> 3CaCO3 + $2NaAl(OH)_4$ +4NaOH [1]

In some processes CaO, soda ash and bauxite are added directly to the Bayer liquor prior to digestion. High caustic concentration of the liquor and competitive formation of calcium aluminate and calcium titanates reduce causticization efficiency. An alternative is to add lime to the overflow of red mud washer unit and liquor.

Another process consists of heating the red mud thickened, introducing it into the caustisization system and adding $Ca(OH)_2$. This enables causticizing the liquor and desilication product contained in the red mud). [1]. Higher causticization efficiency is reached by longer reaction times or increasing agitation (e.g. stirring speed).

In this process step, reactivity in water is the critical lime parameter.

CaO with low specific surface area (lower porosity and lower reactivity in water) is preferred. CaO with high reactivity would react first with water (to form $Ca(OH)_2$) while less reactive CaO would react directly with Na_2CO_3.[1]

Sodium aluminate liquor "polish filtration"

Solid residue separation is usually made in three main steps:

1. The sand fraction is separated from the process stream liquid by washing in classifier
2. The fine residue remaining in the liquor is settled in raking thickeners
3. The overflowing solution (pregnant liquor) containing generally less than 0.3g/l of fine solid is removed in "polish filtration" to reduce this amount below 0.5 mg/L. Filter presses are usually applied here. [2]

To enhance the filtration step performance, TriCalcium Aluminate (TCA) - $3CaOAl_2O_3.6H2O$ as filter aid is synthesised in situ - either from CaO and spent liquor or $Ca(OH)_2$ slurry and thickener overflow liquor or CaO and pregnant liquor.

This TCA will:

- Enhance filtration rate by minimising the filter cake resistance
- Lower the calcium concentration in the liquor [1]

In this step, TCA slurry is typically prepared in similar way as for MOL preparation. As an example quicklime is slaked with spent liquor at high

temperature (> 90°C).

The critical lime parameters are the following:

- **Purity**

The TCA synthesis typically does not require the highest lime purity possible. The optimum purity is specific to the given installation and process details. Nevertheless, the more impurities lime contains the more they will occur in MOL.

- **Reactivity with water**

High specific surface area of quicklime (which results in high reactivity with water) is recommended in general. However, specific installations require the reactivity customising to achieve the best TCA particle size distribution.

The critical MOL parameters are the following:

- **Concentration and dosage**

The lime dosage shall be matched precisely to the filtration system; both under- and overdosage can reduce the TCA filtration index dramatically. The lime/carbonate ratio defines the necessary lime/alumina dosage. The NaOH concentration also affects the TCA particle size at its synthesis.

- **Impurities and additives**

Besides the inorganic impurities in lime like typically sulphates, organic additives affecting lime solubility in water can affect the TCA particle size and distribution significantly

- **Particle size distribution and particle shape**

These parameters are critical to TCA filtration speed and specific to the given filtration system

Practical experience from lime customising in operation conditions

Carmeuse Co., a global leading lime producer, performed lime optimising campaigns in two South-Eastern European alumina plants over 2014. Each campaign was aiming at different targets and resulted in more detailed understanding on lime functionalities in the digestion and red mud treatment steps.

Quicklime particle size and purity optimising

The purpose of this trial was to increase the MOL slaking process efficiency and possibly reduce the quicklime consumption by changing its granulation,.

Process description

Lime is delivered in a typical fraction of 20-100 mm and stored in a closed hall.

Separate MOL slakers are installed to feed the bauxite grinding, digestion and filtration parts. The slakers' design is identical – horizontal drum type; each is equipped with a cylindrical screen to remove grits (residual limestone particles) and a MOL storage tank.

Lime is slaked with the attack solution (165 – 170 g/l of NaOH) for bauxite grinding and with the spent liquor (7 – 10 g/l of NaOH) for the filtration step.

Performance indicators monitored during trials.

Several parameters were followed throughout the trial:

- Quicklime dosing rates for MOL production in both for the grinding and the filtration steps
- MOL quality constancy in time
- Effect of the produced MOL on the grinding step (to be kept constant and to avoid overdosing)
- Influence of the produced MOL on the filtration process

Trial results

The tested lime was delivered in a narrow granulation range of 0-10 mm. Its purity reached a typical reactive CaO value above 90 %and the reactivity in water expressed as the t60 value (i.e. the time of reaching 60°C from initial 20°C at a standard lime/water ratio) of typically 220 seconds. The tests showed the main following results:

- **Overall MOL quality**

The MOL quality expressed in concentration, fineness and viscosity remained unchanged comparable with the existing one. The quality was constant in time.

- **Quicklime slaking process economy**

The different granulation resulted in significant reduction of grits (formed of both residual limestone and unslaked particles sticking to the limestone grains). The average grit reduction reached 75%; this means approx. 15% of total lime consumption. See fig. 4 for the main results.

The overall process economy improvement is estimated to be more than equal to lime cost savings as it also includes the costs for grit landfilling.

- **Impact on the filtration step**

No effect on the filtration process was observed during the trial; the TCA particles distribution and filtration efficiency remained constant

Conclusion

In this case, the use of lime with optimised particle size resulted in significant reduction of lime consumption while the rest of process parameters remained constant.

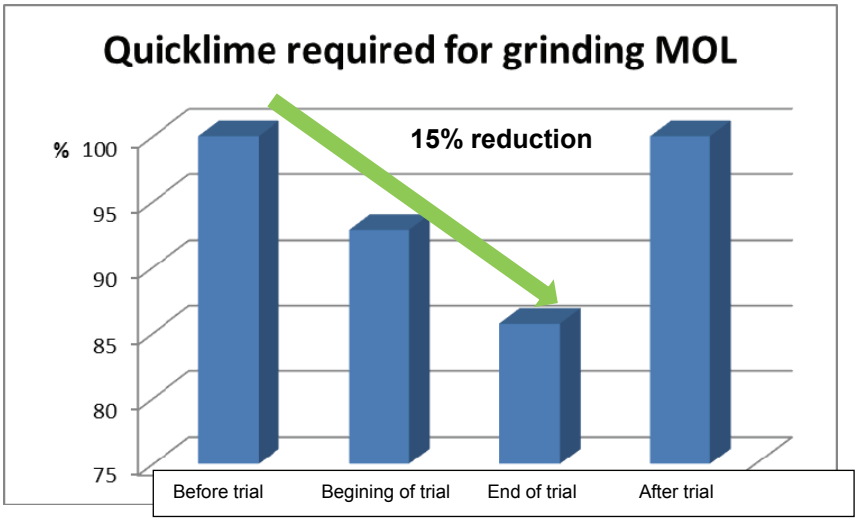

Fig. 4. Average MOL dosing rate before during and after trial with 0-10 mm lime.

Quicklime reactivity customising

In this case, the initial idea was to validate an alternative lime source with higher chemical purity and reactivity. MOL behaviour at the TCA filtration step was studied specifically and this resulted in developing a tailor-made lime product for the given installation.

Process description

MOL is prepared from quicklime in 0-5 mm granulation in a central slaker of a vertical batch design. The MOL density is up 1300 g/L, its concentration is about 150g/l fo dry matter while the spent liquor concentration is 200g/l expressed as NaOH content.

Two types of MOL are prepared:

- One injected at bauxite grinding stage located 170 m away from slaker, to prepare digestion
- The other containing TCA is dedicated to filtration located 500 m way from slaker

See the process flow sheet at Fig 5.

Performance indicators monitored during trials

Several parameters were followed throughout the trial:

- MOL density for both types (grinding and filtration)
- Maximum slaking temperature (should be above 90°C for TCA formation)
- Particle size of MOL for filtration step (medium particle size D50 and amount of particles smaller than 5 µm)
- Effect of the produced MOL on the grinding step

- Influence of the produced MOL on the filtration step (assessed by turbidity and CaO content of filtrate liquor)
- Quality of final products (alumina and zeolite)

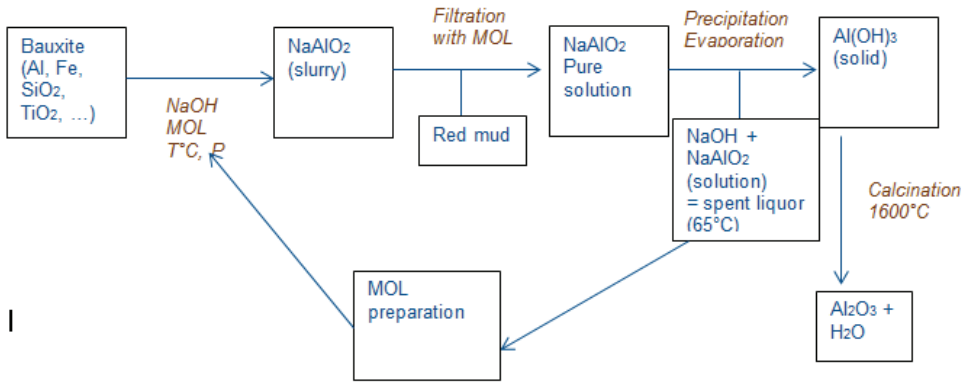

Fig. 5. Simplified process flow sheet

Lime quality and its impact on main process steps

The initial lime batches tested had typical content of reactive CaO of 90% and the typical t60 value of 150 seconds. See Table 1 for main lime parameters. The lime granulation was 0-5mm.

Table 1: Properties of high reactivity lime tested initially

CO2 (%)	***SiO_2 (%)***	***Reactivity in water - t60 (s)***	***<10.0 mm***	***<5.00 mm***	***<1.00 mm***	***Active CaO (%)***
0,7	0,6	148,000	100	99	77	93

The MOL produced for grinding of bauxite had no negative effect on the digestion stage of the process.

Nevertheless, concerning the MOL dedicated to filtration, first trials showed that high reactive lime with highest purity possible does not seem to be the optimum solution for the installation tested. Drawback occurred at two installation steps:

- Quicklime slaking

The batch slaker appeared to be designed for different lime types, produced historically in single-shaft kilns. High reactivity of tested lime increased maximum slaking temperature by 20 °C. This resulted in vigorous reaction with slurry splashing from the slaker. Besides MOL losses, this is a significant safety risk.

- Filtration step

According to the common process knowledge and bibliographic references, high reactivity of quicklime causes coarser TCA particles more efficient as filter aid. The operation results showed the opposite. The medium TCA particle size

achieved (D50) with high reactivity lime was 8 μm and MOL contained17 % of particles below 5 μm. In standard operation D50 = 10 μm and 19 % of particles are below 5 μm.

The smaller TCA particle size resulted in a 30% increase of CaO content in aluminate liquor and a decrease of zeolites quality.

Product customising

Based on the results achieved in first testing campaigns, special lime type with prolonged reactivity was developed and tested again in the industrial size. Typical parameters of this lime were similar to previous lime tested (see Table 1) but the reactivity was lower (t60 value over 300 s). The operation trial confirmed that the new type fits to the installation completely and can achieve operation savings, as expected.

The results showed in particular that:

- The slaking process was moderate without any splashing or irregular reaction
- The MOL concentration was stable and its physical parameters (i.e. density) were unchanged compared with regular operation
- The TCA particle size distribution changed significantly to the medium size of 12 μm; the content of particles below 5 μm was 10%.The total distribution curve is showed in Fig 6.
- Turbidity and CaO content of filtrate liquor were not affected by the trial
- Quality of finals products was not affected as well.

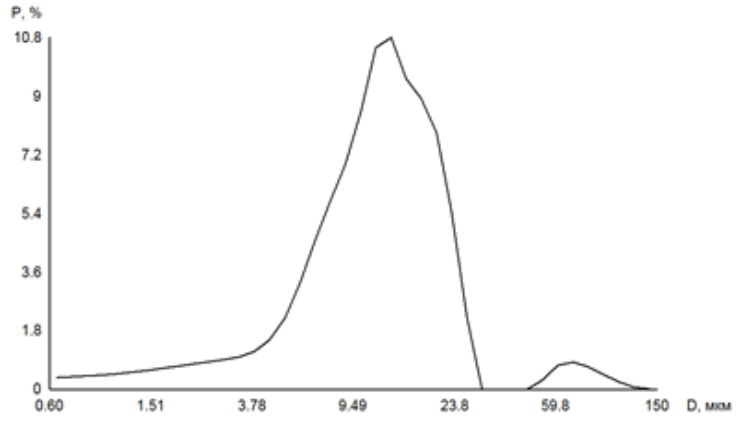

Fig. 6. Particle size distribution curve of TCA slurry produced with optimized reactivity lime

Conclusions

Lime is used in several steps of the Bayer process for alumina extraction and applied mainly in the slurry (Milk Of Lime) form in each of them. Each step has a special set of critical MOL parameters. These depend both on the incoming quicklime quality and the type and operation practices at a given MOL preparation step.

Increasing the quicklime purity and reactivity usually improves the Bayer process economy; the quicklime reactivity shall be matched to the given MOL installation type and process parameters.

The MOL purity, concentration and particle size distribution need to be adjusted individually for each Bayer process step to optimise the process economy and operation efficiency.

The on-site trials showed that:

- The quicklime granulation optimization can reduce the total cost of the liming step significantly
- The quicklime reactivity in general improves the process efficiency but is case specific and shall be optimised to the process parameters in the plant
- Optimised quicklime reactivity can contribute to total operation costs reduction

References

[1] The Chemistry of CaO and Ca(OH)2 relating to the Bayer process, B.I. Whittington, Hydrometallurgy 43 (1996) 12-35

[2] Ullmann's Encyclopedia of industrial Chemistry, Aluminium Oxide, 2002, pages 11 – 29

SECONDARY ALUMINIUM AS A REDUCING AGENTIN THE ALUMINOTHERMIC PROCESSES

Vaso Manojlović[1*], Željko Kamberović[2], Marija Korać[2], Milorad Gavrilovski[3], Miroslav Sokić[1],Branislav Marković[1], Tihomir Kovačević[3]

[1] *Institute for Technology of Nuclear and Other Mineral Raw Materials, 86 Franchet d' Esperey St., Belgrade, Serbia*
[2]*Department of Technology and Metallurgy, University of Belgrade, 4 Carnegie St. 11120 Belgrade, Serbia*
[3] *The Innovation Center at Department of Technology and Metallurgy, University of Belgrade, 4 Karnegy St., 11120 Belgrade, Serbia*
** v.manojlovic@itnms.ac.rs*

Abstract

Aluminothermic reactions are extremely exothermic reactions where aluminium in a powder form is used as reducing agent. In most metallurgical processes the use of powder aluminium, obtained by atomization process of liquid aluminium, is not economically feasible. However, it has the advantage compared with other methods, in the technological point of view. At this paper, the possibility of using the secondary aluminium foil as a replacement for the atomized aluminium powder in aluminothermic processes was investigated. Secondary aluminium was mechanically and thermally treated in order to obtain suitable material for aluminothermic reduction reactions. Detailed apparatus used in the experiment was described. Obtained powdered aluminium from foil was characterized and compared with a standard atomized aluminum powder. It was shown that secondary aluminium, prepared in such a way can be used as replacement for the atomized aluminium in the aluminothermic reduction processes.
Keywords: Aluminium foil, Atomized aluminium, Aluminothermy, Thermite mixture

Introduction

Aluminothermic reactions are thermite reactions in which aluminum metal reacts with some metal oxide reducing it to the pure metal. These reactions are highly exothermic and self-propagating so only initiation is needed to complete the reaction [1]. Aluminothermic reaction has found many applications in production of metals and alloys, welding and coating [2, 3, 4]. For self-propagating thermite reactions the atomized aluminium is commonly used [5, 6]. The general reaction between aluminium and metal oxide can be presented as [7]:

$$3MeO + 2Al = 3Me + Al_2O_3 \quad (1)$$

In this article, the secondary aluminium in the form of powdered coated foil will be compared with commonly used atomized aluminium. Also, the possibility of self-propagating reaction with the powdered aluminium foil will be examined.

The most important parameters for the powdered aluminium, suitable for the thermite reactions, are surface development and size of the particles.

Experimental

The used aluminium foil is taken from the packaging factory, as processing waste. Three type of foil were chosen in a pressed form as it is shown in Figure 1. The physical characterizations of these types of foils are given in Table 1.

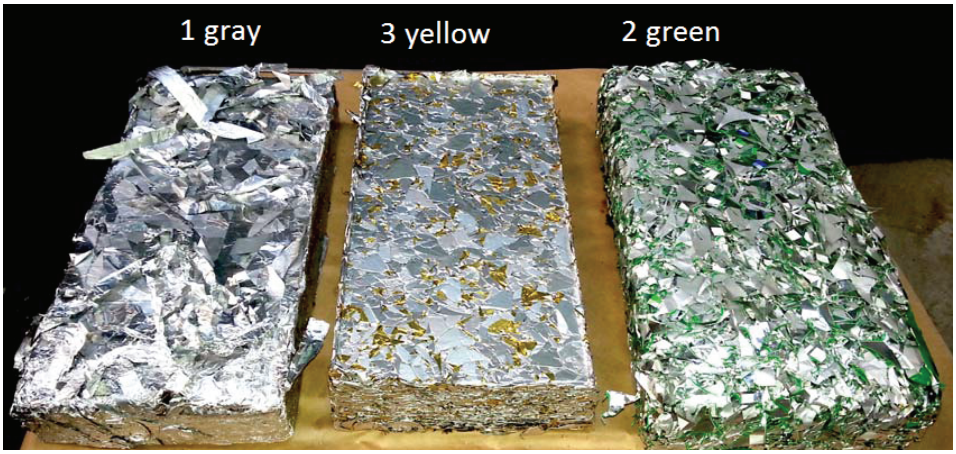

Fig. 1The pressed aluminium foils

Table 1 Physical characterization of pressed secondary aluminium foils

No.	Color	Thickness, μm	Bulk density, kg/m^3
1	gray	15±2	732±3.7
2	green	40±2	359±1.8
3	yellow	120±6	602±3.0

The samples were treated at 105^{o}C in a laboratory dryer, according to the standard SRPS EN 12880:2007, in order to determinate the humidity content. The mean values of humidity in the samples are given in Table 2.

Table 2 Humidity and coating content in the samples

No.	Humidity, wt. %	LOI, wt. %
1	0.01	12.9
2	0.03	7.6
3	0.02	13.6

Pyrolysis of samples was done for 1 hour at 550^{o}C, in nitrogen atmosphere, to determinate the content of organics from the coating. The loss of ignition is given in Table 2. The resin from the pyrolysis has been characterized using Fourier Transform Infrared Spectroscopy (FT-IR).

Pressed bales were cut into the smaller pieces. In this manner saw dust was obtained. This dust was sieved to the particles size in a range of +200 to -400 μm, which is suitable size for the aluminothermic process. The same sized particles of atomized aluminium powder were used for comparison. The purity of atomized aluminium powder was 99.7%.

The thermite mixture of Mill scale and both atomized aluminium and foil aluminium powder was prepared. In the case of aluminium foil, all types of foil were mixed along with a Mill scale. The Mill scale was generated in Metalfer Steel Mill Ltd., Sremska Mitrovica, Serbia. The chemical composition is given in Table 2. The Mill scale, primarily, contains Magnetite (about 40 wt. %), Wustite (57 wt. %) and Hematite (3 wt. %).

Table 3 The Mill scale chemical composition, in wt. %

Fe	Si	Cr	Sn	Ni	C	P	S	Mn	Ca	Al	Mg	Cu
70.87	0.80	0.04	0.01	0.03	0.02	0.03	0.03	0.09	0.39	0.11	0.13	0.30
O (oxides)		LOI		Others								
25.23		1.80		0.12								

Excess of the aluminium was 20%, compared to the stoichiometric proportion. The thermite reaction was done in the preheated magnesia reactor. The ignition of thermite mixture was done with a mixture of magnesium powder, potassium perchlorate and manganese oxide.

Results and discussion

The microstructural comparison of powdered aluminium foil and commercial atomized aluminium was done with the optical microscope, as it can be seen in Figure 3. The shape of particles in the sample 2 was most closed to the atomized aluminium. However, it can be seen that surface is more developed in the samples 1, 2 and 3 then in the atomized aluminium. This is a consequence of thin foil used for powder manufacturing (Table 1).

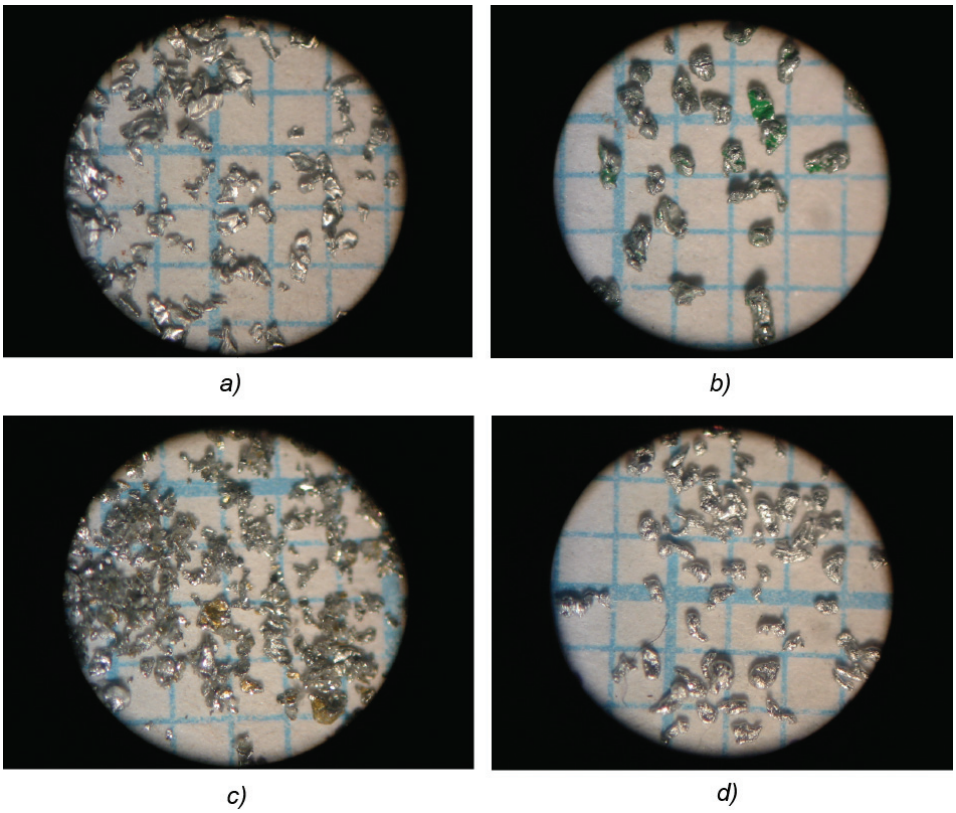

Fig. 3 Microstructural comparisons of aluminium powders on 1x1 mm grid: a) 1 grey b) 2 green c) 3 yellow d) atomized

Based on FT-IR analysis of all samples pyrolysis resigns, the presence of aromatic and particularly aliphatic compounds was registered. A group of ketones and primary amines were dominant. The presence of halogen compounds was not detected. This means that carbon and hydrogen will be included in reduction process along with the aluminium.

The main reactions that occur in the aluminothermic processing of Mill scale are [8]:

$3Fe_3O_4 + 8Al = 9Fe + 4Al_2O_3$ $\Delta H_{293}^{\theta} = -3355.7\ kJ$ (2)

$Fe_2O_3 + 2Al = 2Fe + Al_2O_3$ $\Delta H_{293}^{\theta} = -853.6\ kJ$ (3)

$3FeO + 2Al = 3Fe + Al_2O_3$ $\Delta H_{293}^{\theta} = -873.6\ kJ$ (4)

The overall energy effect will depend on the phase composition in the Mill scale. In this case, the calculated overall released energy will be about - 5871.9 kJ/kg Fe.

After initiation, the reactions were finished at about half of minute. The slag phase was separated from metal phase relatively easy due to the great differences in densities. In the case of aluminium foil, the greater amount of aluminium was taken, according to the coatings content. The reaction with aluminium foil was less aggressive then in the case of atomized aluminium. This can be attributed to the coating layer which does not allow direct exposure of aluminium to the ferrous oxides.

The amounts of metal and slag phases were measured in both aluminothermic reactions with aluminium foil and with the atomized aluminium. The results are presented in Table 4.

Table 4 Material balance of aluminothermic reactions with various aluminium powders

	Input		Output					
	Al, g	Mill scale, g	Metal, g					Slag, g
Al foil	35.00	98.00	63.82 ± 1.2					71.61 ± 2.1
			C, %	P, %	S, %	Al, %	Fe, %	
			0.202	0.024	0.077	1.29	97.2	
Al atom.	30.00	98.00	59.80 ± 1.2					61.82 ± 2.1
			C, %	P, %	S, %	Al, %	Fe, %	
			0.073	0.030	0.085	0.86	97.6	

As we can see form the Table 4, the material balance of aluminothermic reactions with the aluminium foil and atomized aluminium are approximately the same. The loss of material in the case of using the atomized aluminium has emerged because of the material ejection out of the reactor due to the volatile conditions. Greater amount of carbon in the case of using the aluminium foil was expected. This can be avoided by thermal treatment of aluminium foil, but it will increase the economic costs.

Conclusion

The used aluminium foil, taken from the packaging factory as processing waste, was prepared in such a way to be suitable for aluminothermic process. The prepared powder was compared with the atomized aluminium. The microstructural comparison of powdered aluminium foil and commercial atomized aluminium showed their considerable similarity. The surface of powdered aluminium foil is more developed than in the case of atomized aluminium, which is suitable for thermite processes. The termite mixtures were prepared with the Mill scale and both atomized aluminium and powdered aluminium foil. The material balance showed that there are no major differences between using the commercial atomized aluminium and powdered aluminium foil. The higher carbon content in the metal obtained from thermite mixture with the powdered aluminium foil was expected and originates from coatings.

Acknowledgment

The authors wish to acknowledge the financial support from the Ministry of Education and Science of the Republic of Serbia through the projects TR34002 and TR34033.

References

[1] M. Gavrilovski, V. Manojlović, Ž. Kamberović, M. Korać, M. Sokić, Semi-empirical optimization software for aluminothermic and carbothermic reactions processes. Metallurgical and Materials Engineering, 20, 3 (2014) 199-206. ISSN 2217-8961

[2] A. Maleki, M. Panjepour, B. Niroumand, M. Meratian, Mechanism of zinc oxide–aluminum aluminothermic reaction, Journal of Materials Science, 45, 20 (2010) 5574–5580.

[3] J. Meia, R.D. Halldearna, P. Xiaoa, Mechanisms of the aluminium-iron oxide thermite reaction.ScriptaMaterialia, 41, 5 (1999) 541-548.

[4] V. Matković, B. Marković, M. Sokić, V. Manojlović, Valorizacija olova između produkata rafinacije bizmuta postupkom metalotermijske redukcije. Zaštita metarijala, 56, 1, (2015) 59-63.

[5] L. Duraes, B. Costa, R. Santos, A. Correia, J. Campos, A. Portugal, Fe_2O_3/aluminum thermite reaction intermediate and final products characterization. Materials Science and Engineering A, 465 (2007) 199–210.

[6] J. Robinson, Aluminothermic smelting: a versatile process serving demanding markets. International Smelling Technology Symposium (Incorporating the 6th Advances in Sulfide Smelting Symposium), Edited by: J. P. Downey, Th. P. Battle, J. F. White, TMS (The Minerals, Metals & Materials Society), (2012) 3-8.

[7] B.S.B. Reddy, K. Das, S. Das, A review on the synthesis of in situ aluminium based composites by thermal, mechanical and mechanical-thermal activation of chemical reactions. Journal of Materials Science, 42, (2007) 9366-9378.

[8] A. Roine, Chemical Reaction and Equilibrium Software with Thermochemical Database and Simulation Module, HSC Chemistry® 6.1, Outotec Research Oy, Pori, Finland, 2007.

CHARACTERIZATION OF INTERMEDIATE PRODUCTS DURING SECONDARY COPPER PRODUCTION

J. Trpčevská[1], K. Paulovičová[2], M. Laubertová[1], J. Briančin[3]

[1]*Technical University of Kosice, Faculty of Metallurgy, Department of Non-ferrous Metals and Waste Treatment, Letná 9, 043 53, Kosice, Slovakia, jarmila.trpcevska@tuke.sk,*
[2]*Institute of Experimental Physics, Slovak Academy of Sciences, Watsonova 47, 040 01 Kosice, Slovakia,*
[3]*Institute of Geotechnics, Slovak Academy of Sciences, Watsonova 45, 040 01 Kosice*

Abstract

The paper deals with characterization of the intermediate products formed during pyrometallurgical processing of low-grade scrap in secondary black-copper smelter. Blast furnace was used for initial melting and reducing secondary copper. Microstructural evaluation of the black copper, the converter copper (blister copper or rough copper) and the anode copper was realized using light microscopy and scanning electron microscopy in connection with EDX microanalysis. Samples were supplied by Slovak company which is producer of secondary copper.
Keywords: secondary copper, microstructure, black-copper, blister copper, anode copper, scrap

Introduction

Copper derived from a primary raw material is referred as primary copper, while secondary copper refers to all non-primary sources, such as metallurgical, industrial and consumer wastes and scrap. The International Copper Study Group (ICSG) estimates that in 2013, at the refinery level, secondary refined copper reached 18% of total refined copper production [1].

Secondary producers use processes similar to those employed for primary production. Secondary copper can be added at three phases in the primary copper making process. The most common is the converting furnace, but additions are made in the smelting and anode furnaces. Because secondary copper has no sulphur in it, adding it to a smelting furnace is a net energy consumer. This makes it difficult to add to matte smelting furnaces, which already require some fuel. Use of waste materials in the flash furnace is rare because of required waste particles size. Feeding scrap and waste to other types of primary smelting furnace is easier. Both Noranda and Mitsubishi smelting processes have been adopted to include scrap in the feed [2].

Secondary copper smelter can be divided into two groups. The first type is metal smelter, which treats only higher-grade metallic scrap. The second type is black-copper smelter, which processes low-grade scrap and waste along with higher-values scrap [2]. Traditionally, treatment of secondary copper feeds at existing smelting operations was performed in the blast furnace, Peirce-Smith converter and/or anode furnace. In the last 15-20 years however, due to their superior environmental performance and operational flexibility, there has been a shift towards secondary copper processing using bath smelting technologies such as the Outotec Ausmelt Top Submerged Lance (TSL) and the Outotec Kaldo Top-Blown Rotary Converter (TBRC) processes [3].

Metallo-Chimique, Montawerke Brixlegg and Aurubis Lünen are pure secondary smelters in EU. Some have the flexibility to process both primary and secondary feedstocks, like Boliden Rönnskär, KGHM Legnica and Aurubis AG Hamburg [4].

Experimental procedure

Samples for experimental study was supplied by Slovak company Kovohuty, a.s., producer of secondary copper. The company Kovohuty, a.s. in Krompachy, Slovakia as subsidiary of Montanwerke Brixlegg AG, Austria is fully owned subsidiary UMCOR Holding GmbH, Vienna [5].

Waste and scrap with copper content from 5% up to 99% of Cu are processed using three aggregates: Shaft furnace, Converters and Anode furnace. The feed to the shaft furnace is low grade and highly oxidized scrap. It requires reduction to metallic copper. Metallurgical coal is used as reductant and heat source. Product of smelting in the shaft furnace is black-copper with content of 70 - 75% Cu. The black copper with the addition of scrap with Cu content of 60-85% are subsequently processed in converter. The result of oxidation process in the converter is blister copper with content of 95-96% Cu. The blister copper along with high-grade scrap (above 90% Cu) is refined in modern anode furnace MAERZ with OUTOKUMPU casting mechanism. As a result, high-quality anodes with min. 99% Cu are produced.

Provided samples of the black-copper, the blister copper and the anode copper were characterized using light microscopy (Olympus BX 51) and scanning electron microscopy with EDX microanalysis (SEM-TESCAN MIRA3 FE).

Results and Discussion

Black copper is result of low grade scrap smelting in the shaft furnace and is characterized by high content of impurities. Microstructure of the black copper is documented on Fig.1 a-b. Fig. 1a) shows microstructure (un-etched sample) and Fig. 1b) shows etched microstructure at higher magnification. Presence of the several phases in the copper base matrix is observed.

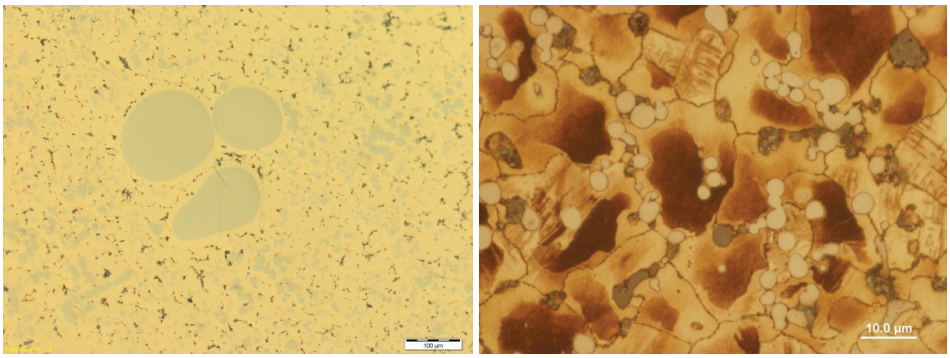

a. *b.*

Fig. 1. Microstructure of black-copper, a) un-etched sample, b) etched sample

Fig. 2 presents EDX spectrum with semi-quantitative EDX analysis of the black-copper sample. The aim of this technique is to determine the elemental composition. The presence of elements as Fe, Ni, Sn, Pb, Zn, S and As which are typically for this product was determined. Percentage of the elements in the copper base matrix slightly differs from data cited in literature [2]. Possible presence of noble metals (Au, Ag, Pt, Pd a.o.) was not detected. Fig. 3 shows SEM micrograph of black-copper microstructure detail with dominating phase and elemental distribution (EDX mapping) of the surface area. EDX mapping of the selected area showed, that phase with larger size is Fe and Ni based. This phase was distinguishable in un-etched sample by grey colour and in etched sample by white colour. EDX mapping showed that phases of smaller size are Pb base. Tin is relatively uniformly distributed in copper base matrix.

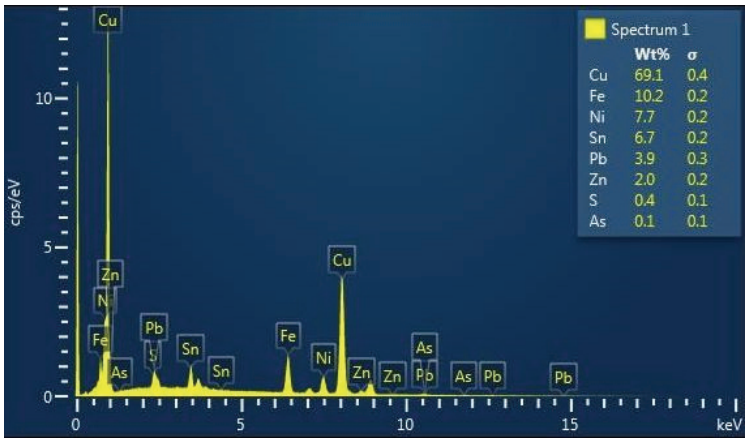

Fig. 2. EDX analysis of the black-copper

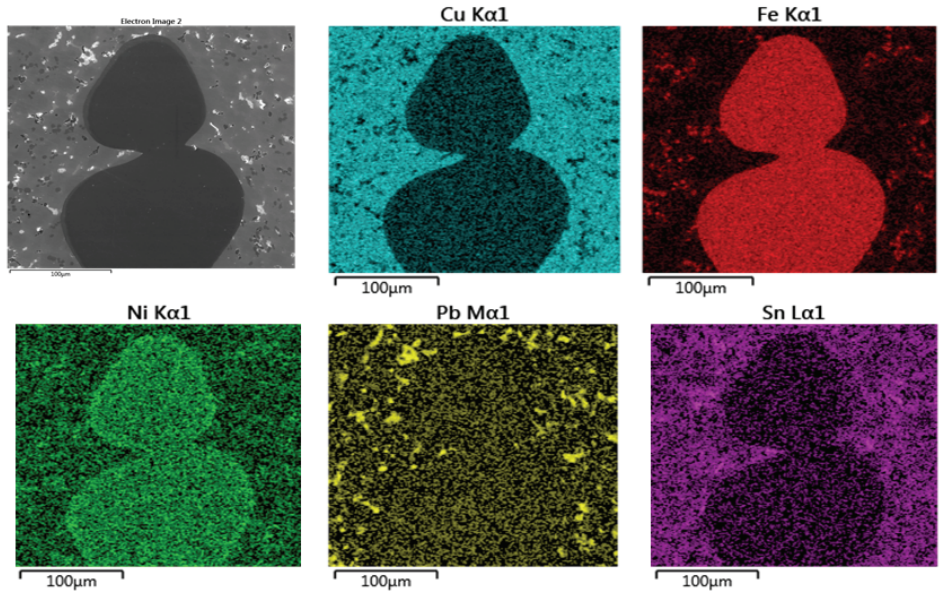

Fig. 3. SE image of the black-copper and corresponding EDX mapping images

Converter copper microstructure is documented in Fig. 4 (un-etched sample). The microstructure consists of Cu and (Cu-Cu_2O) eutectic with characteristic chain form. According to the Cu-O binary phase diagram (Fig. 5) this eutectic reaction occurs around 1066°C for oxygen contents in the melt higher than 0.004% wt%. The presence of Cu_2O in the metal core is typical of copper melted under oxidizing conditions [6, 7]. EDX semi-quantitative analysis revealed following composition of converter copper: 96.9% Cu, 2.3% Ni and 0.7% oxygen. Subsequently EDX analysis from the area with the higher presence of phases revealed some tin content. Fig. 6 shows EDX mapping from this area. Analysis revealed presence nickel and oxygen base particles. They are likely NiO.

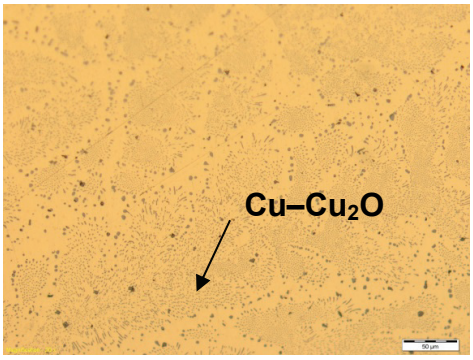

Fig. 4: Converter copper microstructure

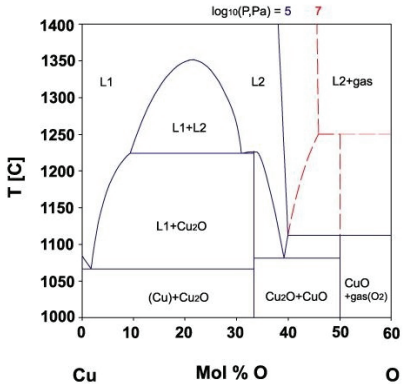

Fig. 5: Cu-O phase diagram

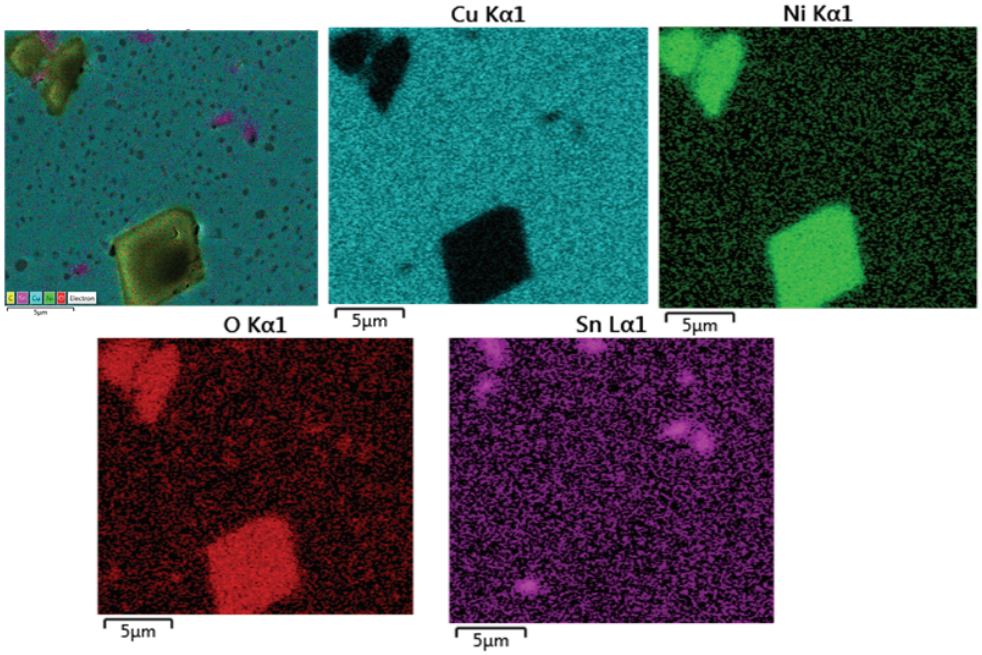

Fig. 6: EDX mapping images of the converter copper

Anode copper microstructure is shown in Fig. 7. In the microstructure the eutectic Cu-Cu_2O is observable, but in the less extent as compared with converter copper. It is related with the process of deoxidation during fire refining. Similar microstructure of copper remelted and cast into a metal mould after deoxidising procedure was observed in [8]. Anode copper is a final product of scrap processing of Kovohuty, a.s. Krompachy. The highest purity is achieved by subsequent electrolytic refining in subsidiary company.

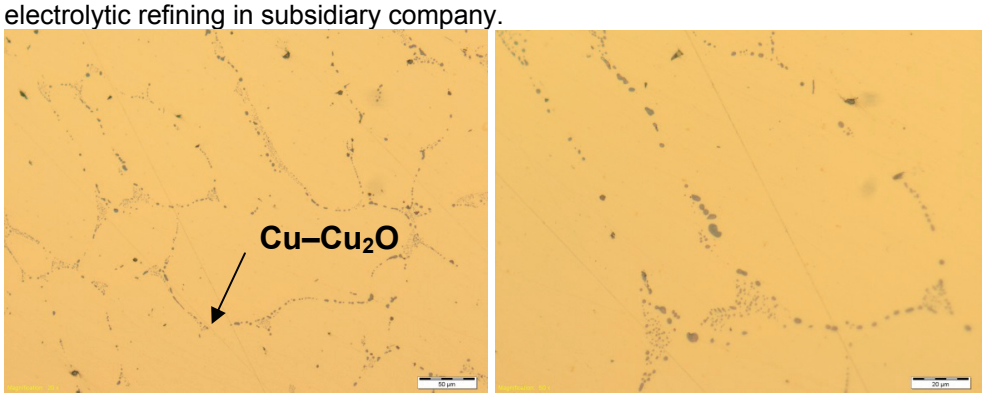

a. *b.*

Fig. 7 a,b: Microstructure of the anode copper at two magnifications.

Conclusion

On the basis of microstructural analysis, the following conclusion can be summarized:

Semi-quantitative EDX microanalysis of the black-copper sample shows the presence of the following elements: 10.2% Fe; 7.7% Ni; 6.7% Sn; 3.9% Pb and 2% Zn. The percentage of the present elements in the black-copper slightly differs from their typical content stated in [2]. A higher content of nickel and iron, but a slightly lower content of lead were determined.

In the black-copper microstructure the appearance of several phases in the copper base matrix was observed. Nickel is present in the copper solid solution, as well as in the form of a separate phase coupled with iron. This phase is clearly distinguishable in the microstructure of the etched sample, as well as the non-etched sample. In the black-copper microstructure the presence of a separate lead based phase is also observed.

In the microstructure of converter (blister) copper a higher portion of the Cu-Cu_2O eutectic was observed. This eutectic is present on the grain boundaries in the chain form at a higher oxygen concentration (above 0.39%). Some contents of nickel and tin were also determined. Nickel is present in the oxide form.

In the microstructure of anode copper compared with blister copper a reduced amount of the Cu-Cu_2O eutectic was observed. This is related with the deoxidizing process, which is performed with the aim to reduce the oxygen content to an acceptable level (~0.03 ÷ 0.05%) in the second stage of fire refining.

Acknowledgements

The authors are grateful for the financial support provided by the grant agency VEGA of the Ministry of Education, Science, Research and Sport of the Slovak Republic through the Project No. 1/0425/14.

References

[1] International copper study group, http://www.icsg.org/index.php/component/jdownloads/finish/170/1997

[2] Schlesinger, M.E., Extractive Metallurgy of Copper, fifth edition, Elsevier Ltd., 2011, ISBN: 978-0-08-096789-9.

[3] Secondary copper processing, http://www.outotec.com/imagevaultfiles/id_567/cf2/secondary_copperprocessing.pdf

[4] Best Available Techniques (BAT) Reference Document for the Non-Ferrous Metal Industries, revised draft 3, march 2014.

[5] Kovohuty, a.s., http://www.kovohuty.sk/En/index.html

[6] Silva, R.J.C. et al.: Microstructure Interpretation of Copper and Bronze Archeological Artefacts from Portugal, Materials Science Forum Vols. 587-588 (2008), pp. 365-369.

[7] Clavaguera-Mora, M.T. et al: Solidification study of Cu-based alloys obtained by Continuous casting, Journal of Materials Science 34 (1999), pp. 4347-4350.

[8] Rzadkosz, S. et al.: Influence of refining operations on a structure and properties of copper and its selected alloys, Archives of Metallurgy and Materials, Vol. 54, (2009), 2, pp. 209-304.

CARBURIZING PROCESS ACCELERATION IN THE PRESENCE OF ALKALINE - EARTH METAL OXIDES

Daniela Dragomir[1, a], Mihai Cojocaru[2, b], Leontin Drugă[3, c]

[1] *UTTIS Industries, 20 Calea Bucureşti, Vidra, 077185, Romania*
[2,] *MSE Faculty, University "Politehnica", Bucharest, 313 Splaiul Independenţei, 060004, România*
[3] *Romanian Academy for Technical Sciences, 26 Dacia Bd., Bucharest, 030971, România*
[a]*dana_dragomir@hotmail.com,* [b]*cojocarumihaiovidiu@yahoo.co.uk,* [c]*ld@uttis.ro,*

This article aimed at study of carburizing performance of Cr-Ni-Mo low alloy steel in solid medium (carburizing paste) in the presence of alkaline-earth metal oxides.

In order to perform a complex assessment of the carburizing performance of Cr-Ni-Mo low alloy steel in this particular carburizing medium, the experimental results have been determined and analyzed by comparison with results of previous researches performed in conventional carburizing media (urban fuel gas) in the presence or in the absence of fluidized state as well as in other solid carburizing media (carburizing paste and in carburizing paste with rare earths additions).

The use of this particular composition of carburizing paste has allow to obtain qualitative conclusions concerning the influence exerted by alkaline-earth oxides on change of the chemical nature of surfaces which are thermochemically processed in this medium and implicitly on the growth carburizing kinetics of steel taken into analysis.

The results of the carburizing experimental researches have confirmed the fact that the presence of alkaline-earth metal oxides in the carburizing paste lead to the acceleration of the growth carburizing kinetics of Cr-Ni-Mo low alloy steel in this medium by comparison with other carburizing media due to the possible occurrence both of the atomic mechanism and ionic mechanism of carburizing.

Introduction

The carburizing is currently a well known case hardening process applied to low carbon steel parts and although it is one of the oldest thermochemical treatments, is undoubtedly an area of significance for both research and industry.

Despite the fact that the carburizing does not represent a new research subject, the carburizing process in carburizing media which are not frequently used in the industrial practice (solid media [1-4], solid media + rare earths additions [5], gaseous media + rare earths additions [6-9] and gaseous media in the presence of fluidized state [10-11]) still causes further interest as it concerns the substantiation of the acceleration mechanisms of the carburized layers kinetics in these particular carburizing media.

In this respect Hosseini et al [1] analyzed the effect of Na_2CO_3 added in the solid carburizing medium (graphite) on the carburizing kinetics of 18NiCr8 steel

and concluded that the maximum case depth has been attained for 11% activator and carburizing time of 12 h; demonstrated that for the parameters considered, at additions of about 15% activator, the decarburizing occurs.

Jiménez et al [2] reported that the addition of carbonates ($BaCO_3$ and $NaCO_3$) to the metallurgical coke enhanced the carburizing kinetics of 21NiCrMo2 steel; demonstrated that for constant carburizing temperature and time, the case depth has increased with the activator content rising and explained this fact by the influence exerted by the activator on the CO proportion augmentation in the carburizing medium.

Khosravi et al [3] observed that the maximum effective case depth obtained on 18CrNi8 steel by pack-carburizing in mixtures + different contents of Na_2CO_3 was attained for an activator amount of 11.5 wt. % while the carburizing time had no significant effect.

In [4] it was concluded that the carburizing kinetics of the 21NiCrMo2 steel in carburizing paste are superior to those attained in urban fuel gas (natural gas from the urban network).

Previous carburizing researches in carburizing paste with rare earths added in certain limits [5] demonstrated that these did not significantly influence the carburizing kinetics of 21NiCrMo2 steel. The rare earths additions affected the reactions in medium as well as at the interface and stabilized the chemical activity of the paste. The intensity of mass transfer processes in the metallic matrix is modified and the bainitic hardenability of steel is increased. Thus, resulted microhardness increase in the superficial zones of the carburized layer and finer microstructures [5]. Other works underline also the fact that the additions of rare earths to the gaseous carburizing medium does not change [6-8] or change somewhat [9] the carburizing kinetics laws.

Certain researches of Gao et al [10] noticed that the dynamics and the composition of the carburising atmosphere from the vicinity of the treated parts in the presence of the fluidized state as well as the geometry of the parts influenced the carbon mass transfer coefficient. Other work [11] outlined the fact that the carburizing kinetics of Cr-Ni-Mo steels during carburizing in urban fuel gas in the presence of fluidized state are superior to those registered in the case of conventional carburizing of 21NiCrMo2 in urban fuel gas.

The article analyzes the carburizing performance of Cr-Ni-Mo low alloy steel in solid medium (carburizing paste) in the presence of alkaline-earth metal oxides by comparison with the carburizing performances registered in conventional carburizing media (urban fuel gas) in the presence or in the absence of fluidized state as well as in other solid carburizing media (carburizing paste with or without rare earths additions).

Experimental

The experimental researches have aimed to study the influence of alkaline-earth metal oxides added to the carburizing paste on the carburizing kinetics of Cr-Ni-Mo low alloy steel with fine hereditary grains and appropriate bainitic hardenability.

Samples of Φ15x20 mm have been executed from annealed bars of 21NiCrMo2 steel with the chemical composition (determined by complete chemical analysis):0,20%C, 0,76%Mn, 0,43%Cr, 0,51%Ni, 0,22%Mo, 0,26%Si (in the limits of W1.6523 steel grade) and used for experiments.

The carburizing paste consists of homogene mixture of fine powdered wood charcoal, $BaCO_3$, $CaCO_3$, $K_4Fe(CN)_6$ and waste heat treatment oil as binder; 10% BaO was added to this mixture.

The carburizing experiments have been performed in laboratory chamber furnace with electric heating and automat control of temperature; the experiments have been realized on basis of the experiment programming method (active factorial experiment) respectively the orthogonal compositional central programming of second order [12]; the couple of investigated parameters was temperature - time($T \in [900°C \div 1000°C]$; $t \in [30 \div 90$ min]).

The carburized and quenched samples were investigated by optic microscopy using Neophot 21 microscope endowed with digital camera and analysis software of the metallographic image), microhardness testing (Reichart type microhardness tester with load of 100g) and EDX (EDAX Sapphire dispersive energy spectrometer with resolution of 128eV).

Results. Discussions

To illustrate the carburizing performance of 21NiCrMo2 steel in solid media (carburizing paste with 10%BaO additions) by comparison with the carburizing performances of this steel in carburizing media which are not frequently used in the industrial practice and implicitly to substantiate the acceleration mechanism of carburized layers growth kinetics in the presence of BaO, have been sleected the carburizing results in these particular media for the couple of parameters: T=950°C, t=30 min.

In table 1 are shown the carburizing kinetics of 21NiCrMo2 steel for carburizing in paste with and without BaO additions.

Table 1 Carburized layers growth kinetics of 21NiCrMo2 steel for carburizing in paste with and without BaO additions.

Carburizing at 950°C/30min)	Carburizing paste+10%BaO	Carburizing paste (without BaO additions)	Average carburizing rates ratio
Effective case depth, mm	0,485	0,450	$V_1/V_2=0,927$
Average carburizing rate, μm/hour	$V_2=970$	$V_1=900$	

The microstructures of the carburized layers obtained on 21NiCrMo2 steel after carburizing at 950°C/30 min in carburizing paste with and without alkaline-earth metal oxides are shown in fig.1; the EDX images and profiles of chemical elements in the carburized layer in carburizing paste with 10%BaO additions are presented in fig. 2 and 3.

The phase composition of the carburized layers consists of martensite + inferior bainite +residual austenite.

The effective carburising case depths and the average carburizing rates in paste with 10%BaO additions are higher than those registered in paste with rare earths additions (10%Ce or 10% mixture that contains Pr+Nd+B) [5] as well as to those registered in carburizing paste or in urban fuel gas, respectively are close to those attained in urban fuel gas in the presence of fluidised state [11].

The microhardnesses were close to those registered in the case of carburizing in paste [4] and lower than those registered in paste with rare earths additions [5] (fig.4).

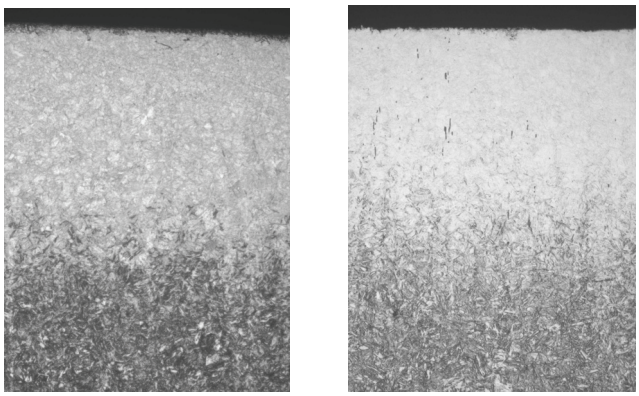

Nital 2% x200 *Nital 2% x200*

Fig.1. Microstructures of carburized layer of 21NiCrMo2 steel after carburizing at 950°C/30 min (a - carburizing in paste; b - carburizing in paste with 10%BaO)

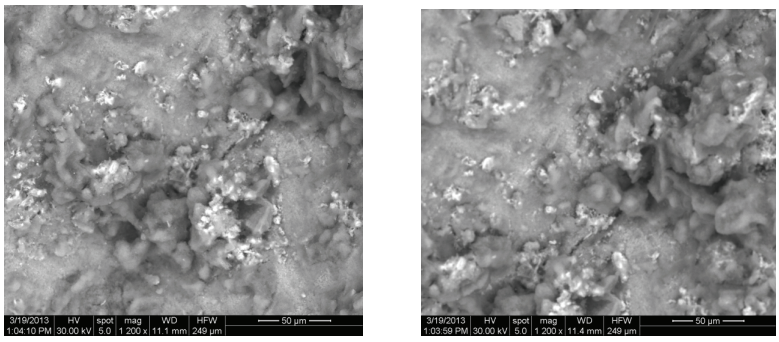

Fig. 2. EDX images of two zones from the carburized layer of 21NiCrMo2 steel; carburizing at 950°C/30 min in carburizing paste with 10%BaO

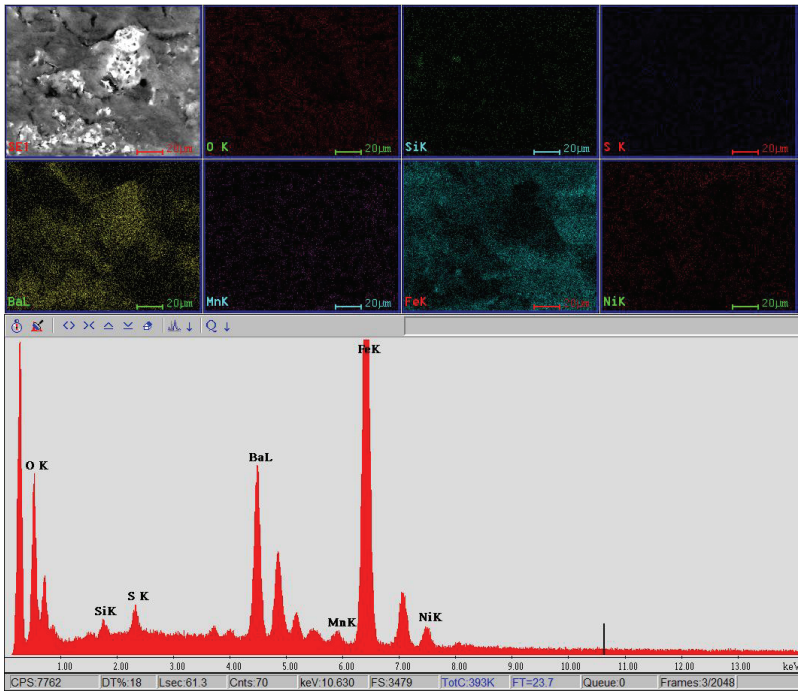

Fig.3. The distribution of chemical elements in the vicinity of carburized layer surface of 21NiCrMo2 steel; carburizing at 950°C/30 min in carburizing paste+10% BaO

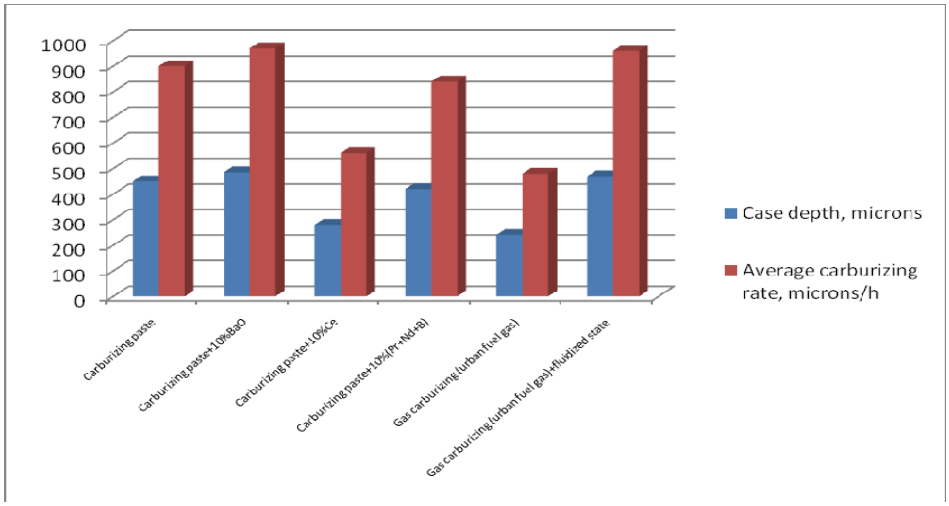

Fig.4. Carburizing case depths and average carburizing rates at 950°C/30 min in the investigated carburizing media

The carburizing transfer mechanism during paste carburizing is governed by the reactions that lead to the formation of the carbon in active state and which take place preponderantly in gaseous phase [4, 5]:

- the decomposition reactions of the carbonates with release of carbon dioxide;
- the reaction between the carbon dioxide (from the decomposition of the carbonates and from the interaction between the excess carbon available in paste and oxygen) with the excess carbon with the formation of the carbon monoxide and release of active carbon;
- the decomposition of potassium ferrocyanide with release of active carbon;
- another source of carbon is represented by the micronic particles of wood charcoal available in the carburizing paste.

In the real conditions of development of thermochemical treatments, the metallic surfaces possess micronic films of oxides, phenomenon that causes a decrease of the energy for release the electron in the surface (initiation of the electron emission process of surface) from 4,31eV (in the case of non-oxidized iron) to 3,0 eV (in the presence of the micronic film of Fe_2O_3); in the presence of BaO adsorbed in reduced quantities, the energy necessary for the electron release is reduced at 1,72eV [13].

As consequence, in the case of carburizing in paste with 10%BaO additions, the electronic emission of the surface is enhanced as well as the adsorption intensity (in a similar mode with the ionic carburizing and nitriding). It is very likely that the carbon adsorption mechanism to change and thus besides the atomic mechanism also the ionic mechanism will develop. As consequence the kinetics of carburizing in paste with 10%BaO additions are accelerated and are reflected in higher case depths and average carburizing rates(than that attained in paste without BaO additions).

Conclusions

The experimental researches aimed to study the carburizing performance of the 21NiCrMo2 steel in carburizing paste with alkaline-earth metal oxides viewed by the perspective of change of chemical nature of the carburized surface as well as the carburizing mechanism in the presence of BaO.

The following aspects have been observed:

- the presence of the alkaline-earth metal oxides in the carburizing paste accelerates the kinetics of carburized layer growth;
- the enhance of the carbon mass transfer processes in the case of carburizing in paste with 10%BaO by comparison with paste without BaO additions or other carburizing media is due to possible occurrence both of the atomic mechanism and ionic mechanism of carburizing.

References

[1] S.R.Elmi Hosseini, „Simulation of Case Depth of Cementation Steel According to Fick's Laws", in Journal of Iron and Steel Research, International.Issue 11, 2012, pp.71-78

[2] H. Jiménez, M.H. Staia and E.S. Puchi, **„**Mathematical modeling of a

carburizing process of a SAE 8620H steel", in Surface and Coatings Technology, 120–121, 1999, pp.358–365

[3] H.Khosravi*, M. Mirzaee-Sisan, S.R.Elmi-Hosseini and M. Askari-Paykani, Modeling of Pack-Carburizing Route by General Factorial Design of Experiment, International Journal of Engineering Research & Technology (IJERT), Vol. 3 Issue 9, September- 2014, 947-951

[4] D.Dragomir, M.Cojocaru and N.Dumitru, The effect of change of carburizing media nature on growth kinetics of layers, U.P.B. Sci. Bull., Series B, Vol. 75, Iss. 1, 2013, pp.181-102

[5] D.Dragomir, Substantiation of the acceleration mechanisms of carburizing layers growth kinetics, Ph.D Thesis, Bucharest, 2014

[6] M.F. Yan, „Study on absorption and transport of carbon in steel during gas carburizing with rare-earth addition", in Materials Chemistry and Physics, no.70, 2001, pp.242-244

[7] Mu-Fu Yan, Zhi-Ru Liu and T. Bell, „Effect of Rare Earths on Diffusion Coefficient and Transfer Coefficient of Carbon during Carburising", in Journal of Rare Earths, vol.19, no.2, 2001, pp. 122-124

[8] M.F. Yan, W. Pan, T. Bell and Z.R. Liu, „The effect of rare earth catalyst on carburising kinetics in a sealed quench furnace with endothermic atmosphere", in Applied Surface Science, no. 173, 2001, pp.91-94

[9] M.F. Yan and Z.R. Liu, „Study on microstructure and microhardness in surface layer of 20CrMnTi steel carburised at 880°C with and without RE", in Materials Chemistry and Physics, no.72, 2001, pp.97-100

[10] W.M.Gao, L.X. Kong, J.M.Long. and P.D. Hodgson, ,,Measurement of the mass transfer coefficient at workpiece surfaces în heat treatment furnaces", in Journal of Materials Processing Technology 209, 2009, pp. 497-505

[11] D. Dragomir, M.O.Cojocaru and L.N.Druga, „Particularities of carburizing kinetics in different media, in JOAM-Journal of Optoelectronics and Advanced Materials, vol 15, No.7-8, July-August, 2013, pp.683-688

[12] D.Taloi, E.Florian,C.Bratu and E.Berceanu, Optimizarea proceselor metalurgice (Metallurgical processes optimizing), Ed.Didactică şi Pedagogică, Bucureşti, 1985

[13] M Cojocaru, I. Ciucă I, L. Drugă L and G. Coşmeleaţă, "Empirical exposition of the adsorption's ionic mechanism on gaseous nitriding (Electriceskoe opisanie mehanizma adsorbţii ionov prigazovom azotirovanii)", in Elektronnaia obrabotka materialov, vol.44, no.5, 2008, pp. 396-400

PREPARATION OF SILVER NANOPARTICLE METAL OXIDE COMPOSITE POWDERS WITH MULTIPLE OXIDES USING TEMPLATE METHOD

V. Ćosović[1], A. Ćosović[2], D. Živković[3], D. Minić[4], N. Talijan[1]

[1] *Institute of Chemistry, Technology and Metallurgy, University of Belgrade, Njegoševa 12, 11000 Belgrade*
[2] *Institute for Technology of Nuclear and Other Mineral Raw Materials, Franse d' Eperea 86, 11000 Belgrade*
[3] *Technical Faculty in Bor, University of Belgrade, Vojske Jugoslavije 12, 19210 Bor*
[4] *University of Priština, Faculty of Technical Sciences, Knjaza Miloša 7, 38220 Kosovska Mitrovica*

Abstract

Template method was adapted and utilized for introduction of SnO_2, ZnO In_2O_3, Bi_2O_3, and WO_3 nanoparticles and preparation of silver-metal oxide composite powders using soluble starch as a soft organic template. Morphology of the starting metal oxide powders and the prepared composite powders was studied using conventional and field emission scanning electron microscopy (SEM/FESEM). The obtained results illustrate and confirm good mixing and high uniformity of the prepared powders as the oxide particles, dissimilar to classical mixing of powders, are encapsulated within silver matrix and segregation is thus avoided. Benefits of using the prepared composite powders for production of electrical contacts are demonstrated on an example of the contact materials prepared via powder metallurgy technique. The samples were found to have improved physical properties such as density and hardness, while electrical conductivity was retained on the level that is comparable with commercial contact materials of this type.

Keywords: template method, silver-metal oxide composite powders, microstructure, electrical contacts, physical properties

Introduction

Since silver metal oxide composite electrical materials find application in a variety of low voltage switchgear devices such as contactors, relays, circuit breakers and switches, they represent rather important functional materials [1]. In recent years, there has been a rapidly growing interest in performance and quality improvement of electrical contacts which is mostly realized through introduction of different metal oxides and improvement of their dispersion within silver matrix i.e. obtaining more uniform microstructures [2]. Such microstructures are advantageous particularly when different metal oxides are used that tailor the materials properties by changing the interaction of silver and the main oxide [3]. Formation of anti-welding characteristics and under certain conditions decrease of

erosion rate is attributed to smaller sizes of metal oxide particles [4]. It was found that the optimal microstructure can be achieved by a homogenous distribution of a preferably monomodal oxide particles with a diameters in range 50-200 nm [4]. Given that conventional mixing techniques have already reached their practical limits at such particle sizes [5] different approach has to be made. Diverse electroless chemical methods based on chemical precipitation as well as modern polymer assisted inorganic nanocomposite formation and bio-casting methods that employ different template materials offer lots of opportunities for preparation of very uniform nanocomposite structures [4-7]. In view of that, in the current study an attempt has been made to increase dispersion of Ag-metal oxide contact materials by introduction of metal oxide nanoparticles in silver matrix and preparation of composite powders using template method. Morphology and microstructure of the obtained composite powders were studied and discussed. Additionally, physical properties such as density, hardness and electrical conductivity of the prepared final silver-metal oxide electrical contact materials were compared to each other and to conventionally prepared materials.

Experimental

Silver-metal oxide composite powders were produced by a modified template method [8] using commercial SnO_2, ZnO In_2O_3, Bi_2O_3, and WO_3 nanoparticles (40-100 nm) and commercial $AgNO_3$ powder as precursors. The applied synthesis method utilizes starch as a soft organic template and it is based on a simple principle that $AgNO_3$, unlike most metal nitrates, when heated thermally decomposes to elemental Ag instead of its respective oxide. In the first step soluble starch was added into distilled water, preheated at 40-50^oC under continuous stirring. Solution was further heated up to boiling point (~100^oC), where it was kept for 15 min, and then cooled down to 50-70^oC. Previously prepared metal oxide nanoparticle suspensions were slowly added to solution during vigorous mixing. After few minutes $AgNO_3$ water solution was slowly added. Both $AgNO_3$ and metal oxide particles were added in quantities necessary to achieve desired Ag to metal oxide weight ratio in final material i.e. Ag-SnO_2 (92:8); Ag-ZnO (92:8); Ag-$SnO_2In_2O_3$ (89.1:8:2.9); Ag-SnO_2WO_3 (90:9.5:0.5) and Ag-$SnO_2In_20_3Bi_2O_3$ (89.2:8.7:0.5:1.6). The prepared mixtures were dried at 80^oC in chamber dryer until water was evaporated and solid composites were obtained. The solid composites were subsequently burned and put into a muffle furnace pre-heated at 650^oC, where they were calcinated for 4h. During the combustion and later calcination, silver nitrate was transformed to elemental Ag with embedded metal oxide nanoparticles and the starch template was removed. Samples of final Ag-metal oxide contact materials were prepared from the obtained composite powders via conventional powder metallurgy route. The samples were produced by cold pressing of the obtained composite powders into blocks with dimensions 25.4×11×3 mm, by applying pressure of 360 MPa. The obtained green compacts were sintered for 3h at 820^oC in the air atmosphere and subsequently forged at 800^oC with the low degree of reduction. The obtained samples were then annealed at 750^oC for 30 min and quenched in water. Morphology and microstructure of the starting metal oxide powders and the prepared composite powders were studied

using JEOL JSM 6610LV scanning electron microscope (SEM) and Tescan MIRA3 XM field emission scanning electron microscope (FESEM). Density of the samples of final electrical contact materials was determined by standard methods. Hardness measurements were carried out on polished samples at room temperature using a Vickers hardness tester applying load of 5 kp. The reported hardness values are an average of five readings. Electrical conductivity of the investigated materials was measured using Foerster SIGMATEST 2.069 eddy current instrument with an 8 mm diameter probe.

Results and Discussion

FESEM/SEM images illustrating morphology of the starting commercial SnO_2 nano powder (Sigma Aldrich) as well as morphology and structure of the prepared silver-metal oxide composite powders are presented on Fig. 1.

The presented FESEM image of the used SnO_2 nano powder (Fig. 1a) reveals particle size of about 40-100 nm. The obtained SEM images of the prepared composite powders (Fig.1 b-f) demonstrate and confirm good mixing and high uniformity. The obtained results (Fig.1) also suggest that the applied process is very suitable for simultaneous introduction of different metal oxide particles. This is primarily because in course of the applied template process oxide particles are encapsulated within silver matrix and thus segregation is avoided. Accordingly, the prepared composite powders represent very favorable precursors for the production of electrical contact materials. In order to illustrate benefits of using composite powders for production of electrical contacts five samples of Ag-SnO_2 and Ag-ZnO contact materials were prepared by powder metallurgy method. Comparative presentation of the physical properties of the studied electrical contact materials is given in Table 1.

The determined values of density and measured hardness (Table 1) clearly illustrate influence of the introduction of nanoparticles and method of their introduction into a silver matrix on mechanical properties of the studied materials. The samples prepared using template method exhibit notable increase of density and hardness compared to conventionally prepared materials, particularly one containing micro particle metal oxide particles. It is evident that with the increase of density and more uniform distribution of metal oxide nanoparticles greater dispersion hardening was obtained which resulted in higher values of hardness.

From Table 1 it can be seen that the contact material containing micro particle tin oxide has the highest value of electrical conductivity. This can be ascribed to the presence of the oxide free zones in microstructure which results in better connectivity of individual silver grains. On the other hand, somewhat lower values of electrical conductivity observed for the materials prepared from the obtained composite powders can be generally associated with presence of pores, straining of silver lattice and particle spacing which all influence mean free path of conduction electrons and thus electrical conductivity [4,5,9].

The greater metal oxide dispersion of the prepared composite powders as well as high density and hardness of the produced electrical contact materials are all prerequisites for better wear resistance and longer exploitation life. However, it

is evident that such fine oxide dispersion cannot be achieved by conventional powder mixing. Hence, the benefit of application of the template method of preparation with soluble starch is illustrated by enhancement of structure dependent properties.

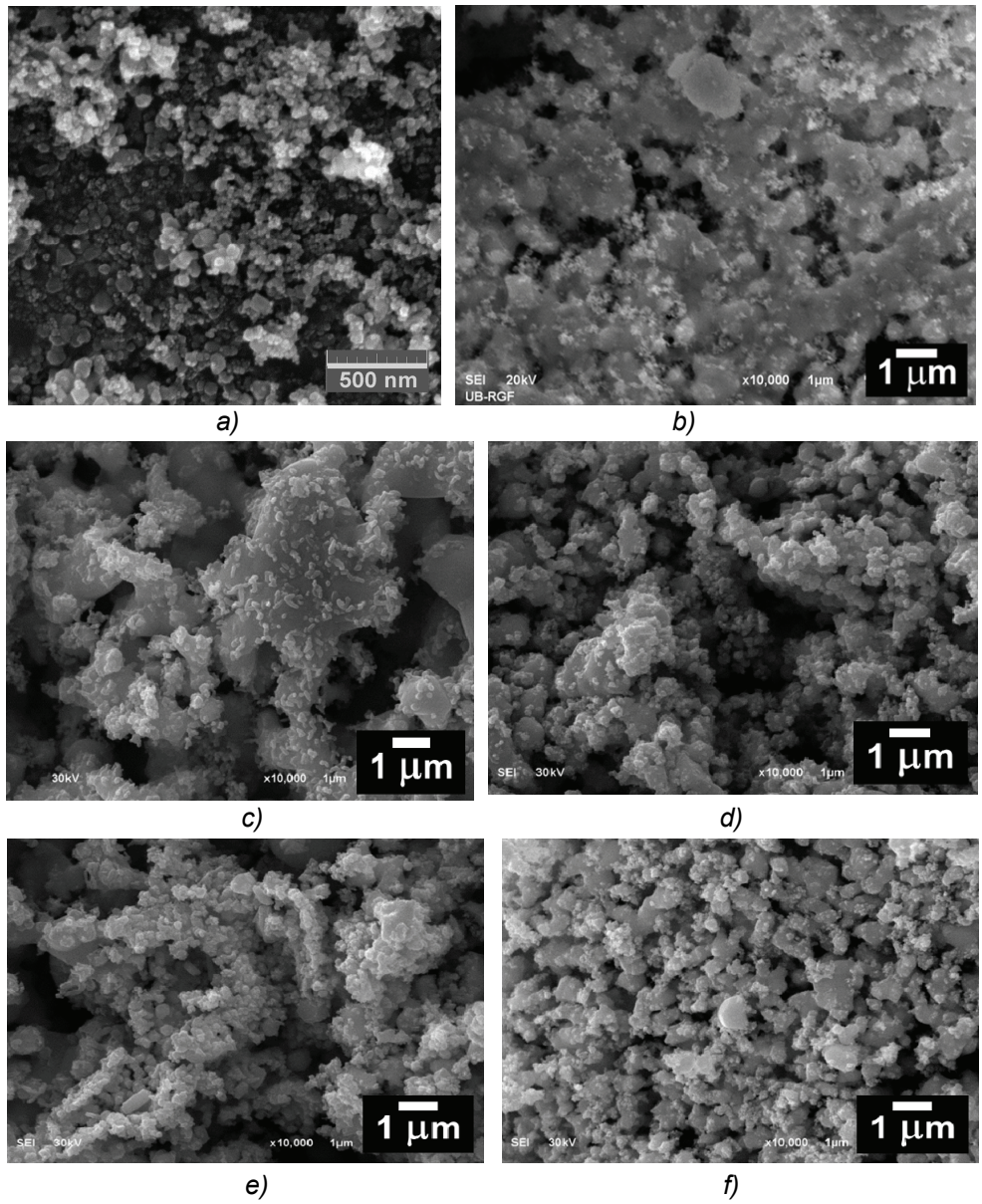

Fig. 1. Morphology of the starting SnO_2 powder a) and the prepared Ag-metal oxide composite powders: b) Ag-SnO_2, c) Ag-ZnO, d) Ag-$SnO_2In_2O_3$, e) Ag-WO_3 and f) Ag-$In_2O_3Bi_2O_3$

Table 1. Comparative presentation of physical properties of the prepared electrical contact materials

Preparation method	Composition	Density [g/cm^3]	Hardness [HV5]	Conductivity	
				[MS/m]	[%IACS]
Template method / powder metallurgy	Ag-SnO_2 (92:8) nano	9.86	123	38.92	67
Conventional mixing / powder metallurgy	Ag-SnO_2 (92:8) micro	9.53	87	44.75	77
	Ag-SnO_2 (92:8) nano	9.69	102	37.63	65
Template method / powder metallurgy	Ag-ZnO (92:8) nano	9.55	96	35.27	61
Conventional mixing / powder metallurgy	Ag-ZnO (92:8)	9.49	82	38.65	67

Conclusion

As an attempt to improve dispersion of metal oxide in electrical contact materials a modified template method was applied for introduction of metal oxide nanoparticles in silver matrix and preparation of composite powders. Since in the course of the used template process metal oxide particles were encapsulated in silver matrix and their segregation was suppressed, the prepared composite powders were found to exhibit high degree of mixing and good dispersion of oxide particles. Furthermore, it was demonstrated that the applied template method is very suitable for simultaneous introduction of multiple metal oxides into silver matrix. Benefits of using template method for preparation of composite powders and their further use for production of electrical contact materials are primarily illustrated as an improvement of physical properties such as density and hardness while the electrical conductivity was retained on the level that is comparable with commercial contact materials of this type.

Acknowledgement

This work has been supported by the Ministry of Education, Science and Technological Development of the Republic of Serbia (Projects OI 172037 and TR 34023).

References

[1] M. Braunović, N.K. Myshkin, V.V. Konchits, Electrical contacts – Fundamentals, Applications and Technology, CRC Press, Taylor and Francis Group, Boca Raton, 2007.

[2] N. Lorrain, L. Chaffron, C. Carry, P. Delcroix, G. Le Caër, Mater. Sci. Eng. A

– Struct. 367 (2004) 1.
[3] V. Ćosović, N. Talijan, D. Živković, D. Minić, Ž. Živković, J. Min. Metall. Sect. B-Metall. 48(1)B (2012) 131.
[4] F. Heringhaus, P. Braumann, D. Ruhlicke, E. Susnik, R. Wolmer, On the Improvement of Dispersion in Ag-SnO_2 based Contact Materials, Proc. 20th Int. Conf. on Electr. Contact Phenom. Stockholm 2000, 199-204.
[5] R. Wolmer, M. Mueller, D. Ruehlicke, D. Goia, US patent Pub. No.: US 2001/0051102 A1
[6] B.A. Rozenberg, R. Tenne, Prog. Polym. Sci. 33 (2008) 40.
[7] C.K. Sia, Y. Sasaki, N. Adachi, T. Ota, J. Ceram. Soc. Jpn. 117 (9) (2009) 958.
[8] V.Ćosović, A. Ćosović, N. Talijan, D. Živković, D. Manasijević, D. Minić, J. Alloy Compd. 567 (2013) 33-39.
[9] S. Link, M.A. El-Sayed, J. Phys. Chem. B 103 (1999) 8410.

INTERGRANULAR CORROSION SUSCEPTIBILITY OF AN AA5083 Al-Mg ALLOY PROCESSED BY ACCUMULATIVE ROLL BONDING (ARB)

Ana Alil[1], Miljana Popović[2], Tamara Radetić[2], Endre Romhanji[2]

[1]*Innovation Center of the Faculty of Technology and Metallurgy, University of Belgrade,*
Karnegijeva 4, 11 120 Belgrade, Serbia
[2]*Dept. Metall. Eng., Faculty of Technology and Metallurgy, University of Belgrade,*
Karnegijeva 4, 11 120 Belgrade, Serbia
alil@tmf.bg.ac.rs

Abstract

Intergranular corrosion (IGC) susceptibility of an AA5083 Al-Mg alloy sheets, highly deformed by accumulative roll-bonding (ARB), was investigated. It was shown that ARB processed specimens were resistant to IGC as the mass loss was <15 mg/cm^2. The degree of plastic strain during ARB processing did not affect IGC susceptibility and a value of corrosion potential. After sensitization treatment at 150°C, ARB processed specimens stayed resistant to IGC, in spite of β-phase precipitation along grain boundaries and within the structure. A high degree of deformation achieved by ARB processing, and a large amount of β-phase precipitated during the sensitization, did not cause an increase in IGC susceptibility due to favorable morphology and a distribution of β-phase in the structure.
Keywords: Intergranular Corrosion, Accumulative Roll Bonding, Al-Mg alloy

Introduction

Accumulative roll-bonding (ARB) is one of the severe plastic deformation (SPD) processing techniques, developed to obtain ultrafine-grained (UFG) structures in bulk and sheet materials. ARB process was originally proposed by Saito et al. [1,2], as an innovative process of plastic deformation for manufacturing of multilayered sheet materials with refined microstructure and a high strength level. Microstructure refinement and mechanical properties of Al-Mg alloys subjected to ARB processing had been extensively investigated [2–7]. However, a general need for improving the strength parameters is usually followed by a requirement for the preservation of corrosion resistance of these alloys. Intergranular corrosion (IGC) is one of the most critical corrosion processes in Al-Mg alloys. It occurs in the grain boundary region, due to a localized decomposition of solid solution or a presence of anodic β-phase particles [8]. Currently, a little is known about corrosion behavior of the Al-alloys fabricated by ARB process and other SPD novel processing techniques. A certain number of studies [9–11] have shown that SPD processes can either increase or decrease corrosion resistance of various Al alloys. Due to a great potential of ARB processing to be introduced into

industrial practice [2,12], there is a great interest in the examination of the corrosion behavior of ARB processed Al-Mg alloys.

The aim of this study was to investigate the influence of high plastic deformation imposed by ARB processing on the intergranular corrosion (IGC) susceptibility of an AA5083 Al-Mg alloy multilayered sheets.

Experimental work

Material used in this study was industrially produced. It was supplied by Impol-Seval Aluminium Mill (Sevojno, Serbia) as hot rolled 10.6 mm thick plates of an AA5083 type Al-Mg alloy, with chemical composition given in Table 1.

Table 1.Chemical composition of the studied and standard AA5083 type alloys (wt.%)

Alloy	Mg	Mn	Cu	Si	Fe	Cr	Zn	Ti
Studied	4.16	0.47	0.0076	0.149	0.288	0.0599	0.0182	0.0086
AA5083	4.0-4.9	0.4-1.0	<0.1	<0.4	<0.4	0.05-0.25	<0.25	<0.15

Hot rolled plates were further laboratory processed by cold rolling and inter-annealing up to 1 mm in thickness. Final annealing was performed at 320 °C/3h. 1 mm thick specimens were used for ARB processing (Fig.1) that was performed at room temperature. It was possible to achieve maximum 6 ARB cycles with short annealing between ARB cycles at 320 °C for 5 min. ARB processed sheets were characterized by resistivity measurements, corrosion testing and optical microscopy.

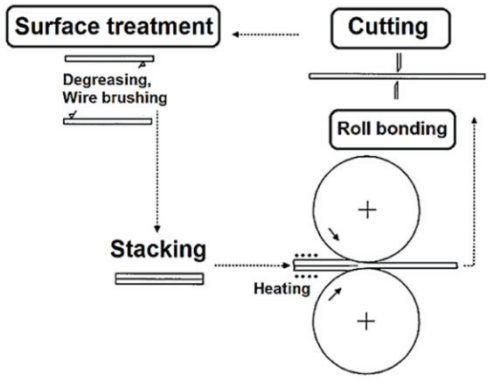

Fig. 1.Schematic illustration of accumulative roll-bonding (ARB) process [1].

The conductivity measurements were performed using Sigmatest 2.069 equipment, at operating frequency of *f* = 240 kHz and conductivity was converted to resistivity values. For the corrosion testing purposes, one group of ARB processed specimens was sensitized at 150 °C for 7 days. The susceptibility to intergranular corrosion (IGC) was determined on the ARB processed

(unsensitized) and sensitized specimens by NAMLT test (Nitric Acid Mass Loss Test) according to ASTM G67 standard. It consists of the immersion of the tested specimens with dimensions of 50×6 mm, in concentrated HNO_3 at 30 °C for 24 h, and the measurements of mass loss during testing. Specimens susceptible to IGC lose 25-75 mg/cm^2, while the specimens resistant to IGC lose between 1-15 mg/cm^2. Corrosion potential of the ARB processed specimens was measured by FLUKE77 multimeter according to ASTM G69. Testing was performed at room temperature using a solution that contains 58.5±0.1 g NaCl and 9±1 ml 30% H_2O_2. The reference electrode was a saturated calomel electrode (SCE) with a potential of 0.244 V at 25 °C. Characterization of the microstructure after sensitization treatment was conducted by means of light optical microscopy (LOM) with a Reichert-Jung MeF3 optical microscope. Specimens for LOM were prepared by etching in 10% H_3PO_4 at 50 °C for 30 s, in order to reveal β-phase precipitates in the structure.

Results and Discussion

Starting material for ARB processing was 1 mm thick fully annealed Al-Mg alloy sheet. Microstructure of the initial state was completely recrystallized before ARB deformation with an average grain size of ~23 μm [13]. ARB processed specimens with 1 mm in thickness consisted of 2 layers after the first ARB cycle and up to 64 layers after 6 ARB cycles. The thickness of each layer was ~500 μm after first ARB cycle and approximately 15 μm, after 6 ARB cycles. ARB processing refined the microstructure. The grains within layers became elongated in the rolling direction, and a significant reduction in grain thickness occurred, from ~ 23 μm, before ARB process, to ~ 3 μm after 6 ARB cycles [13]. Mechanical properties of ARB processed specimens are given in Table 2. They were significantly improved after ARB processing as the maximum value of hardness became greater twice, and yield strength was increased almost three times, in comparison with the initial state of material before ARB.

Table 2. Mechanical properties of accumulative roll bonded AA5083 Al-Mg alloy

Mechanical properties	Initial state – before ARB	Number of ARB cycles					
		1	2	3	4	5	6
Brinell hardness, HB	68	91	105	112	112	105	101
Yield strength, YS (MPa)	132	260	342	366	368	357	/

It is well known that Al-Mg alloys with high Mg content (> 3% Mg) may become prone toward intergranular corrosion (IGC), as supersaturated solid solution decomposes and the excess of Mg atoms precipitate out in the form of anodic β-phase (Mg_5Al_8) along the grain boundaries [14]. Precipitation of electrochemically active β-phase occurs slowly even at room temperature, and could be significantly accelerated at high temperatures (> 65 °C) rendering grain boundaries susceptible to intergranular corrosion [15]. The extent of IGC susceptibility depends on many factors, such as material chemistry, environment

and thermo mechanical treatment [12,15]. In the present study, influence of high plastic deformation imposed by ARB process, and a presence of interfaces between the layers, on the IGC susceptibility of Al-Mg alloy laminates was investigated. In order to accelerate precipitation of β-phase in ARB processed specimens, a sensitization annealing at 150 °C for 7 days was performed.

Figure 2 shows the results of NAML test and a mass loss of ARB processed specimens before and after sensitization treatment. According to ASTM G67 standard, it is considered that both groups of specimens are resistant to IGC, as the mass loss was below 15 mg/cm^2. For ARB processed specimens, a mass loss was less than 4 mg/cm^2, and large plastic deformation during ARB processing (up to ε=4.8 after 6 ARB cycles) did not affect IGC susceptibility. Sensitization of the specimens in initial state and after 1 ARB cycle brought a mass loss of ~6.5 mg/cm^2, while in case of specimens processed with 2 up to 6 ARB cycles a mass loss was almost unchanged after sensitization treatment. Measurements of the corrosion potential of ARB processed specimens, performed according to ASTM G69 standard, are shown in Figure 3. It is obvious that number of ARB cycles, i.e. a large deformation imposed by ARB processing, did not affect the value of corrosion potential of the tested Al-Mg alloy.

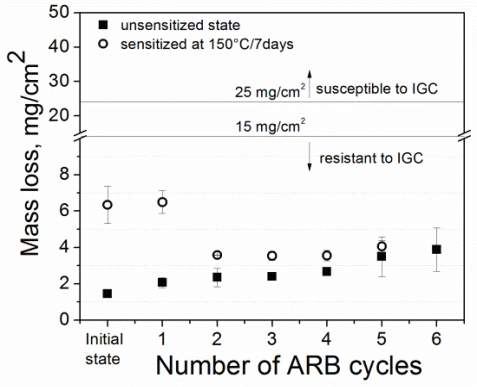

Fig. 2. IGC susceptibility of ARB processed specimens before and after sensitization treatment at 150 °C.

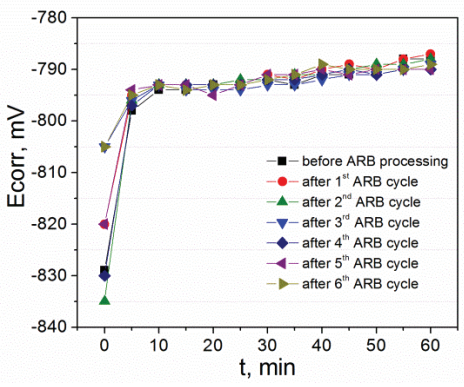

Fig. 3. Influence of the number of ARB cycles on the corrosion potential of tested Al-Mg alloy.

Since IGC occurs due to β-phase precipitation at grain boundaries or inside the grains, a variation in Mg concentration in solid solution (precipitation/dissolution of Mg) was followed by resistivity measurements. Figure 4 shows that the electrical resistivity of ARB processed specimens slightly increases (not more than 0.1 Ωcm), while after sensitization the electrical resistivity of ARB processed specimens decreases significantly. Increase in resistivity with increasing the number of ARB cycles can be attributed to the gradual increase in dislocation density during ARB deformation, while decrease in resistivity after sensitization occurs due to β-phase precipitation and a reduction of Mg solute atoms in solid solution.

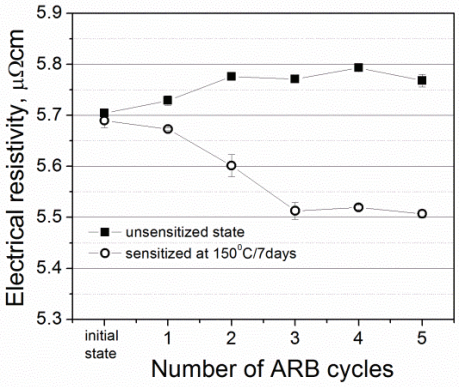

Fig. 4. Variation in electrical resistivity of ARB processed specimens after sensitization treatment at 150°C.

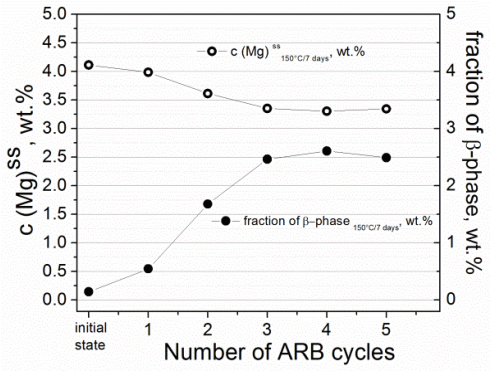

Fig. 5. Influence of sensitization treatment on Mg concentration change in the solid solution and a fraction of β-phase particles in the structure of ARB processed specimens.

Electrical resistivity of the initial state (before ARB processing) was slightly decreased, while in case of ARB processed specimens a significant decrease in electrical resistance was observed after sensitization treatment. Maximum drop in resistivity of approximately 0.27 μΩcm was attained after sensitization of ARB specimens processed with 3-5 ARB cycles, as shown in Fig. 4. Decreasing in resistivity values was correlated with a change of Mg solute atoms concentration in solid solution and a precipitation of β-phase in the structure. Based on the resistivity change values that occurred due to sensitization treatment, a concentration of Mg solute in solid solution was calculated, and the amount of β-phase precipitates was determined by a lever rule. Fig. 5 shows that Mg concentration in solid solution was gradually decreased, from 4.16 to 3.3 wt% Mg, while the fraction of β-phase precipitates was increased up to 2.6 wt.% with increasing the number of ARB cycles. We suppose that increasing the number of ARB cycles increases a density of dislocations in a deformed structure which present favorable places for the precipitation of β-phase particles. Influence of the number of ARB cycles on the shape and distribution of β-phase precipitates was revealed by metallographic etching in 10% orthophosphoric acid of sensitized specimens. Fig. 6 shows optical micrographs of the specimens after sensitization treatment as follows: initial state (Fig. 6a), specimen after 1 ARB cycle (Fig. 6b), and specimen after 4 ARB cycles (Fig. 6c).

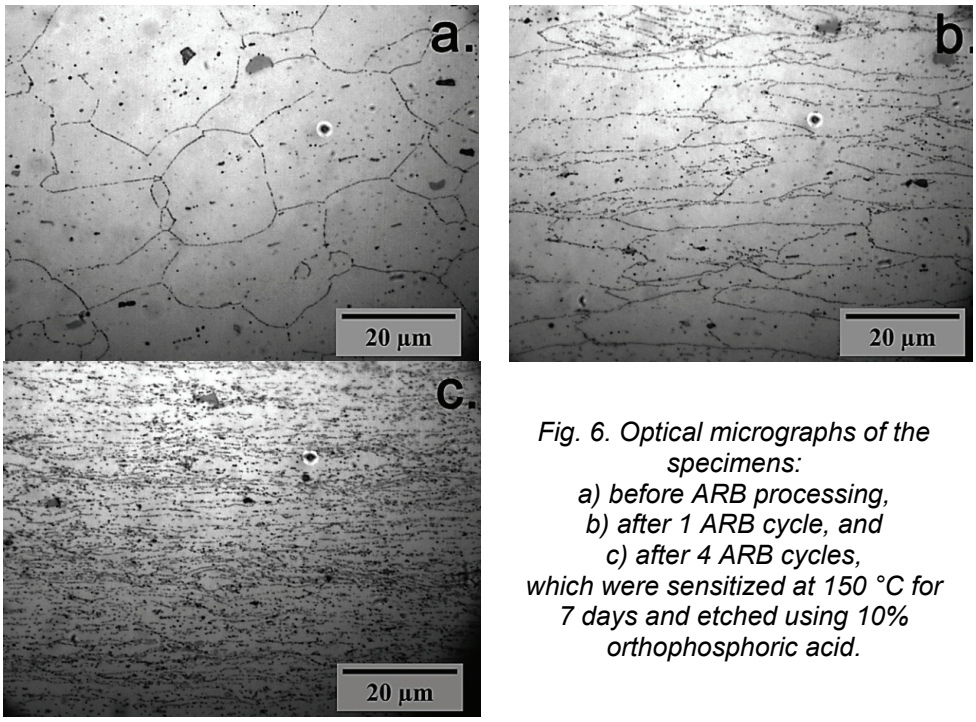

Fig. 6. Optical micrographs of the specimens:
a) before ARB processing,
b) after 1 ARB cycle, and
c) after 4 ARB cycles,
which were sensitized at 150 °C for 7 days and etched using 10% orthophosphoric acid.

Fig. 6a shows that during sensitization of the specimens in the initial state and processed by 1 ARB cycle, β-phase precipitated along the grain boundaries. However, in the initial state grains were polygonal while after being processed by 1 ARB cycle, grains become elongated (Fig. 6b). The amount of β-phase precipitates in these two cases was 0.15, and 0.55 wt.%, respectively (Fig. 5). In case of highly deformed specimens, with more than 3 ARB cycles, β-phase precipitates are distributed homogeneously throughout the structure, as Fig. 6c shows for the specimen after 4 ARB cycles. The fraction of β-phase particles precipitated in the structure of this specimen was approximately 2.6 wt.% (Fig. 5). However, a mass loss was smaller, and IGC resistance better, than for the specimen in the initial state and after 1 ARB cycle (Fig. 2). In spite of the small amount of β-phase precipitates (0.15 and 0.55 wt.%), a mass loss for these specimens was about ~6.5 mg/cm^2. That can be attributed to the localized precipitation of β-phase along/at the grain boundaries, which cause a higher mass loss. However, the specimens were still resistant to IGC as β-phase precipitates were formed semi-continuous coverage of grain boundaries.

Conclusion

In this study, the effect of accumulative roll bonding (ARB) process on the susceptibility to intergranular corrosion (IGC) of an AA5083 Al-Mg alloy was investigated. It was shown that:

ARB processed specimens were resistant to IGC as the mass loss was less than 15 mg/cm^2 even after sensitization treatment at 150 °C for 7 days;

The degree of plastic strain during ARB processing did not affect IGC susceptibility and a value of corrosion potential. Increasing the number of ARB cycles increases the amount of β-phase precipitates but the material stayed resistant to IGC;

The results showed that the distribution of the β-phase precipitates had greater influence on the IGC susceptibility than the precipitated amount.

Acknowledgements

This research was supported by the Ministry of Education, Science and Technological Development, Republic of Serbia, and Impol-Seval Aluminium Mill, Sevojno, under contract grant TR 34018.

References

[1] Y. Saito, H. Utsunomiya, N. Tsuji, T. Sakai, Acta Mater*,* 47 (1999) 579-583
[2] M.F. Naeini, M. H. Shariat, M. Eizadjou, J. Alloys Compd, 509 (2011) 4696–4700
[3] H.R. Song, Y.S. Kim, W.J. Nam, Metals and Materials, 12 (2006) 7-12
[4] H. Sheikh, Scripta Mater, 64 (2011) 556–559
[5] S.H. Lee, Y. Saito, N.Tsuji, H. Utsunomiya, T.Sakai, Scripta Mater, 46 (2002) 281-285
[6] H.W. Kim, S.B. Kang, N.Tsuji, Y.Minamino, Metall Mater Trans A, 36A (2005) 3151-3163
[7] R. Shibayan, B.R. Nataraj, et.al, Mater Des, 36 (2012) 529–539
[8] "Corrosion of Aluminum and Aluminum Alloys", ed. by J.R. Davis & Associates, ASM Intl., Metals Park OH, USA, 1999.
[9] W. Wei, K.-X. Wei, Q.-B. Du, Mater. Sci. Eng. A, 454-455 (2007) 536-541
[10] I. Sabirov, M. Y. Murashkin, R. Z. Valiev, Mater. Sci. Eng. A, 560 (2013) 1-24
[11] M. Kadkhodaee, M. Babaiee, H. D. Manesh, J. Alloys Comp. 576 (2013) 66-71
[12] A. Halap, T. Radetić, M. Popović, E. Romhanji, Metall Mater Trans A, 45A (2014) 4572-4579
[13] A. Alil, M. Popović, T. Radetić, E. Romhanji, Metall. Mater. Eng., 20 (4) 2014 285-295
[14] L.F. Mondolfo, "Aluminum Alloys - Structure&Properties", Butterworths&Co. Ltd., 1979
[15] S. Jain, M.L.C. Lim, J.L. Hudson, J.R. Scully, Corros. Sci., 59 (2012) 136–147

PRESSURE EQUIPMENT DIRECTIVE 97/23/EC- FUNDAMENTAL SAFETY PRINCIPALS, IMPLICATIONS AND CHALLENGES FOR BUSINESS

M. Matijasevic-Clarke[1], P. Swinnen[2]

Lloyds Register EMEA Antwerp, Belgium
Email: [1]milena.matijasevic-clarke@lr.org, [2]pieter.swinnen@lr.org

Abstract

The purpose of the Pressure Equipment Directive (97/23/EC)-(PED) is to harmonise national laws of Member States regarding the design, manufacture, and testing and conformity assessment of pressure equipment and assemblies of pressure equipment. PED has to be adopted in Member States laws and failure to comply means that such pressure equipment or assemblies cannot legally be placed on the market or put into service in the Member States Community. PED Law is changing after 17 years. The new Pressure Equipment Directive (2014/68/EU) will be applicable from 1st of June 2015.

PED aims to ensure safety and ease of market entry of equipment within the European Union and the European Economic Area. This approach allows European industry to develop new techniques thereby increasing international competitiveness. PED is one of a series of technical harmonisation directives.

EC Directives apply in all 28 EU Member States. Product Directives also apply in the European Economic Area, in the candidate countries: Serbia, Montenegro, The Former Yugoslav Republic of Macedonia, Turkey and Iceland, and potential candidate countries: Albania, Bosnia and Herzegovina, and Kosovo.

This paper will cover:

- scope of the Directives
- importance for safety and ease of market entry
- implications in the manufacturing process
- what is changing in the new Directive
- common challenges that manufacturers are facing
- effective change management processes

Keywords: Pressure Equipment Directive, technical harmonisation, design, manufacture and conformity assessment of pressure equipment

Introduction

The EC Pressure Equipment Directive 97/23/EC is a Global Approach Directive aimed at harmonising regulations across Europe for the design, manufacture and conformity assessment of certain types of pressure equipment [1]. Failure to comply with the Pressure Equipment Regulations is illegal and can result in prosecution and penalties on conviction of a fine, imprisonment or both.

The Pressure Equipment Directive (97/23/EC) was adopted by the European Parliament and the European Council in May 1997. From 29 November 1999 when it initially came into force until 29 May 2002 manufacturers had a choice between applying the Pressure Equipment Directive (PED) or continuing with the application of the existing national legislation. Since 30 May 2002 the Pressure Equipment Directive (PED) is obligatory throughout the European Union (EU) and it also applies to new Member States from the dates of joining the European Union (EU) [1].

Lloyds Register acts as Notified Body (Nobo) with identification number CE 0038 for surveying and the certification of pressure equipment which comply with the PED. As a legal requirement such products must be approved by a Notified Body in order to receive the CE mark and go to market.

Scope and type of equipment

The Directive applies to items of pressure equipment: vessels, pressurised storage containers, heat exchangers, steam generators, boilers, industrial piping, safety devices and pressure accessories. Such pressure equipment is widely used in process industries (oil & gas, chemical, pharmaceutical, plastics and rubber and the food and beverage industry), high temperature process industry (glass, paper and board), and energy production and in the supply of utilities, heating, air conditioning and gas storage [1-2].

The Directive applies to the design, manufacture and conformity assessment of pressure equipment and assemblies of pressure equipment with a maximum allowable pressure greater than 0.5 bar (gauge) [1-2]. Some specific items are excluded from the Directive either because; they are already covered by other EC Directives, they are covered by other International Agreements or their hazard due to pressure is not significant. In total there are 21 exclusions that are listed in PED [1].

Importance for safety and ease of market entry

The ability to trade goods freely throughout Europe did not exist because the laws of each member state differed. This meant that in order to sell products in more than one member state a manufacturer would be required to have the products (such as pressure equipment) tested and approved in several countries. The process was time consuming and costly and therefore acted as a ‘Barrier to Trade’. The Pressure Equipment Directive (97/23/EC) arises from the European Community's programme for the elimination of technical barriers to trade and is formulated under the "New Approach to Technical Harmonisation and Standards". Its purpose is to harmonise national laws of Member States regarding the design, manufacture, and testing and conformity assessment of pressure equipment and assemblies of pressure equipment [1]. It therefore aims to ensure the free placing on the market and putting into service of the equipment throughout the European Union and the European Economic Area.

Implications in the manufacturing process

In general, pressure equipment must be designed, manufactured and checked, and if applicable equipped and installed, in such a way as to ensure its safety when put into service in accordance with the manufacturer's instructions, or 'reasonably foreseeable conditions'. Equipment must have the correct technical documentation and satisfy appropriate conformity assessment procedures in order to carry the CE marking and have a Declaration of Conformity.

Essentially, the PED requires the level of hazard of pressure equipment to be assessed and classified into 5 categories, which are: SEP (Sound engineering practice- for pressure equipment and assemblies of pressure equipment classified below the specified pressure / volume thresholds) and Category I to IV. The higher the level of hazard, the more extensive the level of quality assurance required during the design, manufacture and testing of the equipment. It is generally the manufacturer's responsibility to determine the hazard category of each particular equipment item and system. There are 9 separate classification charts [1] (also called tables in the PED) as shown in the table 1. One for each of the possible combinations of equipment type, fluid state and fluid group, the volume or diameter (in litres or as DN respectively) and the maximum allowable or design pressure in bar. Once it is determined that the equipment is covered by the PED, the classification has 6 steps: 1. Determine the type of pressure equipment being considered 2. Determine the state of the fluid in the equipment 3. Determine the hazard group of the fluid in the equipment 4. Select the appropriate hazard category chart 5. Determine the maximum allowable pressure and the defining dimension of the equipment 6. Determine the PED hazard category.

Table 1. Classification Charts for current PED [1]

Equipment Type	Fluid State	Fluid Group	Chart
Vessel	Gas	1	1
Vessel	Gas	2	2
Vessel	Liquid	1	3
Vessel	Liquid	2	4
Steam Generator	N/A	N/A	5
Piping	Gas	1	6
Piping	Gas	2	7
Piping	Liquid	1	8
Piping	Liquid	2	9

When the PED category has been established for equipment, the conformity assessment requirements can be defined. In effect, the conformity assessment is the quality assurance required to validate the design, manufacture, testing and inspection of the equipment. The PED category defines the required conformity assessment module. Where multiple module choices apply, the equipment manufacturer may select the module(s) best suited to their particular requirement [3].

Equipment classified in Categories I to IV will be required to meet requirements for design, manufacture, testing, marking, labelling, instructions and materials which are considered essential for safety reasons. This also includes safety accessories and pressure accessories intended for equipment classified in the above categories. Assemblies which include at least one item of pressure equipment classified in Categories I to IV, which the manufacturer intends to be placed on the market and put into service, will also be required to meet these essential requirements [5, 6]. The essential safety requirements (ESR's) are a general list relating to the design and construction of the pressure equipment. The manufacturer must have evidence (technical documentation) which demonstrates how the "essential safety requirements" (ESR's) have been met.

The use of specified Design Codes / Codes of Construction is expected. Where a harmonised European standard (EN number with an Annex Z referring to the PED) is used a "presumption of conformity" (the standard is approved for use by the EU) can be granted. If a non-harmonised standard is used (e.g. ASME Boiler and Pressure Vessel Code, Section VIII, Division 1) then the manufacturer must demonstrate how his equipment meets the applicable essential requirements [1-6].

All modules are divided into design, inspection and Quality Assessment Modules. Notified Bodies' involvement increases with risk category. All requirements are explained in details in the directives but in brief, for Category I - no Notified Body involvement, Category II – survey by Notified Body, Category III - type examination and survey by Notified Body and for Category IV - type examination and verification by Notified Body is needed.

What is changing in the new Directive

PED 97/23/EC is changing into a new number – 2014/68/EU [4].

For manufacturers there are no substantive changes to the technical requirements and the process is the same as what is understood for the current Directive. However, the arrival of the new Directive (2014/68/EC) will mean that manufacturers will need to review their CE marking procedures and documentation for pressure equipment. The Directive will be implemented into force in two stages: Article 13 on Classification shall enter into force on the 1st June 2015 and the remainder of the Directive will enter into force on the 19th July 2016.

While there are no changes in the technical scope of the PED, Hazard category tables and to the essential safety requirements, there is a fundamental change to the safety philosophy of the PED [3]. There is now an obligation for manufacturers to analyse the risks of pressure equipment as well as the hazards. This will take more investigation and interpretation to fully gauge its impact on both manufacturers and Notified Bodies [3].

The Directive has been rewritten to make the requirements much clearer for the different types of economic operators. The Directive now identifies the 4 types of operators (Manufacturers, Importers, Distributors and Authorised Representatives).

In the new PED it is not just manufacturers who have a role to play in ensuring that only safe, compliant products reach the EU market, but the whole

supply chain must play its part, and so the new PED now incorporates the term "economic operators," and lays down legal obligations for each [4]. The revision also makes clear that if an importer or distributor places pressure equipment or assemblies on the market under their own names or trademarks, or modifies the equipment in a certain way; they will be considered manufacturers and will therefore have to take legal responsibility for the product's compliance including conformity assessment. The Declaration of Conformity has changed, as follows in 'EU Declaration of Conformity' [4].

The current basis for the determination of fluid group (1 or 2) in PED Article 9 (i.e. Directive 67/548/EEC) is being replaced by a new Classification, Labelling and Packaging Regulation from 1st June 2015 [4]. All details can be found in the new Directives.

According to the new directive, existing approvals are valid. Some conformity assessment modules have been renamed as shown in the table 2 and the requirements for manufacturers and notified bodies restructured.

Table 2. Conformity assessment module/procedure changes [3]

97/23/EC	2014/68/EU
A1	A2
B	B (Production type)
B1	B (Design Type)
C1	C2

Conformity assessment module/procedures changes as below in the tables. Table 3 shows current conformity assessments modules and table 4 conformity assessment module/procedure according to the new PED. Conformity assessment tables (charts) are in Annex II in the new PED [4].

Table 3. Conformity assessment modules in current PED

PED Category	**Module**
SEP	Sound engineering practice
I	A
II	A1, D1, E1
III	B1+D, B1+F, B+E, B+C1, H
IV	B+D, B+F, G, H1

Table 4. Conformity assessment module/procedure according to new PED [4]

Category I (Module)	Category II (Modules)	Category III (Modules)	Category IV (Modules)
A	A2 D1 E1	Modules B (design type) + D B (design type) + F B (production type) + E B (production type) + C2 H	B (production type) + D B (production type) + F G H1

As seen, the most significant change is around the quality system requirements mentioned in modules, D, D1, E, E1, G, H and H1.

Challenges for the manufacturers and change management processes

Manufacturers and notified bodies will have to familiarise themselves with the new requirements so as to be able to apply them to new equipment being placed on the market after 1st June 2015. The key impact for the manufacturers is to understand the implications of new modules, fluid categorisation, analyse hazards and risks, as well as modifications of all internal documents, procedures and certificates.

These changes will now mean that other Economic Operators other than manufacturers, as importers and distributors will need support from Nobo's. Lloyd's Register is continuing to examine the wording of the new PED to fully understand the implications for us as a PED Notified Body as well as for all economic operators [3]. Some useful websites are listed in the references [7-11].

References

[1] DIRECTIVE 97/23/EC OF THE EUROPEAN PARLIAMENT AND OF THE COUNCIL of 29 May 1997 on the approximation of the laws of the Member States concerning pressure equipment LR, Official Journal of the European Communities No L 181/1.
[2] Guidelines related to the Pressure Equipment Directive 97/23/EC (PED).
[3] Lloyds Register PED Course Rotterdam 2015, Pimley Colin.
[4] Official Journal of the European Union, Volume 57, 27 June 2014.
[5] Principles for the Assessment of Assemblies (Version 17. June 2014), CABF PED/SPVD 2014-06-17(previous document N 13/046 rev2).
[6] Guiding Principles for the contents of Particular Materials Appraisals, PE- 03-28 - rev 5 21 November 2006.
[7] EU Commission PED webpage: http://ec.europa.eu/enterprise/sectors/pressure-and gas/documents/ped/index_en.htm
[8] Working Group Pressure (WGP) Guidelines http://ec.europa.eu/enterprise/sectors/pressure-and-gas/documents/ped/guidelines/index_en.htm
[9] PED Harmonised standards: http://ec.europa.eu/enterprise/policies/european-standards/harmonised-standards/pressure-equipment/
[10] New Approach Guide: http://www.newapproach.org
[11] New Legislative Framework: http://ec.europa.eu/enterprise/policies/single-market-goods/documents/new-legislative-framework/

3D MODELS ASSEMBLING FOR T-x-y DIAGRAMS Fe(Ni)-Cu-S

V.I. Lutsyk [1,2], V.P. Vorob'eva [1], A.M. Zyryanov [1]

[1] *Institute of Physical Materials Science SB RAS, Russia*
[2] *Buryat State University, Russia*
E-mail: vluts@ipms.bscnet.ru

Abstract

3D computer models of T-x-y diagrams of subsystems Fe-FeS-Cu_2S-Cu (68 surfaces and 29 phase regions) and Ni-NiS-Cu_2S-Cu (45 surfaces and 22 phase regions) have been designed. The special features of shaping of the solidus surfaces, connected with liquid immiscibility, are in consider.

Systems Fe-Cu-S and Ni-Cu-S are studied as boundaries of the 4-component system Fe-Ni-Cu-S within the framework of complex experimental investigation and computer simulation [1,2]. Both diagrams are limited by the congruently melting sulfides FeS, NiS, Cu_2S, and subsystems Fe-FeS-Cu_2S-Cu=A-R1-R4-C and Ni-NiS-Cu_2S-Cu=B-R2-R4-C, where A=Fe, B=Ni, C=Cu, S=D, R1=FeS, R2=NiS, R4=Cu_2S, are in consider (Figure 1). The incongruently melting compound R3=Ni_3S_2 is formed in the binary system Ni-S=B-D.

Key words: phase diagrams, liquid immiscibility, 3D visualization, computer-aided design of materials, metal-sulfide systems, alloys of iron, obtaining of nickel and copper

Binary Systems

The system Fe-Cu=A-C is characterized by two phase reactions: the metatectic transformation δ-Fe$\rightarrow\gamma$-Fe+L (k_{A1C}: A$\rightarrow$L+A1) at 1477°C from the high-temperature iron polymorphous modification δ-Fe to intermediate one γ-F and the peritectic reaction L+γ-Fe$\rightarrow$Cu (p_{A1C}: L+A1$\rightarrow$C) at 1094°C (Figure 1a). The same polymorphous transformation δ-Fe$\rightarrow\gamma$-Fe+L (k_{A1R1}: A$\rightarrow$L+A1) at 1365°C and the eutectic reaction L$\rightarrow\gamma$-Fe+FeS (e_{A1R1}: L$\rightarrow$A1+R1) at 988°C take a place in the subsystem Fe-FeS=A-R1. The eutectic reaction L$\rightarrow$FeS+Cu_2S (e_{R1R4}: L$\rightarrow$R1+R4) is observed in the subsystem FeS-Cu_2S=R1-R4 at the temperature 940°C.

Continuous series of solid solutions are formed in the system Ni-Cu=B-C (Figure 1b). There are the peritectic L+NiS$\rightarrow$$Ni_3S_2$ (p_{R2R3}: L+R2$\rightarrow$R3) at 637°C and the eutectic L$\rightarrow$Ni+Ni_3S_2 (e_{BR3}: L$\rightarrow$B+R3) at 806°C reactions in the subsystem Ni-NiS=B-R2. The subsystem NiS-Cu_2S=R2-R4 is the simple eutectic with the reaction L$\rightarrow$NiS+Cu_2S (e_{R2R4}:L$\rightarrow$R2+R4) at 760°C.

The subsystem Cu-Cu_2S=C-R4 is characterized by the liquid immiscibility and its curve $m_{CR4}k_{CR4}n_{CR4}$ gives correspondent immiscibility surfaces in both ternary subsystems Fe-FeS-Cu_2S-Cu=A-R1-R4-C and Ni-NiS-Cu_2S-Cu=B-R2-R4-C. The immiscibility surface is within the liquidus Cu_2S=R4 field in the subsystem Ni-NiS-Cu_2S-Cu=B-R2-R4-C (Figure 1b). The compound R4 participates in two invariant reactions: the quasi-peritectic L+NiS$\rightarrow$$Ni_3S_2$+$Cu_2S$ (Q2: L+R2$\rightarrow$R3+R4) at

724°C and the eutectic L→Ni(Cu)+Ni_3S_2+Cu_2S (E2: L→B(C)+R3+R4) at 585°C. As for the subsystem Fe-FeS-Cu_2S-Cu=A-R1-R4-C, its immiscibility surface intersects the line Q1E1 of co-crystallization of the polymorphous modification γ-Fe=A1 with the compound R4 (Figure 1a). The line Q1E1 connects invariant reactions: the quasi-peritectic L+γ-Fe→Cu_2S+Cu (Q1: L+A1→C+R4) at 1070°C and the eutectic L→Cu_2S+FeS+γ-Fe (E1: L→A1+R1+R4) at 914°C. The invariant monotectic reaction L1→L2+γ-Fe+Cu_2S (or M(N): L1→L2+A1+R4) at 1074°C corresponds to immiscibility.

3D Simulation

Design of 3-dimensional (3D) computer model of T-x-y diagram includes some stages [3]. The analysis of the T-x-y diagram geometric structure is presented as the scheme of uni- and invariant states. For instance, 3 invariant transformations of the subsystem Ni-NiS-Cu_2S-Cu=B-R2-R4-C, in accordance with the temperature row, are written to the scheme of uni- and invariant states (Table 1), where every 3-phase reaction has the record of the trajectory (first and end base points) of interacting phases concentrations change. Contours of the diagram surfaces are combined from these lines. For example, lines $e_{CR4}E2$, $C_{R4}C_{E2}$, $R4_CR4_{E2}$ correspond to change in the liquid (L), and solid (C and R4) phases concentrations in the reaction L→C+R4. The line $e_{CR4}E2$ is one of the contour lines of the solid solution Ni(Cu)=B(C) liquidus, while the line $C_{R4}C_{E2}$ is one of its solidus contour. The line $R4_CR4_{E2}$ participates in the shaping of solidus R4 contour. Thus the scheme makes it possible to calculate type (ruled, unruled, plane, etc) and number of all surfaces, to indicate their contours and to determine all phase regions. As a result, the T-x-y diagram Ni-NiS-Cu_2S-Cu is formed by 45 surfaces and 22 phase regions.

Table 1. Scheme of uni- and invariant states of the subsystem Ni-NiS-Cu_2S-Cu=B-R2-R4-C, B>k>R4>m(n)>C>e_{CR4}>K2>R2>p_{R2R3}>e_{R2R4}>Q2>e_{BR3}>E2 (Figure 1b)

B-D=Ni-S	B-C-D=Ni-Cu-S	B-C=Ni-S	C-D=Cu-S
	L1→L2+R4 $n_{CR4}K2$, $m_{CR4}K2$, $R4_{m(n)}R4_{K2}$		
L+R2→R3 $p_{R2R3}Q2$, $R2_{R3}R2_{Q2}$, $R3_{R2}R3_{Q2}$	L→R2+R4 $e_{R2R4}Q2$, $R2_{R4}R2_{Q2}$,$R4_{R2}R4_{Q2}$		L→C+R4 $e_{CR4}E2$,$C_{R4}C_{E2}$, $R4_CR4_{E2}$
	Q2: L+R2→R3 +R4		R2+R3+R4 $R2_{Q2}R2^0_{Q2}$, $R3_{Q2}R3^0_{Q2}$, $R4_{Q2}R4^0_{Q2}$
L→B+R3 $e_{BR3}E2$, $B_{R3}B_{E2}$, $R3_BR3_{E2}$	L→R3+R4 Q2E2, $R3_{Q2}R3_{E2}$, $R4_{Q2}R4_{E2}$		
	E2: L→B(C)+R3+R4		
	B(C)+R3+R4 $B_{E2}B^0_{E2}$, $R3_{E2}R3^0_{E2}$, $R4_{E2}R4^0_{E2}$		

Further the scheme of uni- and invariant states is transformed from the tabular form into the graphic one. Firstly the horizontal (isothermal) planes, which correspond to the complexes of invariant reactions, are designed. Then the ruled surfaces - boundary of the 3-phase regions are attached to them. Later the unruled surfaces (liquidus, solidus, solvus, transus) are constructed. As a result, the T-x-y diagram prototype is obtained. It is converted into the real system T-x-y diagram 3D model, when experimental data (concentrations and temperatures of base points) are introduced, and the curvature of lines and surfaces is specified.

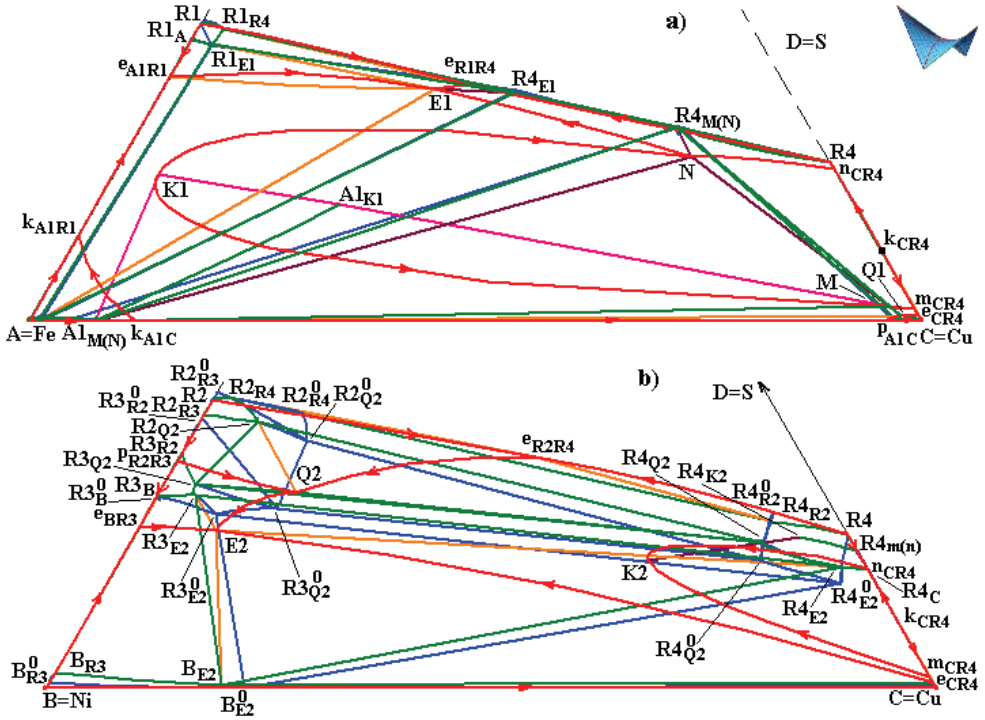

Fig. 1. Projections of the Fe-Cu-S=A-C-D (a) and Ni-Cu-S=B-C-D (b) T-x-y diagrams (subsystems Fe-FeS-Cu_2S-Cu=A-R1-R4-C, Ni-NiS-Cu_2S-Cu=B-R2-R4-C)

Immiscibility in the Subsystem Fe-FeS-Cu_2S-Cu=A-R1-R4-C

Because of the liquid L immiscibility it is necessary to distinguish, with what precisely liquid, L1 or L2, coexist the crystals γ-Fe=A1, Cu=C, Cu_2S=R4. Since the monotectic reaction in the binary system Cu-S=C-R4 is carried out in the form L1→L2+R4, then the 2-phase region L+R4 in its lower part (between the lines of m_{CR4}M and p_{A1C}Q1) must be as L1+R4 and in its upper part as L2+R4. And liquidus q_{R4} and solidus s_{R4} surfaces are divided into two parts.

Crystals A1 and R4 interact with L1, with L2, and together in the monotectic invariant reaction L1(M)→L2(N)+A1+R4. Therefore there are 3-phase regions: L1+L2+A1, L1+L2+R4, L2+A+C. Thus, the T-x-y diagram of the subsystem Fe-

FeS-Cu_2S-Cu includes 6 regions L+I and 6 I+J; 5 homogeneous regions I=A, A1, C, R1, R4; the region of the liquid immiscibility; 9 3-phase regions with the liquid and 2 ones without it. Boundaries of these phase regions are 33 ruled surfaces: 5 surfaces of liquidus and 5 – solidus; 2 surfaces of transus; 10 solvus surfaces; the immiscibility surface; 12 horizontal simplexes of 3 invariant reactions. As a result, the T-x-y diagram consists of 68 surfaces and 29 phase regions.

Since the liquidus q_{A1} is given by 9 base points: k_{A1C}, k_{A1R1}, e_{A1R1}, E1, N, K1, M, Q1, p_{A1C}, and then the correspondent solidus s_{A1} must be of 9 base points (Figure 1a). However, them only 8: $A1^{A}{}_{C}$, $A1^{A}{}_{R1}$, $A1_{R1}$, $A1_{E1}$, $A1_{K1}$, $A1_{M(N)}$, $A1_{Q1}$, $A1_{C}$. Basic innovation in 3D models consists of the presence of pseudo-fold $A1_{K1}A1_{MM(N)}$ on the solidus s_{A1}. It is directing line of two ruled surfaces and it does not influence the smoothness of the solidus surface. Upper point $A1_{K1}$ has a temperature of the critical point K1 at the intersection of the immiscibility surface with the liquidus q_{A1}. Because of the fold, which is begun at point $A1_{K1}$, liquidus and solidus are topologically equivalent, because the curve $A1_{K1}A1_{M(N)}$ is the conjugate with two branches of the arc NKM.

Analogously, the solidus surface of R4 has a fold $R4_{m(n)}R4_{K2}$, conjugated with the lines $m_{CR4}K2$, $n_{CR4}K2$ in the subsystem Ni-NiS-Cu_2S-Cu=B-R2-R4-C. These three lines are the directing ones of the ruled surfaces. They form the region of the monotectic transformation L1$\rightarrow$L2+R4.

Surfaces of solvus in [4, P. 221, Fig. 218] are designed so that two lines of its contour are vertical. Therefore the x-y projections of some points are merge, and the contour of the solvus is open [5]. Solidus surface in T-x-y diagrams with immiscibility are designated illegibly in [6, P. 296-297, Fig. 4.58], and it is difficultly to understand, if the solidus has the pseudo-fold, which makes it possible to preserve the topological equivalence of conjugated surfaces, or not.

Conclusions

The obtained 3D models allow, besides the visualization (rotation of 3-dimensional figures, projections, any sections construction), to predict the crystallization schemes for any 3-component concentration, to carry out the calculations of the mass balances of the coexisting phases at any temperature and taking into account the stages of their formation, to serve the source of obtaining additional information about the stages of crystallization and microstructure forming, to give possibility to qualitatively and quantitatively evaluate phase composition for the given mixture. This study of the system properties creates theoretical base for the experimental work and planning of the experiment during the study of 3- and 4-component systems.

Acknowledgements

The work was partially supported by the Russian Foundation for Basic Research (projects 14-08-00453 and 14-08-31468).

References

[1] Vorob'eva V., Lutsyk V., Shodorova S., Zyryanov A., Proc. 46th Intern. October Conf. on Mining and Metallurgy. Bor (Serbia), 2014. P. 144.
[2] Sineva S.I., Starykh R.V. et al. Russian Metallurgy (Metally). 2010, 3, 286-294; 2010, 11, 1025-1031.
[3] Lutsyk V.I., Vorob'eva V.P. Therm. Anal. Calorim. 2010. 101 (1), 25-31.
[4] Prince A. Alloy Phase Equilibria. Elsevier Publ. Comp., Amsterdam-London-New York, 1966. 290 p.
[5] Lutsyk V., Zelenaya A., Vorob'eva V., Abstr. Intern. Conf. CALPHAD XXXVIII. 2009. Prague, Czech Rep. P. 146.
[6] Khaldoyanidi K.A. Phase Diagrams of Heterogeneous Systems with Transformations, Novosibirsk, Institute of Inorg. Chem. SB RAS, 2004, p. 382 (In Russian).

SAMPLING PROCEDURE OF INPUT MATERIALS AT SECONDARY COPPER PROCESSING

M.Laubertová[1], J. Trpčevská[1], J.Pirošková[1]

[1]*Technical University of Kosice, Faculty of Metallurgy, Department of Non-ferrous Metals and Waste Treatment, Letna 9, 043 53, Kosice, Slovakia, martina.laubertova@tuke.sk*

Abstract

Sampling in metallurgy is an essential part of the production process controlling. This process takes into account the input materials sampling, final products or semi-final products and by-products. These materials are of various origins, of different composition, the different bulk size, homogeneity and heterogeneity. The analytical testing cannot be implicated at all the material, only a certain part of the whole. This part of the whole, which is called the sample, should be collected qualifiedly so the collected sample is representative and should have unchanged value and information. Subsequently the required analysis will be performed from such sample - the content of the components, which are subject of interest for the customer or consumer, will be identified. Both parties are interested in obtaining a reliable result, but also have an interest in economic and budgetary use of the goods. The past experience has proved that it is not possible to take a sample of the whole material and completely randomly, because most materials in general have certain heterogeneity. The character of the raw material used during the cooper production has been changing over the years. There is an increased evidence of waste from electrical and electronic equipment in the secondary sources of copper. This fact is also reflected in the technological process of copper. The secondary copper heterogeneity and inconsistent processes lead to inefficiencies and may affect the final result. The aim of this paper is to inform about the sampling procedure during the secondary copper production. A representative sample is obtained by re-melting. The copper quantity in the sample is determined by gravimetric method.

Keywords: secondary copper, sampling, waste, sample

Introduction

Metal recycling is an important source of raw materials – especially for Europe Union with few natural resources. With close to 40% of the copper consumed each year coming from secondary sources, it is difficult to ignore the dynamics and influence of copper scrap. Sampling and assaying are the first step in the recycling flow, prior to the treatment of the incoming material and the subsequent refining of the recovered metals. Determining the exact metal content of the supplied materials is essential as it forms the contractual basis for metal value payment or physical metal return to the supplier [7][8]. An efficient and transparent sampling and assaying process is essential. The extended, continuously changing mix of complex feed materials such as e-scrap, catalysts,

tank house slimes, etc. make sampling and assaying a key success factor for sustainable precious metals recycling [9]. An accurate determination of the exact composition and the precious metal content of the received materials is crucial to enable a correct settlement with the customers, but also to steer the optimum processing of the material through the plant. The sampling and assaying processes are continuously innovated in close collaboration with the suppliers; most of the technologies applied are in-house developed. Automation and information management are important supporting tools to achieve maximum accuracy. The full range of industrial by-products and recyclable materials are sampled on site. The operations undergo independent, internal and external assessments regularly[10]. World leaders in recycling of non-ferrous metals are Umicore Hoboken, Belgium, Germany Aurubis, Boliden Rönnskär in Sweden[11][16] . The sampling and assaying processes are continuously innovated in close collaboration with the suppliers; most of the technologies applied are "*in-house"*. Standardized analytical method that ensures performance of analytical measurements in the same way for waste is not known at present. Such an approved written document should include a detailed description of how the measurement is carried out, and also include a description of the taking and preparing of waste sample. The document should be clear and complete, including the method of calculation and expression of the measurement result[12][13]. Russian Standard shows granularity sample waste under 0.3 mm, this standard is not yet indicated in the EU[14]. The modification of material granularity less than 1 mm is obtained by grinding multi-stage, followed by milling of the sample. Sampling processes in Aurubis: Copper scrap like an alloy scrap in the form of chips and pieces, metal bars, CuFe materials, shredder, scrap, granules are mixed, reduced, sawed, drilled and melted. The final sample is analysed by wet chemistry end then it is evaluated[10]. Sampling of metallic material in Umicore: Primary sample preparation: Manual sampling (3t), Induction melting, Dip sampling in liquid bath (15kg), Drilling of sampling bars, Sampling of drillings (2kg). Final sample preparation: Drying, Milling Screening to diameter 0,1 or 0,3 mm(1,5kg). Final sample is divided in 16 bags, packed and sealed (100g) and send to Umicore laboratory (4x100g), customer (4x100g) and also spare samples. The samples are subsequently sent to the in-house analytical laboratories where a combination of advanced instrumentation and conventional fire assays contribute to the accurate identification and assessment of the metals contained in the sample [11][15]. Montanwerke Brixlegg AG, Austria and as well as Kovohuty, a.s. as its subsidiary have been officially acquired by the Swiss Group UMCOR AG, through its fully owned subsidiary UMCOR Holding GmbH, Vienna[17]. The effective copper extraction from recycled raw materials and its re reintroduction into the production cycle is the main mission of producing non-ferrous metals from secondary raw materials. The anode copper is the main product in the production of copper. Input materials are mainly copper waste chemical composition from the 5 to 99% Cu. In the production of secondary copper from recycled raw materials are used different types of input materials: Fe-Cu bimetallic strips, slag and mattes, turnings, cut wire, brass and bronze, bronze ash and dust, dross, Fig.2. Process of pyrometallurgy is running in 3 production stages - Smelting (Shaft furnace), Converting (Converters) and Fire refining (Anode furnace). Scheme of the secondary copper processing is in Fig.1. Scrap

copper content from 5% up to 99% of Cu are processed by pyrometallurgy way. In dependence on copper content and granulometry are these materials processed individually on production aggregates as follows - shaft furnace 5-60% Cu, converters 60 - 85% Cu, and anode furnace above 90% Cu. For the modification of copper dust material is used pelletization disk and the output is a dust material rolled up to firm pellets. **Smelting** - in Shalf furnace is the process of smelting reduction of Cu materials As a fuel is used coke and the outcome of smelting is black copper (70 - 75% Cu) and shaft slag - artificial stone for building works. **Converting** - is processing the product of shaft furnace smelting - Cu black with the input materials with Cu content of 60 -85%. The result of oxidation process is a blister copper with content of 95 -96% of Cu. **Fire Refining** - the Anode furnace is the heart of the new modern line for the production of Cu anodes. Processed is the material with Cu content above 90% and blister from the own converter production, the output are the copper anodes as a final product for commercial use.

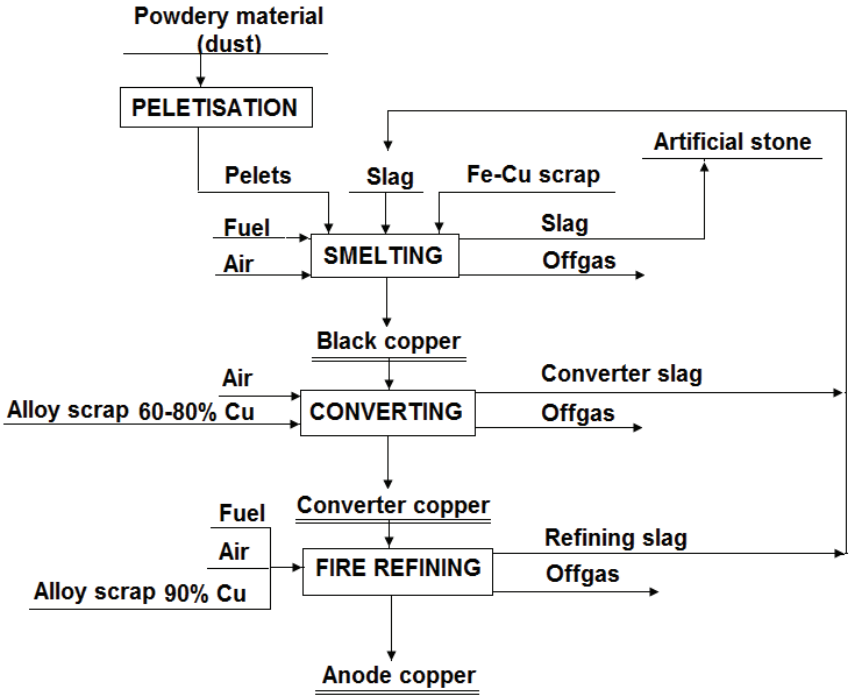

Fig. 1 Scheme of secondary copper processing

Fig. 2 Different types of raw materials
a-Cu wire, **b**-Fe-Cu Bimetal, **c**- Bronze millings, **d**- Copper scrap type Birch - Cliff

Procedure of taking gross sample

Raw materials are transported to the plant by freight transport (trucks). They are first weighed and materials are recorded. Depending on the type of the material, its different grain size and its homogeneity the increment can be taken by an excavator, a pricking steel probe or a shovel. A minimum 10% of deliveries are taken. The date, a car number, type of material, supplier and weight of waste are filed for each delivery. Sample treatment operation is carried out in “Sampleroom”.

The material was recorded relevant documents after arriving in showroom. The increments are mixed to give the 20 kg gross sample followed by quartering. Raw sample was dried (105°C) to constant weight, provides the moisture. From the gross sample is collected 5 kg to the reserve after drying. Of this stock is kept at least until such time as it is to establish a business contract. The material must first be adapted to the sample became homogeneous. The homogeneity of the sample is obtained by melting the material. From the resulting homogeneous the cast is then standardized procedure [18] sampled for chemical analysis.

Procedure of final sample preparing

Gross samples (8 kg) are taken for the smelting. The sample is melted in a ceramic crucible, previously cleaned borax at a temperature of 1200-1300°C in a crucible furnace heated gas. The sample is cast into the mold after smelting, Fig.3. If the material contains a higher content of Fe, then the sulfur is added, or aluminum to the melt. The addition of aluminium to reduce the melting temperature and the resulting cast is simply more brittle, more processable.

Example of sampling the selected waste

Sampling was implemented in the waste Cu (copper cut wire). The gross sample was 16,380 g. The entire test sample was dried to constant weight to determine the moisture content. Humidity was around 20 g, (0,12%). Gross sample (8,000 grams) cut up copper wire was weighed. The cast (METAL I) 7 690 g, slag 300 g and losses 10 g, which burned in a furnace, were obtained from the melting process, Fig.4. From cast (METAL I) sample was taken (chips) by cutting according to standard [18], Fig.5. Procedure for sampling (chips) was as follows: after degreasing the surface was adjusted optimal cutting speed of cutting machine to prevent overheating of the material (oxidation). Cutting of sample (METAL I) was running without of cooling liquids without the lubrication, the three sampling points at equal distances from the center of 1/4 and 1/3 of the length of cast its depth. Slag was milled in a vibration mill finely. Milled slag was sieved by sieving equipment to these fractions <+2>, <+2-0, 2>, <+ 0.2-0> mm, Fig.6.. The oversize fraction share <+2> were added, the (METAL I) (60 g + 7 690 g) and the fraction <2 to 0.2 +> represented (METAL II) (20 g). The fine fraction is weighed only be estimated, (300 g - 60 g - 20g = 220g) by reason of dusting, Tab.1.

Table. 1. Weight of each fraction

Name of the fraction	weighed portion [g]	weighed portion [%]	weighed portion for analysis [g]
Metal I.	7750	96,88	0,9988
Metal II.	20	0,25	0,0025
Fine fraction	220	2,75	0,0275
Heat loss	10	0,12	0,0012
sum		**100,00**	**1 g test sampling**

A sample (0.9988 g) obtained from (METAL I), sample (0.0025 g) obtained from (METAL II) and sample (0.0275 g) of the fine component was taken. Test sample (1g) after adding the statement come alive for chemical analysis. The samples were stored for 3 months as the samplegroom, as well as in the laboratory. A chemical analysis was carried out by the gravimetric method.

Fig. 3. Casting samples into the forms

Fig. 4. Sample: Cast and Slag

Fig. 5. Sampling of cast according to (STN 421303)

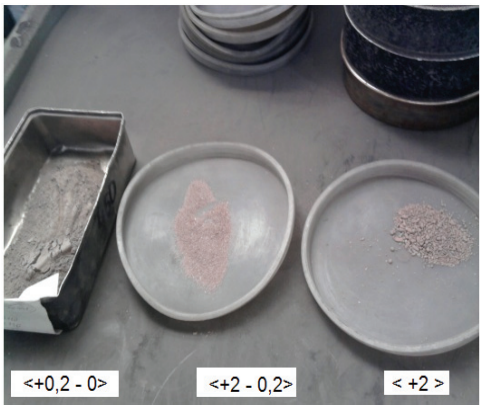

Fig. 6. Slag fraction of after sieving

Conclusion

The sampling and assaying processes in many companies producing metals from secondary input materials are continuously innovated in close collaboration with the suppliers; most of the technologies applied are "*in-house*". Because there is not known procedure for sampling of electronic waste at the moment. This designed procedure of input material at secondary copper processing could be the example for sampling of electronic waste, Fig.7.

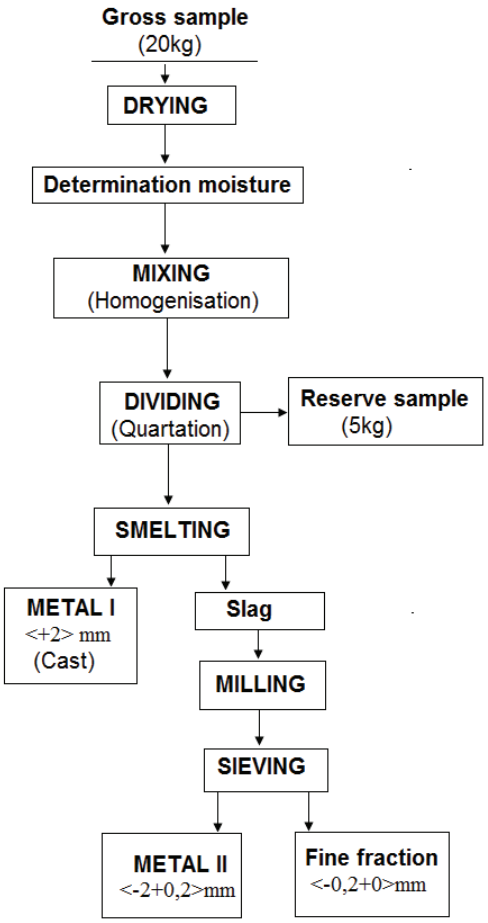

Fig. 7. Sampling procedure of input material sl

Acknowledgement

This work was supported by Ministry of Education of the Slovak Republic under grant VEGA 1/0293/14 and grant VEGA 1/0425/14. Article is the result of the Project implementation: University Science Park TECHNICOM for Innovation Applications Supported by Knowledge Technology, ITMS: 26220220182, supported by the Research & Development Operational Programme funded by the ERDF." The authors are grateful Kovohuty, a.s. for the support provided of practical part of diploma thesis.

References

[7] Sampling and assaying. [online] [cit. 2015-04-10]. Available at:<http://www.preciousmetals.umicore.com/PMR/Process/samplingAndAssaying/>
[8] Havlik T.: Vzorkovanie tuhých materiálov. Emilena Košice, 2006, str. 219
[9] Horálek V., Ševčík, J.G.K., Čurdová E., Helán V. a kolektiv: Vzorkování I – obecné zásady 2 THETA Český Těšín 2010, ISBN 978-80-86380-53-7
[10] Recycling Brochure Aurubis. [online] [cit. 2015-04-10]. Available at:<https://www.aurubis.com/site/binaries/content/assets/aurubis-en/dateien/image--product-documents/recycling-broschuere_2013_en.pdf>
[11] Umicore Precious Metals Refining Excellence in recycling. April 2014. [online] [cit.2015-04-10]. Available at: <https://ws.elance.com/file/2014_UmicorePMR_process_1.pdf?crypted=Y3R4JTNEcG9ydGZvbGlvJTI2ZmlkJTNEMTI3ODQ5MTkyJTI2cmlkJTNELTElMjZwaWQlM0Q1NjY1ODk2>
[12] STN EN 14899: 2006, Charakterizácia odpadov. Odber vzoriek odpadových materiálov. Rámec prípravy a použitia plánu odberu vzorky
[13] STN 01 5111:1974 ,Vzorkovanie sypkých a zrnitých materiálov
[14] GOST 28192:1989, Gost Waste of non-ferrous metals and alloys. Methods of sampling, sample preparation and test methods.
[15] Mark Caffarey, Umicore Precious Metals Refining A key partner in closing the life cycle of EEE (Electrical and Electronic Equipment), 2012 https://www.serdc.org/Resources/Documents/Summit%20Presentations/SERDC%20Summit%20Presentation%20-%20Mark%20Caffarey.pdf 315/201
[16] Boliden Rönnskär Sampling and Assaying. [online] [cit. 2015-04-10]. Available at:<http://partner.boliden.com/www/en/bolidenen.nsf/951b4d7cbfc58bc6c1256df80037d8f3/abeac9d6794dd756c1256e51004964ef?OpenDocument>
[17] KOVOHUTY, a.s., [online] [cit. 2015-04-10]. Available at: <http://www.kovohuty.sk/En/index.html>
[18] STN 42 1303:1986, Non-ferrous metals and alloys. General requirements for sampling and preparation of samples for chemical analysis

DETERMINATION OF MICROCONSTITUENT SETS BY MEANS OF MASS BALANCE DIAGRAMS

V.I. Lutsyk[1,2], A.E. Zelenaya[1], E.R. Nasrulin[1]

[1]*Institute of Physical Materials Science SB RAS, Russia*
[2] *Buryat State University, Russia*
E-mail: vluts@ipms.bscnet.ru

Abstract

The technology of two-, one- and zero-dimensional concentration fields analysis by means of the computer models of ternary systems phase diagrams is considered to study the stages of crystallization. Investigations are confirmed by the vertical mass balances. They permit to carry out the qualitative and quantitative analysis of coexisting phases in the entire temperature range for given mass center. A comparison of intersected phase regions (for given composition) and the phase reactions identify the concentration fields with unique and coinciding sets of microconstituent. As an example T-x-y diagrams with incongruently melting compound were used, that can be apply for the description of metal, oxide and salt systems.

Keywords: phase diagrams, computer model, microconstituent, mass balances.

Introduction

A comprehensive investigation of phase diagrams involves the analysis of crystallization processes on any of their fragments. The microstructural constituents forecast for concentration fields of different dimensions (obtained by projecting all the elements of phase diagram into the Gibbs triangle) can reduce the volume of further experimental study. The literature reproduces a manual method of processing the crystallization schemes for concentration fields. For example, in [1] the projection of T-x-y diagram with binary incongruently melting compound (R) into the concentration simplex produces 5 zero-dimensional (Q, E, Q_e=e_{AB}∩BR, Q_A=AQ∩BR, E_R=RE∩pQ), 18 one-dimensional ($e_{AB}Q_e$, Q_eQ, pE_R, E_RQ, QE, $e_{AC}E$, $e_{BC}E$, A_QA, Q_AQ, BQ_e, BQ, BE, CE, RQ_A, Q_AQ_e, RQ, R_ER, E_RE) and 14 two-dimensional concentration fields (1-14) (Fig. 1a). The crystallization stages and phases trajectories were considered for each field. I was revealed that five concentration fields coincide by the list of crystallization schemes with neighboring fields of higher dimension.

V. Danek [2] considered the crystallization paths for five compositions given in two-dimensional fields 1, 3, 5, 8, 12. A more detailed analysis of the crystallization processes and microconstituent for each concentration field was made in [3-4].

Similarly, authors of [1] investigated the crystallization stages for T-x-y diagram with ternary incongruently melting compound (R) and obtained the dividing into 65 concentration fields: 11 - zero-dimensional (Q, E, P, R, Q_A, Q_e, E_R, P_A, P_c, P_R, R_C), 32 – one-dimensional and 22 two-dimensional (1-22) ones (Fig. 1b). It was

found [5] that 1 two-dimensional field (22=12), 12 one-dimensional fields ($AP_A \in 3$, $BQ \in 19$, $Q_CQ \in 7$, $CP_C \in 16$, $E_RR_C \in 13$, $RP_R \in 9$, $P_AP_R \in 8$, $QP \in 20$, $P_RP \in 10$, $E_RP \in 12(22)$, $P_CP \in 21$, $PE \in 20$) and 6 zero-dimensional fields ($Q \in QE$, $P \in 20$, $P_C \in EP_C$, $P_A \in P_AQ_A$, $P_R \in P_RQ$, $E_R \in E_RE$) do not have unique sets of microconstituent.

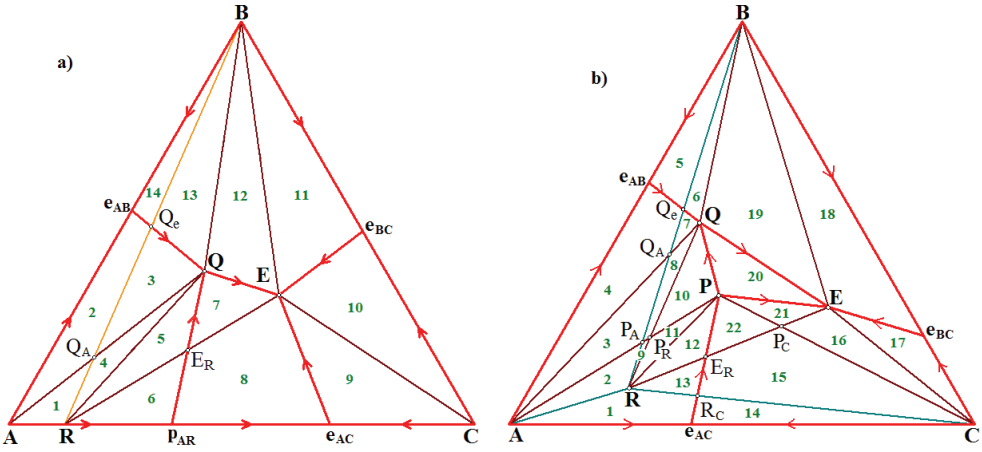

Fig. 1. Dividing by the concentration fields of T-x-y diagrams with binary (a) and ternary (b) incongruently melting compounds

We propose to use the computer models of phase diagrams for obtaining of complete data about the crystallization stages and the final set of microconstituents for each crystallization field. For this purpose, the spatial model of T-x-y diagrams including all geometric elements are produced. As an example, we consider the T-x-y diagram model of system NaCl-$CaCl_2$-$MgCl_2$ (A-B-C) with binary incongruently melting compounds R1=Na_2MgCl_4 and R2=$NaMgCl_3$ in binary system NaCl-$MgCl_2$.

T-x-y diagram model of system NaCl-$CaCl_2$-$MgCl_2$ (A-B-C)

The information about the structure of binary systems, the liquidus surfaces and 15 isopleths are used as initial data for the model [6]. The system is characterized by three invariant transformations: two quasiperitectic (L_{Q1}+A→B+R1 и L_{Q2}+C→B+R2) and one eutectic (L_E→B+R1+R2). The obtained model of phase diagram (Fig. 2a) includes 5 liquidus surfaces (q_A, q_B, q_C, q_{R1}, q_{R2}), 14 ruled surfaces (q^r), 3 horizontal complexes at the temperatures of invariant points (h_{Q1}, h_{Q2}, h_E) and two vertical planes (v_{BR1}, v_{BR2}; really they are two pairs of degenerated ruled surfaces bounding two-phase regions B+R1 and B+R2). Phase diagram involves 7 two-phase regions (L+A, L+B, L+C, L+R1, L+R2, B+R1, B+R2) and 10 three-phase regions (L+A+B, L+A+R1, L+R1+R2, L+C+R1, L+B+C, L+B+R1, L+B+R2, A+B+R1, B+R1+R2, B+C+R2). The projecting of all phase regions divides Gibbs triangle to 22 two-, 30 one- and 9 zero-dimensional concentration fields. It was established, that the 12 concentration fields do not have unique sets of microconstituents. Two one-dimensional (B-$Q_1 \in 9$, B-$Q_2 \in 10$) and two zero-dimensional ($Q_1 \in Q_1$-E, $Q_2 \in$ E-Q_2) coincide with neighboring concentration fields of

higher dimension by the list of intersecting surfaces and phase regions (for the given center of mass in this field), the schemas of phase reactions and the set of microconstituents. Four one-dimensional fields (p_{CR2}-$E_{R2}\in$ 18, p_{AR1}-$E_{R1}\in$ 19, E_{R1}-$Q_1\in$ 21, E_{R2}-$Q_2\in$ 20) and two zero-dimensional fields ($E_{R1}\in E_{R1}$-E, $E_{R2}\in E_{R2}$-E) coincide by the microconstituents and crystallization stage, but differ the intersected surfaces. One more two zero-dimensional fields (Q_{1e}-$Q_1\in$ 3, Q_{2e}-$Q_2\in$ 14) have the same microconstituents with neighboring one-dimensional field, but they differ the crystallization stage.

The phase diagram has a symmetrical topological structure relative to the "axis" $CaCl_2$-E-eR_1R_2 (in projection). Namely, the "left" and "right" parts of projection of phase diagrams contain the same quantity of concentration fields with a similar structure. For example, two-dimensional field 2 is bounded by the fragments of liquidus curve $e_{AB}Q_{1e}$ and two segments $NaClQ_{1A}$ и $Q_{1e}Q_{1A}$. The mass center given in this field intersects the liquidus surface (q_A with contour $NaCle_{AB}Q_1p_{AR1}$), ruled surface (q^r_{AB}: $e_{AB}Q_1A_{Q1}A_B$), horizontal invariant plane at Q_1 and three phase regions (L+A, L+A+B, A+B+R1). It is characterized by the following phase reactions: $L^1\rightarrow A^1$, $L^e\rightarrow A^{e(B)}+B^{e(A)}$, $L^{Q1}+A\rightarrow B^{Q1}+R1^{Q1}$. "Symmetrical" field 13 is bordered by the fragment of liquidus curve ($e_{BC}Q_{2e}$) and two segments ($MgCl_2Q_{2C}$, $Q_{2e}Q_{2C}$), and has similar characteristics, only relative to phase regions L+C, L+B+C and B+C+R2. Concentration fields with coinciding microconstituents are arranged symmetrically relatively the "axis" $CaCl_2$-E-e_{R1R2} too.

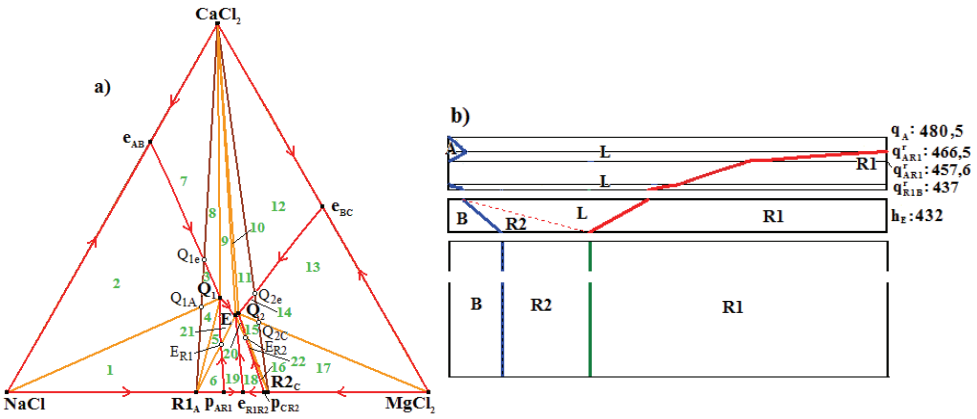

Fig. 2. Dividing of XY projection for phase diagram of system NaCl-$CaCl_2$-$MgCl_2$ into concentration fields (a), diagram of vertical mass balance for field 6 (b)

Analysis of crystallization scheme using the diagrams of vertical mass balance

Diagrams of vertical mass balance permit to analyze in detail the crystallization stages for the chosen mass center. For considered phase diagram of system NaCl-$CaCl_2$-$MgCl_2$ author of [6] analyzed all 22 two-dimensional concentration fields, formed the crystallization schemes and obtained the sets of microstructural constituents. Nevertheless, the products of monovariant peritectic

reaction don't include the microconstituents for fields 5, 6 and 22, whereas this reaction present in the schema of crystallization stage. Let's consider in more detail the crystallization stages for the field 6 using the diagram of vertical mass balance (Fig. 2b). Given mass center intersects the liquidus surface q_A and fall into two-phase region L+A, where the reaction of primary crystallization $L^1 \rightarrow A^1$ takes place. The melt intersects the ruled surface q^r_{AR1} on the border of three-phase region L+A+R1 with the proceeding of monovariant peritectic reaction $L^p+A^1 \rightarrow R1^p$, where the crystals A consumed and the crystals R1 grow (so crystals A are not included in the final set of microconstituents). Next, the melt gets into the two-phase region L+R1, which is characterized by postperitectic primary crystallization $L^{1p} \rightarrow R1^{1p}$ and then melt fall into three-phase region L+B+R1, where the secondary postperitectic crystallization $L^{ep} \rightarrow B^{ep(R1)}+R1^{ep(B)}$ takes place.

When mass center gets to the horizontal complex h_E at the temperature of ternary eutectic E, then the invariant eutectic reaction $L^E \rightarrow B^E+R1^E+R2^E$ ends with the deficit of melt and below there are only crystals B, R1 и R2. So this field is characterized by the following set of microconstituents: $R1^p$, $R1^{1n}$, $B^{en(R1)}$,$R1^{en(B)}$, B^E, $R1^E$, $R2^E$. Since the phase R1 appears and increases as a result of reaction $L^p+A^1 \rightarrow R1^p$, then $R1^p$ crystals have to be included in the microconstituents.

Vertical mass balance diagrams make possible to compare the processes in different concentration fields and qualitatively show that some concentration fields differ by the schemes of phase reactions, but have the same microconstituents. For example, the two-dimensional field 3 is characterized by the following list of phase transitions: $L^1 \rightarrow A^1$, $L^e \rightarrow A^{e(B)}+B^{e(A)}$, $L^{Q1}+A \rightarrow B^{Q1}+R1^{Q1}$, $L^{en} \rightarrow B^{en(R1)}+R1^{en(B)}$, $L^E \rightarrow B^E+R1^E+R2^E$ (Fig. 3a).

The resulting set of microconstituents $B^{e(A)}$, B^{Q1}, $R1^{Q1}$, $B^{en(R1)}$,$R1^{en(B)}$, B^E, $R1^E$, $R2^E$ not includes the crystals A, as they are completely consumed during the invariant quasiperitectic reaction $L^{Q1}+A \rightarrow B^{Q1}+R1^{Q1}$. One-dimensional field Q_{1e}-Q_1 is a part of monovariant liquidus curve $e_{AB}Q_1$, so the mass center for this field at once gets into three-phase region of L+A+B (Fig. 3b). Otherwise, the proceeding processes coincide with the field 3, as we can see from the diagrams of vertical mass balance. Although there is no the reaction of primary crystallization $L^1 \rightarrow A^1$ for the field Q_{1e}-Q_1, it coincides by microconstituents set with the field 3, because crystal A does not influence the microconstituents.

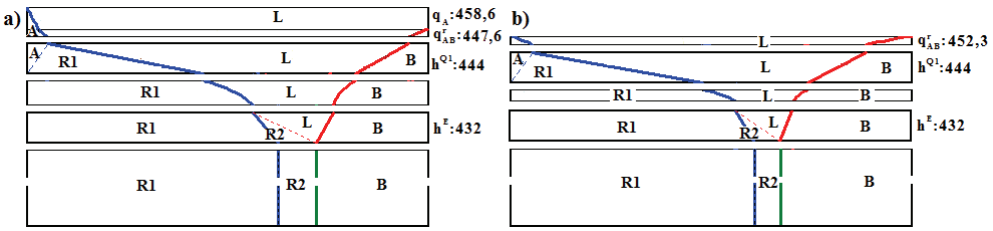

Fig. 3. Diagrams of vertical mass balance for fields 3 (a) and Q_{1e}-Q_1 (b)

Summary

The method based on the using of phase diagram model is considered as a tool to microconstituents design of alloy. All possible crystallization schemas of considered system and the content of each microstructural constituents taking into account its origin are analyzed by means of phase diagram model.

Acknowledgements

The work was partially supported by the Russian Foundation for Basic Research (projects 14-08-00453 and 14-08-31468).

References

[1] Palatnik L.S., Landau A.I. Phase Equilibria in Multicomponent Systems. Holt, Rinehard, Winston Inc., N.Y. 1964. 454 p.
[2] Danek V. Physico-chemical analysis of molten electrolytes. Elsevier Science Ltd. 2006. 464 p.
[3] Lutsyk V.I., Vorob'eva V.P. Rus. J. Inorg. Chem. 1995. 40, 1697-1703.
[4] Lutsyk V.I., Vorob'eva V.P. Rus. J. Inorg. Chem. 1997. 71, 331-334.
[5] Lutsyk V.I. Bulletin Buryat Scientific Centre SB RAS. 2012. 1(5), 78-97. (In Russian).
[6] Matiašovský K. Chemické Zvesti.1959. XIII, 78-95.

THE INFLUENCE OF INDUCED THERMAL STRESSES ON THE MEASURED HARDNESS IN EN AW6060 ALLOY BILLET PRODUCED USING DIRECT CHILL CASTING PROCEDURE

A. Beroš, I. Buljeta

Faculty of Metallurgy and Materials Science, University of Zenica, Bosnia and Herzegovina

Summary

Residual elastic stresses occur throughout the bulk of billets after casting procedure *Direct Chill*. Rapid cooling of the shell, contraction and shrinkage due to solidification mechanism cause thermally induced deformation, which affects the size of the measured hardness and provide insight into the development of thermomechanical regimes casting. The Brinell hardness was measured at three different classes of samples, lengthwise cross section of the billet before and after (1) homogenizing heat treatment, (2) natural aging, and (3) the relaxation cutting. Alloy EN AW6060 shows the possibility of establishing a relation between residual stresses and hardness.

Keywords: residual stresses, hardness, alloy EN AW6060, direct chill casting process

Introduction

During the solidification of continuously cast billets, thermally induced deformations can generate casting defects as hot cracks, distortion or residual stresses. Contraction and mechanism of shrinkage due to solidification, and its mechanical aspects, are associated with the origin mentioned defects. Thermal gradients or temperature differences through parts of billet follow uneven thermomechanical mode, creating thermal stresses. If one part of such stress release through creep mechanism, initiation of cracks or distortion, and the remaining part are measurable residual stresses that are measured and assessed at room temperature after fully finished contraction billet. Measurement of residual stresses on the billet destructive methods (Holle drilling method) or using neutron diffraction (XRD method) are limited by the very wide class of cast billets, the size of equipment and samples or test cost. Tests for mechanical properties of alloy EN AW6060, except in the context of quality billet, can be further used to assess the thermo-mechanical control regimes casting procedure [1]. Selecting a suitable simple standard mechanical methods, applicable in operation foundry after making billets, which can be linked to defects caused by thermal deformation, favors the process of measuring hardness.

The effect of elastic deformation on the hardness. Surface residual elastic deformation after casting alloys EN AW 6060 affecting the size of the measured hardness. The results should show a consistent pattern of residual stresses which vary between tension and pressure that would open a new field of interrogation

techniques. At the appropriate hardness test, applied load corresponds to the size and hardness of the indenter material. The effect of residual stresses on the hardness has a maximum impact at the beginning of plastic deformation. This means that the indenter penetrates deeper into the sample; the effect of residual stress is reduced. The existence of simple measurement techniques that allow mapping and distribution of residual deformation by measuring the hardness in the airline industry [2], supports efforts to apply similar methods to aluminum castings billets.

Experiment

Two phases of experimental studies were performed on samples of aluminum billets which are cast in the foundry "Aluminij" d.d Mostar with Direct Chill process:(1) the chemical composition and mechanical properties of the billets that had thermally induced hot cracks and (2) billets were cast in the required quality.

Mechanical testing of hardness along the billet

At this stage, the phenomena of hot tearing DC cast billet diameter of 178 mm was investigated. As-Cast billet alloy AA6060 EN containing internal cracks on casting 7500 mm was used for testing.

Material

Single billet was taken out and cut into cylinders of a thickness of 20 - 25mm. The first five samples were taken for every 100 mm tree. How not observed visually internal cracking, the distance is increased to 500 mm for the other samples. In this way are obtained 19 cylindrical samples measuring 178×20×25mm. For metallographic and other tests from 19 samples were selected seven samples, which involved three phases of casting: startup, work and final phase of casting.

Results and discussion

Hardness along the billet and chemical changes of composition

The first stage was carried out cutting the cylindrical sample into smaller samples (with marks 2, 7, 12, 16, 17, 18 and 19). Each sample, cut the central part of the width of 40 mm and is divided into four parts (Figure 1a). Analysis of the microstructure showed initial cracks in the sample number 17 and open cracks in the samples No.18 and 19 (Figure 1b), which appeared in the last stages of casting on the casting length 6500-7500 mm [3].

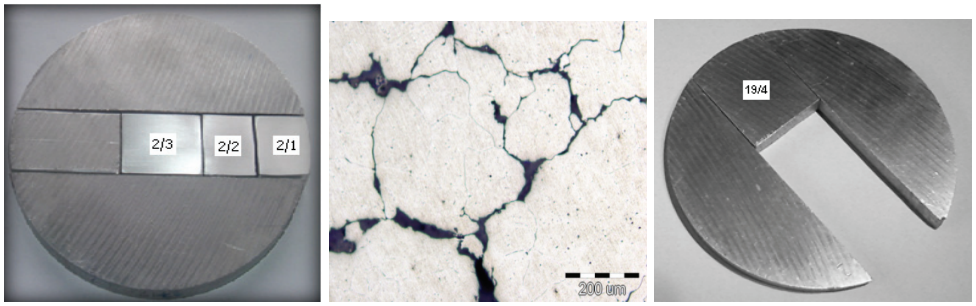

a) b) c)

Fig. 1. The individual sample a), the microstructure of open cracks b) and sample intended for testing the hardness over the length of the billet c)

Samples in the center and on the surface of the billet reflect changes in the structure, chemical composition and mechanical properties caused by rapid cooling. The transition area with a relatively stable, steady-state conditions, cooling and solidification is located between these zones therefore suitable for additional testing of mechanical properties along the billet (Figure 1c). The preparation of individual samples for hardness measurement was performed in the fourth degree (sandpaper quality 180, 250, 300, and 400 final) with SiC abrasive particles. Chemical analysis was performed on the OE spectroscopy and hardness with portable device IMPACT method Brinell. Measurement of on the samples was selected at three locations: A~1cm from the edge, B in the center of the sample, C~0.5-1cm from the peripheral surface and D on the peripheral surface of the sample (Figure 2a). For each measuring point were made 9 hardness measurements (Figure 2b) and 3 measurements of the chemical composition (Figure 2c). Samples are multiple times cut and relaxed from residual stress, so the effect of residual stress is reduced to a minimum. Hardness testing on samples is performed ~ 48 months after casting, which leads to stabilizing the hardness of the alloy EN AW 6060.

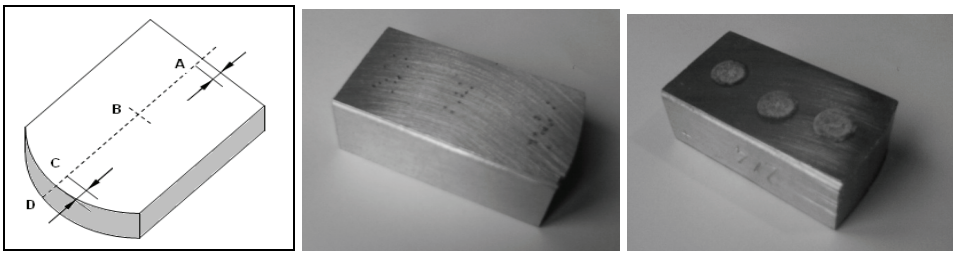

a) b) c)

Fig. 2. Scheme of measurement points a) and sample after testing the hardness b) and chemical composition c)

Results of measurement of hardness in Figure 3a shows a steady decrease on the hardness of the measuring points A, B and C until the appearance of the initial crack on the sample 17. When the hardness of the sample is rapidly growing. The measurements on the the point D, the outer surface of the billet, have fluctuations in the value of hardness and indicate the non equilibrium conditions of the formation of intermetallic AlFeSi phases.

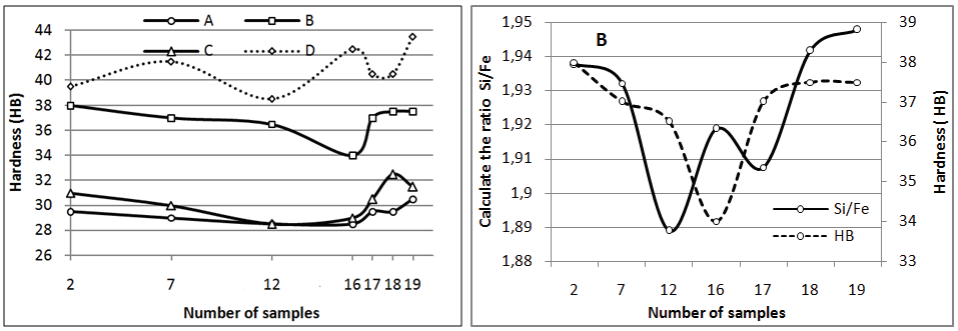

a) *b)*

Fig. 3. Change in hardness along the billet a) and the dependence of hardness compared to calculate the ratio of Si / Fe in case B b)

Measurement of chemical composition performed on the measuring points A, B and C. The calculated ratio of Si and Fe are essential to form a hard AlFeSi particles and shown in relation to the measured hardness (Figure 3b). variances between the curves show that in addition to the impact of hard AlFeSi particles, there are additional factors that affect the measured hardness.

Mechanical testing of hardness along the billet

The next step is performed further investigations of the same alloy, which are extended to test the cross-section in multiple directions, but reduced to two critical stages of casting: start and end of casting, the foot and head of the billet with diameter 203 mm.

Chemical Composition

For this test is again selected alloy EN AW6060 required composition (Table 1) from that in the foundry Aluminj d.d. Mostar with technology Wagstaff AirSlip were cast billets with diameter of 203 mm to a length of 7500 mm

Table 1. Chemical composition of the alloy EN AW6060

Composition	Elements (%)								
	Si	**Fe**	**Cu**	**Zn**	**Mg**	**Mn**	**Ti**	**Cr**	**Na**
Required	0,42 0,48	0,15 0,25	- 0,1	- 0,1	0,42 0,48	- 0,1	- 0,02	- 0,05	0,007
Measured	0,4259	0,1751	0,0013	0,0109	0,4302	0,0413	0,0085	0,0014	0,0016

In order to comprehensive tests were allocated after casting batch class 3 billets: 1) rejected the billet with internal cracks, 2) non homogenized and 3) homogenized billet required quality. From every billet cut are two cylindrical sample foot and head thickness 60 mm (Figure 4).

Hardness

Results of measurement of residual stresses for this type of alloys show changes in tensile and compressive stresses on the ~1/5 diameter billet [4]. The samples were divided into three circular zone (center: 30 mm diameter, mean: 80 mm diameter and surface: at a distance of 10mm from edge of the tree) and 6 of circular segments. Size circular zone is approximately determined according to the results of measurement of residual stresses by neutron diffraction on the basis of transition in tensile compressive stresses [4]. Tests Brinell hardness was measured on the 18 radial directions in the middle part and the surface of the billet (Figure 4b). In the central part of the measurement is reduced in 6 sections due to the width of the head of the measuring device.

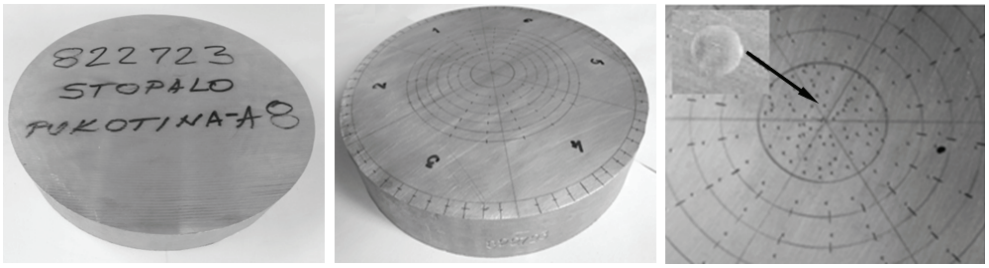

a) *b)* *c)*

Fig. 4. The sample of the foot billet a), a sample prepared for measuring the hardness b) the details of the indentation after the measurement c)

Number of measurements per single the section: Central 10, middle 15 and the flange 10 (4c). The measurement results are due to better observation and establish links hardness - residual stresses - internal cracks shown in the radar chart (Figure 5). The curves labeled full (red) relating to data hardness of the central part, the dashed lines in black for the middle section, a black spot on the surface of the tree. The graphs show a decrease of hardness in the interior of the tree that had cracks Contrary, homogenized billet cast in the required quality in this zone shows the highest amounts fields of hardness cross section of tree.

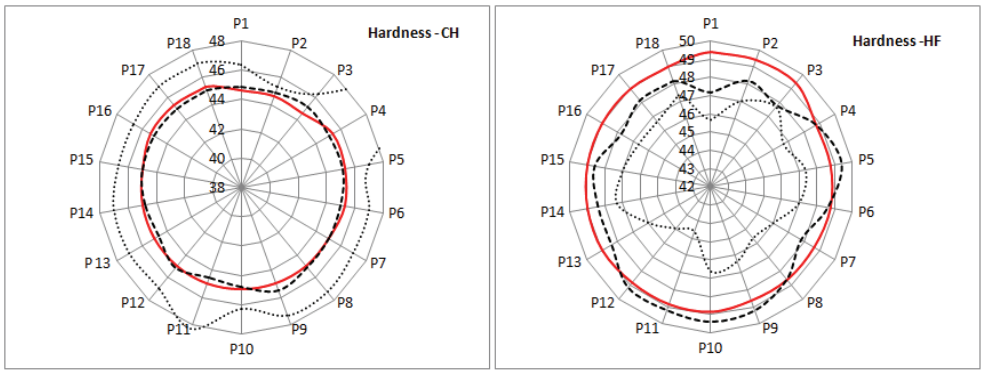

a) *b)*

Fig. 5. Change in total hardness head cracked a) and homogenized foot billet b) alloy EN AW6060 [1]

The influence of residual stresses on the hardness

The diagrams in Figure 6 show the relationship of the mean hardness of the intermediate part (samples 1-6) and the central part of the billet (sample 7) and the calculated Si/Fe ratio. Establishment of relations between hardness and content AlFeSi particles does not show good agreement with the patterns of logs with a crack (Figure 6a) while in the billets that are not homogenized this ratio has good agreement with the results of the measured hardness (Figure 6b).

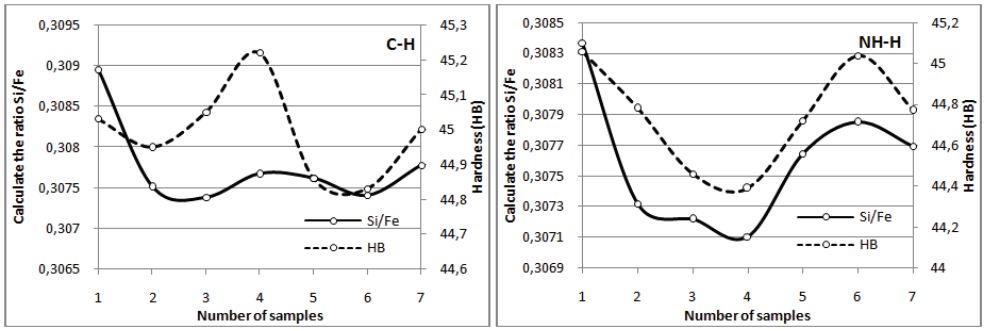

a) *b)*

Fig. 6. The ratio of hardness and the calculated ratio Si / Fe head cracked a) and not homogenized b) billet alloy EN AW6060

The figure 6a indicate presence of accumulated additional stress. After completion of the test the hardness of the samples cylinder (Figure 4) were further sectioned to a thickness of ~25 mm and new sample (circular sections): central and transitional part of billet (Figure 7a). Two samples of the transitional areas were selected: Section of the foot cracked billet (P3/2) and the head of as - cast billets (S5/1). On them is again measured hardness at a distance ~5 mm

indentation of the original measurements in the three measuring directions (Figure 7b). Calculating the ratio between additional measurements (hardness relaxed samples) and previous measurements, as an indicator of change was taken coefficient $k_{\Delta HBsr}$ in table 2.

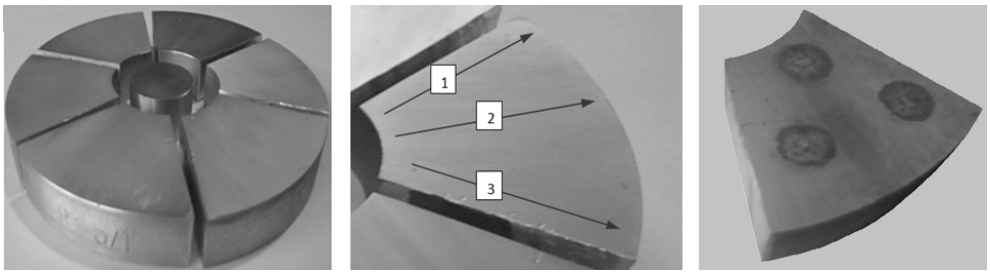

a) *b)* *c)*

Fig. 7. Sampling a) and directions of re-measuring the hardness b) and samples after measurement of chemical composition c)

Table 2. Values of the coefficient changes hardness $k_{\Delta HBsr}$ - Sample P3/2

Number of measurements	Measuring direction 1		Measuring direction 2		Measuring direction 3	
	Type of measurement		Type of measurement		Type of measurement	
	Previous	Additional	Previous	Additional	Previous	Additional
	1	2	3	4	5	6
1	44	47	44	43	47	-
2	45	30	44	41	46	41
3	45	32	45	37	46	33
4	46	28	47	32	45	30
5	45	30	46	35	45	42
HB_{SR}	45	33,44	45,20	37,6	45,8	36,50
$k_{\Delta HB}$	0,742		0,831		0,796	
$k_{\Delta HBsr}$	0,790					

Results in Table 2 show that the samples P3/2 underwent relaxation after cutting and have lower hardness value $k_{\Delta HBsr}$ = 0.79. Similar results were shown samples S5/1 of the head as cast billet where the $k_{\Delta HBsr}$ = 0.72. The calculated mean value indicates that the variation in hardness caused by residual stresses, which can be measured and opens up additional field research.

Conclusion

Mechanical testing the hardness of the alloy EN AW6060 along the tree in the transitional area of the cross section, showing the same trend in the working phase of casting, while the to cracks formation, hardness alloy sample increases. Comparison of Si/Fe ratio of key elements and hardness alloys exhibit area fits-flow curve, while deviations indicate the influence of residual stresses. This further confirms the measured hardness and hardness values of the coefficient changes.

References

[1] I.Buljeta, A.Beroš, J.Pristavec, B.Veber, Model hardness fields as projections thermally induced stresses in the en aw 6060 billet made by the direct chill, International MAGMA User Meeting, Germany, 2014

[2] John E. Wyatt, John T. Berry, Mapping of Superficial Residual Stresses in Machined Components, Journal of Industrial technology, 2009.

[3] I. Buljeta, A. Beroš, Z. Zovko Brodarac, R. Udovičić, Morphology of AlFeSi intermetallic phases and internal defects in AlMgSi billets, 46th IOC, Mining and Metallurgy, 2014.

[4] J.-M. Drezet and A.B. Phillion, As-Cast Residual Stresses in an Aluminum Alloy AA6063 Billet: Neutron Diffraction Measurements and Finite Element Modeling, 2010.

UTILIZATION PROPERTIES OF Ni-Pd/Al_2O_3 CATALYST SUPPORTED ON ALUMINA BASED FOAM

Vesna Nikolić[1], Željko Kamberović[2], Marija Korać[2], Miroslav Sokić[3], Zoran Anđić[4]

[1] *Innovation Center of the Faculty of Technology and Metallurgy, University of Belgrade, Karnegijeva 4, Belgrade, Serbia*
[2] *Faculty of Technology and Metallurgy, University of Belgrade, Karnegijeva 4, Belgrade, Serbia*
[3] *Institute for Technology of Nuclear and Other Mineral Raw Materials, Bulevar Franš d'Eperea 86, Belgrade, Serbia*
[4] *Innovation Center of the Faculty of Chemistry, University of Belgrade, Studentski Trg 12-16, Belgrade, Serbia*
[*] *Corresponding author; e-mail: vnikolic@tmf.bg.ac.rs*

Abstract

The aim of this study was to examine utilization properties of Ni-Pd/Al_2O_3 catalyst supported on α-Al_2O_3 based foam in the dry methane reforming. The catalyst was synthesized by using aerosol route. Non-calcined chloride precursors for Ni and Pd were reduced by hydrogen at very low temperature of 533 K. The reforming test was carried out for 3 h. Standing time was set to 1 h for each of the following temperatures: 873, 973 and 1023 K. Yields of CO and H_2 were determined and conclusions on selectivity, catalytic activity and stability were made on the basis of obtained results.

Keywords: Nickel-based catalyst, Alumina based foam, Dry methane reforming

Introduction

In the recent research, dry reforming of methane (DRM) have drawn considerable attention due to processing of two main greenhouse gases, CO_2 and CH_4. The DRM process is carried out over noble and non-noble metal based catalysts at temperatures from 973 to 1173 K in order to produce synthesis gas. Synthesis gas is a mixture of CO and H_2 and it is a valuable raw material used, as an example, for liquid fuels production. Considering high reactivity and favorable price of Ni, Ni-based catalysts such as Ni/Al_2O_3 are suitable for utilization in industrial conditions [1, 2]. Main disadvantages of Ni-based catalysts are rapid deactivation, caused by deposition of byproducts on active particles and sintering of active particles at high temperatures. To overcome these problems, Ni-based catalysts can be modified by only 0.4 to 0.5 wt. % of Pd [3,4].

Ceramic foams as catalyst supports have low pressure drops during the fluid flow, good mass transfer and good heat conductivity [5]. Therefore, the authors previously prepared Ni-Pd/Al_2O_3 catalyst supported on α-Al_2O_3 based foam via aerosol route [6]. The foam was synthesized as described earlier [7]. Using of chloride precursors for Ni and Pd provided elimination of the calcination and the

catalyst was reduced at 533 K [6]. Moreover, oxides obtained by calcination have lower reducibility than chlorides [8].

The present study aims to examine utilization properties of Ni-Pd/Al_2O_3 catalyst in the DRM process. Yields of H_2 and CO at three process temperatures were determined and conclusions on selectivity, activity and stability of the catalyst were made.

Experimental

To prepare the catalyst, $NiCl_2 \times 6H_2O$, $PdCl_2$ (MERCK, pro analysis) and α-Al_2O_3 based foam were used. The foam was synthesized earlier by polymer replication [7]. According to previously presented method [6], chloride solution was ultrasonically nebulized and deposited to the foam at 473 K. After drying at 473 K for 1 h, the sample was reduced with H_2 (flow rate: 20 L h^{-1}) at 533 K for 1.5 h. Metal content was 20 wt. % of Ni modified with 0.1 wt. of % Pd. After the reduction, microstructure of the catalyst was investigated by using a JEOL JSM-5800LV scanning electron microscope (SEM).

Apparatus for the DRM experiment is presented in Fig. 1.

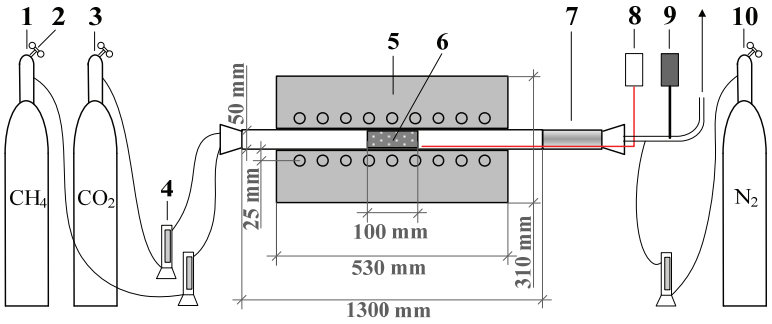

Fig. 1. Apparatus for the dry methane reforming: 1 – high-pressure CH_4 bottle, 2 – reducing valve, 3 - high-pressure CO_2 bottle, 4 - rotameter, 5 - electric resistance furnace, 6 – Ni-Pd/Al_2O_3 catalyst, 7 - water-cooled condenser, 8 - thermo couple, 9 – flue gas analyzer, 10 - high-pressure N_2 bottle

The reforming experiment was performed for 3 h in a quartz reactor at atmospheric pressure, without changing the catalyst. Standing time was 1 h at each of the following temperatures: 873, 973 and 1023 K. After reaching 873 K, inlet stream of CH_4 and CO_2 (CH_4:CO_2 = 1:1) was set to a total flow rate of 6 L h^{-1} (24 L g^{-1} h^{-1}). Flowing N_2 (2.5 L h^{-1}) was used to dilute outlet stream. CO and H_2 concentrations were measured with Testo 340 Flue Gas Analyzer. At the process temperature of 973 K, N_2 flow rate was set to 1.0 L h^{-1} and remained constant until the end of the DRM experiment. To investigate stability of the catalyst, CO and H_2 concentrations were measured at 1023 K at the end of the DRM experiment. Yields of CO and H_2 were determined by using equations 1 and 2, taking into account the dilution with N_2. Based on CO and H_2 yields, the authors reached conclusions on activity, selectivity and stability of the catalyst.

$$Y_{CO}\ \% = \frac{C_{CO\ out}}{C_{CH_4\ in} + C_{CO_2\ in}} \times 100 \quad (1)$$

$$Y_{H_2}\ \% = \frac{C_{H_2\ out}}{2C_{CH_4\ in}} \times 100 \quad (2)$$

Y_X represents yields of the products (vol. %), $C_{X_{in}}$ and $C_{X_{out}}$ denote concentration of gases in the inlet and outlet stream, respectively (mol).

Results and discussion

Morphology of surface of the reduced Ni-Pd/Al_2O_3 catalyst is presented in Fig. 2.

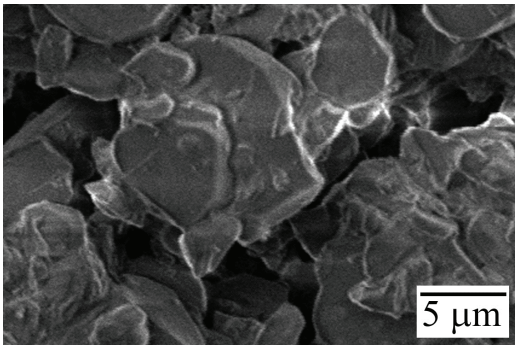

Fig. 2. Micrograph of Ni-Pd/Al_2O_3 reduced at 533 K for 1.5 h, metal content (wt. %): 20 % Ni and 0.1 % Pd

It was noted that, after the reduction at 533 K, relatively smooth metallic film was formed over the whole foam surface (Fig. 2). No undesirable agglomerates were detected and obtained surface morphology could be suitable for catalytic processes. Reduction of chloride precursors for Ni and Pd in flowing H_2 resulted in almost complete transfer to metallic phases. The chlorides reached a reduction degree of 98.2 wt. % [6]. Different than that, our previous study showed that only 20.0 wt. % of oxide precursors for Ni and Pd, obtained by calcination, was reduced at the same reduction conditions. Therefore, the synthesis of active catalytic components from chloride instead of oxide precursors can provide energy savings due to elimination of the calcination step [6]. In addition, after kinetic analysis of NiO and $NiCl_2$ reduction by H_2, the authors concluded that the chloride phase has higher reducibility [8].

Utilization properties of the prepared Ni-Pd/Al_2O_3 catalyst were examined in the DRM process. Results obtained at 873 K are presented in Fig. 3.

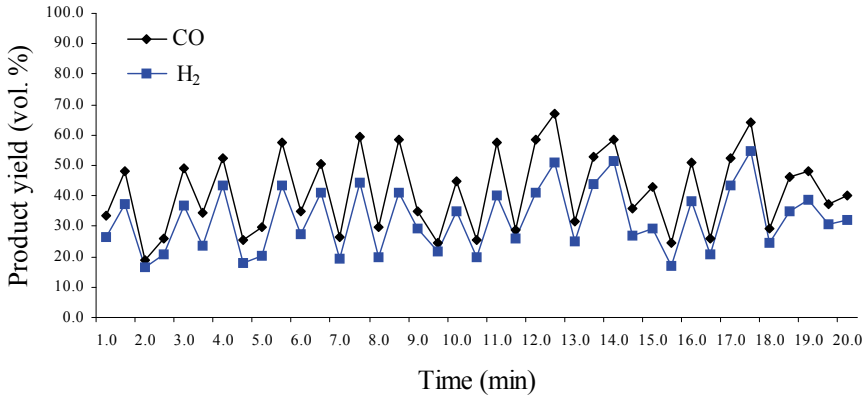

Fig. 3. CO and H_2 yields at 873 K

The results obtained at 873 K varied in a great extent. CO yield ranged from 18.8 and 67.1 %, with mean value of 41.5 %. Values of H_2 yield ranged from 16.6 and 54.8 %, ant the mean value was 32.2 %. Nevertheless, nearly constant H_2/CO molar ratios were achieved during the period of 20 minutes, with the mean value of 0.8. Yields of CO and H_2 during the reforming at 573 K indicated the requirement for higher process temperature.

Results obtained at process temperature of 973 K are presented in Fig. 4.

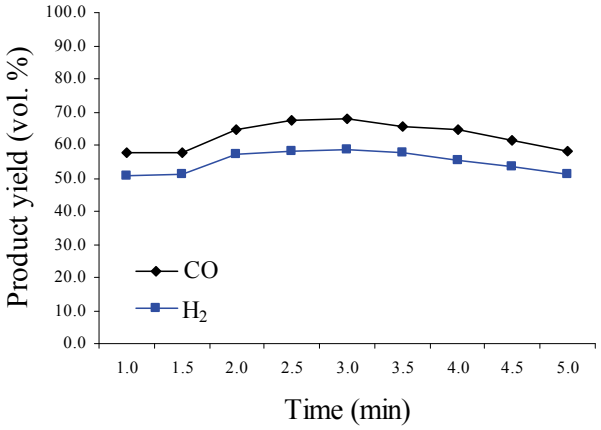

Fig. 4. CO and H_2 yields at 973 K

The reforming results significantly improved at the process temperature of 973 K. Obtained values varied in the following ranges: CO yield – from 57.7 to 68.0 % (mean value: 62.8 %) and H_2 yield – from 50.6 to 58.8 % (mean value: 54.8 %). Those yields were relatively constant. After 1.5 minutes, concentrations of CO and H_2 increased and then slightly declined after 3 minutes. Nearly constant and more favorable molar ratio of H_2 and CO was achieved than at 873 K, with the mean value of 0.9.

The reforming results at process temperature of 1023 K are shown in Fig. 5.

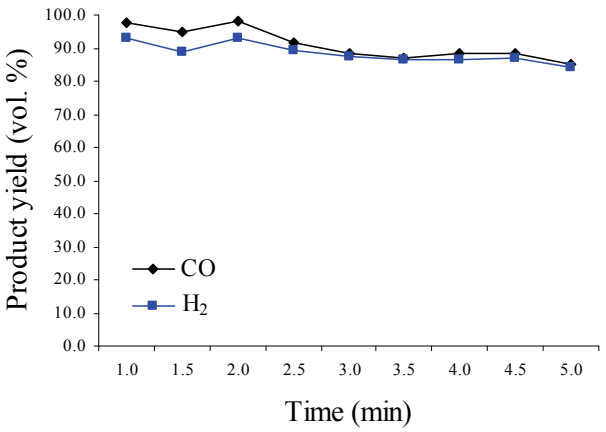

Fig. 5. CO and H_2 yields at 1023 K

Performance of the tested catalyst was the most pronounced at 1023 K, where yields of the main products reached nearly maximal values. CO yielded from 85.0 to 98.1 %, with the mean value of 91.0 %. H_2 yielded between 84.3 and 93.2 %, and the mean value was 88.5 %. A slight decrease of CO and H_2 yields was noted after 2 minutes. After 2.5 minutes, the yields reached close values and remained relatively constant until the end of the investigation. H_2/CO molar ratio had the most favorable mean value of 1.0 and was almost constant during the measuring. It was concluded that the catalyst had good selectivity for CO and H_2. High yields of those gases after 3 h of testing indicate that the catalyst possesses high activity and stability.

Conclusions

Performance of Ni-Pd/Al_2O_3 catalyst supported on α-Al_2O_3 based foam was examined in the dry methane reforming process. The catalyst was synthesized via aerosol route. To obtain Ni and Pd, corresponding chlorides were reduced with H_2 at 533 K, without previous calcination. Relatively smooth metallic film was formed over the foam surface. The reforming experiment lasted for 3 h at different temperatures, without changing the catalyst. Mean results of the reforming at 873 K were the following: CO yield – 41.5 %, H_2 yield – 32.2 % and H_2/CO molar ratio – 0.8. Considerable improvement of the reforming efficiency was achieved at 973 K. Mean values of CO and H_2 yields were 62.8 and 54.8 %, respectively. Mean H_2/CO molar ratio reached 0.9. The most favorable results were achieved at 1023 K, when mean yields of CO and H_2 reached 91.0 % and 88.5 %, respectively. Mean H_2/CO molar ratio was near 1.0. The catalyst was highly active and stable, and had good selectivity for CO and H_2.

Acknowledgements

This work was financially supported by the Ministry of Education, Science and Technological Development of the Republic of Serbia and is a result of projects No. 34033 and No. 34023.

References

[1] J. Ma, N. Sun, X. Zhang, N. Zhao, F. Xiao, W. Wei, Y. Sun, Catal. Today 148 (2009) 221-231.
[2] J. Gao, Z. Hou, H. Lou, X. Zheng, Fuel Cells: Technologies for Fuel Processing, Chapter 7: Dry (CO_2) Reforming, Amsterdam, Netherlands, 2011.
[3] S. Damyanova, B. Pawelec, K. Arishtirova, J. L.G. Fierro, Int. J. Hydrogen Energ. 36 (2011) 10635-10647.
[4] S. Damyanova, B. Pawelec, K. Arishtirova, J. L.G. Fierro, C. Sener, T. Dogu, Appl. Catal. B – Environ. 92 (2009) 250-261.
[5] M. V. Twigg, J. T. Richardson, Chem. Eng. Res. Des. 80 (2002) 183-189.
[6] V. Nikolić, Ž. Kamberović, Z. Anđić, M. Korać, M. Sokić, V. Maksimović, Int. J. Min. Met. Mater. 21 (2014) 806-812.
[7] V. Nikolić, Ž. Kamberović, Z. Anđić, M. Korać, M. Sokić, Materials and Technology 48 (2014) 45-50.
[8] M. Sokić, Ž. Kamberović, V. Nikolić, B. Marković, M. Korać, Z. Anđić, M. Gavrilovski, Sci. World J. (2015) http://dx.doi.org/10.1155/2015/601970

Poster session

COPPER LEACHING FROM CHALCOPYRITE CONCENTRATE IN OXIDATIVE SULPHURIC ACID SOLUTION

Miroslav D. Sokić[1], Branislav R. Marković[1], Vladislav Lj. Matković[1], Željko J. Kamberović[2], Dragana T. Živković[3], Nada D. Štrbac[3], Jovicu N. Stojanović[1]

[1] *Institute for Technology of Nuclear and Other Mineral Raw Material, Belgrade, Serbia,*
[2] *University of Belgrade, Faculty of technology and metallurgy, Belgrade, Serbia*
[3] *University of Belgrade, Technical Faculty at Bor, Serbia*

Abstract

The copper leaching from chalcopyrite concentrate with sulphuric acid solution and hydrogen peroxide as oxidant at standard conditions is reported in this paper. The influence of temperature, time, stirring speed and hydrogen peroxide concentration on the leaching degree of copper were experimentally determined. Chemical analysis and qualitative and quantitative mineralogical analysis were used for the phase fraction determination of the concentrate and leach residue.
Keywords: chalcopyrite concentrate leaching, hydrogen peroxide, sulphuric acid

Introduction

Chalcopyrite is the most important commercial copper sulphide mineral. It usually occurs with other sulphide minerals, such as galena, sphalerite and pyrite in disseminated form and fine-grained structures [1]. These minerals are generally separated from each other by flotation and treated by conventional pyrometallurgical processes, where the main problem is pollution of the environment with sulphur dioxide [2]. Hydrometallurgical methods were developed opposed to the pyrometallurgical routes due to stringent regulations on SO_2 emission.

Chalcopyrite is the most abundant mineral and the most refractory and difficult to leach [3-4]. For that reason, numerous leaching studies have been performed by many researchers using various oxidants in acidic media. Ferric and cupric ions, oxygen, other oxidants and bacteria have been used as oxidative leaching agents of chalcopyrite in sulphate, chloride and nitrate media, under atmospheric or pressure conditions [4-14].

Hydrogen peroxide is a strong oxidizing agent with a standard redox potential of 1.77V in acidic solution, and promotes the leaching potential of sulphuric acid [4-5].

The oxidative effect of hydrogen peroxide in acidic solutions is based on its reduction according to the equation [4]:

$$H_2O_2 + 2H^+ + 2e^- = 2H_2O \quad (1)$$

Hydrogen peroxide can also act as a reducing agent:

$$H_2O_2 = O_2 + 2H^+ + 2e^- \quad (2)$$

It is known that hydrogen peroxide is relatively unstable compound, whose decomposition can be catalysed by Fe^{3+} ions, metal surfaces (Pt, Ag) etc. [5]. The products of decomposition are oxygen and water:

$$2H_2O_2 = O_2 + 2H_2O \quad (3)$$

and this equation is the sum of equations (1) and (2).

Using XRD analysis of the residue after chalcopyrite leaching in a solution containing 0.5 M H_2O_2 and 2M H_2SO_4, at the copper leaching of 11,1%, Antonijević et al. [2] have found the absence of elemental sulphur and indicated that the sulphide sulphur oxidized to sulphate. However, XRD analysis of the residue of the leaching at 5M H_2O_2 and 2M H_2SO_4 during which 55% of the chalcopyrite was dissolved revealed small amounts of elemental sulphur. Accordingly, the dominant leaching reaction is:

$$2CuFeS_2 + 17H_2O_2 + 2H^+ = 2Cu^{2+} + 2Fe^{3+} + SO_4^{2-} + 18H2O \quad (4)$$

and a small part of sulphide sulfur is transformed into elemental form:

$$2CuFeS_2 + 5H_2O_2 + 10H^+ = 2Cu^{2+} + 2Fe^{3+} + S^0 + 10H_2O \quad (5)$$

According to Mahajan et al. [6], chalcopyrite leaching by hydrogen peroxide results in dissolution of copper and iron ions from the chalcopyrite according to equation:

$$CuFeS_2 \rightarrow Cu^{2+} + Fe^{2+} + 2S^0 + 4e^- \quad (6)$$

Antonijević et al. [2] and Adebayo et al. [7] were determined that the dissolution kinetic to follow to shrinking-core model, with surface chemical reaction as the rate-determining step, and activation energy of 60 kJ mol^{-1} and 39 kJ mol^{-1}.

On the other hand, Misra and Fuerstenau [8] established that most of the sulphide sulphur is transformed into elemental forms. Olubambi and Potgieter [9] noticed that the increase in the porous and crystalline nature of the residues with increasing hydrogen peroxide concentration reduced the passive nature of chalcopyrite.

Jiang et al. [10] studied the dissolution kinetics of manganese-silver associated ores by hydrogen peroxide and sulphuric acid, and found that the silver leaching diffusion-controlled.

Agacayak et al. [11] investigated chalcopyrite concentrate leaching in a hydrogen peroxide medium without sulphuric acid. The maximum copper extraction was obtained with the following conditions without stirring: 240 min of leaching time, 3.0M hydrogen peroxide concentration, 40°C leaching temperature and 53-75 μm particle size fraction. It was found that stirring speed has no effect on the leaching.

In this study, the sulphuric acid leaching process of chalcopyrite concentrate from Serbian deposit in the presence of hydrogen peroxide was investigated. Dutrizac [12] observed significant differences ~50% in leaching rates of eleven

chalcopyrite concentrates from different localities under the same leaching conditions.

Experimental

All leaching experiments were carried out in a glass reactor equipped with a teflon stirrer, condenser, thermometer, glass funnel for adding the solid sample and a sampling device. The calculated volumes of H_2SO_4 and H_2O_2 solutions were added to the glass reactor and heated-up to the selected temperature. When the temperature was reached, the solid concentrate was added and the reaction commenced. After selected time intervals, the solution samples were taken for chemical analysis, which was carried out by AAS (Perkin Elmer). The leach residues were filtered, washed with distilled water, and dried. The phase content of complex concentrate and leach residue were determined by reflected light microscopic (Carl Zeiss-Jena, LENAPOL-U).

Temperatures was provided in the range of 25 to 45^{o}C and leaching times of 20 to 240 min. The particle size was -37μm, the stirring speed was 100 rpm, the H_2SO_4 and H_2O_2 concentrations were 1.5 M and 1.0 M, and the phase ratio was 2 g/dm^3.

Results and discussion

The chalcopyrite concentrate, enriched in the „Rudnik" flotation plant (Rudnik-Serbia), with 27.1% of Cu, 25.1% of Fe, 4.2% of Zn and 2.3% of Pb was used in the work.

Qualitative and quantitative mineralogical analyses using light microscopy of the complete sample of chalcopyrite concentrate is shown in Table 1. Chemical analysis of Cu, Zn and Pb were used for quantitative analysis corrections.

Table 1. Mineral composition of chalcopyrite concentrate

Mineral	Mass %
Chalcopyrite	78.247
Sphalerite	6.249
Galena	2.633
Pyrrhotite	1.161
Pyrite	0.099
Arsenopyrite	0.211
Covellite	0.081
Native bismuth	0.031
Limonite	0.118
Gangue	11.170
Total:	100.000

The influence of temperature on the copper extraction, under following conditions: particle size -37μm, stirring speed 100 rpm, 1.5 M H_2SO_4, 0.6 M H_2O_2, and phase ratio 2 g/dm^3, is shown in Figure 1.

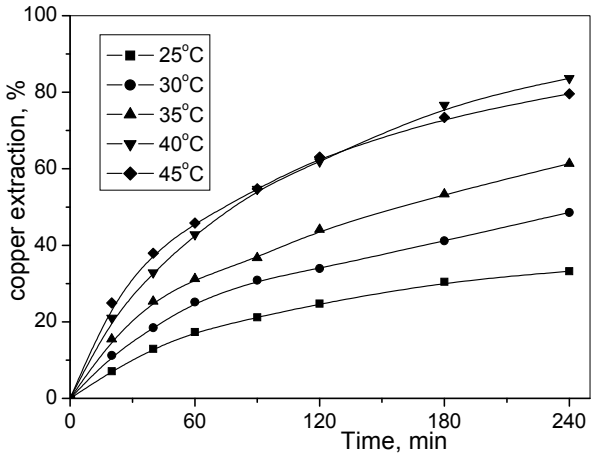

Fig. 1. Effect of temperature on the copper leaching

The temperature has a strong influence on the leaching rate. As expected, copper dissolution increases with increasing the temperature. At 25°C, 33.2% copper was extracted after 240 min, increasing to 83.6% at 40°C. A significant slowing down of the leaching rate with increasing temperature above 40°C was noted. The reason for this retardation is a very rapid decomposition of H_2O_2 at elevated temperatures [13].

The influence of stirring speed on the dissolution of chalcopyrite was investigated at stirring speeds of 100 rpm, 300 rpm and without stirring at 40°C in solutions containing 1.5 M H_2SO_4, 1.0 M H_2O_2, phase ratio 2 g/dm^3, and particle size -37μm (Figure. 2).

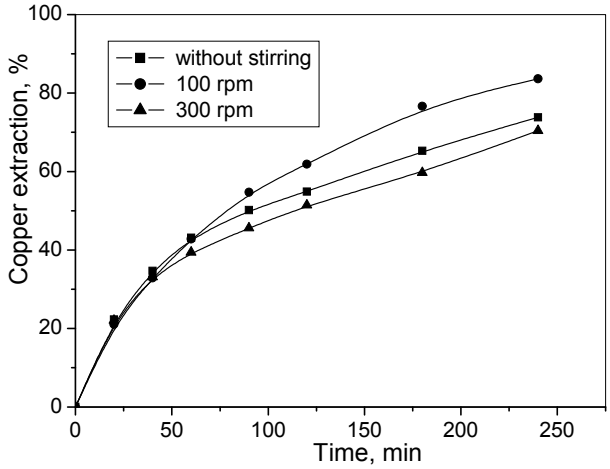

Fig. 2. Effect of stirring speed on copper leaching

The results showed that stirring speed does not significantly influence the rate of chalcopyrite dissolution. The rate of dissolution is maximal at a stirring speed of 100rpm. The same results were obtained during the leaching of chalcopyrite by hydrogen peroxide in the presence of ethylene glycol by Mahajan et al. [6]. An optimum in stirring speed of 100 rpm was observed, where dissolution actually decreasing with higher stirring speed. Antonijević at al., (1997) noticed that the rate of pyrite dissolution increasing as the stirring speed decreases due to better contact between pyrite particles and peroxide.

The influence of H_2O_2 concentration on the degree of copper leaching was investigated in the solutions containing different initial H_2O_2 concentrations (0.2, 0.5, 1.0, and 2.0 M) at 40°C and 100 rpm in solutions containing 1.5 M H_2SO_4, and phase ratio 2 g/dm^3 and particle size -37μm (Figure 3).

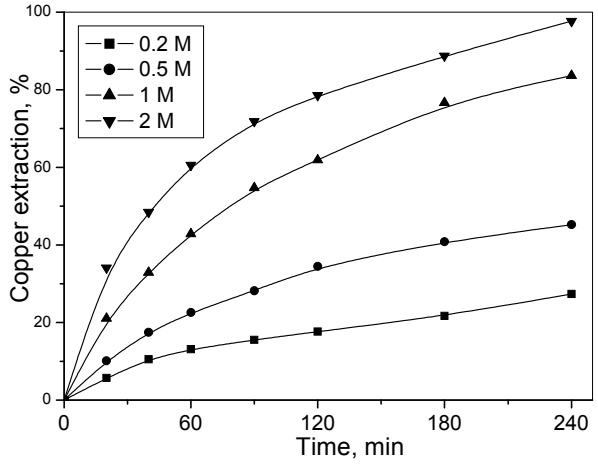

Fig. 3. Effect of H_2O_2 concentration on copper leaching

The increase of hydrogen peroxide concentration in the solution has a major impact on increasing the speed of leaching, because the more peroxide adsorbed on the surface of chalcopyrite. The copper leaching increased from 27% to 97% after 240 min, when the concentration of H_2SO_4 was increased from 0.2 M to 2.0 M.

The leach residue, obtained at 40°C under the following conditions: leaching time 240 min, particle size -37μm, stirring speed 100 rpm, 1.5 M H_2SO_4, 1.0 M H_2O_2, and phase ratio 2 g/dm^3, was chosen for chemical and qualitative and quantitative mineralogical analysis.

The chemical composition of the leach residue presented in Table 2. At the beginning of the leaching process the concentrate quantity was 1,2g. Increase of the total sulphur content is a result of oxidation a part of sulphide sulphur to elemental form during the leaching process. At the same time, a part of sulphide sulphur is oxidized to sulphate during the leaching.

Table 2. Chemical composition of leach residue

Mass (g)	Content (%)				
	Cu	Zn	Fe	Pb	S overall
0,36	21,80	0,142	23,10	2.80	41,34

A qualitative and quantitative mineralogical analysis of the leach residue is shown in Table 3. The major phases identified by mineralogical analyses were chalcopyrite and elemental sulphur, which confirms that the sulphide sulphur is first oxidized to elemental sulphur, which is, then, partially oxidized to sulphate ions [9].

Table 3. Mineral composition of leach residue

Mineral	Mass %
Chalcopyrite	63.002
Sphalerite	0.222
Galena	0.217
Pyrrhotite	6.215
Pyrite	0.099
Anglezite	4.454
Sulphur	18.887
Gangue	6.700
Total:	100.000

Conclusion

The leaching process of chalcopyrite concentrate from the Rudnik polymetallic ore by sulphuric acid and hydrogen peroxide was studied in this paper. Chemical and mineralogical analysis of the concentrate reveals that the sample contains mainly the chalcopyrite with small amount of sphalerite.

The temperature influence on the reaction rate is significant: a temperature increase from 25 to 40^{o}C was accompanied by an increase in leaching degree from 33.2% to 83.6% after 240 min. A significant slowing down of the leaching rate with increasing temperature above 40^{o}C was noted. The dissolution of copper increased with increasing hydrogen peroxide concentrations, and decreased with increasing stirring speed.

A qualitative and quantitative mineralogical analysis of the leach residue confirms formation of elemental sulphur during the leaching process, which then is partially oxidized to sulphate ions.

Acknowledgement

The authors wish to thank the Ministry of Education, Science and Technological Development of the Republic of Serbia for the financial support through the project 34023.

References

[1] P. Ramdohr P.: The Ore Minerals and Their Intergrowths, Pergamon Press in two volumes, Oxford, (1980) 1230.

[2] Antonijević M., Janković Z., Dimitrijević M.: Kinetics of chalcopyrite dissolution by hydrogen peroxide in sulphuric acid, Hydrometallurgy 71 (2004) 329-334.

[3] Vanhanen M.R., Finnish expert report on best available techniques in copper production and by-production of precious metals, The Finnish Environment, Finland, 1999.

[4] Cotton F.A., Wilkinson G., Advanced Inorganic Chemistry,5th ed., Wiley, New York, 1988, 456-458.

[5] Greenwood N., Earnshaw A.: Chemistry of the Elements, Pergamon Press, Oxford, (1984) 736-745.

[6] Mahajan V., Misra M., Zhong K., Fuerstenau M.: Enhanced leaching of copper from chalcopyrite in hydrogen peroxide-glycol system, Minerals Engineering 20 (2007) 670-674.

[7] Adebayo A., Ipinmoroti K., Ajayi O.: Dissolution kinetics of chalcopyrite with hydrogen peroxide in sulphuric acid medium, Chem. Biochem. Eng. Q., 17, 3 (2003) 213-218.

[8] Misra M. and Fuerstenau M.: Chalcopyrite leaching at moderate temperature and ambient pressure in the presence of nanosize silica, Minerals Engineering, 18 (2005) 293-297.

[9] Olubambi P. and Potgieter J.: Investigation on the mechanism of sulfuric avid leaching of chalcopyrite in the presence of hydrogen peroxide, Mineral Procesing & Extractive Metall. Rev., 30 (2009) 327-345.

[10] Jiang T., Yang Y., Zhang B. Huang Z.: Kinetics of silver leaching from manganese-silver associated ores in sulphuric acid solution ni the presence of hydrogen peroxide, Metallurgical and Metarials Transactions B. 33B (2002) 813-816.

[11] T. Agacayak, A. Aras, S. Aydogan, M. Erdemoglu, Leaching of chalcopyrite concentrate in hydrogen peroxide solution, Phisicochemical Problems of Mineral Processing, 50, 2 (2014) 657-666.

[12] Dutrizac, J.: Ferric ion leaching of chalcopyrites from different localities, Metallurgical and Metarials Transactions B, 13B (1982) 303-309.

[13] Dimitrijević M., Antonijević M., Dimitrijević V.: Investigation of the kinetics of pyrite oxidation by hydrogen peroxide in hydrochloric acid solutions, Minerals Engineering 12, 2 (1999) 165-174.

[14] Prasad S. & Pandey B.: Alternative processes for treatment of chalcopyrite – a review, Minerals Engineering, 11 (1998) 763-781.

[15] Sokić M., Marković B., Živković D.: Kinetics of chalcopyrite leaching by sodium nitrate in sulphuric acid, Hydrometallurgy 95 (2009) 273-279.

[16] S.Aydogan, G.Ucar, M.Canbazoglu, Dissolution kinetics of chalcopyrite in acidic potassium dichromate solution, Hydrometallurgy 81 (2006) 45-51.

THERMODYNAMIC AND KINETIC ASPECTS OF COPPER CONCENTRATE ROASTING PROCESS FROM THE ORE DEPOSIT VELIKI KRIVELJ

N. Štrbac[1], M. Ćirković[2], A. Mitovski[1], D. Živković[1], M. Sokić[3], D. Manasijević[1]

[1]*University of Belgrade, Technical Faculty in Bor, Bor, Serbia*
[2]*Institute for Mining and Metallurgy, Bor, Serbia*
[3]*Institute for Technology of Nuclear and Other Raw Materials, Belgrade, Serbia*

Abstract

The paper presents the results of copper concentrate roasting process from the ore deposit Veliki Krivelj (Bor, Serbia). The oxidation process was investigated from thermodynamic and kinetic aspects. Thermodynamic analysis included calculation and drawing the equilibrium composition diagrams of the equilibrium oxidation products, under various molar amounts of the solid and gaseous phase. Characterization of the initial concentrate samples was done by chemical analysis (ICP-AES), XRD, DTA/TG and SEM/EDS analyses. According to DTA/TG results, the mechanism of the oxidation proces was proposed. For the defining the kinetic parameters of the roasting process and activation energy calculation, Borchardt and Daniels method of non-isothermal kinetics was used.
Keywords: roasting, concentrate, equilibrium composition, non-isothermal kinetics

Introduction

Copper based sulfide ores mainly have complex, polymetallic composition. They consist of various metal sulfides and other heavy non-ferrous metals. The most common are ZnS, PbS, nickel (pentlandite), iron (pyrite and pyrrhotite), HgS (cinnabar). In addition, copper ore deposits often include precious metals (gold, silver and platinum), and rare metals such as selenium, tellurium, indium, thallium, etc.

Knowledge of the composition and characteristics of copper concentrates, thermodynamic and kinetic parameters of the oxidation process and the mechanisms of oxidative roasting is an essential prerequisite for efficient management of technological processes in industrial conditions [1-3]. Due to these, physical, chemical, structural and thermal characteristics of copper concentrate from ore body “Veliki Krivelj” near Bor (Serbia), as well as kinetic behaviour of the concentrate components during oxidative roasting in the air atmosphere were discussed in this paper.

Experimental

Experimental investigations were done on concentrate samples in the powder form. Experiments included chemical analysis, done on ICP-AES “Spectro Ciros Vision“. XRD analysis was done on the initial sample on X-ray diffractometer

"Phillips" PW 1710, with a curved graphite monochromator and a scintilation counter on polycrystalline powder samples. Intensity of the X-rays CuKα (λ = 1,54178 Å) was measured at room temperature at 0,02 ° 2θ intervals and 0,5 second, in the range 4 – 65 ° 2θ. X-ray tube was loaded with 40 kV voltage and 30 mA current. DTA/TG analysis was done on thermal analyzer "Netzsch" STA 409 EP on a sample of 100 mg, under heating range 25 – 1000 °C in the air atmosphere, at heating rate 10 °C/min. SEM/EDS structure analysis was done for the initial sample on scanning electron microscope "Tescan" Vega 3LMU, with EDS analyzer „TA Instruments". Surface evaporation of the samples was done with carbon.

Results and discussion

Quantitative chemical analysis (main elements) of the initial concentrate sample is shown in Table 1.

Table 1. Chemical composition of the concentrate sample (main elements)

Element	Cu	Fe	S	Zn	As	SiO_2	Element	Ag	Au
%	21,34	30,16	33,44	0,076	0.003	7,62	g/t	15	1

Chemical composition showed that the initial sample mainly consisted of iron and sulfur with one third and copper with one fifth of total concentrate amount. The other present elements participate with less than 0,1 %. In the concentrate are also present silver and gold.

The X-ray analysis of the inital sample is presented in Figure 1.

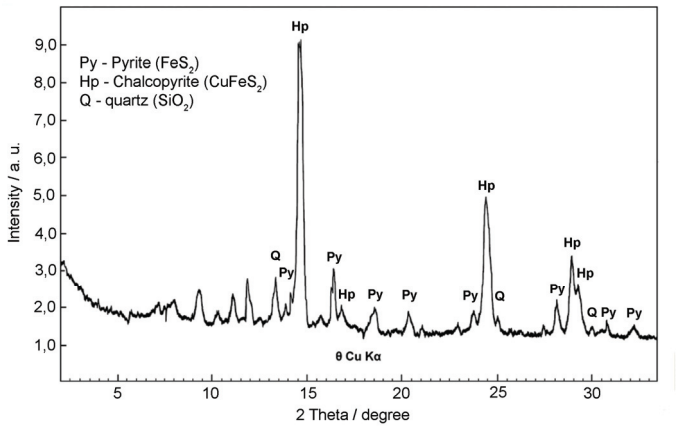

Fig. 1. XRD analysis of the initial concentrate sample

According to the results of chemical and XRD analysis, it can be observed that in the initial sample copper, sulfur and iron were distributed in chalcopyrite and pyrite. The detected gangue mineral was quartz.

Results of DTA/TG analysis are shown in Figure 2.

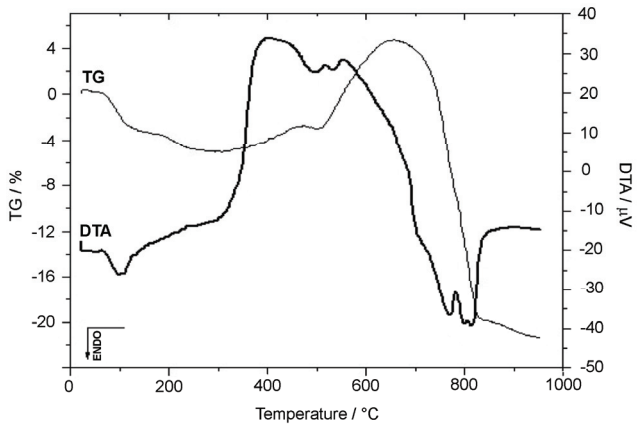

Fig.2. DTA/TG analysis of the inital sample

DTA/TG results showed that in lower temperature range roasting process occures with exothermal effects (between 300 °C and 650 °C) followed by mass increase according to TG curve, which corresponds to pyrite and chalcopyrite oxidation and sulfates and oxysulfates formation. Further temperature increase led to sulfates and oxysulfates decomposition into copper and iron oxides with characteristical endothermal effects. The processes were followed by considerable mass decrease on TG curve at temperatures 750 °C and higher [4-8].

The equilibrium composition diagram was calculated for the molar ratio between gas and charge of 10 : 1. According to chemical analysis, possible condensed phases (oxydes, sulfates, oxysulfates, ferrites and sulfides) were defined for further calculation (Table 2).

Table 2. Possible condensed phases in the system

Oxydes, sulfates, oxysulfates, ferrites	CuO, Cu_2O, $CuO{\cdot}CuSO_4$, $CuO{\cdot}Fe_2O_3$, $Cu_2O{\cdot}Fe_2O_3$, $CuSO_4$, Cu_2SO_4, FeO, Fe_2O_3, Fe_3O_4, $FeSO_4$, $Fe_2(SO_4)_3$, SiO_2, ZnO, $ZnO\cdot2ZnSO_4$, $ZnSO_4$, Al_2O_3, CaO
Sulfides	$CuFeS_2$, Cu_5FeS_4, CuS, Cu_2S, FeS, FeS_2, ZnS

Initial conditions for the calculation of the equilibrium composition diagram were also defined, shown in Table 3. Initial conditions included defining the gas amount and mineralogical composition of the investigated concentrate.

Table 3. Initial conditions for the calculation of the equilibrium composition diagram

Gas amount (kmol)		Concentrate (kg)	Gas : charge (molar ratio)
N_2 (g)	O_2(g)		
6,652 (79%)	1,768 (21%)	100 (56,95 kg $CuFeS_2$, 20,30 kg FeS_2,0,12kg ZnS, 19,65 kg SiO_2, 2,44 kg Al_2O_3, 0,54 kg CaO)	10 : 1

Equilibrium composition diagram for the gas vs. charge molar ratio of 10 : 1 is given in Figure 3.

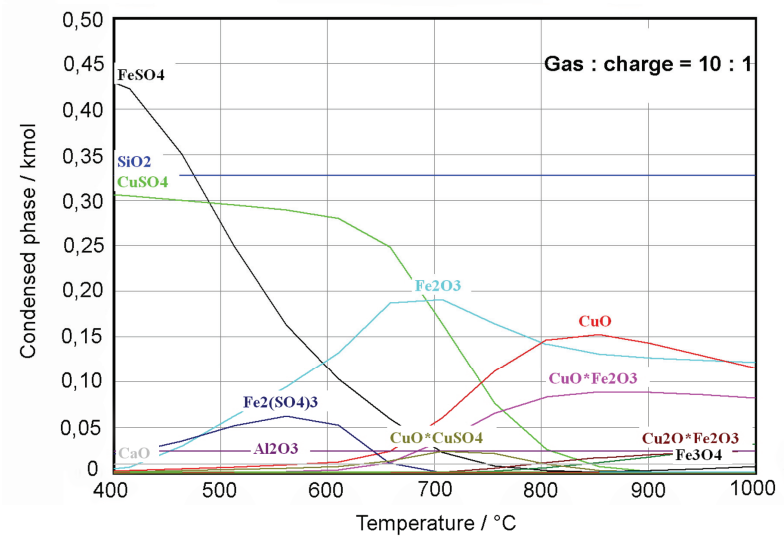

Fig. 3. Equilibrium diagram for calculated molar ratio gas:charge = 10:1

At given initial conditions, calculation showed that there is enough oxygen for the oxidation of present sulphides in the concentrate. It is evident that at lower temperatures roasting upon reaching thermodynamic equilibrium copper is predominantly located in the form of $CuSO_4$. With temperature increase, the content of $CuSO_4$ decreases while the contents of CuO and $CuO{\cdot}Fe_2O_3$ increases. Also, there can be observed minor amount of $CuO{\cdot}CuSO_4$ phase. Upon reaching thermodynamic equilibrium at lower temperatures, iron is found in the form of $FeSO_4$. At higher temperatures content of $FeSO_4$ reduces, so the iron is predominantly found in the form of Fe_2O_3 and copper ferrites, $CuO{\cdot}Fe_2O_3$ and $Cu_2O{\cdot}Fe_2O_3$. Zinc in the calcine at lower temperatures in the equlibrium conditions occurs as $ZnSO_4$, while at higher temperatures is stable in oxide form ZnO.

SEM micrograph of the inital concentrate sample is given in Figure 4. EDS elemental analysis of the site of interest, which was done in three points, is shown in Table 4.

Table 4. EDS results in the marked points in site of interest in Figure 4

	Element / mass %					
Point	Cu	Fe	S	O	Si	Al
1	22,32	21,81	28,40	27,46	0,0	0,0
2	0,3	2,96	2,52	59,78	26,16	8,29
3	33,07	30,08	24,91	11,59	0,36	0,0

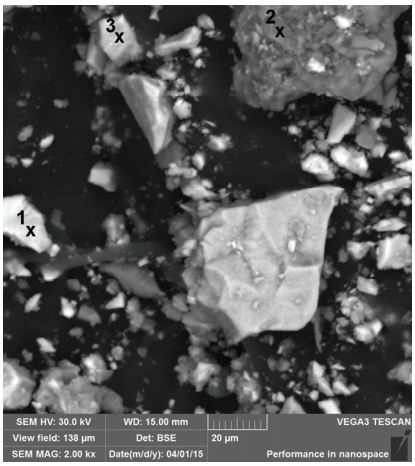

Fig. 4. SEM results of the inital sample site of interest

EDS results showed good agreement with the chemical analysis and XRD results.

Kinetic analysis was done according to Borchardt and Daniels non-isothermal method [9] for peaks which occur at DTA curve in temperature range 350 - 800 °C. The results of calculated activation energies are summarized in Table 5.

Table 5. Activation energies for the roasting process

Peak temperature (°C)	350	515	750	800
Ea (kJ/mole)	123	113	80	125

The activation energies for the roasting process of the investigated concentrate showed that oxidation reactions are temperature depending, occur in the kinetic field and are chemically controlled. The lowest value of activation energy is 80 kJ/mole at 750 °C, which corresponds to copper sulfates and oxysulfates decomposition and CuO formation.

Conclusions

The paper presents the results of copper concentrate roasting process from ore body Veliki Krivelj near Bor (Serbia). The experimental work included chemical, structural, thermodynamic, thermal and kinetic analysis of the inital sample and oxidation products. Chemical and XRD analysis showed that concentrate is chalcopyrite-pyrite type. DTA/TG results showed that oxidation mechanism followed the oxidation reactions with exothermal effects at lower temperatures and endothermal effects at temperatures above 750 °C, which implies that sulfides are unstable in the oxidative conditions, forming sulfates and oxysulfates and their

further decomposition into oxides at high temperatures. Equilibrium composition diagram was done for molar ratio gas : charge = 10 : 1, which showed that, under these conditions, in the system is enough oxygen for the oxidation of all present metal sulfides. SEM/EDS analysis for the initial sample showed good agreement with chemical and XRD results. Kinetic investigation was done by Borchardt and Daniel method of non-isothermal kinetics for temperature peaks in range 350-800 °C. The calculated activation energies showed that all investigated process stages occur in the kinetic field, are chemically controlled and temperature depending.

Acknowledgement

The authors are grateful to the Ministry of Education, Science and Technological Development, Republic of Serbia, for the financial support, as this research is part of Projects TR 34023 and TR 34033.

Type of presentation

Poster

References

[1] Schlesinger M.E., King M.J., Sole K.C., Davenport W.G., Extractive metallurgy of copper, Elsevier, 2011.

[2] Lindkvist G., Holmstrom A,. Advances in Sulfide Smelting, Proceedings of the 1983 International Sulfide Smelting Symposium and the 1983 Extractive and Process Metallurgy Meeting of the Metallurgical Society (ed., by Sohn H Y, George D.B, Zunkel A.D) San Francisco.U.S.A, 1983, 451–472.

[3] Goh S.W., Buckley A.N., Lamb R. N., Copper(II) sulfide, Minerals Engineering, 19(2)(2006), 204–208.

[4] Sargsyan L.E., Hovhannisyan A.M., Investigation of chalcopyrite cuprum concentrate roasting, by thermogravimetric and differential-thermal analysis, Metallurgical and Mining Industry, 2(3)(2010), 225-229.

[5] Bayer G., Wiedemann H.G., Thermal analysis of chalcopyrite roasting reactions, Thermochim. Acta, 198(1992), 303-312.

[6] Sokić M., Ilić I., Živković D., Vučković N., Investigation of mechanism and kinetics of chalcopyrite concentrate oxidation process, Metallurgy, 47(2)(2008), 109-113.

[7] Cocić M.B, Logar M., Cocić S.Lj., Dević S.S., Manasijević D.M., Transformation of chalcopyrite in the roasting process of copper concentrate in fluidized bed reactor, JOM, 63(2011), 55-59.

[8] Štrbac N., Živković D.,Živković Ž., Mihajlović I., Sulfidi-termijska, termodinamička i kinetička analiza, Punta, Niš, 2005.

[9] [Borchardt H.J., Daniels F., J. Am. Ceram. Soc., 41(1957), 73.

MECHANOCHEMICALLY HEAT TREATMENT TO OBTAIN THE MASK PIGMENT

Milan Petrov, Miroslav Sokić, Ljubiša Andrić, Zvonko Gulišija, Vladislav Matković, Jovica Stojanović,

Institute for Technology of Nuclear and Other Mineral Raw Materials, Franchet d'Eperea 86, Belgrade

Abstract

In this study, the possibility of obtaining masking pigment mechanochemically thermal process as energetic participation mechano-chemical treatment in obtaining masking pigment stoichiometric formula $Co_{0,51}Zn_{0,29}Mg_{0,41}Cr_{1,24}Al_{0,24}Ti_{0,31}O_4$. Mechanochemical and heat treated samples of the mixture in order to obtain a complex oxide spinels were experimentally investigated in a series of the experiment, with the changed parameters related to the operation of high energy vibratory mechanoaktivator. Mechanochemical activation of a mixture of (Cr_2O_3, CO-oxide, ZnO, TiO_2, MgO and Al_2O_3), in the vibrating mechanoactivator with rings from 30; 60 and 90 min, and then heat treatment in an electric furnace, when the retention time of 1 hour the sample, provided the spinel structure material which is useful as pigment in the masking military industry.

Keywords: spinel, mechanochemical activation, vibrating mehanoactivator, annealing

Introduction

In the process of pigments is very important homogenization of the starting components before heat treatment process. After the thermal treatment of oxide components are obtained spinels which represent a new composite phase. Spinelli constitute a large group of compounds characteristic crystalline structure ($MgAl_2O_4$) [1]. The most frequent examples of this group are: MAl_2O_4, MCr_2O_4, M_2TiO_4 $M2GeO_4$ and, where M is a divalent cation, such as Mg^{2+}, Zn^{2+}, Ni^{2+}, or Co^{2+}. Therefore, this is a method that is commonly used for the synthesis of spinel thermal reactions in the solid state between solid starting components. It is known that the grain size and the homogeneity of the reaction mixture the most important criteria that may have an impact on the temperature and time of annealing. Mechanochemical (MH) process by treating the starting components of an energy balance of the mixture becomes more favorable, there is an increase of reactivity, which in particular has the effect of reducing the temperature and annealing time required for the synthesis.

Pigments

Inorganic pigments to create colored coatings are used to protect metal, concrete, wood corrosion, abrasion, erosion, etc. [2]. Special inorganic pigments

are pigments for ceramics and glass, which is different from the other pigments high thermal and chemical resistance. According to this classification, pigments are classified into fourteen groups, where each group pigments have the same qualities, which are characteristic date of the crystal lattice (olivine, rutile, zircon, spinel, borates, etc.). The optical properties of the crystalline substances consisting, in the fact, from the selective adsorption of the radiation in the visible spectral region, wherein coloration occurs. Creating color is the result of installing transition metal ions in the basic crystal lattice, without changing its structure. To a substance used as a pigment, it must be insoluble in the solvent in which it is dispersed therein in the preparation of organic coatings, resistant to the agents which it is exposed, and to have a large hiding power.

Mechanochemical treatment

The subject of this paper is to determine the quantitative share of MH treatment in the process of obtaining the mask pigment and the process of obtaining of spinel, stoichiometric formula $Co_{0,51}$ $Zn_{0,29}$ $Mg_{0,41}$ $Cr_{1,24}$ $Al_{0,24}$ $Ti_{0,31}$ O_4, and define the necessary energy in the optimization of the new mechanochemically-thermal (MHT) procedure. During MH treatment reducing the size of the crystals is accompanied by an increase of mechanical energy stored in the material. For pure metals excess enthalpy values measured by differential scanning calorimetry range from 1.0 to 7.4 kJ mol 1 w. from 6 to 43% of the enthalpy of melting of [3].

The reactions in the solid phase,

Frequently used for the initial synthesis of polycrystalline solid materials is a direct reaction in the solid state, starting from a mixture of solid starting components (powders). Macroscopic view of particle size distribution of powders used for the synthesis is shown in Figure 1 Rosin Ramler diagram of grain size.

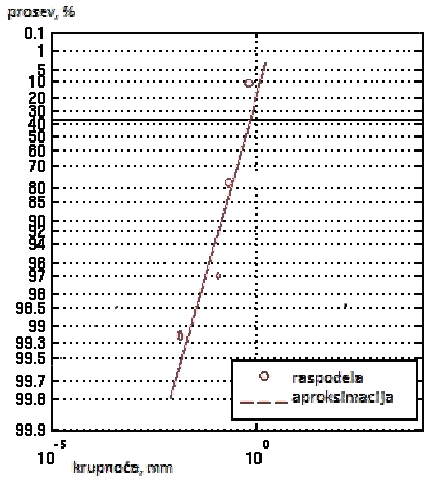

Fig. 1. Diagram Rosin Ramler starting powders

The most important factors that influence on the rate of reaction in the solid phase of the contact area between responders phase, temperature and time of thermal treatment of the reaction mixture, structural factor, the concentration of defects and others. [4]. Surface energy between responders component increases with increasing temperature. The observation that the MH treatment size of crystallites can not be reduced to the atomic level is explained using the model of reinforcement materials by reducing the grain size. Lattice defects educated large plastic deformations, as well as a short-term rise in temperature at the time of impact pellet facilitate diffusion, leading to the formation of amorphous composites by reaction in the solid state amorphization. When mixtures of MH treatment is considered to be crystalline powders, that amorphization takes place by reactions in the solid state in a manner similar to diffusion pairs. Initially MH treatment, sequential splicing and fracturing of powder particles are formed very fine composite powder with a very large interfacial area between the constituent elements. In this way formed by diffusion couples, amorphization reaction takes place by diffusion.

Influence of temperature

The reaction rate in the solid phase temperature impact is significant and can be represented Arrhenius plot (Arrhenius) equation [5]:

$$k = A \cdot e^{\frac{-E_a}{RT}} \quad (1)$$

where is

k - the rate constant,

A - preexponential factor, frequency factor,

E_a - experimental energy of activation.

Materials and methods

The test was performed in vibro mill with rings Humboldt Wedag with the characteristics of batch [6,7,8,9] that allow intensive MH treatment necessary components; Cr_2O_3, CoO-oxide, ZnO, TiO_2, MgO and Al_2O_3. We used three different times MH treatment: t_1 = 30, t_2 = 60 and t_3 = 90 minutes. Component materials before treatment at the mill heated to 363 K, 333 K and 303 K. Only after MH treatment, it was observed that there was a reaction of thermal diffusion, whose visual effect light green color. On the basis of the data presented, we determined the temperature dependence of the speed of MH reactions. After MH treatment heat treatment in an electric furnace at 1100 ° C at the retention time of 1 hour sample obtained material spinel structure throughout the volume that is suitable as a masking pigment in the defense industry. Upon receipt of the spinel structure was carried out by blanking pigment disintegration in the flow mill to obtain a pigment dispersed phase. Characterization of masking pigment samples was performed using the method of X-ray diffraction, electron microscopy and EDX analysis and IR reflection. He also recorded a macroscopic composite powder

paint after MH and MHT treatment and granulometric analysis of the same composite powder.

Results and discussion

At the beginning of the presentation of results should be noted that the reaction of the formation of pigment can happen without the kinetic energy of the mill, which was experimentally confirmed [10]. The thermal process requires consumption of more energy to achieve the necessary quality of the pigment as compared to a method that we applyed MHT in operation. As is well known, most reactions and processes taking place faster, at higher temperatures. The rate constant (k) is expressed by Arrhenius plot equation and depends on the temperature. In several preliminary experiment it was observed that less time mechanochemical treatment corresponds to higher temperatures and vice versa, longer treatment times lower temperatures.

Equation (1), which describes the process of mechanochemical treatment by logarithm ,translate into a linear form:

$$\ln k = \ln A - \frac{E_a}{R \cdot T} \tag{2}$$

By the experimental technique mechanochemical treatment in vibro mill with rings [11] we checked the linearity of equation 2 in the coordinates (lnk = f (1 / T)).

Table 1 - Dependence of the reaction rate constants of MH treatment temperature

Temperature (K)	303	333	363
The rate constant (s^{-1})	0.000185	0.000277	0.000555

To check the linearity of the equation 2, the following were used MH treatment time: 90 min at a temperature of 303 K, 60 minutes at a temperature of 333 K and 30 min at a temperature of 363 K, where it calculates the ratio of the reaction rate is 1/5400 = 0.000185 s s^{-1} at 303 K with a 1/3600 = 0.000277 s^{-1} at 333 K, and 1/1800 s = 0.000555 s^{-1} at 363 K. The results of measuring the rate constant as a function of temperature are shown in Table 1 and graphically in Figure 2, to to observe the primary structure The linear dependence. The coefficient experimentally obtained the right direction is EA / R, respectively

Ea = slope * R * = 1992.7* 8.314 = 16567.3 J / mol

In the present budget we determined the activation energy of the vibrating mill and Ea is 16.5 kJ mol^{-1}. On a semi-logarithmic plots are given a linear equation in which the value of the free member represents lnA. Preexponential factor adjusted equation has a value of A = 0.125 s^{-1}. Mechanochemical treatment of any raw material in the plate mill causes a temperature increase of about 65 ° C.

Increment temperature of 65 ° C triples the speed of the reaction (1.64 + 1.78 = 3.42), but it is not enough that the activation energy causes the formation of spinel. Quotients rate coefficients at MH treatment indicate how many times it increases the reaction rate for a given temperature difference (ΔT), as shown in Chart of Accounts.

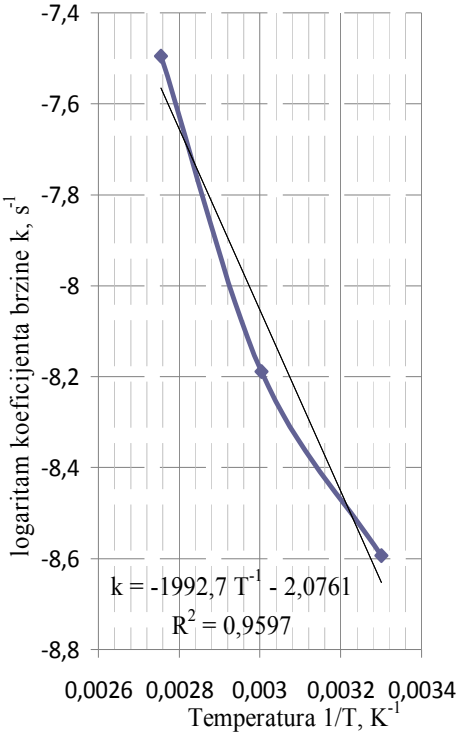

Figure 2 - Diagram of dependence of the rate constant MH reaction and the temperature

$$\frac{k(90^0C)}{k(60^0C)}=\frac{e^{-5,49}}{e^{-5,98}}=\frac{0,0041}{0,0025}=1,64 \quad \text{And} \quad \frac{k\left(60^0C\right)}{k\left(30^0C\right)}=\frac{e^{-5,98}}{e^{-6,58}}=\frac{0,0025}{0,0014}=1,78$$

$$\frac{E_A}{R\cdot T}=\frac{16567,3}{8,314\cdot 363}=5,49 \text{ And } \frac{E_A}{R\cdot T}=\frac{16567,3}{8,314\cdot 333}=5,98 \quad \frac{E_A}{R\cdot T}=\frac{16567,3}{8,314\cdot 303}=6,58$$

Energy required for the formation of spinel can be calculated by calculating the change in energy that occurs when molecules emitted phonon in the visible region of λ = 540 nm, a wavelength of green. Using equation

$$E_{vise}-E_{nize}=h\cdot\nu \tag{3}$$

where h - Planck's constant and amounts to 6,626 10^{-34} Js, and interaction with the wavelength of the microwave frequencies shown by equation

$$\nu = \frac{c}{\lambda} \tag{4}$$

where is the velocity of light c = 2.998 108 ms^{-1}
receives the requested change of energy:

$$E_{vise} - E_{nize} = h \cdot \nu = 6{,}626 \cdot 10^{-34} \cdot 5{,}56 \cdot 10^{14} = 3{,}68 \cdot 10^{-19} J$$

If the energy obtained expressions per mole, molar energy is obtained:

$$\Delta E = 6{,}022 \cdot 10^{23} mol^{-1} 3{,}68 \cdot 10^{-19} J = 221853{,}85 \frac{J}{mol}$$

MHT treatment of inorganic materials is the energy contribution of chemical and physico-chemical changes of matter for the formation of spinel. MH treatment occurs under the influence of mechanical energy [12]. a measure of the activation state of thermal (T) procedure is equal to the difference of the free enthalpy MHT activated and transitional MH-activated materials [13].

$$A_k = \Delta H = H^* - H \tag{5}$$

Where

H - is the free enthalpy of transition MH-activated materials

H^* - free enthalpy MHT activated materials

$$A_k = 221853{,}85 - 16567{,}3 \approx 205286 \frac{J}{mol} \tag{6}$$

Reducing the heat needed for the formation of spinel phase in the process of annealing component is due to the activation state of the resulting MH treatment. In the process of mechanochemical activation of solid inorganic materials with crystalline structure occurring materials with thermodynamic and structurally unstable arrangement of the elements of the crystal lattice, which in comparison with an ideal or a little disturbed crystalline state have increased the free enthalpy and increased chemical reactivity. Activated state inorganic material occurs as a consequence of the increase of surface thermal diffusion and a very high concentration of dislocations.

MH treatment for these reasons that cause the formation of an amorphous phase [14,15,16,17]. Based on these data we calculate the activation energy of the impact of temperature and time on the degree of amorphization powder which is shown in Figure 3. Quotients rate coefficients indicate the degree of amorphization. The highest intensity MH-activated component has a peak Cr (Figure 3a) and is 180 arb units, corresponding to MH treatment time of 30 min. The following Cr peak intensity (Figure 3b) has 154 units and arb corresponds to the time MH treatment of 60 min. At the end of the peak intensity of Cr (Figure 3c) has 120 units and arb corresponds MH treatment time of 90 min. Ratio 1.78 indicates that the peak in Figure 3b by 22% lower than the same peaks as shown on Figure 3a.

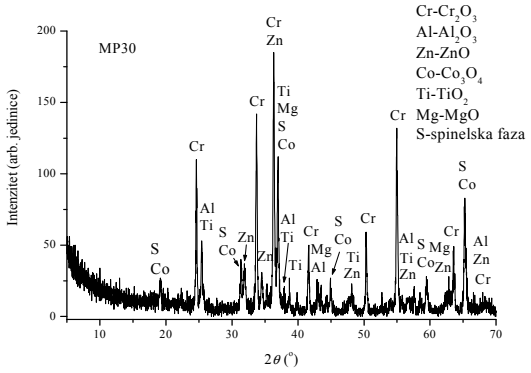

a)

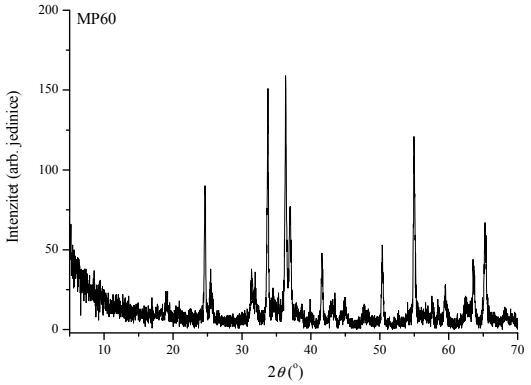

b)

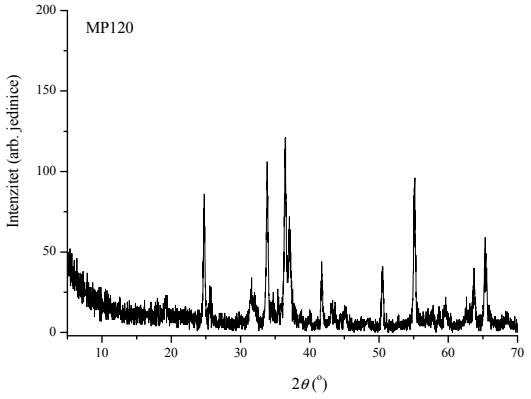

c)

Fig. 3. X-ray diffraction patterns of the powder after mechanohemistry treatments: a) 30 min, b) 60 min, c) 90min

We also see that the peak in Figure 3c corresponds to the quotient of 1.64 because it is 12% lower than the peak in Figure 3b. A total of 34% (0.34 * 180 = 61 and 180-61 = 119) peak in Figure 3c the peak is less than in figure 3a. Other peaks follow this trend. XRD was found to be present the next phase of Cr_2O_3, Al_2O_3, ZnO, spinel phase, Co_3O_4, TiO_2, MgO. The most significant are present Cr_2O_3, Al_2O_3, Co_3O_4, ZnO, while TiO_2 in the anatase form and MgO are less frequent. Co_3O_4 spinel belongs to the group. They are very different views on the process of formation of the amorphous phase depending on the temperature at which performs MH treatment. Amorphization during mixing involves the formation of micro-diffusion pairs of particles that interact powders by solid-state amorphization reaction. Accordingly, with the increase of the milling temperature, an increase of the kinetics amorfizacionog process [18, 19]. Diffraction patterns of samples MP60 and MP90 (Figure 3b and 3c) have the same phase or the intensity of peaks decreased in the same amount, which confirms that there has been amorphization powder. Since the content of the same phase to the thermal treatment in order to obtain the spinel powders were selected that were treated 30 and 60 minutes. After thermal treatment of the sample MP30 at 1100 oC and 1180 oC and sample MP60 at 1100 oC, by X-ray diffraction in all three samples analyzed, the presence of only a spinel phase.

Powder diffractogram of MP30 after annealing at 1100 ° C is shown in Figure 4.

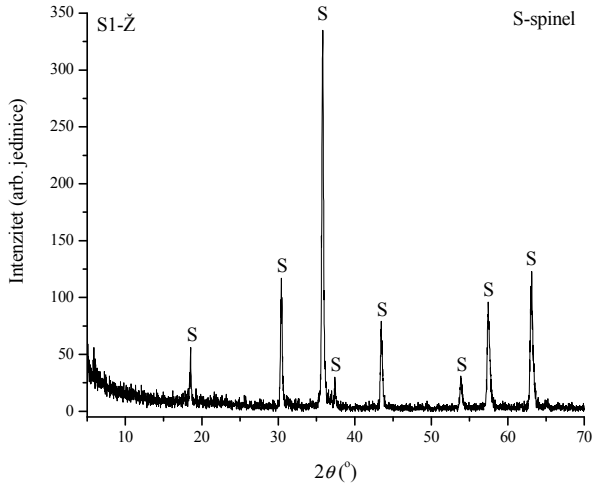

Fig. 4. The pattern of powder MP30 after annealing

In order to study particle shape and size pigments after annealing was analyzed by Scanning Electron Microscope with detector type SE (Secondary Electron).

Figure 5 shows the appearance of powder MP30 after annealing, and Figure 6 after annealing and disintegration of one minute in turbopleks mill.

In Figure 5 it is evident the presence of large agglomerates, so it was necessary after preheating, disintegration of the particles. After the disintegration

was performed dispersion of the powder and the presence of agglomerated particles is minimized (Figure 6). EDX quantitative analysis in clause served to establish the relationship of chemical elements in a six component spinel.

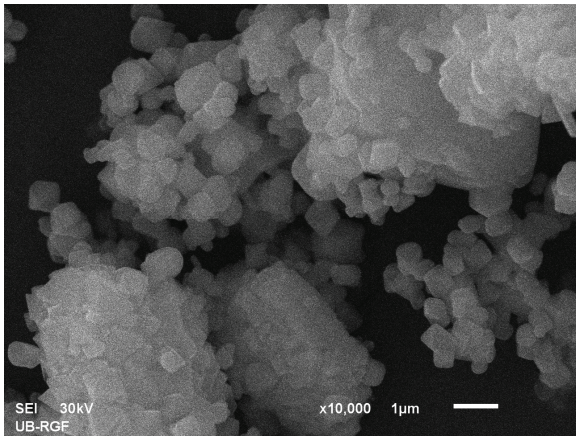

Fig. 5. SEM powder MP30 after annealing

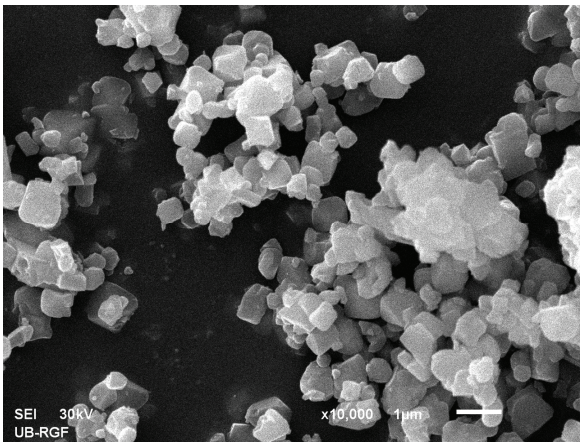

Fig. 6. SEM powder MP30 after annealing and disintegration

Figure 9 shows the EDX spectrum of the powder MP30 after annealing at 1100 ° C.

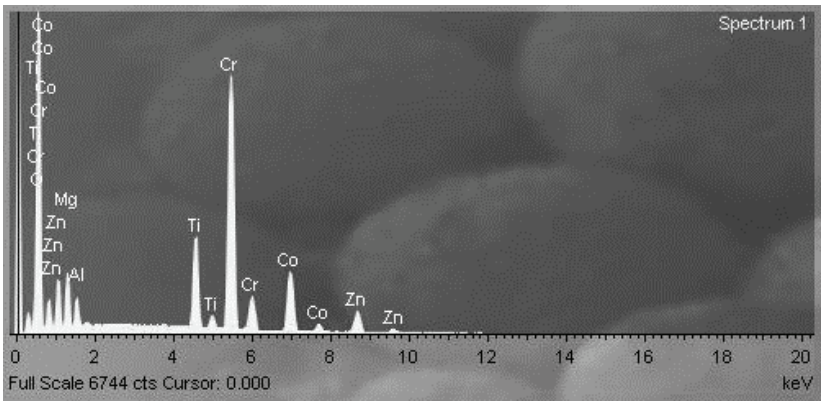

Fig. 7. EDX spectrum of the powder after MP30 annealing and disintegration

Table 2. EDX analysis of powder MP30 after annealing and disintegration

About Element	O	Mg	Al	Ti	Cr	Co	Zn	Total
Content, wt. %	53.13	5.37	1.52	6.91	23.21	7.14	2.74	100.00

Table 2 shows the results of quantitative EDX analysis. It is observed that the ratio of the O and Mg in accordance with the formula for spinel, which was confirmed by Ro analysis.

In order to determine the characteristics of the pigment in terms of masking of reflection, the samples were examined for the infrared Spectrometer and the results are shown in Table 3.

Table 3. Comparative results of infrared reflectance samples tested masking pigment

Wavelength (nm)	650	675	700	750	800	1000
Request R (%)	0-15	0-15	0-40	30-53	40-65	40-65
MP30 annealed at 1100 ° C, R (%)	9,80	9,33	12,06	49,78	57,88	61,10
MP30 annealed at 1180 ° C, R (%)	9,81	9,31	12,00	48,20	56,91	62,28
MP60 annealed at 1100 ° C, R (%)	9,77	9,36	12,27	43,60	50,91	61,09

Conclusion

Mechanochemical process can be performed by mechanoaktivator, graduating working body of a chemical potentials to another. After activation mixture of oxides in the vibrating mill

- Do not come to the appearance of the diffraction maxima new phase;

- diffraction peaks oxide in activated compositions are wider than the diffraction peaks of pure oxides which indicates the partial destruction of the crystal structure (the appearance of amorphization);
- Activation time no visible impact than has its optimum value.

In order to obtain the mask certain characteristics of the pigment was applied mechanochemical treatment in order to establish optimal conditions for sintering of multicomponent oxide systems. Dependence is defined Arrhenius plot equation (1) is derived from the Boltzmann distribution at energies where the exponential factor indicates the part of the molecule that has enough free energy to achieve the reaction. From the results, it can be seen that it is necessary when applying masking pigment include three technological operations.

- Mechanochemical treatment components for reasons of good homogenization
- Annealing homogenized powder
- Disintegration after annealing

Mechanochemical activation mixture Cr_2O_3, CO-oxide, ZnO, TiO_2, MgO and Al_2O_3 appropriate stoichiometric ratio in the vibrating mehanoaktivatoru with rings 30; 60 and 90 min, and then heat treatment in an electric oven at 1100oC, the retention time of the sample of 1 h, the material receives a spinel structure that is suitable as camouflage pigment in the defense industry.

References

[1] J.Lemić, thermal mechanochemical process of obtaining šestkomponentnog spinel (Cr2O3, TiO2, CoO, ZnO, Al2O3 and MgO), Master's thesis, TMF Belgrade 2,001th

[2] L. Pomenić, Protection Material, TFRDepartment of Materials Department of the structure and properties of materials korozijahttps: //www.pfst.hr/ old/data/materijali/skripta (zasmtr) .pdf

[3] M. Zduić, structure and characteristics of thermal mechanochemically treated metal powders, PhD Thesis, TMF Belgrade in 1996.

[4] S. Milosevic, M. T. Čanović, M. Petrov, M. Djuričić, R. Dimitrijevic, B. Zivanovic: Amorphization of aluminosilicate Minerals during Micronization Process. American Ceramic Bulletin, 71 (5), p. 771-775 (1992).

[5] PWAtkins, MJClugston, Principles of Physical Chemistry, London: Pitman, in 1982.

[6] M. Petrov, Lj. Andric, Ž. Sekulic, Energy Conversion occuring in Mineral Grains Mixture During Mechanical Activation, 10th European Symposium on COMMINUTION, 2-5 September, 2002, Heidelberg, Germany, www. COMMINUTION 2002.de. Editor: Dr. D. Redeker, D-Walsrode (Chairman), Publisher: VDI-GVC Society of Chemical and Process Engineering, p. P 07th

[7] M. Petrov, Lj. Andric, Ž. Sekulic Thermo kinetics of Mineral Powder Coating, 10th European Symposium on COMMINUTION, 2-5September, 2002nd Heidelberg, Germany www. COMMINUTION 2002.de. Editor: Dr. D. Redeker, D-Walsrode (Chairman), Publisher: VDI-GVC Society of Chemical and Process Engineering, p. B 2.5.

[8] M.PETROV, S.Milošević, The Change of Enthalpy During Mechanical

Activation of Ionic Crystals, Science of. Suntering Vol.29 No. 3, pp 163-170. (1997)
[9] M.PETROV, S.Milošević, Physical properties of mechanically activated grains, Science and Technology of Sintering, p.193-198., 1999 Advanced Science and Technology of Sintering 1999, pp 193-198.
[10] G.Heinicke, Tribochemistry Munich, Carl Hanser Verlag, 19854
[11] V.V.Boldyrev, Ann.Chim. Fr., 6 (1981) 359
[12] VVBoldyrev, Jornal de Chimie Physique, 83 (1986) 821st
[13] T.E.Fisher, Ann.Rev.Mater.Sci., 18 (1988) 303
[14] S.Milošević, Mechanochemical processes in materials science, CMS, Belgrade, in 1992.
[15] M. Kizilyalli, J. Corish, R. Metselaar, Definitions Of Terms For Diffusion In The Solid State, Pure Appl. Chem. Vol. 71, No. 7, pp. 1307-1325, 1999.Printed in Great Britain. © 1999 IUPAC.
[16] EAOlevsky, L.Froyen, Impact of Thermal Diffusion on Densification During SPS, Journal of the American Ceramic Society Special Issue: Ceramic Processing Science, Volume 92, Issue Supplement s1, pages S122-S132, January, 2009.
[17] NNObradović, Influence of additives on the sintering of ZnO-TiO2 accordance synthesis triad structure properties doctoral dissertation, Faculty of Physical Chemistry, Belgrade 2007.
[18] Kimura, H., Kimura, M., Solid State Amorphization of NiTi by Reaction Ball Milling. In Solid State Powder Processing, Clauer, A. H .; De Bardadillo, J. J., Eds. TMS-AIME Warrendale, PA, 1990; pp 365-377.
[19] Lee, CH, Mori, M., Fukunaga, T. Mizutani, U. Effect of ambient temperature on the MA and MG processes in nickel-zirconium alloy system. Japanese Journal of Applied Physics, Part 1: Regular Papers, Short Notes & Review Papers 1990, 29, (3), 540-544.

COMPARATIVE KINETICS INVESTIGATION OF THE TERNARY SYSTEM Fe_2O_3- MnO -V_2O_5, USING WASTE PRODUCT

R. Paunova, D. Grigorova, R. Alexandrova

University of Chemical Technology and Metallurgy,
Department of Ferrous Metallurgy and Metal Foundry, 8 Kl. Ohridsky Blvd.,
e-mail: rossi@uctm.edu; e-mail: d.dimitrova@uctm.edu

Abstract

The kinetics of non-isothermal heating of the ternary system Fe_2O_3 - MnO - V_2O_5 has been investigated. Pure oxides included in the system have been used on the one hand and on the other hand, waste vanadium catalyst (containing ~4.12% V_2O_5) and manganese concentrate containing ~44.56% MnO.

Two mixtures have been prepared. The samples were characterized by DTA and X-ray diffraction analysis (XRD). From DTA and TG curves of the resulting thermograms, the average rate of the processes, rate constant and the activation energy have been defined. (Ea) for mix 1 at temperature range up to 800K is Ea_1 = 7.876kJ/mol and up to 1493K Ea_1 = 16.507kJ/mol. For mix 2 the activation energy at temperature range up to 900K is Ea_1 = 5,604kJ/mol and up to 1493K Ea_1 = 10.119kJ/mol. It has been found that the processes in the ternary system take place in an external diffusion area.

Keywords: kinetics, process rate, activation energy, DTA,

Introduction

Kinetics of processes in the ternary system Fe_2O_3-V_2O_5-MnO is especially important. It is necessary to know in which range the phase transformation processes take place and which parameters should be changed in order to intensify the processes in this system.

The obtained DTA, DSC and TG curves have been used to define activation energy - the main kinetic characteristic. In the papers [1,2] DTA and TG curves are given in order to identify the first-order reaction rate, and in paper [3] for the kinetics of the oxidation processes in the system Zn-Fe-S-O and for calculation of activation energy value.

Thermogravimetric analysis (TGA) of magnetite (Fe_3O_4) oxidation to Hematite (Fe_2O_3) was conducted at temperatures ranging from 750 to 900^oC. The initial oxidation, which happened very quickly, was described using nucleation and growth processes with a low activation energy of about 4.21±0.45kJ/mol. As the reaction developed within the surface, oxygen transported through the product layer and it became the rate controlling step with activation energy of 53.58 ± 3.56 kJ/mol [4].

The kinetics and reaction mechanism of transformation of the goethite to hematite are based upon the results from thermogravimetric analyzer [5].These data helped obtain the activation energy Ea = 169±8 kJ/mol (for an ore mineral)

and Ea = 154±15 kJ/mol (for a recent sedimentary goethite). M.Cornell and U. Schwertmann [6] determined the activation energy of Fe_2O_3 Ea = 47-50 kJ/mol. Thermogravimetric analysis carried out in the temperature range 260-500^oC in the presence of wet air was used to calculate the activation energy of the iron oxide oxidation for which was obtained the value of Ea = 151 ± 30 kJ / mol [7]. This is similar to the obtained by the authors [8.9] - Ea = 134 kJ / mol and Ea = 149 kJ / mol respectively.

During decomposition of NO over Mn_2O_3 and Mn_3O_4 at 773K, Mn_2O_3 has activation energy 46kJ /mol (11 kcal / mol) and Mn_3O_4 - 63kJ / mol (15 kcal / mol) [10]. TG, DSC and XRD curves are used to explain the mechanism of obtaining hausmanite in the thermal decomposition of manganese sulphate [11]. The apparent activation energy of dehydration at temperature range 200-400^oC is 117.11 kJ / mol, and for the decomposition of $MnSO_4$ to Mn_3O_4 in the temperature range 750-1050^oC its value is 226.44kJ / mol. With TG and DSC curves, the authors received the same results and at non-isothermal $MnSO_4$.heating.

Kinetics of cubic Mn_2O_3 was described by reaction of the first order and its activation energy was 61.2 kJ / mol [12].

In paper [13], the prepared and used as a catalyst $MnFe_2O_4$ had apparent activation energy 31.7 kJ / mol.

The oxidation kinetics of FeV_2O_4 was studied using the methods of analysis for isothermal and non-isothermal conditions in the temperature range 200-580^oC. It has been found [14] that the kinetics can be described from the point of view of three different overlapping processes. The first process was the oxidation of a spinel solid solution and it was described by the equation of the first order with activation energy Ea = 61 kJ / mol (for temperature range 180-380^oC). The second process was the oxidation of solid solution in T≈ 360^oC and was described by the diffusion mechanism of activation energy Ea = 240 kJ / mol. The third stage involved the oxidation of residual spinel and was described again with equation of first order with activation energy Ea = 345kJ / mol in T≈ 580^oC.

The purpose of these studies is to identify some kinetic characteristics (activation energy, rate constant and rate of the processes), taking place in the ternary system Fe_2O_3 - MnO - V_2O_5, and to compare results between synthetic mixture of pure oxides Mix 1 and Mix 2 containing manganese concentrate, waste vanadium catalyst and Fe_2O_3.

Experimental and discussion

Materials and apparatus

Manganese concentrate

The manganese deposit “Obrochiste” is located in Varna manganese-ore region and represents an area including a large ore formation not only in this region, but across the country. The content of Mn is – 28.47%. The chemical composition of the manganese concentrate is shown in Table 1.

Table 1. Chemical compositions of manganese concentrate, (mass, %).

MnO	CO_2	FeS_2	Fe_2O_3	P_2O_5	SiO_2	MgO	CaO	Al_2O_3	K_2O+Na_2O
44,56	19,33	2,25	1,79	0,31	12,4	2,00	3,90	2,10	1,15

Waste vanadium catalyst.

Vanadium catalyst is used for the sulphur acid production. It is deposited as waste product after its deactivation. Annually between 500 and 1000 tones vanadium catalyst are liberated from sulfur acid production and in the same time it contains significant quantity of deficit vanadium. The toxicity of the vanadium causes certain environmental problems which is an additional consideration to look for ways to utilize this valuable waste product. The chemical composition of waste vanadium catalyst is shown in Table 2.

Table 2. Chemical composition of the waste vanadium catalyst,(mass %).

V_2O_5	Fe_2O_3	SiO_2	K_2O	Na_2O	Al_2O_3	SO_3
4,12	3,4	57,12	6,71	3,93	0,82	23,88

In carrying out the experiments, waste vanadium catalyst, manganese concentrate as well as chemically pure oxides of Fe2O3, MnO (MnO_2), V_2O_5 and SiO_2 were used as starting materilas. The mixtures with the pure oxides were calculated and prepared in accordance with the percentage in the waste material. Two types of mixtures were prepared for investigation synthetic mixture of pure oxides Mix 1 and Mix 2 containing manganese concentrate, waste vanadium catalyst and Fe_2O_3.

Apparatus.

Thermogravimetric apparatus STA PT1600 was used with following parameters: temperature range of heating from -150 to 1750^{o}C; heating rate from 0.1 to 100 ° C / min; electronic scale; resolution 0.5 μg; ± 1% accuracy.

The maximum mass of the tested samples is as follows: Mix. 1 - 64,5 mg and Mix 2 - 64,5 mg. The heating rate is 10 ° C / min. The received derivatograms show differential temperature change and mass change.

Experimental data and discussion

DTA and TG curves of two mixtures show that when heated, the processes evolve in three stages.

For a mix 1: I stage- 453 - 783K; II stage - 783 - 973K and III stage- 1053 – 1423 K. In each stage, one endothermic peak associated with retention and reducing the sample mass was registered. The first interval is associated with the dissociation of MnO_2 to Mn_2O_3, the second one - in the temperature range 783 - 973K, a solid solution between Fe_2O_3 and Mn_2O_3 from peritektical type is formed, which decomposes at ~ 1203K, and the third one, partial dissociation of Mn_2O_3 to Mn_3O_4 takes place. XRD analysis of the products showed the presence mainly of

rhombic hematite (Fe_2O_3), cubic Mn_2O_3, tetragonal hausmanite (Mn_3O_4) and cristalobalite (SiO_2).

For a mix 2: I Stage - 463 - 733K; II - 733 - 1033 and -1033 III - 1423K. As in mix 1 in each stage, an endothermic peak associated with retention and reducing the mass of the sample was registered. The first two stages are associated with the behavior of the oxides in the waste vanadium catalyst and formation of FeV_2O_4 or FeV_2O_6, and also with the formation of a solid solution of Fe_2O_3 and Mn_2O_3 from peritektical type. The third stage involves the formation of a new phase Jacobsite. XRD analysis of the product showed the presence of Jacobsite (Mn_6Fe_4) ($Mn_4Fe_{1.6}$) O_4, vanadium oxide (V_3O_4), coulsonite (Fe_2VO_4 or Fe_2O_3.VO), hematite Fe_2O_3 and α quartz.

Temperature dependence and mass loss of the studied mixtures are shown in Fig. 1 and Fig. 2. The results of mass loss indicate that up to 1000 K synthetic mixture and mix 2 containing waste vanadium catalyst have similar changes. The losses at this temperature reach up to 15%. That is a result from dehydration processes (evaporation of dampness and oxides dissociation), which is accompanied by endothermic effects. In comparison with the synthetic mixture, mass losses of the second one are significantly higher at temperatures above 1100 K. In sample 2, mass loss of 25.2% was registered at temperature 1493 K, which is the result of impurities in the vanadium catalyst and manganese concentrate (mainly related to the sulfur in the sulphides and sulphites).

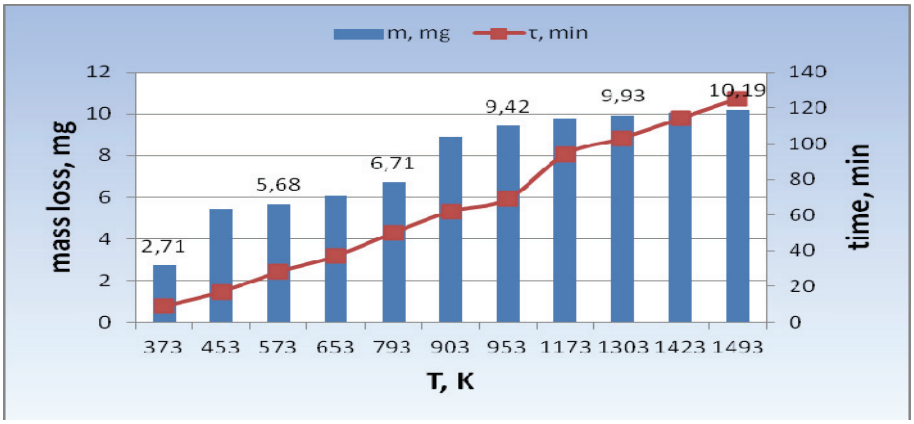

Fig.1. Dependence of mass loss from temperature and time of synthetic mix. 1

Based on the results of the obtained derivatograms, the rate constant, activation energy and process rate were determined.

To this end, the dependence lgm - 2lgT = f (1 / T) was proposed, shown in Fig. 3 and Fig. 4. Using equation (1) the apparent activation energy was calculated. [15]

$$E = 8.31 \times 2.3 \times 10^{-3} \frac{y_1 - y_2}{x_1 - x_2}, \text{ kJ/mol} \qquad (1)$$

Comparative chart of apparent activation energy values for two mixtures is shown in Fig. 5. The heating process of the test mixtures took place in the diffusion area in the whole temperature range.

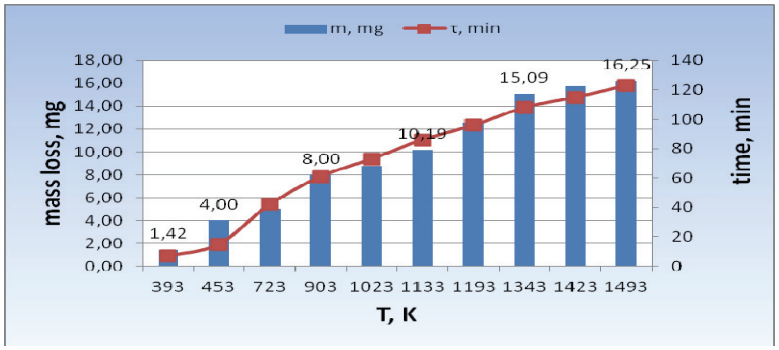

Fig.2. Dependence of mass loss from temperature and time of mix. 2.

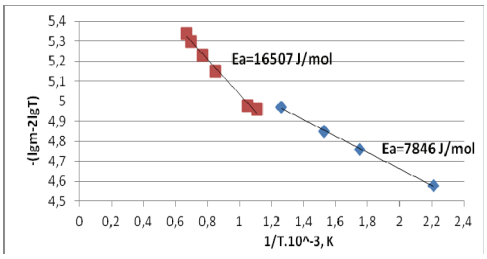

Fig. 3. Dependence lgm - 2lgT = f (1/T) of synthetic mix. 1.

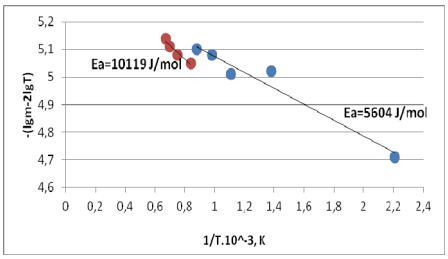

Fig. 4. Dependence lgm - 2lgT = f (1/T) of mix. 2.

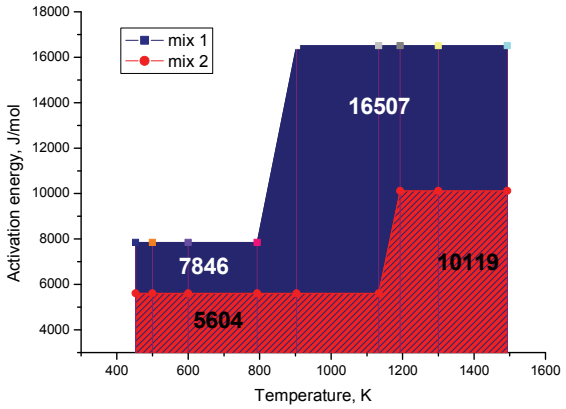

Fig.5. Comparison diagram of the activation energy changing at non-isothermal heating for mix 1 and mix 2.

The low values of the activation energy in temperature range up to ~ 800 K are due to the processes of nucleation and growth of new phases, occurring on the surface due to the dissociation processes. The obtained apparent activation energies at temperatures over 900 K are lower compared with the values of pure oxides obtained from various authors [3, 4, 6, 10, 12, 14]. Lower values of activation energy in the studied ternary system are due to formation of new phases (FeV_2O_4, FeV_2O_6, (Mn_6Fe_4) $(Mn_4Fe_{1.6})$ O_4).

Rate constant equations are derived based on experimental data.

For mixture 1:

$\lg k_1 = \frac{409}{T} - 5.48$; $R^2 = 0.999$; (453K – 793K)

$\lg k_2 = \frac{873}{T} - 5.91$; $R^2 = 0.9912$; (903K – 1493K)

For mixture 2*:*

$\lg k_1 = \frac{288}{T} - 5.36$; $R^2 = 0.9556$; (453K-1133K)

$\lg k_2 = \frac{506}{T} - 5.47$; $R^2 = 0.9446$; (1193K-1493K)

The process rate was calculated by equation (2)

$$\upsilon = \pm \frac{\Delta m}{\Delta \tau . m_o}, \text{ mg/min} \qquad (2)$$

where - υ is the average process rate g / min; Δm is the change of the mass of the mixture, mg; $\Delta\tau$– change over time, min; m_o – the initial mixture mass, g.

Comparison of change of rate processes in mixtures 1 and 2 heated to 1493K is shown In Fig. 6. The figure shows that for mix 1, the maximum rate was reached at T~903K and mix 2 in T~1193K. On the rate curves there is one maximum for mix 1 and two for mix 2. The first maximum of mixture 2 is similar to that of mix 1 (T~930K), which show that at this temperature the same process occurs. This maximum corresponds to the rate of formation of solid solution between Fe_2O_3 and Mn_2O_3 from peritektical type; for the first mixture there is a subsequent decomposition whereas for the second mixture there is a subsequent decomposition as well as Coulsonite (Fe_2VO_4) phase formation. The second maximum of the rate for mixture 2 is associated with the formation a new phase Jacobsite (Mn_6Fe_4) $(Mn_4Fe_{1.6})$ O_4.

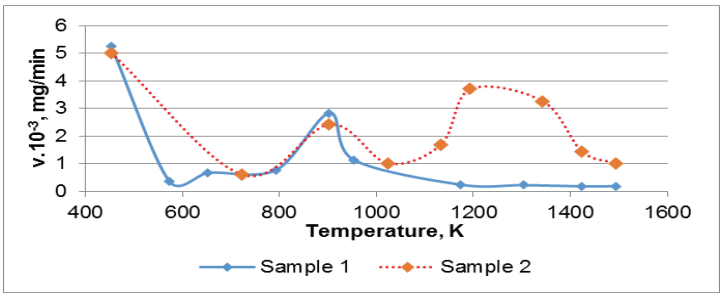

Fig. 5. Depending on the heating rate from the temperature for mixtures 1 and 2.

Conclusion

1. It was found out, analysing the DTA and TG curves of two mixtures that the processes took place in three stages. The first stage involved the dissociation of MnO_2 (mix 1) and vanadium oxides from the waste vanadium catalyst (mix 2). Typical of the second stage is the formation of a solid solution of Fe_2O_3 and Mn_2O_3 from peritektical type that subsequently decomposes. In the second stage of mix 2, a new phase FeV_2O_4 or FeV_2O_6 was also formed. In the third stage, new phases hausmanite Mn_3O_4 (mix 1) and Jacobsite (Mn_6Fe_4) $(Mn_4Fe_{1.6})$ O_4 (mix 2) were formed.

2. The apparent activation energy of the two mixtures was determined experimentally. Activation energy for mix 1 is Ea_1 = 7.876kJ / mol in the range up to 800K, and Ea_1 = 16.507kJ / mol to 1493K. For mixture 2 Ea_2 = 5.60k4J / mol., in the range up to 900K and Ea_2 = 10.119kJ / mol to 1493K. The activation energy values show that heating processes run in an external diffusion area.

3. Based on the experimental results of the heating of two mixtures the equations of rate constant lgK = f (1 / T) were obtained. The maximum rate of the processes in heating a mixture 1 at T ~ 903K, and for a mix 2 was shifted to higher temperatures range (1193K).

References

[1] J. Šesták, P. Holba, Ž.D. Živković, Doubt on Kissinger's method of kinetic evaluation based on several conceptual models showing the difference between the maximum of reaction rate and the extreme of a DTA peak, J. Min. Metall. Sect. B-Metall. 50(1) B (2014), pp 77-81.

[2] Ž.D. Živković, Determination of reaction kinetics based on a part of a differential thermal analysis or thermogravimetric curve, Thermochimica Acta, Vol.32, Iss. 1-2, (September 1979), pp 205-211.

[3] Ž.D. Živković, D. Živković, D. Grujičić, V. Savović, Kinetics of the oxidation process in the system Zn-Fe-S-O, Thermochimica Acta, Vol.315, Iss. 1, (May 1998), pp 33-37.

[4] Esmail R. Monazam, Ronald W. Breault and Ranjani Siriwardane, Kinetics of Magnetite (Fe_3O_4) Oxidation to Hematite (Fe_2O_3) in Air for Chemical Looping Combustion**,** I*nd. Eng. Chem. Res.,* (2014), 53 (34), pp 13320–13328.

[5] C.J. Goss, The kinetics and reaction mechanism of the goethite to hematite

transformation, Minerological Magazine, (September 1987), Vol.51, pp 437-451.

[6] R.M.Cornell, U. Schwertmann, The Iron Oxides, Structure, Properties, Reactions, Occurrenes and Uses, Second Completely Revised and Extended Edition, (2003), p 352.

[7] N. Bertrand, C. Desgranges, D. Poquillon, M.C. Lafont, D.Monceau, Iron Oxidation at Low Temperature (260 – 500°C) in Air and the Effect of Water Vapor, Oxidation of Metals, (2010), Vol. 73, Issue 1-2, pp. 139-162

[8] M.J. Graham, S.I.Ali and M.Cohen, Low Temperature Oxidation (24° to 200°C) and Krypton Adsorption Studies on Polycrystalline and Single Crystal Iron Surfaces **,** Journal of lectrochemical Society, (1970), 117(4), pp 513-516.

[9] H. Sakai, T. Tsuji and K. Naito, O, Journal of Nuclear Science and Technology, February 1(985), 22(2), pp 158-161.

[10] Tatsuji Yamashita, Albert Vannice, NO Decomposition over Mn_2O_3 and Mn_3O_4, Journal of Catalysis, Volume 163, Iss. 1, 15 September 1996, pp 158–168.

[11] SU Haifeng , GAO Jiali , WEN Yanxuan,TONG Zhangfa , HU Xueling, Kinetics of hausmannite preparation by thermal decomposition of manganese sulfate,Journal of Chemical Industry and Engineering(China), February 2008, Vol.59(2), pp 359-365.

[12] Saputra, E., S. Muhammad, H.Sun, M.Ang, M. Tade, S.Wang, "Shape-controlled activation of peroxymonosulfate by single crystal α-Mn_2O_3 for catalytic phenol degradation in aqueous solution", Applied Catalysis B: Environmental. (2014), pp. 246-251.

[13] Yao Y, Cai Y, Lu F, Wei F, Wang X, Wang S, Magnetic recoverable $MnFe_2O_4$ and $MnFe_2O_4$-graphene hybrid as heterogeneous catalysts of peroxymonosulfate activation for efficient degradation of aqueous organic pollutants. J Hazard Mater., 270, (2014), Apr pp 61-70.

[14] C.P.J van Vuuren, P.P. Stander, The oxidation kinetics of FeV_2O_4 in the range 200-580°C, Thermochimica Acta 254, (1995), pp.227 233.

[15] Gorshkov V.S., Thermografia stroitelnih materialov, Moscow, (1968), pp 96-97.

MICROSTRUCTURAL CHARACTERIZATION OF WC AND CrC BASED COATINGS APPLIED BY DIFFERENT PROCESSES

G.M.Bakić[1], V.Maksimović[2], A.Maslarević[3], M.B.Djukić[1], B.Rajičić[1], A. Djordjević[4]

[1] *University of Belgrade, Fac. of Mechanical Engineering, Kraljice Marije 16, 11035 Belgrade, Serbia*
[2] *Vinca Institute of Nuclear Sciences, University of Belgrade, PO Box 522, 11001 Belgrade, Serbia*
[3] *IC Fac. of Mech. Engineering, University of Belgrade, Kraljice Marije 16, 11035 Belgrade, Serbia*
[4] *Messer Tehnogas a.d., Batajnicki put 62, Belgrade, Serbia*
amaslarevic@mas.bg.ac.rs

Abstract

Numerous mechanical structures and assemblies have frequent outages because of wear of machine parts due to the effects of abrasion and erosion. There are several methods to protect parts from wear and one of them is by applying a protective coating on the endangered area. It is well known that the coatings with carbide distributed in a metallic matrix have an excellent wear resistance. In this paper characterization of three coatings were carried out: coating with tungsten carbide (WC) in NiBSiFe matrix, coating with chromium carbides (CrC) in FeNiSi matrix deposited by plasma transferred arc method (PTA), as well as, coating with WC carbide in CrNiBSi matrix deposited by oxy-acetylene thermal spray process. The above mentioned alloys, before application to the base material, were in a powder state. This paper describes applied coating technologies on a substrate - S235JR steel, powders characteristics, microstructure and properties of coatings, phase composition, and micro hardness of different microconstituents.

Key words: PTA, tungsten carbide, chromium carbide, wear resistance

Introduction

Numerous mechanical structures and assemblies have frequent outages because of wear of machine parts due to the effects of abrasion and erosion. There are several methods to protect parts from wear and one of them is by applying a protective coating on the endangered area. It is well known that the coatings with carbide distributed in a metallic matrix have an excellent wear resistance [1,2]. Research has shown that abrasion resistance increase with an increase of carbon content in the matrix of metal. The composition of the matrix of metal also has a significant influence, therefore softer and ductile matrix have a higher impact resistance in comparison to the matrix that have a higher hardness and brittleness [3].

There are different methods of thermal spraying, as well as, welding methods which can be used in order to apply protective coatings onto different substrates

[4]. Due to its outstanding characteristics, but also because of the low-cost filler materials, plasma transferred arc process (PTA) is widely used to protect surfaces from wear [3]. PTA process was developed during the 1960s, as a modification of the already used plasma welding process [5], for the production of high quality welded layers on the surfaces of components of nuclear power plants [6]. PTA process, in comparison with conventional methods of welding, provides the deposition of the larger amounts of filler material per unit of time, the relatively small depth of penetration, lower heat input and relatively small degree of mixing between the filler and the base metal [7-9].

Coatings that consist of a metal matrix with dispersed tungsten carbides (WC) or chromium carbides (CrC) have proved to be an excellent for protection against abrasion and erosion. WC particles in a NiBSi matrix belong to a group of composite materials and have a high resistance to abrasion and erosion at temperatures up to 650°C [10].

The high carbon ferro-chromium (FeCrCo) filler material is a composite material which is characterized by resistance to abrasion and erosion caused by the action of abrasive mineral substances, as well as, high impact loads and it is recommended to be used at temperatures below 600°C [11]. In this paper characterization of three coatings were carried out: coating with tungsten carbide (WC) in a NiBSiFe matrix and coating with chromium carbide (CrC) in a FeNiSi matrix applied by PTA process and the coating with WC carbide in a CrNiBSi matrix applied by oxy-acetylene thermal spray process with a subsequent heating.

Material and experiment

In order to characterize the coating for protection against wear samples were made from: a coating with tungsten carbide (WC) in a NiBSiFe matrix and a coating with chromium carbide (CrC) in a FeNiSi matrix, applied by PTA process, as well as, a coating which consists of the WC carbide in a CrNiBSi matrix that has been deposited on the substrate by oxy-acetylene thermal spray process with subsequent heating. The above mentioned alloys, before application to the base material, were in a powder state. This paper describes applied coating technologies on a substrate - S235JR steel, powders characteristics, microstructure and properties of coatings, phase composition, and micro hardness of different microconstituents.

Powders and processes

As a filler material different powders, with different chemical composition, were used, table 1. Commercial alloys produced by Castolin Eutectic were used. As a base material – substrate, a structural steel S235JR (EN 10025) in the form of plates with dimensions: 100x100x10mm, with an average hardness ~150HV, was used. For plasma powder surfacing, powder which contain 60% of tungsten carbide with a matrix based on nickel (Ni) alloyed with a boron (B) and silicon (Si), with a small amount of a carbon (C), chromium (Cr) and iron (Fe) (WC/NiBSi), as well as, iron-based powder with a higher content of Cr and C, with an addition of a Ni and Si (FeCrC) were used. For oxy-acetylene thermal spray process, a powder which contain 35% WC and Ni based matrix, with an addition of a Cr, B and Si

(WC/NiCrBSi) was used. Surface preparation for PTA process consisted of grinding up to a metallic shine, while preparation for oxy-acetylene thermal spray process consisted of sand blasting of surface, in the aim of removing impurities and oxides, with an additional shot peening in order to increase surface area for bonding.

Table 1. Chemical composition of the powders

Filler material	Chemical composition (wt %)								
	C	Cr	Ni	B	Si	Mn	Fe	Mo	WC
WC/NiBSi	0,1	0,20	Residue	2,47	3,47	-	0,69	-	60
FeCrC	3,9	32,5	4,5	-	1,1	0,25	Residue	0,5	-
WC/NiCrBSi	0,83	15,6	Residue	3,29	4,25		4,0		35

In the case of WC/NiBSi powder, coating is formed due to melting of a Ni based matrix without WC changes. In the case of FeCrC powder, coating is formed by melting in an electric arc or plasma, while during the solidification and subsequent cooling on the surface, hard phase, based on chromium carbide (CrC), was precipitated. Morphology of filler materials - powders are shown in Fig. 1(a-c). Tungsten carbides in WC/NiBSi coating are produced by the process of enrichment of tungsten with carbon at high temperatures and its subsequent grinding to obtain the desired granulation, Fig. 1a. Unlike tungsten carbide in the WC/NiBSi powder, tungsten carbide in the WC/NiCrBSi powder is obtained during the process of agglomeration, which results in porous structure of carbides, Fig. 1c. The matrix for these two coatings (the first ~ 40 wt% and the second ~ 65 wt%) was obtained by the process of atomization which is characterized by spherical shape of particles. The same process was used during the production of FeCrC powder, Fig. 1b.

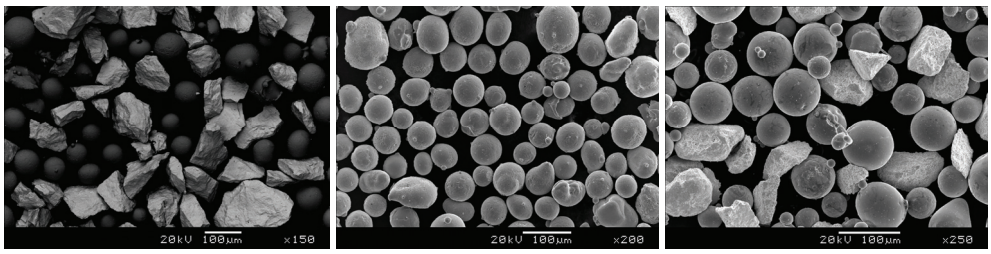

a) WC/NiBSi (SEM-BSE) *b) FeCrC (SEM-BSE)* *c) WC/NiCrBSi (SEM-BSE)*

Fig. 1. Morphology of the powders

Powders used for making coating samples by PTA process have a different chemical composition, table 1. Also, WC/NiBSi powder containing carbide phase before applying to the substrate, which remain unchanged in the coating, while in the case of FeCrC powder, carbides are formed in the process of surfacing. For this reason, powders feeding during PTA process were not identical - the supply of WC/NiBSi powder, which has already formed carbide phase, is behind the plasma

arc, thus preventing combustion of WC carbide, Fig. 2a, while the FeCrC powder is added in the front of the plasma arc in order to foster the development of the carbide phase, Fig. 2b.

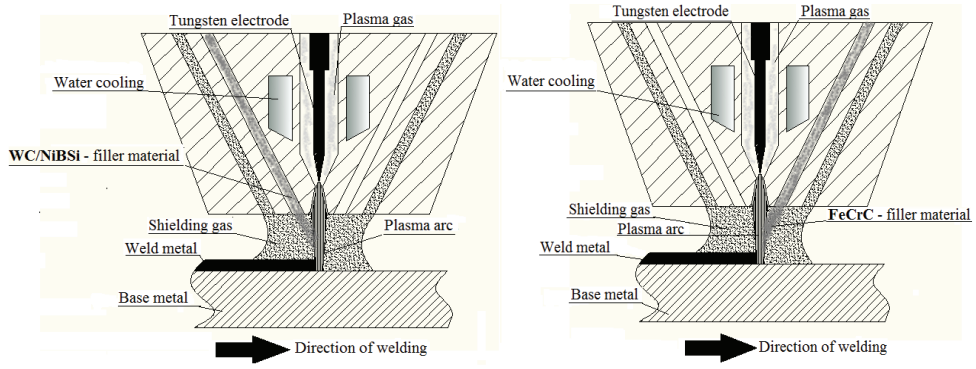

a) *b)*

Fig. 2. Cross section of the PTA torch:
a) WC/NiBSi filler material; b) FeCrC filler material

PTA surfacing was carried out by Eutronic Gap 3001 DC device (Castolin Eutectic). For both coatings, argon (2 l/min) as a plasma gas was used and a gas mixture of 95%Ar + 5%H_2 (14 l/min + 3 l/min), as shielding and transport gas, was used. The addition of hydrogen significantly increases the volume of molten material in the weld pool due to the higher thermal conductivity of argon-hydrogen mixtures, and prevents the oxide formation on the surface of the layer of the weld. Hydrogen solubility in molten metals is very high and may produce gas bubbles and cracks [12]. During the process of PTA surfacing of both alloys, most of the parameters were identical: torch speed in the longitudinal direction: 0,11 mm/s; oscillation width: 100 mm; oscillation velocity: 7 mm/s; arc voltage 27,5 V; deposition rate: 33 g/min. The only parameter that was different is the welding current: 70 A (WC/NiBSi) and 90A (FeCrC), because this material (FeCrC) requires more heat in order to melt completely. WC/NiCrBSi coating is applied by oxy-acetylene thermal spray process using a CastoDyn 8000 device (Castolin Eutectic). The process parameters were: the oxygen pressure: 4 bar, acetylene pressure: 0,7 bar and the distance from the gun to the substrate: 150 mm. After applying of a coating to a substrate, the coating was subjected to post-heating at 1040° C, which results in more complete melting of the coating matrix based on Ni and the reduction of porosity. After surfacing the coating, the samples were cut from the specimens for microstructural examination and hardness measurements. The microstructure of the coatings was examined by scanning electron microscope SEM JEOL JSM 5800LV, while microhardness was measured by Buehler Micromet 5101 Vickers device, with a load of 50gf. Microhardness was measured in different zones of coatings, including matrix and carbides (coatings with WC), as well as, the base material near the weld metal.

Results and analysis

The microstructure of the samples is given in Figs. 3-5. During plasma cladding, melting and solidification occur at very high rates. Because of the small dimension of the molten pool and fast rate of heat transfer, the process exhibits phenomena that are far from equilibrium [13]. For all three coatings, the bright strip represents the bonding zone between the coating and substrate. This thin layer on the interface indicates good structural bonding between the deposited coating and the substrate [14].

Tungsten carbides (WC) in the NiBSi metallic matrix are shown in Fig. 3a. Matrix is composed of γ-Ni dendrites and γNi + Ni_3B lamellar eutectic in the interdendritic region. Blocky precipitates formed both near and away from the WC-matrix interface β-W_2C type with some Cr [15]. Fe based alloy with 35%Cr and 4%C is expected to be hypoeutectic (eutectic for FeCrC ternary system is app. at 30%Cr) and consisted of M_7C_3 primary carbides and γ(Fe+Cr) + M_7C_3 eutectic, Fig. 4 [16]. The diffusion coefficient of carbon in the matrix is usually higher than the diffusion coefficient of the carbide-forming metal. Thus, carbon diffuses much faster out of the carbide, allowing it to form mixed carbides [15]. Microstructure of WC/NiCrBSi coating consists of a nickel-rich dendrite matrix containing borides and carbides with large tungsten carbides agglomerates particles, Fig 5a. Heat treatment promotes growth of precipitates, Cr_7C_3 and CrB type [17]. The coating process has a direct impact on the porosity: both coatings, made by PTA process, have significantly lower porosity than the coating made by oxy-acetylene thermal spray process, regardless of the similarity between WC/NiBSi and WC/NiCrBSi coating matrix.

The microhardness values of the alloys, which contain tungsten carbides (WC), are shown in Figure 3b and 5b. For both of these coatings, lower hardness values were measured in the bonding zone, then in the rest of the coating with a characteristic single-phase structure. The mean microhardness value of the FeCrC coating is 456 HV0,05, but it is also observed that the hardness is lowest immediately above bonding zone, with an average hardness value: 307 HV0,05.

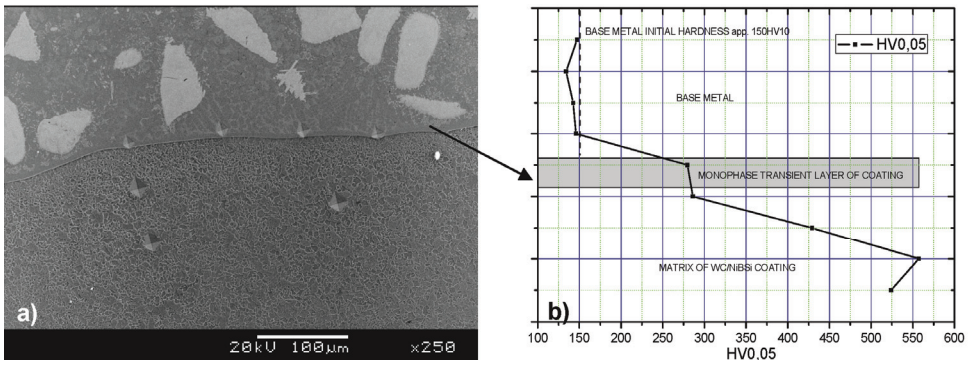

Fig. 3. WC/NiBSi PTA coating: a) microstructure of the border zone coating – substrate; b) changes in microhardness along the fusion line

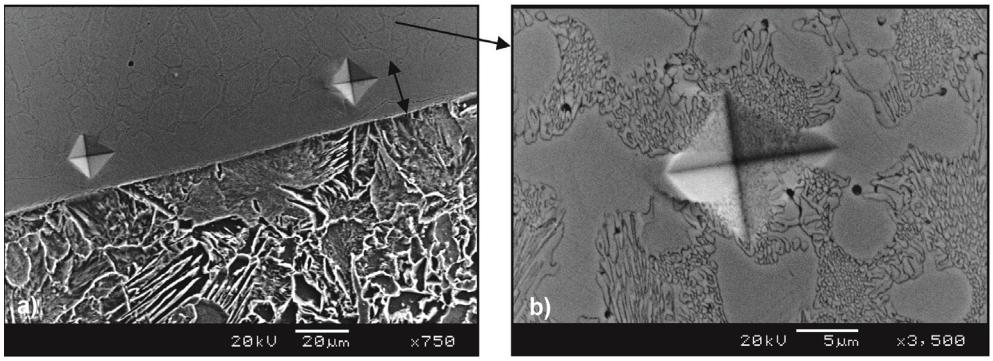

Fig. 4. FeCrC PTA coating: a) microstructure of the border zone coating – substrate; b) detail from Figure 4a

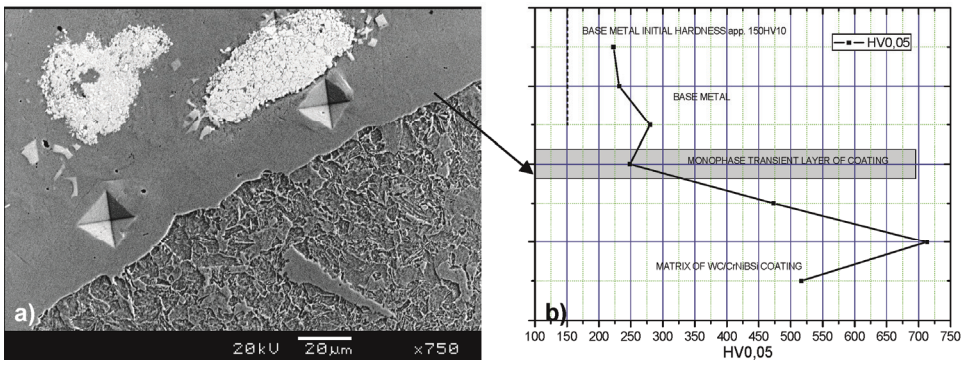

Fig. 5. WC/NiCrBSi oxy-acetylene thermal sprayed coating: a) microstructure of the border zone coating – substrate; b) changes in microhardness along the fusion line

Conclusions

In this paper three coatings, deposited by two different processes with high heat input are presented. Nevertheless, plasma transferred arc (PTA) process provides low heat input to substrate. All three coatings have a common characteristic: a bonding layer of a small thickness, which indicate on the good bonding between coating and substrate. The choice of coating process and the specificity of metal matrix directly affect the qualities of coating in terms of the microstructure and microhardness. The higher heat input during PTA coating process provides better results in comparison to the subsequent heat input after application of oxy-acetylene thermal spray process.

References

[1] S. Shimizu and K. Nagai, Abrasion resistance of carbide dispersion surfacing metals, Welding International, Vol. 5, Issue 1, 1991.
[2] K.H. Zum Gahr, Microstructure and wear of materials, Elsevier Science Publishers B.V., Amsterdam, 1987.
[3] E. Badisch, S. Ilo, R. Polak, Multivariable Modelling of Impact-Abrasion Wear

Rates in Metal Matrix-Carbide Composite Materials, Tribology Letters 36, pp. 55-62, 2009.
[4] J.R. Davis, Handbook of Thermal Spray Technology, pp 54-76, 2004.
[5] R.L. Deuis, J.M. Yellup, C. Subramanian, Metal-matrix Composite Coating by PTA Surfacing, Composites Science and Technology, Vol. 58, (2), pp. 299-309, 1998.
[6] P. Harris, B.L. Smith, Factorial techniques for weld quality prediction, Metal Construction, Vol. 15 (11), pp. 661-666, 1983.
[7] A.S.C.M. D'Oliveira, R.S.C. Paredes, R.L.C. Santos, Pulsed current plasma transferred arc hardfacing, Journal of Materials Processing Technology, Vol. 171, pp. 167-174, 2006.
[8] C. Katsich, A. Zikin, E. Badisch, Wear Protection of Highly Loaded Components: Adventages of Plasma Transferred Arc Welding as Hardfacing Technology, 8th International DAAAM Baltic Conference ''Industrial Engineering''- 19-21 April 2012, Tallinn, Estonia.
[9] H. Hállen, E. Lugscheider, A.Ait-Mekideche, Plasma Transferred Arc Surfacing with High Deposition Rates, Fourth National Thermal Spray conference, Pittsburg, PA, USA, 4-10 May 1991.
[10] Datasheet Metal powder, EuTroLoy PG 6503, Castolin Ges.m.b.H, Vienna, 2005.
[11] Datasheet Metal powder, EuTroLoy 16659, Castolin Ges.m.b.H, Vienna, 2005.
[12] V.V. Çay, S. Ozan, M.S. Gök, A. Erdoğan, The effect of shielding gas composition on microstructure and abrasive wear resistance fabricated with PTA alloying technique, Archives of Metallurgy and Materials, Vol. 58, pp. 1137-1145, 2013.
[13] M. Kirchgaßner, E. Badisch, F. Franek, Behaviour of iron-based hardfacing alloys under abrasion and impact, Wear, Vol. 265, pp. 772-779, 2008.
[14] Gh. Azimi, Microstructure and wear properties of Fe-Cr-C and Fe-Cr-Nb-C clads on carbon steel by TIG surfacing process, International Journal of Surface Science and Engineering, Vol. 6, pp. 15-23, 2012.
[15] T. Liyanage, G. Fisher, A.P. Gerlich, Microstructures and abrasive wear performance of PTAW deposited Ni–WC overlays using different Ni-alloy chemistries, Wear, Vol. 274- 275, pp. 345-54, 2012.
[16] J.F. Flores, A. Neville, N. Kapur, A. Gnanavelu, Erosion–corrosion degradation mechanisms of Fe–Cr–C and WC–Fe–Cr–C PTA overlays in concentrated slurries, Wear, Vol. 267, pp. 1811-1820, 2009.
[17] J.M. Miguel, J.M. Guilemany, S. Vizcaino, Tribological study of NiCrBSi coating obtained by different processes,Tribology International, Vol. 36, pp. 181-187, 2003.

THE EFFECT OF GOLD COMPLEX BASED ON MERCAPTOTRIAZOLE ON PHOTORESIST LAYERS OF PRINTED CIRCUIT BOARDS

Silvana Dimitrijević[1], Zoran Stević[2], Mirjana Rajčić-Vujasinović[2], Vesna Grekulović[2], Stevan Dimitrijević[3], Slađana Alagić[2], Biserka Trumić[1]

[1] *Mining and Metallurgy Institute Bor, Zeleni bulevar 35, 19210 Bor*
[2] *Technical Faculty in Bor, University of Belgrade, Vojske Jugoslavije 12, 19210 Bor*
[3] *Innovation Centre of Technological and Metallurgical Faculty in Belgrade, University of Belgrade, Karnegijeva 4, 11000 Belgrade*
silvana.dimitrijevic@irmbor.co.rs

Abstract

The aim of this work was to investigate the effect of organic gold complex based on mercaptotriazole on photoresist layers used in manufacturing the printed circuit boards (PCB). Investigations were performed by immersion the previously prepared PCB with developed net and lacquered edges – lines in electrolytes with different pH values (pH=2, 4, 7, 9 and 12) at gold concentration of 2.5 g/dm^3 and in electrolytes with different gold concentrations (1.5; 2.0; 2.5; 3.0 and 3.5 g/dm^3) at pH value of pH=9. Experimental results showed that photoresist layers on boards are the most resistant to the effects of electrolyte at pH=9 which is very important since the previous investigations showed that the best coatings were obtained at pH=9 and gold concentration in electrolyte of 2.5 g/dm^3.
Key words: gold, mercaptotriazole, photoresist layers, lacquered edges – lines

Introduction

Electrodeposition of gold is not a new process, but has been widely used in the automotive industry, biomedicine and electronics industry (computers, telecommunications, etc.). Combination of excellent electrical conductivity and high corrosion resistance has led to the adoption of gold as the standard material for interconnectors. Gold coatings are used in electronics industry due to their exceptional characteristics in terms of electrical, chemical and optical properties, such as high purity combined with resistance to abrasion of deposits [1-5].

Electrochemical coatings of gold can be classified as soft gold and hard gold [1].

Baths for gold plating can be classified into different categories depending on which gold salts are used, the reaction mechanism, pH value of baths, as well as the properties of the obtained deposits [6]. However, the basic division of gold plating baths is reduced to cyanide and non-cyanide ones.

The non-cyanide baths in use are: sulphite and amino sulphite baths, Au (I) thiosulfate baths, thiosulphate-sulphite baths, baths on the basis of thiourea, baths

with ascorbic acid, baths without reducing agent, Au (III) halide baths and Au (I) thiomalate baths [1].

Gold plating from cyanide electrolytes is listed as a high-risk technology from the general ecological aspect.

Considering the application of printed circuit board in the industry and in the field of microelectronics and optoelectronics in general, the important fact is that cyanide ions attack the surface between the protective film and base lifting the film, which is manifested by gold deposition under the protective layer, what is very undesirable. This result in changing the form of micro-devices causing the loss of performances called "underplating" [7, 8]. The negative impact of cyanide on the photoresistant layers of printed circuit boards, in addition to toxicity, is considered as the greatest disadvantage of cyanide. Due to this reason, especially in recent years, there are trends in use an electrolyte without content of cyanide. Composition of these electrolytes is mainly based on a gold complex with some organic compounds. Their use, however, has not yet found a satisfactory industrial application due to the low stability constant, which is manifested by decomposition of the complex and precipitation of elemental gold from electrolyte [9, 10].

Gold complex based on mercaptotriazole, in contrast to the previous complexes, has shown sufficient stability in a period of a year and the coatings obtained from this complex fully meet the requirements of decorative coatings. Since detailed testing of this complex was done in the previous research, both in liquid and solid state, the aim of this study was to investigate the effect of complex on the photoresist layers used in making the printed circuit boards [11 -13].

Experimental parts

Study the effect of organic gold complex, based on mercaptotriazole, on photoresist layers that are used in making the printed circuit boards, was done on previously prepared printed circuit boards. Printed circuit boards with a developed network of 1.3x1.3 mm (with edges - lines of 0.7x0.7 mm on which the lacquer was applied) are cut to the dimensions of 15x15 mm.

In the experimental work, the following effects were tested:

a) pH value of electrolyte in the range of its stability (2-12) at optimal concentration of gold (in terms of the coating quality) in electrolyte of C_{Au}=2.5 g/dm^3 [11].

b) concentration of gold (1.5, 2.0, 2.5, 3.0 and 3.5 g/dm^3) at optimum pH value of electrolyte of pH = 9 on photoresist layers [15].

Freshly prepared electrolytes were used for tests [11-13].

Coatings of thickness of 0.1 μm are the most used for electronics industry. Considering the fact that the required time for applying the coatings of this thickness from organic gold complex with mercaptotriazole is 105 s, the tests were carried out up to three minutes (180 s) [11-13].

Tests were carried out by simple immersion of plates into working electrolyte for 30, 60, 90, 120, 150 and 180 s.

The results of these tests are shown on macrophotos and microphotos of plate surface as well on microphotos of their cross section.

Macro and microphotos were recorded with digital photo camera SAMSUNG ES15.

Results and discussion

The effect of electrolytes of different pH values on photoresist layers was tested in the first series of experiment.

It can be seen from Figure 1 showing the macrophotos of plates, treated with electrolyte for different times at different pH values (pH=2, 4, 7, 9 and 12) that the photoresist layers on plates are resistant to the effect of electrolyte at pH values of 2, 7 and 9. At pH 1, the first visual changes can be observed after 150 s until at pH = 12, the first changes occur after 30 s. It can be seen from macro and micro photos (Figure 2) that the plates are the most resistant to the effect of electrolytes with pH value of 9, which is of great importance due to the fact that previous studies have shown that the best coatings are obtained at pH = 9 [11-13].

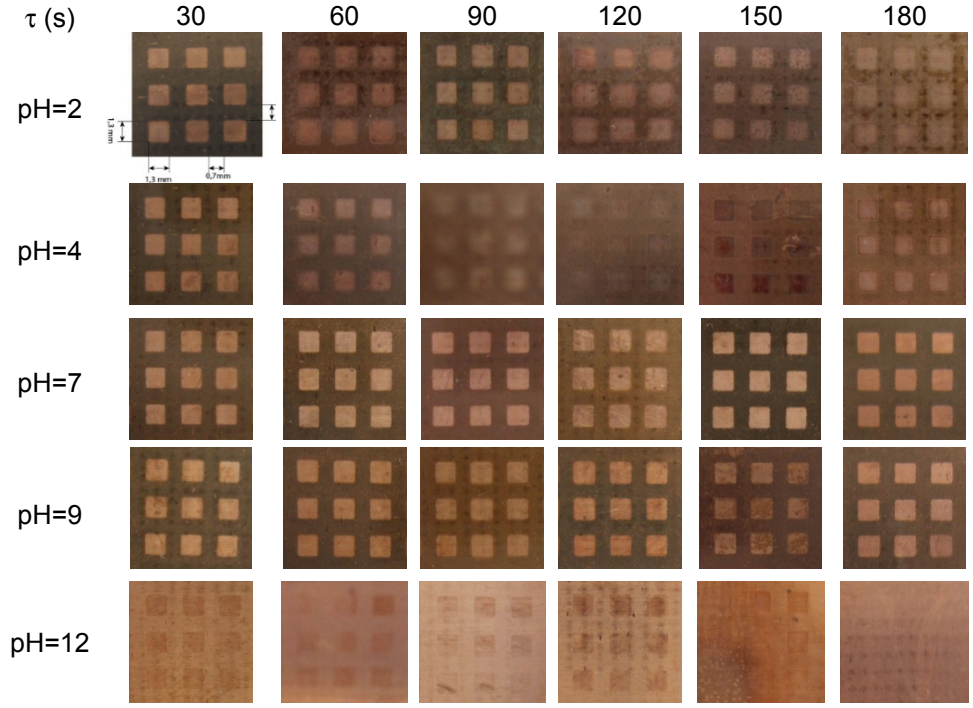

Fig. 1 Macrophotos of plates recorded after 30, 60, 90, 120, 150 and 180 s at pH=2, 4, 7 ,9 and 12

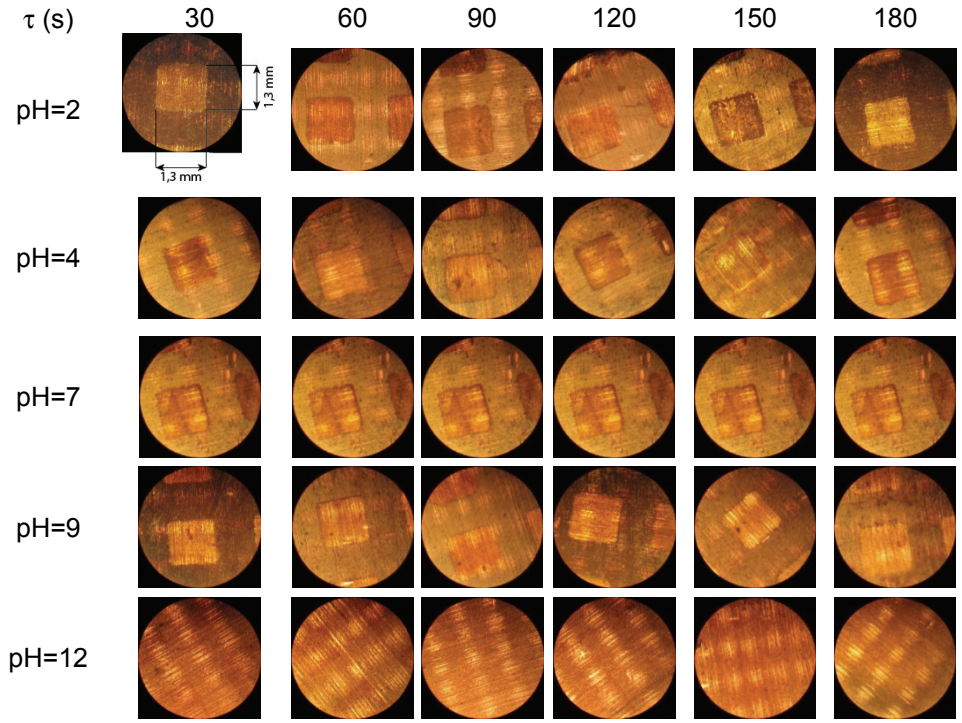

Fig. 2 Microphotos of plates recorded after 30, 60, 90, 120, 150 and 180 s at pH=2, 4, 7 ,9 and 12

The effect of gold concentration in electrolyte on photoresist layers was tested in the second series of experiments. It can be seen from Figure 3 and Figure 4 showing the microphotos of plates treated for different times at different gold concentrations (C_{Au}=1,5; 2,0; 2,5; 3,0 and 3,5 g/dm^3) at pH=9, that the photoresist layers on plates are resistant to the effects of electrolytes at all gold concentrations.

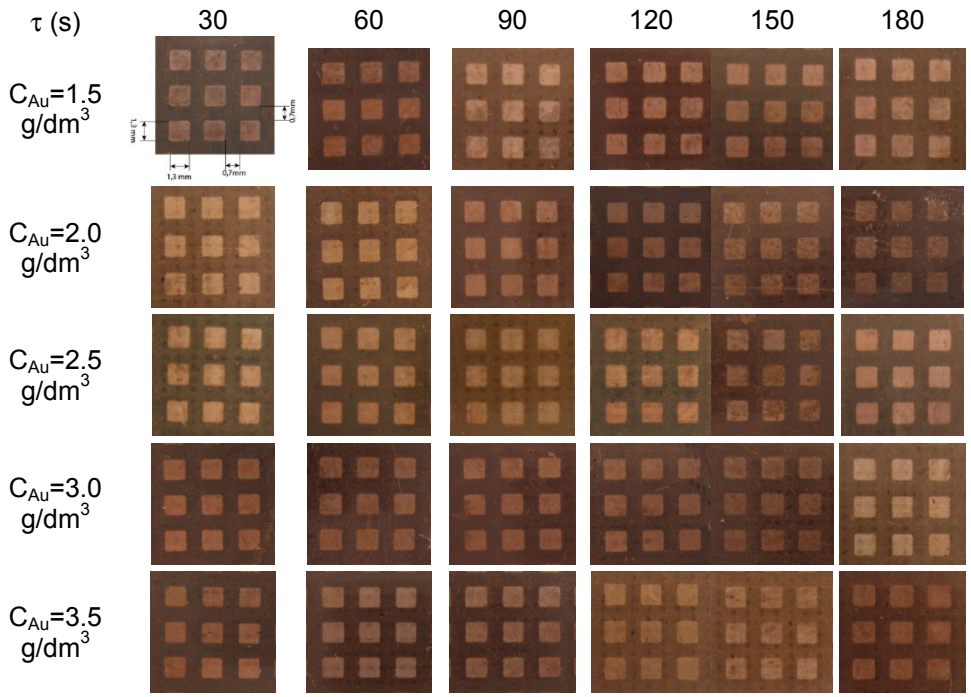

Fig. 3 Macrophotos of plates recorded after 30, 60, 90, 120, 150 and 180 s at pH=9 and gold concentrations in electrolyte of 1.5; 2.0; 2.5; 3.0 and 3.5 g/dm^3

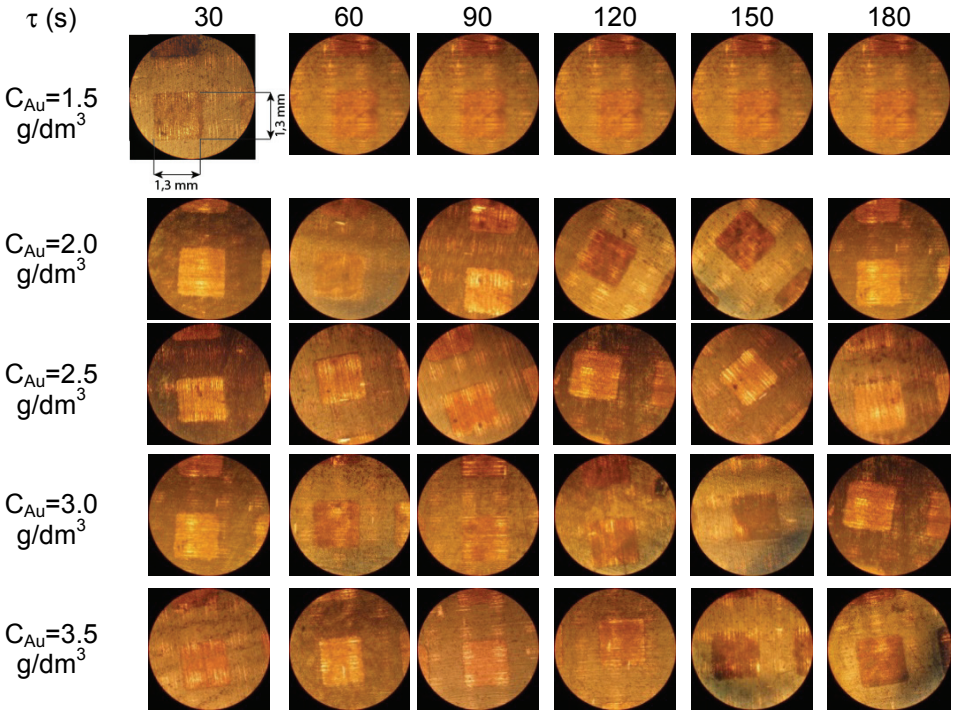

Fig. 4 Microphotos of plates recorded after 30, 60, 90, 120, 150 and 180 s at pH=9 and gold concentrations in electrolyte of 1.5; 2.0; 2.5; 3.0 and 3.5 g/dm^3

Figure 5 shows microphotos of edges of tested plates recorded after 180 s.

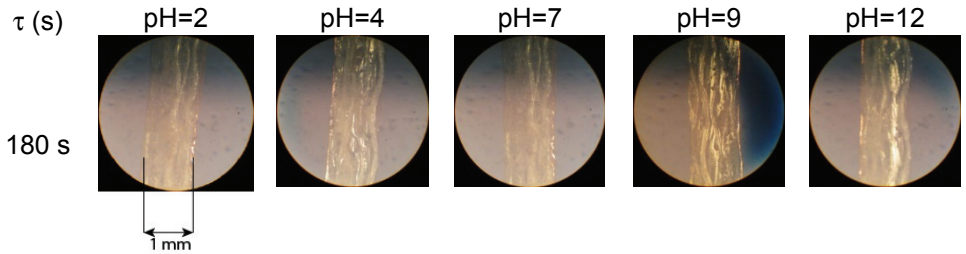

Fig. 5 Microphotos of edges of plates recorded after 180 s at pH=9 gold concentrations of 1.5; 2.0; 2.5; 3.0 and 3.5 g/dm^3

Figure 5, showing the microphotos of edges of plates recorded after 180s of treating the plates with electrolyte at different pH values, clearly confirms that the plates are the most resistant to the effect of electrolyte at pH = 9 and that the largest etching of edges is at pH = 12.

Conclusion

Study the effect of pH value of electrolyte, in the range of its stability (2-12) at optimal gold concentration in electrolyte of C_{Au}=2.5 g/dm^3 on photoresist layers, has found that they are resistant to the effect of electrolyte at pH values of 2, 7 and 9. At pH = 4, the first visual changes can be observed after 150 s, until at pH = 12, the first changes occur after 30 s. It can be also seen from microphotos of surfaces of plates that the photoresist layers of plates are the most resistant to the effect of electrolyte at pH = 2 and pH = 9. At pH = 9, the photoresist layers on plates are resistant to the effects of electrolyte at all tested concentrations of gold.

Acknowledgement

This work is the result of the Projects No. TR 34024: “Development of technologies for recycling the precious, rare and associated metals from solid waste of Serbia to the high-quality products”, and TR 34033: "Innovative synergy of by-products, waste minimization and clean technologies in metallurgy" funded by the Ministry of Education, Science and Technological Development of the Republic of Serbia.

References

[1] M.J.Liew, S.Roy and K.Scoot, Development of a Non-Toxic Electrolyte for Soft Gold Electrodeposition: An Overview of Work at University of Newcastle Upon Tyne, Green Chemistry, 5, (2003), pp. 376-381
[2] Y.Okinaka and M.Hoshino, Some Recent Topic in Gold Plating for Electronic Applications, Gold Bulletin, 31(1), (1998), pp. 3-13
[3] I.R. Christine and B.P. Cameron, Gold Electrodeposition within the Electronics Industry, Gold Bulletin, 27(1), (1994), pp. 12-20
[4] Y.Okinaka, Significance of Inclusions in Electroplated Gold Films for Electronic Applications, Gold Bulletin, 33(4), (2000), pp. 117-127
[5] A. Maner, S. Harsch and W. Ehrfeld, Mass-Production of Microdevices with Extreme Aspect Ratios by Electroforming, Plating Surface Finishing, 75, (1998), pp. 60-65
[6] M. Kato, Y. Okinaka, Some Recent Developments in Non-Cyanide Gold Plating for Electronics Applications, Gold Bulletin, 37(1-2), (2004), pp. 37-44
[7] S. Roy, Electrochemical Gold Deposition from Non-Toxic Electrolytes, ECS Transactions, 16(36), (2009), pp. 667-672
[8] H. Honma, K. Hagiwara, Fabrication of Gold Bumps Using Gold Sulfite Plating J. Electrochem. Soc. 142(1), (1995), 81-84
[9] S. Dimitrijević, M. Rajčić-Vujasinović, R. Jancic-Hajneman, D. Trifunović, J. Bajat, V. Trujić, S. Alagić, Non-cyanide Electrolytes for Gold Plating - A Review of Recent Developments, International Scientific and Professional Meeting Eco-Ist'12, Proceedings, 30/05 – 02/06/2012 Zaječar, Serbia, pp.194-199
[10] W. J. Dauksher, D. J. Resnick, W. A. Johnson, A.W. Yanof, New Operating Regime for Electroplating the Gold Absorber on X-Ray Masks, Microelectronic Engineering, 23, (1994), pp. 235-240;
[11] S. Dimitrijević, M. Rajčić-Vujasinović, S. Alagić, V. Grekulović, V. Trujić,

Formulation and Characterization of Electrolyte for Decorative Gold Plating Based on Mercaptotriazole, Electrochemica Acta, 104, (2013), pp. 330-336

[12] S.B. Dimitrijević, M.M. Rajčić-Vujasinović, R.M. Jančić-Hajneman, J.B. Bajat, V.K. Trujić, D.D. Trifunović, Temperature Effect on Decorative Gold Coatings Obtained from Electrolyte Based on Mercaptotriazole – Comparison with Cyanide, International Journal of Materials Research, pp. 272-281

[13] S. Dimitrijević, M. Rajčić-Vujasinović, S. Alagić, V. Grekulović, V. Trujić, Chemical and Electrochemical Characterzation of Gold Complex Based on Mercaptotriazole in Alkine Media, XXI International Scientific and Professional Meeting Ecological Truth, Proceedings, 04-07/06/2013 Bor Lake, Bor, Serbia, pp.148-155

WETTING CHARACTERISTICS AND SOLDERING OF CHEMICAL NICKEL COATINGS

Z. Karastojković[1], D. Stojiljković[2], Z. Janjušević[3], R. Perić[4], N. Bajić[5], T. Stožinić[1]

[1]*Technical college, 11070 Novi Beograd, Serbia, bul. Dr. Z. Đinđića 152a.*
[2]*SPIT, 16215 Bošnjace, Serbia*
[3]*Institute for technology of nuclear and other mineral raws, 11000 Beograd, Serbia, Franchet d´Esperey 86.*
[4]*„PERIĆ&PERIĆ&Co" d.o.o., 12000 Požarevac, Srbija, Dunavska 116.*
[5]*IHIS-Tehnoexspert, 11080 Beograd-Zemun, Serbia, Batajnički put 23.*
e-mail: zoran.karastojkovic@gmail.com

Abstract

Soldering is treated as a single process in the aspect of melting temperature, when pretty well wetting characteristics are needed. The wetting ability is judged by the angle of tangent to the surface of a blob of solder toward the substrate's surface. Chemical nickel coatings are hydrophobic, it means that wetting angle of chemical nickel coating usually is large, and from that point of view, such surface is not adequate for soldering. The poor wetting characteristics of chemical nickel coating remains unchanged after age hardening treatment, without using a protective atmosphere – just in air. This treatment is used for improving the surface characteristics, as hardness, wear properties, etc. When coated material undergoes to soldering, the surface must be heated-up. However, experiments were shown that chemical nickel coatings are usable for soldering. The advantage of chemical nickel coating is in a possibility to deposition on different substrate materials. Here are checked the properties of soldering the surface with chemical nickel coating by using tin-based braze filler metal.
Keywords: brazing, chemical nickel coating, wetting characteristics, tin-base filler metal

Introduction

In many technologies for metal treating and processing, the wetting characteristics should be taken in consideration, especially during casting, soldering and wearing conditions. The wetting characteristics usually are judged by using the contact (also called – wetting) angle. This angle is pretty well explained in proper literature [1-6]. Generally is accepted, that the high value of this angle is not desired in many technological processes, particularly for casting of thin-wall components, in soldering of both ferrous- or non-ferrous metals, and rarely in some welding processes. Soldering is an important technology in electronics for joining of silicon wafers, and so on. Decreasing of the wetting angle is the matter for many activities dedicated to metallurgists for decreasing that angle and improving of some important technological properties. It is worth to mention two technological

properties, castability and solderability, when the free running is of an extra importance.

Another application in which the wetting angle is of importance is wearing, when two surfaces are in close contact (sliding or rolling), but this is one quite different field of use.

For many other physico-chemical and technological properties the wetting properties play an important role, so those properties should be studied.

Chemical Nickel Deposition

Metal layers (coatings) can be deposited from aqueous solutions not only by electric current but also by strong reducing agents [3-7]. This process is based on catalytic chemical reduction. One of the oldest chemical processes for deposition of a metal is silvering of glass.

Chemical deposition of nickel can be deposited both on metallic or nonmetallic substrates, as commonly used to say a metalizing of plastics. This process has found a variety of industrial applications. Deposited layer is corrosion-resistant, hard and wear-resistant layer. Those properties are of extremely importance for industry. This process produces a material with new and considerably improved surface properties.

The chemical nickel layer is deposited at a uniform thickness on the piece being coated wherever it is in contact with the hot solution. More precisely, the geometry of the piece for chemical deposition does not represent a problem, as in electrolytic plating process. During chemical nickel deposition is obtained rather non-porous coating. The best results in deposition of such coatings were obtained when the working temperatures in range 80-85°C. One example of microstructure at surface after nickel coating is deposited is shown in Fig. 1.

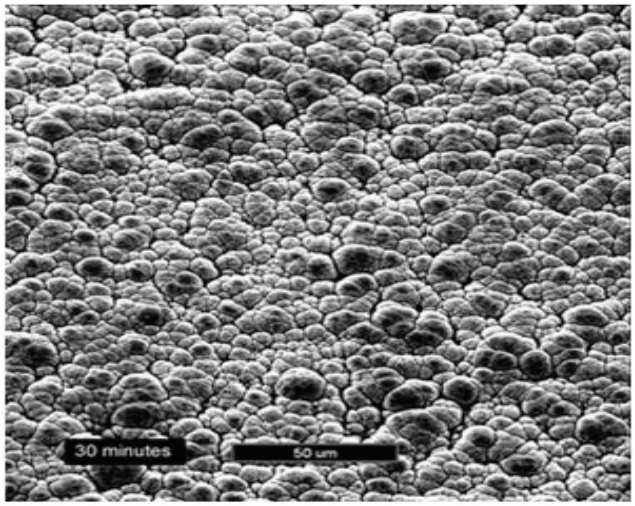

Fig. 1. Outer look of the column structure of chemical nickel coating, after 30min. deposition

The kind of chemical nickel coating, porous or nonporous, considerably depends from the processing conditions [10,11]. This layer is hard, adheres well to parent material(s). The hardness of such layer can be further increased by heat treatment [9-11]. In this experiment the thickness of chemical nickel coating was about 25μm on the wall, while the outer dimensions of used piston were Ø11x75mm.

Wetting Characteristics

The wetting characteristics usually are defined by using one parameter-wetting (or contact) angle. The contact angle is the angle, conventionally measured through the liquid, where a liquid/vapor interface meets a solid surface [2,10]. A given system of solid, liquid, and vapor at a given temperature and pressure has a unique equilibrium contact angle. It is accepted that when the contact angle is between 0° and 90° the surface of a solid is wettable or such surface is *hydrophilic*, and above 90° is not wettable (or such surface is *hydrophobic*). The nickel chemical coating is known as a hydrophobic in its nature.

A water drop at surface on coated piston from Fig. 1, is shown in Fig. 2. The shape of this water drop indicates in simple way fact about large value of contact angle.

Fig. 2. Water drop on chemical nickel coating at one piston from fuel engine, photographed in vertical position of the piston

Wetting characteristics of chemical nickel coatings are of importance generaly for surface treatment process, also in electronics for soldering of some specific components [12,13]. According to the relatively large contact angle of chemical nickel layer (>90°), such coating may be regarded as non-wettable. Only a few irregularities, such as hydrogen embrittlement, may be appeared in deposited chemical nickel [14-17].

Soldering

Soldering has been defined as a joining process that takes place below 450 (500)ºC using filler metals or alloys which flows by capillary forces, and whose melting temperature is lower than the *solidus* temperature of the base material.

Filler metals or alloys should adhere to the surface of the base materials [18]. The criterion takes into account the processing temperature, the type of filler alloy, use of fluxes and the soldering atmosphere [18-20]. For soldering, the Sn- or Pb-based filler alloys are mostly used along with fluxes in order to: a) prevent oxidation and b) improve wetting of the substrate [10,20]. Wetting is of importance especially during soldering of thin walls. An illustration of influence of contact angle on wetting the tubes with different diameters is given in Fig. 3. Such cases are frequently present in soldering technologies.

When the contact angle is below 90°, the fluidity of solder is pretty well and such surface is defined as *hydrophilic for soldering,* case a) from Fig. 2. In the case when the contact angle is higher than >90°, the fluidity of molten solder metal is poor, and such surface is *hydrophobic for soldering*, case b) from Fig. 2.

As a filler metal for soldering the structural steel (Č1530) with the chemical nickel coated surface here is used tin alloy (60%Sn, rest Pb), with $ZnCl_2$ as a flux.

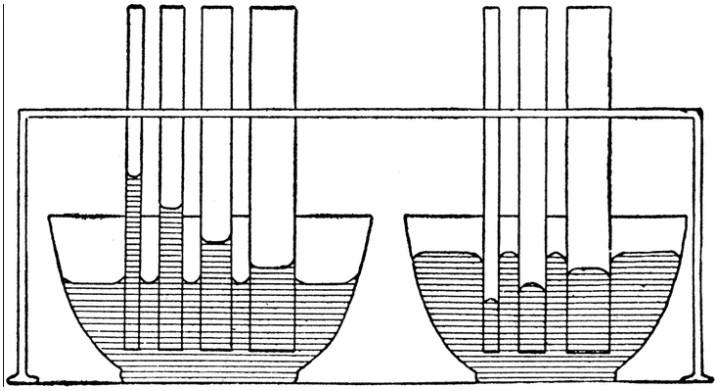

Fig. 2. Influence of contact angle on wetting characteristics during soldering: a) hydrophilic (<90°) and b) hydrophobic (>90°)

For successful soldering are desired the hydrophilic surface, for achieving a well fluidity of molten filler metal.

Discusion

Wetting is of great importance especially during soldering of thin wall products, which are commonly present in electronics. For judging wetting properties, the contact angle of the solid surface with the liquid represents an important technological factor.

The temperature of bath for chemical nickel coating is pretty low, less than 85°C. The contact angle of such coating is relatively high, about 90°. This angle usually determines the surface as non-wettable. The thickness of chemical nickel coatings, however, does not play an important role for contact (or wetting) angle.

From the other side, for soldering is not desired the high value of contact angle. It is considered that when the contact angle is high, usually 90°or more, than the fluidity has to be poor, also a solderability. Soldering is judged by ability of solder filler metal to run freely. But, the chemical nickel surface, in spite of that contact angle is about 90°, has shown a pretty well fluidity when is used solder metal Sn-Pb (60-40), and $ZnCl_2$ as a flux material for joining with structural steel Č1530.

Contact angles are extremely sensitive to contamination of the surface, so both surfaces to be soldered must be carefully cleaned up. In this case, after chemical nickel layer is deposited, such surface must be wash-out.

Conclusion

According to the relatively large contact angle of chemical nickel layer (≈90°), such coating may be regarded as non-wettable.

But, here is approved that chemical nickel coating, either posses a high value of contact angle - about 90°, has shown a good wettability when tin-based (60-40) alloy with $ZnCl_2$ as a flux are used, as in case for soldering to the structural steel Č1530.

The explained properties, poor wetting but satisfactory fluidity during soldering, may be regarded as contradictory in their nature.

References

[1] А. Кнаушер: Повишение качества поверхности и плакирование металлов, Москва 1984, Металлургија, стр. 94-98.
[2] M. Schlesinger, M. Paunović: Modern Electroplating, New York 2000, John Wiley&sons Inc, str. 667-684.
[3] D.R. Gabe: Principles of Metal Surface Treatment and Protection, Oxford 1972, Pergamon Press, str. 59-64.
[4] Л.Г. Заљцман, С.М. Чернаја: Спутник галъваника, Киев 1989, Техника, стр. 71-76.
[5] F.A. Lowenheim: Electroplating, New York 1978, McGraw-Hill Book Co, стр. 389-409.
[6] К.М. Вансковскаја: Галванические покритија, Ленинград 1984, стр. 83-86.
[7] М. Павловић, Д. Станојевић, С. Младеновић: Корозија и заштита материјала, Зворник 2012, Технолошки факултет, стр. 434-442.
[8] З. Карастојковић, З. Ковачевић: Нитрирање – термодифузиона метода заштите површина, у монографији: Корозија и заштита материјала, Београд 2012, ИТНМС и ИДК, стр. 657- 714.
[9] Z.Karastojković, Z.Janjušević: *Chemical Nickel Coatings for Reparation of one Pneumatic Controller*, 8th International Tribology Conference, Belgrade 2003, Proceed. Book, str. 133-136.
[10] V. Sedlaček: Non-ferrous metals and alloys, Amsterdam 1986, Elsevier, str. 356-360.
[11] А.А. Вабад-Захрјапин: Дефекти покритиј, Москва 1987, Енергоатомиздат, стр. 16-38.
[12] R.A. Walsh: Machining and metalworking, New York 1999, McGraw-Hill, str.

1459-1509.
[13] B. Malinović, J. Mandić, S. Bunić: Hemijsko taloženje kalaja na aluminijumu i njegovim legurama, Zaštita materijala, 54/2013/3, str. 297-300.
[14] Л.С. Мороз, Б.Б. Чечулин: Водороднаја хрупкост металлов, Москва 1967, Металлургија, стр. 7-116.
[15] Т.М. Ненадовић, Т. Павловић: Физика и техника танких слојева, Београд 1997, Институт Винча и Универзитет у Нишу, стр. 2-160.
[16] Л.И. Тушинскиј, А.В. Плохов: Иследование структури и физико-механических својств покритиј, Новосибиорск 1986, Наука, стр. 21-120.
[17] А.Л. Суворов: Структура и својства поверхностних атомних слоев металлов, Москва 1989, Енергоатомиздат, стр. 57-134.
[18] В.Е. Хрјапин: Справочник пајалшчика, Москва 1981, Машиностроение, стр. 67-72.
[19] А.П. Лопатко, З.В. Никофорова: Новие методи сварки и пајки, Москва 1979, Висшаја школа, стр. 59-80.
[20] Л.Л. Гржимаљскиј, А.И. Губин, и др.: Справочник по пајке, Москва 1984, Машиностроение, стр. 7-57.

ELECTROMAGNETIC FIELD AS A GRAIN REFINING TOOL IN Al ALLOYS

Aleksandra Patarić[1], Marija Mihailović[1], Zvonko Gulišija[1], Zoran Janjušević[1]

[1]*Institute for Technology of Nuclear and Other Mineral Raw Materials, Franchet d'Esperey 86, 11000 Belgrade, Serbia*

Abstract

In this paper the effect of electromagnetic field (EMP) during the continuous casting process of an AA7075 Al alloy was investigated. Results showed that EMP can efficiently refine the grain structure of the ingots, which resulted in a reduced inhomogeneity of alloying elements distribution along the radius of ingots, as well as in a reduced porosity of interdendritic type, which can provide better mechanical properties of the tested AA7075 Al alloy. It was also observed that more uniform and homogeneous microstructure of the castings can be achieved using an optimal electromagnetic frequency.

Keywords: Al alloy, electromagnetic field, microstructure

Introduction

Electromagnetic casting process is one of the most promising technologies developed by combining the magneto hydrodynamics and casting techniques. Electromagnetic casting (EMC) provides the opportunity which has never been achieved by conventional casting process. At the beginning of the invention, the application of electromagnetic casting had been aimed in order to obtain a better ingot surface quality, due to the reduced contact pressure between the mould and the metal. The reduced contact pressure is the result of potential force acting, as a horizontal component of Lorentz force density, which is being balanced by static pressure of the molten metal, thus resulting in the formation of the convex surface meniscus [1-5]. The other component of the Lorentz force density is a rotational component, resulting in a forced convection in the molten metal, enabling enhanced flow of the melt and homogeneous bulk distribution of alloying elements [6-9]. Some researches show that combining the main operating parameters of electromagnetic field, such as frequency and strength of electromagnetic field, this process can efficiently eliminate different defects present in the as cast ingots. In this way, the great savings in energy and time can be achieved. The investigations on the effect of electromagnetic, magnetic and hydrodynamic phenomena in producing of Al ingots started over a decade ago, but very little attention was paid to the characterization of microstructure and evaluation of the quantitative microstructural parameters.

In this paper the special attention was paid to the effect of electromagnetic field on the microstructure of AA7075 Al alloy. The aim of this research was to establish the possibility to improve the structure and to obtain better quality of

ingots at the beginning of production process through the proper combination of the main operating parameters.

Experimental

Chemical composition of the tested EN AW 7075 alloy is given in Table 1.

Table 1 Chemical composition of alloy EN AW 7075 (wt%)

Element	Zn	Mg	Cu	Mn	Cr	Fe
Content (wt%)	5.51	2.29	1.45	0.13	0.19	0.14

This alloy is among heat treatable Al alloys with very high strength level and a wide range of applications in aero and military industry. However, it is characterized by a number of defects that occurs during conventional solidification process, such as porosity, hot cracks, non-uniform grain size and crystal segregation.

Electromagnetic casting process was performed using a medium frequency induction furnace with 100 kg capacity, equipped with a drainpipe at the bottom of the furnace, and a graphite crystallizer that was intensively water cooled. The low frequency magnetic field was placed around the crystallizer. The testing samples were taken out of ingots with a diameter of 80 mm, obtained by vertical continual casting. The casting temperature was in the range of 710-720°C and the average casting speed was 1,5 mm/s. The frequency of electromagnetic field was 30 Hz, according to our previous experience which showed that this is the optimal frequency [10]. The current intensity was 200 A.

The microstructure and the frequency of the electromagnetic field are closely related. The samples series 1 were obtained from the ingot casted without the presence of electromagnetic field to enable the evaluation of the field effect on the microstructure at samples series 2, obtained from the ingot casted in the presence of electromagnetic field with the frequency of 30 Hz.

Microstructure of the tested samples was examined by optical microscopy using the image analysis device Leica Q500MC. Specimens were prepared by standard metallographic procedure and etched by Keller's reagent in order to reveal the morphology of Al segregation-solid solution and inter-metallic phases. The variation in content of the main alloying elements, Zn and Mg, was determined by chemical analysis of the samples taken from the cross section of both ingots: those obtained with and without the influence of electromagnetic field.

Results and Discussion

Microstructure of the samples produced without the effect of electromagnetic field (marked as sample 1 from series 1) was compared with microstructure of the samples from series 2 (marked as sample 2), which were obtained under the influence of electromagnetic field (Fig. 1). It is obvious that the structure of sample 1 is more dendritic than the structure of sample 2, which is more finer with pronounced cells in the structure. The characteristic microstructure appearance at the cross section of samples casted under different conditions is shown in Figure 1. As it is shown, the cellular/dendritic morphology is the result of Al segregation from

the solid solution during the solidification process. Nevertheless, the morphology of the samples casted without the electromagnetic field effect, Figure 1a, is more dendritic, in comparison with very pronounced cells shown in Figure 1b, for the specimen obtained under the influence of electromagnetic field.

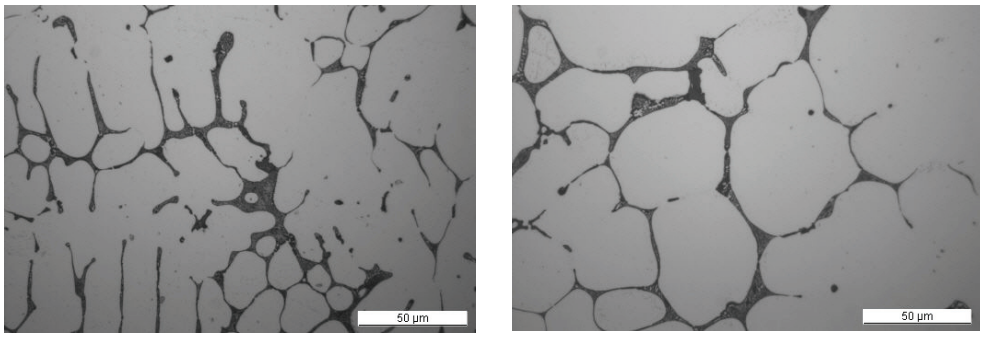

(a) *(b)*

Fig. 1. Microstructure of the cross section of the: sample 1 cast without EMP (a) and sample 2 cast under the effect of EMP (b). Etched by Keller's reagent, 500x.

Besides that, the presence of porosity of interdendritic type was established in sample 1, which was taken from the ingot casted without the electromagnetic field effect, as can be seen in Figure 2.

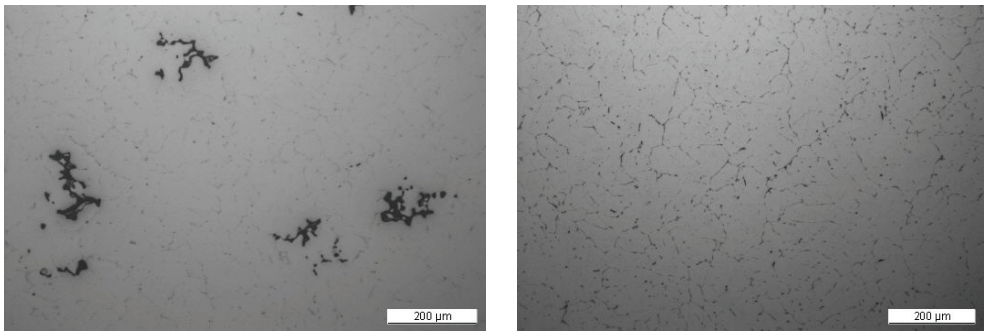

(a) *(b)*

Fig. 2. The porosity of interdendritic type: sample 1 (a) - without the electromagnetic field effect, and sample 2 (b) - with the electromagnetic field effect. Etched by Keller's reagent, 100x.

The influence of the potential component of the Lorentz force density, besides the microstructure, can be observed at the macro level of the surface quality, as well. The quantitative measure of this influence can be followed through the analysis of the alloying elements content from the ingot surface, in sequential steps measurements, towards the ingot center.

The variation of elements content through the entire cross section was examined using chemical analysis. Figure 3 shows the distribution of two alloying elements, Zn and Mg, along the radius of ingots. Large inhomogeneity in the distribution of alloying elements can be observed for the castings that were produced without the influence of electromagnetic field, while those produced under electromagnetic field were characterized by more homogeneous distribution of Mg and Zn.

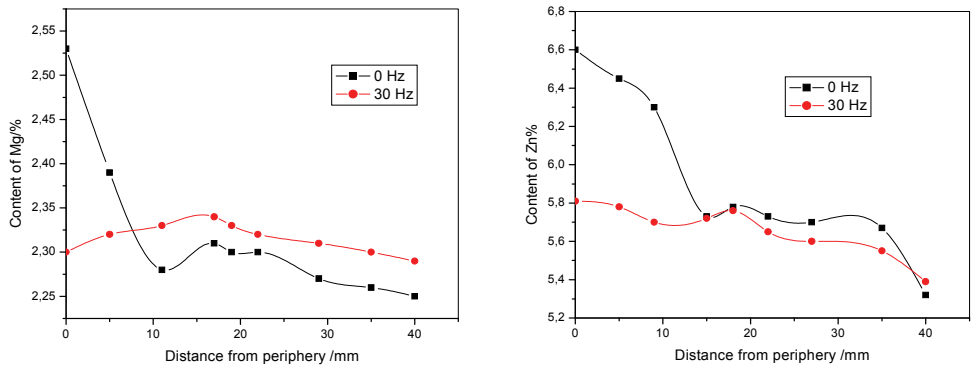

(a) *(b)*

Fig. 3. Content of Mg element (a) and content of Zn element (b) along radius of samples produced under different casting conditions.

On the surface of ingots the content of alloying elements is significantly higher than in the center. It was supposed that application of the electromagnetic field reduces the undercooling effect because the contact line between mold and metal is smaller, as the result of potential force, a horizontal component of Lorentz force density acting. In this way the inhomogeneity of alloying elements distribution is reduced.

Conclusion

The results of this study indicated the evident influence of electromagnetic field on the casting process of AA7075 Al alloy. It was shown that electromagnetic casting (EMC) process has the advantages over conventional casting in terms of obtaining better surface quality and more uniform fine-grained microstructure of the ingots.

The specimens obtained by electromagnetic casting process, with a frequency of 30 Hz, have finer and more homogeneous microstructure than those produced without electromagnetic field influence. The porosity of interdendritic type and inhomogeneity in distribution of the alloying elements through the entire cross section of the specimens are reduced after EMC process.

Better surface quality of the EMC produced specimens could eliminate the subsequent surface machining, while the uniform and finer microstructure gives the possibility to shorten the time of heat treatment. Avoiding the necessity for the

machining and prolonged homogenization, significant savings in casting material, energy and time can be achieved.

Acknowledgement

The authors wish to acknowledge the financial support from the Ministry of Education, Science and Technological Development of the Republic of Serbia through the project TR34002.

References

[1] Zhihao Z, Jianzhong C, Jie D (2007) Effect of low-frequency magnetic field on microstructures and macrosegregation of horizontal direct chill casting 7075 aluminum alloy. J Mater Process Technol 182:185-190

[2] Zhihao Z, Jianzhong C, Jie D, Zhefeng W (2005) Effect of low- frequency magnetic field on microstructures of horizontal direct chill casting 2024 aluminum alloy. J Alloy Comp 396:164-168

[3] Beijiang Z, Guimin L, Jianzhong C (2002) Effect of Electromagnetic Frequency on Microstructures of Continuous Casting Aluminum Alloys. J Mater Sci Technol 18:401-403

[4] Zhang B, Cui J, Lu G, Zhang Q, Ban C (2003) Effect of electromagnetic field on macrosegregation of continuous casting 7075 alloy. Trans Nonferrous Met Soc China 13:158-161

[5] Zhu Q, Zhao Y, Cui J, Zuo B, Qu F (2008) Effect of low-frequency electromagnetic field on the as casting microstructures and mechanical properties of HDC 2024 aluminum alloy. Acta Metall Sin 21:205-210

[6] Jie D, Jianzhong C, Fuxiao Y, Chunyan B, Zhihao Z (2004) Effect of low-frequency electromagnetic casting on the castability, microstructure and tensile properties of direct chill cast Al-Zn-Mg-Cu alloy. Metall Mater Trans 35:2487-2494

[7] Yubo Z, Jianzhong C, Jie D, Fuxiao Y (2005) Effect of low frequency electromagnetic field on the constituents of a new super high strength aluminum alloy. J Alloy Comp 402:149–155

[8] Jie D, Cui J, Yu F, Zhao Z, Zhuo Y (2006) A new way to cast high-alloyed Al–Zn–Mg–Cu–Zr for super-high strength and toughness, J Mater Process Technol 171:399–404

[9] Cui J, Zhang Z, Le Q (2010) DC casting of light alloys under magnetic fields. Trans Nonferrous Met Soc China 20:2046-2050

[10] Patarić A, Gulišija Z, Marković S (2007) Microstructure Examination of Electromagnetic Casting 2024 Aluminum Alloy Ingots. Prakt Metallogr 44:290-298

THE APPLICATION OF THE DENSE COMPOSITE POLYMER MEMBRANES FOR THE WASTE GASES TREATMENT

Dragutin Nedeljkovic, Aleksandar Grujic, Aleksandar Stajcic, Mirko Stijepovic, Jasna Stajic-Trosic

University of Belgrade, Institute of Chemistry, Technology and Metallurgy, Njegoseva 12, 11000 Belgrade, Serbia

Abstract

The main task of this work is to construct the polymeric membrane that could be used for the waste gases treatment. The constructed membranes were of a dense type, based on a solubility/diffusivity mechanism. The feasibility of the application of poly(ethyleneoxid)-*co*-poly(phtalamide) was tested. Three types of used zeolites were with the 3-dimensional pores (ZSM5; Faujasite, Linde type A) and one type was with the 1-dimensional pores (Linde type L). As an additive, n-tetradecyldimethylamonium bromide– n-C14TMABr was tested. The best results in carbon dioxide/hydrogen selectivity and permeability were obtained with the membrane constructed with PEBAX 1657 and surface treated zeolite. The obtained permeability of carbon dioxide was 128 Barrer, and the carbon dioxide/hydrogen selectivity was around 10.

Keywords: waste gases treatment, gas separation, composite membranes, zeolite, membrane permeability

Introduction

In recent decades, the global warming appeared as one of the major threat to the environment. The carbon dioxide is emitted in the atmosphere trough the various processes of combustion. The carbon dioxide separation based on the membranes is suitable in small and medium scales with moderate requirements concerning the purity of the products. [1]. The interest for the membrane material suitable for the CO_2 separation has rapidly increased in last 25 years, and during that time, various polymer materials were examined [2], [3], [4] and [5]. In recent years [11], the ethylene oxide units in polymer chains have been proved to enhance the solubility of the carbon dioxide and to achieve the high selectivity of carbon dioxide versus other gases. Commercially available polymer under the name PEBAX (supplier Arkema, formerly Atotech) has the structure of poly(amide-*b*-ether) and can be used as good alternative material for this purpose [6].

The chemical, physical and mechanical properties of both of the polymers can be easily modelled by the simple variation of the molar ratio of the blocks [7]. Both Pebax and Polyactive have been shown as promising membrane materials for acid gas treatment [8], [9], [10] and [11]. The high selectivity of the carbon dioxide versus nitrogen and hydrogen was reported for the membranes based on those polymers [8]. In order to improve selectivity and permeability, various particles can be added. Those particles can be zeolites, carbon molecular sieves

or nanoparticles. Due to the flexibility of the polymer used as the matrix, the fragility as the main problem of the inorganic membrane is avoided.

Experimental

The Pebax and Polyactive polymers were supplied by the Arkema and IsoTis OrthoBiologics respectively. The zeolites were supplied by the Institute of Technology of Nuclear and Other Mineral Raw Materials.

Table 1. Properties of different types of zeolite used for the preparation of the membrane

Type	Framework type code	Channel system, dimension	Pore size, nm
ZSM-5	MFI	3d	0.52 X 0.55
Faujasite	FAU	3d	0.74 X 0.74
Linde Type L	LTL	1d	0.71 X 0.71
Linde Type A	LTA	3d	0.41 X 0.41

Ethanol, chloroform, zeolite and n-tetradecyl trimethylammonium bromide (NTAB) were used as received. The aim of the addition of the filler is to provide good contact between the highly charged zeolite particles and hydrophobic polymer matrix. The Pebax was dissolved in the distilled water/ethanol mixture (70/30 wt.%). The solution was stirred for two hours at the 80°C under reflux. In the case of the Polyactive membranes, the chloroform was used as a solvent, and the solution process was conducted at the room temperature. At the same time, the zeolite particles were dissolved and the additive was added (for the samples with the additive). This dispersion was poured in the solution of the polymer and stirred overnight. The viscous solution that came as the result was casted on the Teflon surface. The solution was covered with non-woven textile and left overnight to dry at the room temperature and ambient pressure. Afterwards, the membrane was placed on the high vacuum line in order to remove any traces of the residual solvent.

The gas permeability measurements were carried out by the time lag method. The solubility (S), diffusivity (D), permeability (P) and selectivity (α) were determined by the equations [10] and [11]:

$$P = DS = \frac{V_p l (p_{p_2} - p_{p_1})}{ART\Delta t (p_f - (p_{p_2} + p_{p_1})/2)}$$

$$D = \frac{l^2}{6\theta}$$

$$\alpha_{A/B} = \frac{P_A}{P_B} = \frac{D_A S_A}{D_B S_B}$$

In those equations, Vp stands for the constant permeate volume, l for the thickness of the membrane, A for the area of the membrane, R for the universal

gas constant, Δt for the time that permeate pressure needs to increase from the value p_{p1} to the value p_{p2}, p_f for the feed pressure, and θ for the time lag. The solution-diffusion model was used for the analysis of the gas transport properties of the membranes [12]. The selectivity of the membrane for the gas A versus gas B was defined as the ratio of their permeability.

The procedure of the permeability measurements was as follows: After 30 minutes at the high vacuum line, the gas was applied at the one side of the membrane, while the other side was kept on vacuum. The change of the pressure during the time was measured at the vacuum side of the membrane, and the permeation properties of the membrane were determined by the equations 1-3.

Results and discussion

Six different series of the membranes were prepared, three with the each polymer. In the first series, no additive was added, and membranes were madefrom polymer and zeolite. In the second series, the additive was NTAB. The composition and the appearance of the membranes are presented in Tables 2 and 3.

Table 2. The composition and the appearance of the membranes

Number of Series	Polymer	Additive
Series I	Pebax	-
Series II	Pebax	NTAB
Series III	Polyactive	-
Series IV	Polyactive	NTAB

The composition and evaluation of the membranes from the series I are given in Table 3.

Table 3. The composition and the appearance of the membranes of the Series I

Membrane Number	Zeolite Filler	Filler, %	Appearance
I-1	FAU	22	white
I-2	FAU	22	white
I-3	FAU	22	white spots
I-4	LTA	22	white
I-5	LTA	22	white areas
I-6	LTL	22	transparent
I-7	ZSM	22	white

From the data presented in Table 3, it is obvious that only the LTL type of the zeolite can be used for the construction of other membranes. The contact between the polymer matrix and the particles of FAU, LTA and ZSM zeolites was not good, but the construction of the membranes with those fillers and the NTAB was attempted. White spots on the membrane made with FAU came as a consequence of the agglomeration of the zeolite particles. The possible reason for this

agglomeration is strong electrostatic forces between the particles of the filler that overcome the viscosity of the polymer solution during the drying procedure. The areas of the uneven color indicate the non-stationary drying process which causes rapid local variations in viscosity of the solution, and therefore, the agglomeration was allowed is some areas of the membrane.

Table 4. The composition and the appearance of the membranes from the Series II

Membrane number	Porous Filler	Filler, %	Additive, %	Appearance
II-1	-	-	3.3	transparent
II-2	FAU	22	3.3	white
II-3	FAU	22	3.3	transparent
II-4	FAU	22	3.3	white areas
II-5	LTA	22	3.3	white spots
II-6	LTL	22.5	2.2	transparent
II-7	LTL	23	1.1	transparent
II-8	ZSM	22	3.3	white

The membrane II-1 was made solely of polymer and detergent additive in order to check their compatibility. As the transparent membrane was yielded, it is reasonable to conclude that this detergent is a promising additive for the compatibillisation. Analyzing the appearance of the membranes constructed with this additive and other zeolites, it is obvious (Table 4) that only FAU and LTL types of zeolite could be used for the preparationof the acceptable membrane.

The Polyactive based membranes (Series III-IV) were made in the manner similar to the Pebax ones (Series I-II). The composition and the evaluation are presented in Table 5.

Table 5. The composition and the appearance of the membranes of the Series III

Membrane number	Porous Filler	Filler, %	Appearance
III-1	-	-	Transparent
III-2	LTA	22	Transparent
III-3	LTA	22	Transparent
III-4	LTA	32	white spots
III-5	FAU	22	white spots
III-6	FAU	22	white spots
III-7	LTL	22	Transparent
III-8	LTL	22	Transparent
III-9	ZSM	22	White

The samples III-2 and III-3 were made with LTA zeolite, and the first evaluation gave the good results. However, when the increase in the concentration of the zeolite was attempted (Sample III-4), the agglomeration occurred, and the white spots became visible. Similarly to the Pebax based membranes (Series I),

the LTL was shown as a good additive, resulting in the smooth, transparent membrane (Samples III-7 and III-8). The Samples III-5 and III-6 (made with FAU) contained white spots on the surface. Although this result appeared similar to that of the Pebax based membranes, the agglomeration was present in this case instead of the bad surface contact. . The composition of the membranes and their evaluation is presented in Table 6.

Table 6. The composition and the appearance of the membranes from the Series V

Membrane number	Porous Filler	Filler, %	Appearance
IV-1	-	-	Transparent
IV-2	LTA	22	white areas
IV-3	LTA	22	white areas
IV-4	FAU	22	white spots
IV-5	LTL	22	Transparent
IV-6	LTL	22	Transparent
IV-7	ZSM	22	White

Based on the observation of the Sample IV-1, it can be seen that the NTAB itself does not agglomerate, and therefore it can be used as an additive. Nevertheless, similarly to the analogous Pebax membranes, only the LTL resulted in a transparent and smooth membrane. The addition of the NTAB to the LTA type of zeolite (Samples IV-2 and IV-3) resulted in the formation of white areas on the membranes. This might be the consequence of excess of the zeolite. The presence of the additive does not influence the appearance of the membranes made with FAU and ZSM zeolites (IV-4 and IV-7 respectively). The sample IV-4 shows the strong agglomeration of the inorganic filler, while the sample III-7 provides no contact between the zeolite particles and the polymer.

For the measurements of the gas permeability and the selectivity, only smooth and transparent membranes were chosen. The results of permeability and selectivity measurements are compiled in Table 7.

Table 7. The results of the permeability measurement of the membranes

Membrane number	Thickness, μm	P (CO_2), Barrer	α (CO_2/H_2)	α (CO_2/O_2)	α (CO_2/N_2)
II-3	252	88	9.1	23	48
II-6	174	128	9.7	22	55
II-7	150	131	9.4	20	52
IV-2	217	142	11.8	23.5	62.4
IV-3	191	139	10.9	21.7	60.4
IV-7	121	130	9.2	20.9	54.7
IV-8	162	135	9.5	21.1	54.8
V-5	232	142	11.6	22.0	61.1
V-6	199	137	11.3	21.7	60.5

It should be noted that the usual unit for the gas permeability of the membrane in the membrane research community is Barrer. One Barrer is the permeability of 1 cm^3 of a gas under the standard pressure and temperature conditions, trough the 1 cm^2 of the area and 1 cm of the thickness driven by the pressure gradient of 1 cmHg in 1 s divided by the factor of 10^{-10}. Analyzing the permeability data presented in the Table 7, it is obvious that all of the membranes that appeared transparent have shown good and comparable permeability and diffusivity properties. The best results regarding the permeability and selectivity were gained by the dispersion of the LTA type of zeolite in the Polyactive. The results were good for both surface treated and non-treated zeolite. Concerning the Pebax based membranes, FAU and LTL yielded acceptable results, with the permeability and selectivity comparable to the Polyactive based membranes.

Conclusion

In this paper, the possibility to prepare the mixed matrix membrane based on the polymer matrix and the surface treated inorganic powder was examined. Concerning the membranes based on Pebax, only the LTL and FAU types of zeolites are compatible with both, the surface treatment reagent and the polymer. In the case of the ZSM5 and LTA types of zeolite, good contact between the particles and polymer chains could not be provided. In the case of the Polyactive based membranes, only the untreated LTL and LTA could be used. The NTAB has been shown to be good additive that does not negatively influence the properties of the membranes. The permeability of the polymer membrane filled with the zeolite increased by approximately the factor of 2, with the retaining the selectivity of the membrane. Therefore, it may be concluded that the mentioned polymer-zeolites combinations and NTAB as an additive are promising base for the future research. However, the downsizing of the thickness of the membrane will be the main challenge for the future work.

Acknowledgement

The authors would like to acknowledge the financial support of the Ministry of Science of Serbia, trough the research projects TR 34011 and III 45019.

References

[1] W.J. Koros and G.K. Fleming, Membrane-based gas separation. J. Membr. Sci., 83 (1993), pp. 1–80

[2] S.P. Nunes, K.-V. Peinemann, Editors , Membrane Technology in the Chemical Industry, (2nd edition), Wiley-VCH Verlag GmbH, Germany (2006), pp. 53–150

[3] K. Ghosal and B.D. Freeman, Gas separation using polymer membranes: an overview. Polym. Adv. Technol., 5 (1994), pp. 673–697

[4] R.W. Baker, Membrane Technology and Applications, McGraw-Hill, New York (2000), pp. 301–392

[5] R.W. Baker, Future directions of membrane gas separation technology. Ind. Eng. Chem. Res., 41 (2002), pp. 1393–1411

[6] P. Yu, Yampol'skii, I. Pinnau and B.D. Freeman, Materials Science of

membranes, John Wiley& Sons, England (2006), pp. 1–47
[7] H. Lin and B.D. Freeman, Materials selection guidelines for membranes that remove CO2 from gas mixtures. J. Mol. Struct., 739 (2005), pp. 57–74
[8] L.A. Utracki, History of commercial polymer alloys and blends, . Polym. Eng. Sci., 35 (1995), pp. 2–17
[9] G. Deleens, N.R. Legge, G. Holder, H.E. Schroeder, Editors , Thermoplastic Elastomers: A Comprehensive Review, Hanser Publishers, New York (1987), pp. 215–230
[10] M. Yoshino, K. Ito, H. Kita and K.-I. Okamoto, Effect of hard-segment polymers on CO2/N2 gas separation properties of poly(ethylene oxide)-segmented copolymers. J. Polym. Sci. Part B Polym. Phys., 38 (2000), pp. 1707–1715
[11] V. Bondar, B.D. Freeman, I. Pinnau and Gas Sorption, Characterization of poly(ether-b-amide) segmented block copolymers. J. Polym. Sci. Part B Polym. Phys., 37 (1999), pp. 2463–2475
[12] G. Wijmans and R.W. Baker, The solution–diffusion model: a review. J. Membr. *Sci.*, **107** (1995), pp. 1–21

EFFECTS OF THE ANNEALING TEMPERATURE AND TIME ON THE MICROSTRUCTURAL CHANGES AND CORRESPONDING MECHANICAL PROPERTIES OF COLD-ROLLED PdNi5 WIRES

Aleksandra T. Ivanović[1], Biserka T. Trumić[1], Svetlana Lj. Ivanov[2], Saša R. Marjanović[2], Silvana B. Dimitrijević[1], Vesna M. Marjanović[1]

[1]*Mining and Metallurgy Institute Bor, Zeleni bulevar 35, Bor, Serbia*
[2]*University of Belgrade, Technical faculty in Bor, VJ 12, Bor, Serbia*
aleksandra.ivanovic@irmbor.co.rs

Abstract

The microstructural changes and corresponding mechanical properties of cold-rolled PdNi5 wires were investigated in the function of annealing temperature (200-1000 ^{o}C) and annealing time (20-45 min) at a constant deformation degree. During the annealing of cold-rolled PdNi5 wires, decrease in the value of hardness (HV) and tensile strength (R_m) with an increase in value of elongation (A) was attributed to changes in the microstructure which occurred during recrystallization annealing. Annealing temperature of 500 ℃ was enough to activate the energy for various recrystallization processes which caused a change in the mechanical properties of cold-rolled PdNi5 wires. The annealing time, at constant annealing temperature, almost did not affect a recrystallization temperature and the mechanical properties of the cold-rolled PdNi5 wires.
Key words: PdNi5 wires, mechanical properties

Introduction

Phase diagram of PdNi shows that these components form solid solutions across all compositions with minimum on the liquidus and solidus curve (1273^{o}C at 45% Pd) [1]. This diagram was the subject of numerous researches [2-5]. Electric and magnetic behavior of the system Ni-Pd alloys were studied in the papers [6,7] and thermodynamic properties of Ni-Pd system alloys were investigated by authors [8]. The structure and surface of Pd-Ni alloys have been studied by different techniques [9,10]. Stress-rupture curves are often used to specify the high temperature performance of structural materials. According to the autor [11] pure platinum and palladium and their alloys, unlike nickel, do not suffer from a generic form of high temperature embrittlement or weakening on exposure to environments containing oxygen. The rupture properties of high purity palladium wires at 1200^{o}C were similar to those of the less purity. The catalytic activity of palladium is slightly changed by alloying with nickel [12-14]. Pure palladium is too soft to be used for chemical application in the production process of nitric acid [15]. Alloying palladium with nickel increases its mechanical properties significantly while the catalytic activity is not reduced.

The aim of this paper is to contribute to the establishment of a database of platinum metals, primarily a database on palladium and its alloys. For that purpose,

the hardness, tensile strength and elongation were investigated in the function of annealing time and annealing temperature at a constant deformation degree.

Experimental

All experimental investigations were carried out on PdNi5 samples with content of Ni in all samples 5%mass, Pd - purity 99,99% and Ni - purity 99,95%. Palladium, used for making all the samples, originating from the RTB Bor production of electrolytic copper, was obtained as a by-product. The additional refining treatment in the Mining and Metallurgy Institute was carried out in order to increase the purity of palladium. Impurities in the samples were: Ag, Cu, Fe, As, Sb and Bi. In order to achieve better compacting of materials, Pd-powder and Ni-sheet metal were pressed in a hydraulic press with pressure of 270 daN/cm^2.

Melting of PdNi5 alloy was carried out in the medium frequency induction furnace, in the MgO casting pot, size h_1xh_2 = 85x80mm, d_1xd_2 = 65x55mm. The casting temperature of the PdNi5 alloy was 1520^{o}C. Molten batch was overheated before casting for 150-170^{o}C. Casting was done in graphite mold, pre-heated at a temperature of 350-400ºC. Homogenization annealing of samples was carried out in an electric resistance furnace of chamber type LP08 at 900^{o}C for 30 minutes according to previous research [2,17]. Plastic processing of samples was performed on the two-cage rolling mills for wire, from 200x120mm to the dimensions of 1.7x1.7mm. After the rolling, PdNi5 alloy samples, in the form of wire, with the deformation degree of 97%, were subjected to recrystallization annealing as a type of heat treatment.

Hardness measurement was performed on the combined device for measuring the hardness by Vickers and Brinell, WPM (Werkstoffprüf-maschinen), Leipzig, Germany, with an applying force range from 5 to 250 daNmm^{-2}.

Mechanical characteristics of wire (Rm and A), were tested on a universal material testing machine Instron 1332, 100kN. The tubes were tightened by mechanical jaws and stretched with a speed of 10mm/s. Prior to testing all specimens were cut to a length of 150mm.

Chemical analysis of samples was done on the atomic absorption spectrometer (AAS, Produced by: Perkins & Elmer, Model: 403, Detection limit: <0, 0001g/dm^3).

Microstructure testing of the alloy was done on samples with a diameter of 20 mm and 5 mm in height. The samples were prepared according to standard procedure. The general morphology of the samples was tested using the scanning electron microscope (SEM model: JEOL JSM - 6610LV).

Results and discussion

The results of dependence of the hardness, HV, of cold deformed samples, in the function of annealing temperature and time, for $\varepsilon = 97\%$, are shown in figure 1. The results of dependence of tensile strength, Rm, in the function of annealing temperature and time, for $\varepsilon = 97\%$, are shown in figure 2. The results of dependence of elongation, A, in the function of annealing temperature and time,

for $\varepsilon = 97\%$, are shown in figure 3. The results of microstructure testing are shown in figure 4.

Based on the presented results of investigations of hardness changes as a function of annealing temperature (Fig. 1) it can be concluded that the hardness values of the cold deformed alloy for temperatures below 400°C do not change, but internal stresses are removed. There are no structural changes compared to the structure of the cold-deformed sample, which was registered by metallographic tests (Fig. 4a)). In the temperature range of 400-500°C, the recovery interval of crystals, there is a slight decrease in hardness due to the removal of internal stresses as well as the recovery of the crystal structure by removing small defects in the lattice due to the increased speed of diffusion of atoms. At 500°C hardness decreases sharply which indicates that a texture change occured, ie. a new structure has been formed.

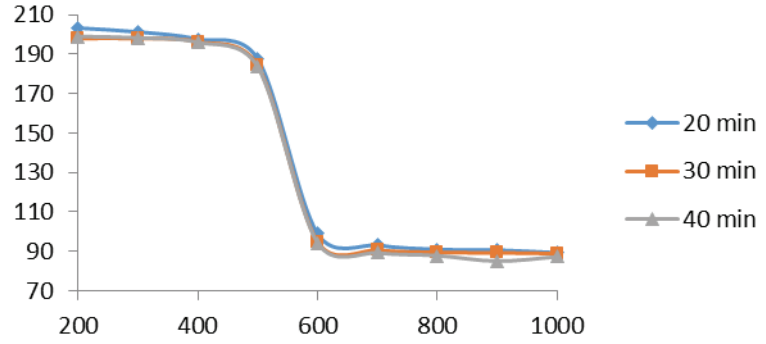

Fig. 1. Dependence of PdNi5 hardness of annealing temperature and annealing time

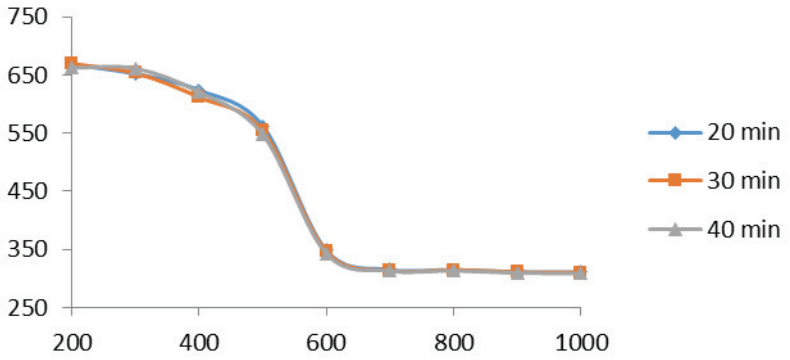

Fig. 2. Dependence of tensile strength of annealing temperature and annealing time

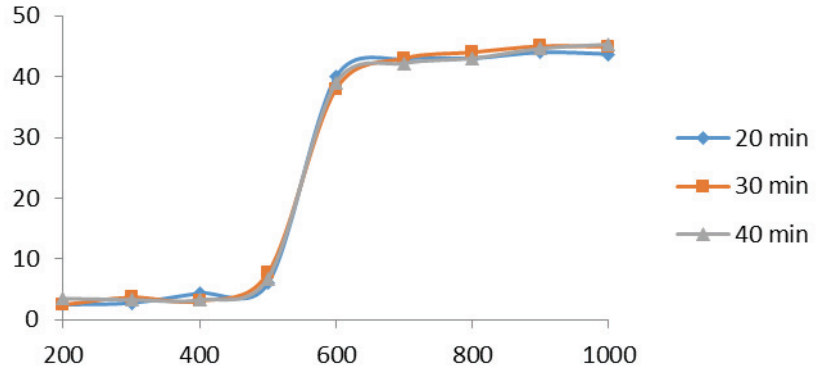

Fig. 3. Dependence of elongation of annealing temperature and annealing time

In the temperature range of 400-500℃, the recovery interval of crystals, there is a slight decrease in hardness due to the removal of internal stresses as well as the recovery of the crystal structure by removing small defects in the lattice due to the increased speed of diffusion of atoms. At 500℃ hardness decreases sharply which indicates that a texture change occured, ie. a new structure has been formed . The newly formed structure, during the primary recrystallisation which occurs in a narrow temperature range from 500-600℃, is polygonal with unstrained grains (Fig. 4b)). Further increase of the annealing temperature above 600℃ leads to a gradual, but quite small, hardness decrease, due to an increase in grain size, which is a sign of secondary recrystallization (Fig. 4c)).

Based on the presented results of investigations of tensile strength changes as a function of annealing temperature (Fig.2) it can be seen that the tensile strength of cold-worked and differently heated PdNi5 alloy samples in the form of wire, does not change continuously with increasing temperature annealing. Tensile strength practically does not change to a temperature of 400℃, while in the temperature range 400-500℃ there is a slight decrease in its values. This is a result of reducing the concentration and redistribution of errors in the lattice. At 500℃ there is a sharp decrease of tensile strength. This change takes place in a very narrow temperature range (500-600℃) and is the result of progression of the recrystallization process and the formation of a new, undeformed structure, which is registered by metallographic examination (Fig. 4b)). Further increase of the annealing temperature, above 600℃, leads to grain growth which causes a further slight decline in tensile strength as a consequence of the occurrence of secondary recrystallization, that is coarsening of the structure (Fig.4c)).

From the presented results of investigations of relative elongation changes as a function of annealing temperature (Fig. 3) it can be seen that the relative elongation with an increase in the annealing temperature to 400℃ practically does not change, while in the temperature range 400-500℃ there is a slight increase in the values of relative elongation. At 500℃ there is a rapid increase in the relative elongation values. Further increase of the annealing temperature, above 600℃, causes a slight increase in the relative elongation values. Considerations related to

the causes of the of tensile strength behavior apply also for the relative elongation changes.

Also, it was observed that time of recrystallization annealing insignificantly affects recrystallization temperature, and thus the mechanical properties of the alloy PdNi5. The values of the mechanical characteristics (HV, Rm and A) almost have identical values for different times at the same annealing temperatures.

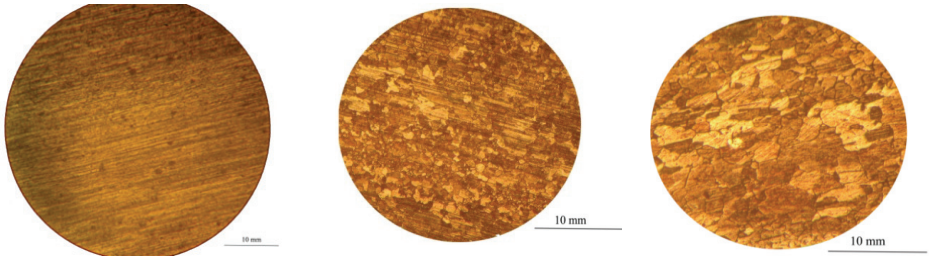

a) *b)* *c)*

Fig. 4. Optical microphotographs of the alloy deformed 97 %, after annealing for 30 minutes at: (a) 500°C, (b) 700°C, (c) 900°C. The samples are quenched in water.

The energy that accumulates during deformation makes cold-worked metal thermodynamically unstable. Therefore, there is a tendency that cold-worked metal go back to a state with lower Gibbs energy, which is closer to equilibrium-undeformed state. This transition is caused by a number of mechanisms that are associated with thermal mobility of atoms of the crystal lattice, with the diffusion processes, recreep of dislocation, transverse slide of dislocation [18]. These processes gradually activate during alloys heating, leading to a reduction in the orientation of the metal grains - distorted parts of structures and restoring the properties to a state similar to that before deformation.

In our case, for all samples, regardless of the duration of the recrystallization annealing process, annealing temperature of 500^0C was enough to activate the necessary energy for taking place of various processes which cause a change in the mechanical properties of the PdNi5 alloy. As a result there has been a decline in the value of the hardness and tensile strength, at the expense of an increase in elongation as a function of annealing temperature.

Concrete contribution of these investigations results is precise determination of heat treatment parameters in the processing of platinum metals in Mining and Metallurgy Institute Bor.

Conclusions

By analyzing the obtained results of tests conducted on PdNi5 alloy samples it can be concluded the following:

- By testing the hardness of PdNi5 alloy samples as a function of annealing temperature, for the deformation degree of 97%, it was observed a sudden

decrease that corresponded to the recrystallization temperature of the tested samples.

- Annealing time almost did not affect a recrystallization temperature, and therefore the mechanical properties of the PdNi5 alloy samples.
- In the temperature range of 400-500℃, that is in the interval of recovery of crystals, there is a slight decline in the values of hardness and tensile strength, while the relative elongation values slightly increase, due to the removal of internal stresses as well as the recovery of the crystal structure by removing small defects in the crystal lattice due to increased rate of the atoms diffusion.
- Due to the progression of the recrystallization process and the formation of a new, undeformed structure at 500 ℃ there is a rapid decline in the values of hardness and tensile strength with a simultaneous increase in the relative elongation values. These changes take place in a very narrow temperature range of 500-600 ℃.
- Further increase of the annealing temperature above 600 ℃ leads to the gradual, but quite small, decline in the values of hardness and tensile strength with a simultaneous slight increase in the relative elongation values as a result of the occurrence of secondary recrystallization that is coarsening of the structure.

Acknowledgement

The research results presented in this paper are the result of technological development project TR 34029 "Development of production technology of Pd catalyst-catchers to reduce losses of platinum in high temperature catalysis processes", funded by the Ministry of Education, Science and Technological Development.

References

[1] http://resource.npl.co.uk/mtdata/phdiagrams/ nipd.htm

[2] Ivanović Aleksandra T., Trumić Biserka T., Ivanov Svetlana Lj., Marjanović Saša R., Modeling the effects of temperature and time of homogenization annealing on the hardness of PdNi5 alloy, Hem.Ind. , 68(5)2014, 597-603.

[3] P. V. Petrenko, A. V. Gavrilyuk, N. P. Kulish, N. A. Mel'nikova and Yu. E. Grabovskii, Structural Changes During Annealing of Deformed Pd-25 at % Ni Alloy, The Physics of Metals and Metallography, Volume 108(5)2009,449-454.;

[4] S. Helfensteyn, J. Luyten, L. Feyaerts, C. Creemers, Modelling Surface Phenomena in Pd–Ni Alloys, Applied Surface Science 212–213 (2003),844–849.

[5] Thomson, A. I. and Winterbottom, J. M. (1987), Silica-supported alloy catalysts for triglyceride hydrogenation: The preparation and properties of Pd–Ag and Pd–Ni systems. J. Chem. Technol. Biotechnol., 37(4): 257–270.

[6] H. Takahashi, S. Fukatsu, S. Tsunashima, S. Uchiyama, Perpendicular Magnetic Anisotropy of Pd/Co- and Pd/Ni-multilayers, Journal of Magnetism and Magnetic Materials 104–107(3)(1992), pp. 1831–1832.

[7] A Tari, B. R. Coles, Electrical Resistivity and the Transition TO Ferromagnetism in the Palladium-nickel Alloys, Journal of Physics F: Metal Physics 1(6) L69(1971).
[8] L. R Bidwell, R Speiser, The Relative Thermodynamic Properties of Solid Nickel-palladium Alloys, Acta Metallurgica,13(2)1965, 61–70
[9] T. Piotrowski, D.J. Acchinno, Materials Characterization,39 (2-5) (1997) 299.
[10] M. Kasprzak, D. Baither and G. Schmitz, Diffusion-induced Recrystallization in Nickel/palladium Multilayers, Acta Materialia, 59(4)2011,1734–1741.
[11] P. G. Boswell, The High Temperature Stress-Rupture Properties of Platinum and Palladium, The effect of environment and composition on service performance, Platinum Metals Rev., 1982, 26, (l), 16-19
[12] Zhaolin Liu, Xinhui Zhang, Liang Hong,Physical and electrochemical characterizations of nanostructured Pd/C and PdNi/C catalysts for methanol oxidation, Electrochemistry Communications, 11(4)2009, 925 -928.
[13] Cuicui Qiu, Ran Shang, Yafei Xie, Yanru Bu, Chunyun Li, Houyi Ma, Electrocatalytic activity of bimetallic Pd–Ni thin films towards the oxidation of methanol and ethanol, 120(2-3) 2010, 323-330.
[14] Chunyu Du, Meng Chen, Wengang Wang, Geping Yin, Pengfei Shi,Electrodeposited PdNi2 alloy with novelly enhanced catalytic activity for electrooxidation of formic acid, Electrochemistry Communications 12(6)2010, 843-846.
[15] Grigory Raykhtsaum, Leach Garner, PGM Highlights: Platinum Alloys: A Selective Review of the Available Literature, Platinum Metals Rev., 2013,57,(3),202-213
[16] B.Trumić, D.Stanković, A.Ivanović, The Impact of Cold Deformation, Annealing Temperatures and Chemical Assays On the Mechanical Properties Of Platinum, Journal of Mining and Metallurgy, Section B: Metallurgy 46B (1)-2010., 51-57.
[17] Aleksandra T. Ivanovic, Biserka T. Trumic, Nikola S. Vukovic, Sasa R. Marjanovic, Bata R. Marjanovic, The influence of melting atmosphere and casting on the mechanical and structural characteristics of palladium-nickel alloy, Journals of optoelectronics and advanced materials, 16(7-8), 2014, p. 925 – 932.
[18] Bosko Perovic, “Physical Metallurgy”, University of Montenegro, Faculty of Metallurgy and Technology, Podgorica, 1997.

IMPROVEMENT OF EJECTION TEST USED FOR EVALUATION OF SOLDERING TENDENCY BETWEEN CASTING AND DIE MATERIALS

P. Terek *, L. Kovačević, A. Miletić, D. Kukuruzović, B. Škorić, D. Kakaš

Faculty of Technical Sciences, Trg Dositeja Obradovića 6, 21000 Novi Sad, Serbia, palterek@uns.ac.rs*

Abstract

Alloy soldering is a serious issue in high pressure die casting of Al-Si alloys. It impairs the tool integrity, affects the casting quality and causes production downtime. In development of new materials resistant to soldering, ejection test is conveniently employed for soldering tendency evaluation. The aim of this research is to investigate the parameters that predominantly affect the ejection test results and on that basis make improvements. Examination was conducted concerning two currently used and one newly proposed method for obtaining the pin-casting assembly by gravity die casting of Al-Si alloy. After the pin ejection, the casting and pin surfaces were optically examined. Deeper insight into the solidification pattern is obtained through casting process simulations. It was found that both current testing procedures result with insufficient or oxidized casting-pin contact that markedly affects the attained results. A new design of experimental die used for producing the pin-casting assembly is proposed for obtaining improved sample quality and increased test reliability.

Keywords: die casting, soldering tendency, aluminium, ejection test

Introduction

Molten aluminium has a high affinity towards the iron contained in steel used for die casting dies [1] [2]. Interaction of an Al-Si alloy and steel die during the die casting process induce formation of intermetallic layers. Consequently the cast alloy easily adheres to these layers and develop an even thicker soldering built-up layer [1]. During the high pressure die casting process developed soldering severely affects the casting quality and on the long run impairs the tool integrity [1][3]. Therefore, development of materials less prone to the soldering in contact with Al-Si alloys is an ever challenging task [1][2][3]. Evaluation of soldering tendency is usually done by in-plant trials, on particular production tools [2], or conveniently by more practical ejection test [1][3][4][5].

In ejection test, pin made of desired material is used as a central core for casting a cylinder with hole made of an alloy of interest. A pin-casting assembly produced in this way represents the sample used for the ejection test. Pin ejection is carried out by tensile testing machine while a load displacements curve is recorded. This “ejection curve” contains information about the joint strength where the maximal force is a measure of soldering tendency (adhesion) between tested materials [1][3].

So far, the ejection test has been employed in different variations by two groups of researchers [1][3][4][5]. These tests mainly differ in the casting method applied for the production of ejection test samples. The thing in common for these casting procedures is the orientation of the pin in the casting experiment. In both cases pins protrude vertically downward into the casting and the pin immersion depth is determined form the melt free surface. Additionally in both cases feeders were not applied. Such tool arrangement and casting design does not provide sufficiently good conditions for achieving a sound casting volume around the experimental pin.

Considering the rules of the casting technology together with the physics of examined tribo-system, concern is raised about the quality of the results published so far in this field. Major concerns are directed towards quality of the pin-casting contact. Therefore, the motivation of the presented investigation is to eliminate the formation of casting defects that affect the test results and accordingly to increase the reliability of the ejection test.

Experimental methodology

Cylindrical pin samples with dimensions of ϕ15x100mm (Figure 1 a) were used as a sample cores for obtaining pin-casting assembly used for the ejection tests Figure 1 b). Pins were made of X38CrMoV5 hot-working tool steel fine grinded and polished with diamond paste (granulations 6μm, 3μm) what was followed by plasma nitriding. Casting alloy used in investigation is a commercial EN AB46200 alloy. Alloy was melted in resistance furnace, heated to a temperature of 730°C and held for few hours before casting. In all tests casting process was performed by gravity melt pouring using a graphite ladle. Die used for casting was made of X38CrMoV5 hot-working tool steel and it is used in two setups for obtaining the pin-casting assemblies. Firstly the die was specially set up for replication of currently used methods. The bottom hole made for a pin placement in a new method, was closed to form the casting flat surface Figure 1 d). While secondly, for the newly proposed method, this bottom hole was used to place the pin protruding from the bottom into the die cavity, Figure 1 c).

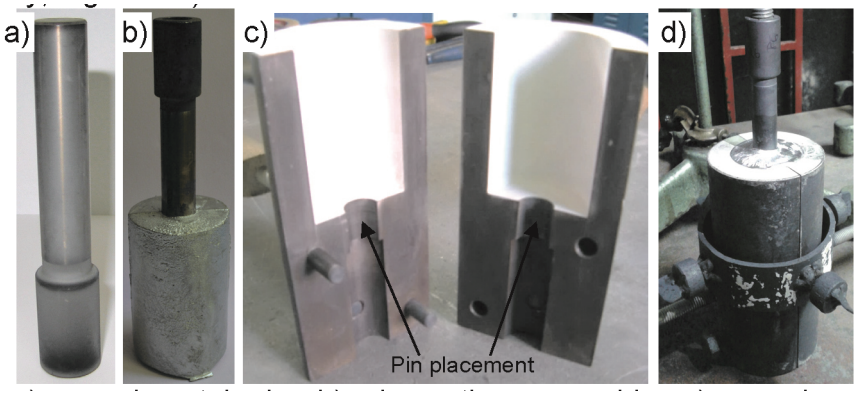

Fig. 1. a) experimental pin, b) pin-casting assembly, c) experimental die d) experimental set up for casting Methods 1 and 2

Pin-casting assemblies were obtained applying three different methods:

Method 1 – After pouring the cylindrical die cavity with Al-Si melt, samples were immediately immersed into the liquid casting, protruding from the top free surface. The experimental pin was held by special fixture used to maintain the pre-set pin immersion depth of 20mm. As a result of solidification of such assembly sample for ejection test is obtained. In this method the die and the pin were not heated prior to the casting process.

Method 2 – The experimental pin was placed in the die cavity, by holding arm that ensured the immersing depth of 20mm, set from the top free surface. Liquid metal was poured into the die near the pin. As in the previous *Method 1* die and the pin were not preheated.

Method 3 – The Newly proposed method – Prior to casting, the samples and die were preheated to a temperature of 320°C. Sample was positioned in the die, protruding 20mm into the cavity from the bottom. After 120 seconds, casting with in-casted sample was taken out from the die and the whole casting cycle is repeated for next sample.

Mechanical tensile testing machine was employed for the ejection test. The outcome of the ejection test is the so called ejection curve which is basically a force-displacement curve. The ejection curve includes information about the soldering and adhesion of aluminium in contact with the tested pin. Maximal force recorded during the tests represents the adhesion force of a joint and it is used for comparison of different materials or surface layers tested. Additionally, after the ejection tests pins were subjected to macroscopic and microscopic examinations.

Insight into the solidification pattern and temperature fields provides valuable information for the comparison and evaluation of investigated methods. Therefore the investigated casting methods were numerically simulated by MAGMA^5 5.2 software. Inputs in numerical simulations were the used casting parameters and the one determined by thermal analyses carried out during experiment.

Results and Discussion

Appearances of sample assemblies casted by different methods are presented in Figure 2. A surface near the location where the pin enters the casting differs depending on the casting method applied. Method 1 and 2 resulted with irregular surfaces covered with oxides and wrinkles. On the other hand, sample assemblies produced by newly proposed method 3, have flat and very smooth surfaces where the material is evenly spread around the circumference of the pin.

The observed differences arise as a consequence of a different solidification pattern. In investigated methods relative orientation of pin and a casting free surface are different. These differences induce different feeding behaviour during the casting solidification and accordingly different conditions for shrinkage and piping formation.

In methods 1 and 2, the casting free surface is the highest point in the casting and it coincides with location of the pin placement. In these cases, the region around the pin is the one that solidifies the last and consequently the one that will provide liquid metal for other parts of the solidifying casting. Due to the

shrinkage, in this region cavities are formed and the casting free surface lowers and cause decrease of immersion depth.

In method 3 the castings free surface is also the highest point of the casting while it still does not correspond to the surface where the pin enters the casting. In this method the pin is located on the casting side opposite to the casting free surface. Therefore, it is ensured that pin proximity will be away from the region where the shrinkage cavities form and the lowering of the free surface occur. In such method an even immersion depth is assured that could be repeated in every casting test.

Irregular casting surface around the pins consequently induce variable pin immersion depth, difficult depth repetitiveness, large test scatter and uneven spread of load during the pin ejection. Generally all these consequences would lead to uncertain results of ejection test and thus difficult comparison of different samples. Although methods 1 and 2 were applied in investigations presented in in papers [1][3][4][5] previously discussed issues of casted assemblies were not considered.

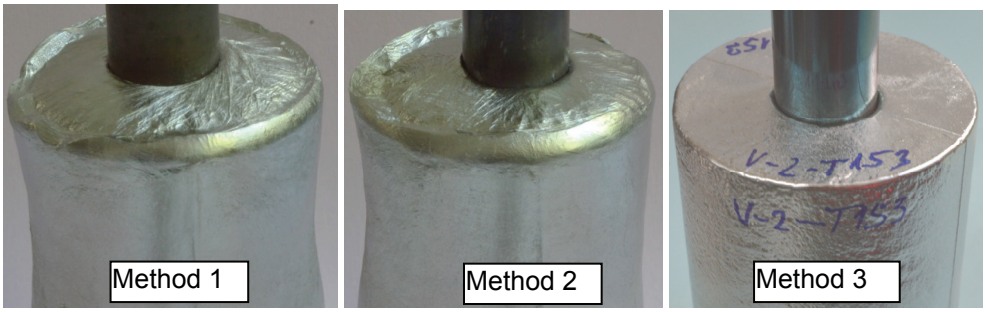

Fig. 2. Appearance of sample assemblies produced by different methods

After the ejection test detailed examination of pins and castings surfaces led to additional findings. Images of castings inner walls and corresponding pins are presented in Figure 3. These images provide information about the solidification in contact zone and therefore about the contact quality. It have to be pointed out that the most important factor affecting the quality of the ejection test results is the characteristic of the contact achieved between the casting and the experimental pin. Examination of the pins revealed that surfaces of all pins are covered by the soldering built up layer of Al-Si casting alloy. This built up layer is not uniformly spread on all pins. Pins ejected from the castings made by method 1 and 2 display a non-uniform coverage by Al-Si layer. This is explained by morphology of corresponding inner casting face that is formed by pin.

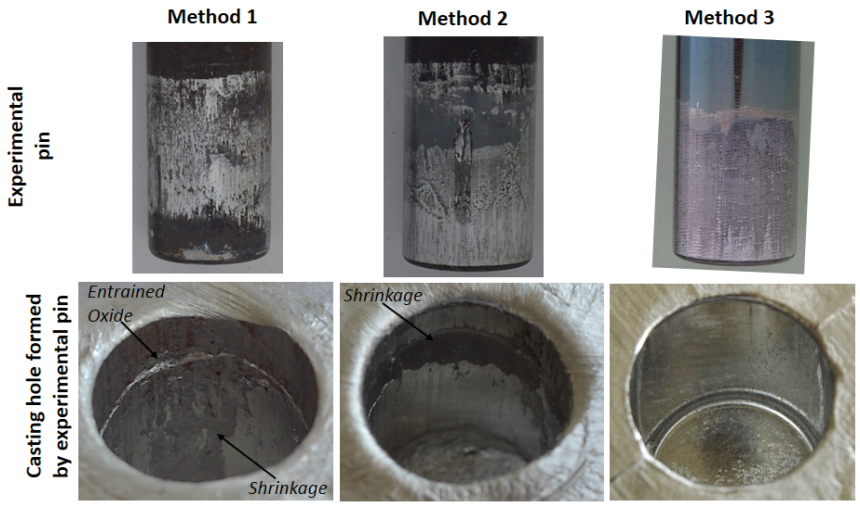

Fig. 3. Appearance of casting holes formed by experimental pin and corresponding pins ejected from the casting

Inner casting surfaces produced by method 1 and 2 contain a lot of irregularities and depressions. Surface of casting produced by method 1 contains massive oxide films and shrinkage cavities. During the process of pin immersion oxide films from the casting free surface were entrained into the bulk, while depressions in the wall or shrinkage are a direct consequence of the solidification pattern. In Methods 1 and 2, region around the pin is the last solidifying region of the casting. Accordingly this region provides liquid metal for the casting regions located below that currently solidify. Further, during the solidification of region around the pin in absence of liquid metal shrinkage cavities are formed. This finding is proved by results of the casting simulations presented in the second part of the paper. Sample assemblies produced by method 2 do not contain oxide films in pin-casting contact while shrinkage cavities are still present. After the test pin from the method 3 assembly is characterised by uniformly spread soldering layer. This is a consequence of a defect free face of the casting and a complete pin/casting contact. In method 3 the zone around the pin is constantly fed by liquid metal so the formation of cavities due to shrinkage is avoided.

Results of the casting simulations of all methods investigated are presented in Figure 4 and Figure 5. Results of temperature fields immediately after metal pouring revealed that pins in method 1 and 2 are much colder, Figure 3 a). Considering that the soldering tendency of an alloy is highly dependent on the contact temperature [3] this is a significant drawback of these methods. Additionally a casting oxide skin formed on colder pins should promote the formation of face depressions and shrinkage on contact surfaces. The likelihood of defect formation in Al-Si castings is increased in regions where the most oxidised melt ends up. In cases of casting by method 1 and 2 this occurs mostly in the proximity of the pin. Therefore, once again method 3 would give better contact faces.

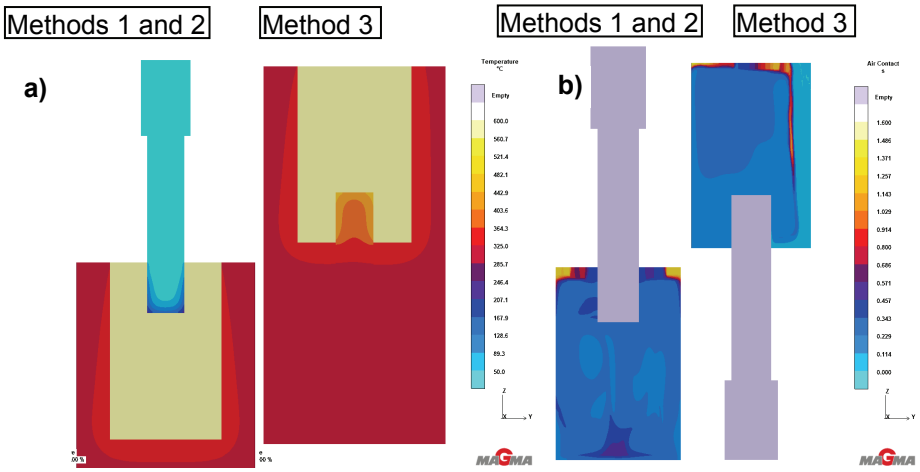

Fig. 4. a) temperature field immediately and b) air contact after complete casting filling

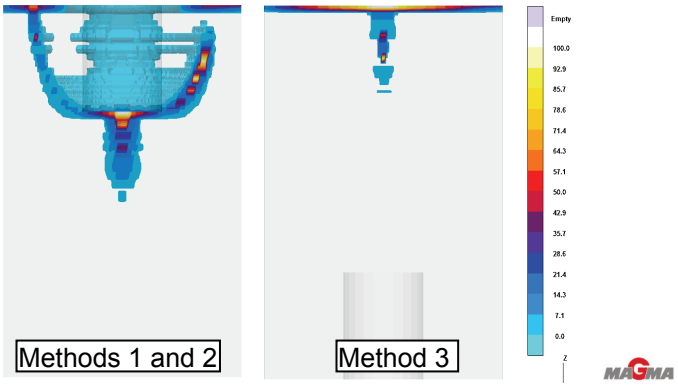

Fig. 5. Regions in castings prone to the shrinkage and porosity formation

The major drawback of casting the sample assembly by method 1 and 2 is that the regions around the experimental pins are highly prone to the porosity and to shrinkage formation, see Figure 5 left. Conversely, pin orientation in method 3 assures good solidification conditions that together with quality filling, without oxide incorporation in critical zones, results with defect free structure around the pin, Figure 5 right.

Forces recorded during the ejection test of castings produced by method 3 are considerably higher and these curves appear differently than those obtained using the samples made by method 1 and 2. Decreased ejection forces are a consequence of pin-casting contact deterioration due to the presence of oxide films and shrinkage.

Considering all previous findings it is apparent that applying method 1 and 2 results with decreased pin-casting contact area. On the other side, oxides are basically a third material in examined contact whose presence introduces

uncertainty in the experiment. In previous investigations [1][3][4][5] where these methods, 1 and 2, were employed the quality of the pin-casting assembly was not considered nor discussed. This suggest that the final results of the ejection test from the [1][3][4][5] investigations are questionable.

Conclusions

Ejection test applied for evaluation of alloy soldering tendency on die surfaces was investigated. Investigation focused on different casting methods utilised for obtaining the pin-casting assembly used as a sample in the ejection test. In this investigation two currently used methods and one newly proposed method were examined.

Analysis revealed a series of drawbacks of two currently used methods. The specific die setup and casting procedure applied does not ensure a precise control over the pin immersion depth. Casting solidification pattern, of both current methods, is not appropriate and thus facilitate shrinkage cavity formation in the regions of the pin-casting contacts. Additionally, oxide films are incorporated into the contact regions around the pin. All mentioned phenomenon deteriorate the pin-casting contact quality which induce decreased test repeatability, wrong experimental conditions and eventually inaccurate results.

A newly proposed experimental die and casting method eliminated the issues concerning the assembly accuracy, increased the casting quality in crucial zone and made the test more practical. Therefore, new method provides high grade of process replication, flexibility during operation and increased accuracy of the ejection test.

Acknowledgements

The authors gratefully acknowledge financial support provided by the Serbian Ministry of Education, Science and Technological Development.

References

[1] V. Joshi, K. Kulkarni, R. Shivpuri, R.. Bhattacharya, S.. Dikshit, D. Bhat, Dissolution and soldering behavior of nitrided hot working steel with multilayer LAFAD PVD coatings, Surface and Coatings Technology, Vol. 146-147., pp. 338–343., 2001

[2] S. Gulizia, M.Z. Jahedi, E.D. Doyle, Performance evaluation of PVD coatings for high pressure die casting, Surface and Coatings Technology, Vol. 140., pp. 200–205, 2001

[3] J. Lin, S. Carrera, A.O. Kunrath, D. Zhong, S. Myers, B. Mishra, et al., Design methodology for optimized die coatings: The case for aluminum pressure die-casting, Surface and Coatings Technology, Vol. 201., pp. 2930–2941, 2006

[4] V. Joshi, A. Srivastava, R. Shivpuri, E. Rolinski, Investigating ion nitriding for the reduction of dissolution and soldering in die-casting shot sleeves, Surface and Coatings Technology, Vol. 163-164., pp. 668–673, 2003

[5] V. Joshi, a Srivastava, R. Shivpuri, Intermetallic formation and its relation to interface mass loss and tribology in die casting dies, Wear, Vol. 256., pp. 1232–1235, 2004

LONG-TERM BEHAVIOR OF DEPLETED URANIUM IN THE ENVIRONMENT

Mirjana Stojanović[1],Č. Lačnjevac[2],J. Milojković[1], Z. Lopičić[1],M. Mihajlović[1], J.Petrović[1], M. Stanojević[1]

[1]*Institute for Technology of Nuclear and Other Mineral Raw Materials, Belgrade, Serbia*
[2] Faculty of Agriculture, University of Belgrade, Serbia

The widespread use of depleted uranium (DU) munitions in past wars has generated a great deal and fear of concern of potential impact on the environment and human health. During the NATO operations in the former Yugoslavia in 1999.y, Kosovo and Metohiaand southern Serbia, were bombed with around 10 tons of DU munitions. Sixteen years ago there was very little available information about the behavior of ecological systems damaged by DU ammunition fired and the factors that control the corrosion of DU and its subsequent migration through the environment. Today we are faced with the "invisible threat" of DU, which has a strong radioactive and hemotoxic impact on human health. This paper provides a latest finding of corrosion and corrosion behavior of DU and environmental factors that control corrosion, together with indicators of environmental impact in order to highlight areas that need further attention in developing remediation programs.
Keywords: depleted uranium, corrosion, behavior, environment

Depleted uranium – characteristics- corrosion behavior

Depleted Uranium is a by-product of nuclear fuel cycle that occurs in the process of isotope ^{235}U separation from the natural uranium, whereby its concentration decreases from 0.7% up to 0.2-0.3% and has a status of radioactive waste. The use of uranium as nuclear fuel requires its enrichment with isotope 235U so that the percentage of the uranium-235 isotope is increased, typically to 3 to 5%. The specific activity of DU is about 14.83 $Bqmg^{-1}$, and 30-40% less radioactive than natural uranium (25.4 mCi / mg), with the same half-lives of about 4,468 × 109 year [1].

It is estimated that worldwide about 1.1 million t of DU located at various landfills, where this amount each year added another minimum 46 thousand tonnes [1].

During all the wars in the past 20 years (1991 Gulf War,~300tDU, in Bosnia in 1994,~3t, , the bombing of Serbia~10t, in 1999 and 2003. In Iraq in ~1000t) were fired approximately 1.4 million du projectiles[2,3].

Migration potential of uranium depends on the physico-chemical properties of soil and soil solution and oxidation products of DU. On the mobility of dissolved uranium products, predominantly affecting the pH values , Eh, and the presence of organic and inorganic complexing agents in the local groundwater.Hexavalent uranium U (VI) exists in solution as uranyl ion ($UO_2^{2+)}$ and he is more mobile than U

(IV) because it builds more easily soluble complexes with ligands present in the soil solutions. [4].

Uranium (including DU) environmental pathways and potential risk to human health are shown in Figure 1.

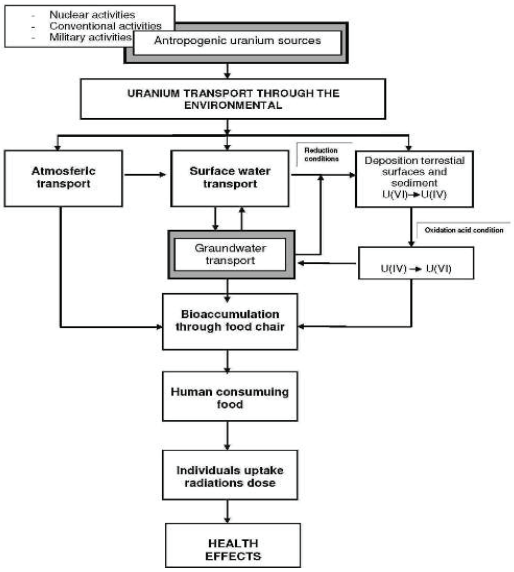

Fig. 1. Uranium environmental pathways and potential risk to Human health

How will penetrator behave and to what depth will penetrate depends on the angle of entry into the soil and soil physical properties. So, on clay soils, penetration goes up to 2 m [5] and on the sandy soils of 6-7m [3].

Studies conducted by UNEP, in post-conflict zones, have revealed numerous corroded penetrator in the surface soil layers [3,6]. In Serbia and Montenegro during 2002, from the soil surface, sampled penetratorswith highdegree of corrosion and it is estimated that a complete corrosion will be complite for 20 years[7].After 18 months of aggression, was found penetrator in Djakovica at 5 cm depth, with the loss of mass of 2-8%, due to oxidation and leaching of atmospheric precipitation, and the remnants of DU penetrators were found below a depth of 12.5cm. Based on these findings, it is estimated that in 15-30 years, penetrator can completely dissolveor get into the compound $UO_3 \cdot nH_2O$ [8].

Radenkovic et al.,(2008) investigated what happened with released DU corrosion products in three years elapsed, in soil (Bratoselce, southern Serbia) contaminated during the military actions,by applying a sequential extraction procedure for determination of geochemical fractionation and speciation of radionuclides in soils.DU penetrator was found in the soil at 0.5 m depth, covered with oxides. Soil samples were collected in the surrounding impact zone at the position of the projectile entrance into ground, the path through the subsurface ground, soil layer just next to DU penetrator, and different distances down along the depth profile. The specific activity of ^{238}U in the soil sample taken at the spot of

the projectile entrance into the ground was about 90 kBq/kg, in the projectile path it was near 78.5 kBq/kg and in the soil layer next to the penetrator it was about 263 kBq/kg and contamination decrease with the distance from the source through the soil profile.DU fractionation indicated an increase of mobile fraction of uranium in contaminated sites than the control, which confirms the rule that the anthropogenic uranium origin more easily included in the food chain from natural uranium. significant [9].

Depleted uranium is thermodynamically unstable and is therefore expected its corrosion in natural systems. Corrosion and solubility DU occurs in two phases [10]:

I) oxidation of uranium metal, with zero valence state, to U(IV), which builds a mineral,uraninite - UO_2 and II) oxidation of U (IV) to U (VI).

The First phase is favorable from the viewpoint of environmental protection because the resulting insoluble products which, under certain soil conditions (pH and redox potential) move into phase 2, which leads to the formation of soluble species, such as uranyl ions (UO_2^{2+}) and minerals, eg., schoepite (UO_3 $2H_2O$) which under certain conditions can be released UO_2^{2+} ions, which are easily transported by soilsolutions and include in the food chain.

Depending on the redox potential and pH, uranium metal may be corroded in water, that the passivated, or may be an inert.In the field of corrosion degradation of metals occurs, while in the domain of passivation, becomes coated metal oxides, hydroxides or salts, giving different degrees of protection from further corrosion, and in the domain of inertia, corrosion of metals is not thermodynamically possible [11].The process of deposition of uranium with reduction is an invaluable significance, since it excludes the uranium from aqueous streams and consequently suspended its expansion process through the environment. Table 1 provides information on the structure of corrosion products, which enabled the definition of a conceptual model of corrosion products penetrators of DU in various real-world conditions (Figure 2).

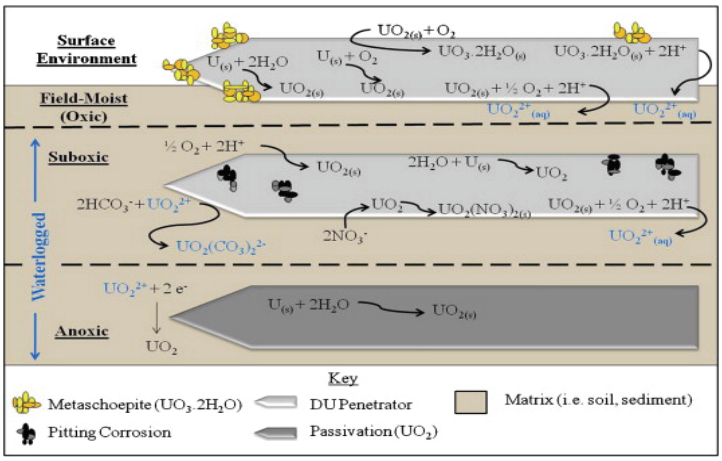

Fig. 2. Conceptual model of the major mechanisms of DU penetrators corrosion in soil conditions [2]

Table 1 .DU corrosion products under different conditions[2]

Mineral	Formula	Comments
URANITE	UO_2	Predominant corrosion product of waterlogged and low oxygen environments
ŠCHOEPITE	$UO_3 \cdot 2H_2O$	Predominant corrosion product of low-moisture oxygenated environments
METAŠCHOEPITE	$(UO_2)_8O(OH)_{12} \cdot 10H_2O$	
URANPHIT	$NH_4(UO_2)\ (PO_4) \cdot 3H_2O$	Observed in phosphate soils and/or in phosphate solutions under sterile conditions and in the presence of microbes and fungi
CHERNICOVITE	$(H_3O)_2(UO_2)_2(PO_4) \cdot 6H_2O$	
META-AUTUNITE	$Ca(UO_3)\ (PO_4) \cdot 4H_2O$	
SABUGALITE	HA $(UO_2)_4(PO_4)_4 \cdot 16H_2O$	

The corrosion rate of DU can be calculated using the equation 1, which includes a linear corrosion DU. Recent studies have found that unburt penetrator DU follows latent, corrosion period between 33 and 242 days, depending on the geochemical conditions, and it is recommended that this latent period is subtracted from the total time, which would provide a more accurate rate of corrosion annually [2]:

$$\text{Corrosion rate (g cm}^{-2}\text{y}^{-1}) = \frac{365 \times \text{weight loss (g)}}{\text{metal surface (cm}^2) \times \text{time(days)}} \quad (1)$$

In laboratory tests confirmed that the presence of chloride ions accelerate the corrosion process. The corrosion rate was 0.07 g cm $^{-2}$ s $^{-1}$ in water, 0.40 g cm $^{-2}$ s^{-1} in 3.5% NaCl solution, a corrosion rate of 1.47 g cm $^{-2}$ s $^{-1}$ to 5% NaCl solution [12].

The fate of unburned penetrators from DU-Ti alloy was tested in the salt waters, in situ, and it was determined the corrosion rate of 2.9 g cm^{-2} s^{-1}, which is an order of magnitude greater than the laboratory results at about the same content of chloride ions (3.5% NaCl) [13]. On the surface penetrators is detected the presence of a majority uranitit UO_2 and in the surrounding waters presence UO_2^{2+} ions. Corrosion rate in seawater was higher than the corrosion rate in the surface sediments (1.6 g cm^{-2}s $^{-1}$) and 0.17 g cm^{-2}s $^{-1}$ in the send [14]in any case have been detected black and yellow corrosion products to UO_2 and schoepit or metaschoepite [14]. Corrosion follows a linear trend from 9% weight loss for 500 days.A similar mechanism of corrosion was observed in DU penetrators, collected from two soil types from Kosovo (sandy-loam and clay-like sedimen). Samples were treated in the laboratory at 20°C, Sprinkler systems [15]. Fortified corrosion products are black and yellow and negligible differences in corrosion rates between these two types of land (0.19 ± 0.03 g cm $^{-2}$ s $^{-1}$), which had similar pH values (5.6-5.8) and the same content of organic matter (2.1%). The study also showed that corrosion DU is not linear, and that the time is accelerating. In the first year of the corroded ~1.6% of DU and after 3 years, the rate of corrosion of DU was increased to 2.7% per year [16].Hendley-Sidhu et al., set up the equation for calculating the total time required to complete corrosion "Charm 3" penetrators, approximate weight of 4500g and 150 cm^2 surface (Equation 2) [15]

Bottom of Form

$$\text{Complete corrosion(year)} = \frac{4500\ (g)}{\text{Corrosion rate } (g\ cm^{-2}\ y^{-1}) \times 150(cm^2)} \quad (2)$$

Handley-Sidhu et al., examined the impact of PO_4^{3-} ions, with an average P_2O_5 content of 27 mg kg^{-1} originating from agricultural land, treated with phosphate mineral fertilizers, on corrosion of DU penetrators and conclude that the presence of PO_4^{3-} ions in the soil protects against further corrosion of depleted uranium [16].

A critical role in controlling corrosion DU play redox potential, and takes place under oxidizing conditions, with excess oxygen in accordance with thermodynamic conditions and Eh / pH [2,15].Knowledge of global uranium cycle not only aimed to determine the level of contamination and the finding of the consequences, but the acquisition of knowledge by which we can safely predict all the processes that affect its transport and fixation and so develop models of environmental protection.

Bioavailability - absorption by plants

There is little studies on the adoption of U by the plant but it is known that DU behaves like a natural.Research DU toxicity to plants, grasses and ferns, sampled from the shooting ranges in the UK confirmed the maximum contamination is 3:38 mgU kg^{-1} dry weight of plants. Depleted uranium is also detected in the black oaks that grew in swampy sites contaminated with depleted uranium. The concentration in the tree plants was measured over 10 years and found that the concentration equivalent concentrations of groundwater. The authors suggest that the oak is used as a bioindicator of contamination of different media with DU [17].

Because of the similar ionic radii with a radius of Ca^{2+}(r = 1.06 Å), uranium (r = 1.05 Å) replacescalcijum, so that from the point of dislocation of uranium from the soil into the plant, calcium is considered a metabolic analogue of uranium [18].In the Western Balkans, confirmed the high level of activity of ^{238}U, from 1130-5390 Bq kg^{-1} in the moss, lichen and fungiand can be utilized as cheap and readily available bioindicators of contamination by DU [19].

Conclusion

The aim of this paper is to contribute to the understanding of the processes and factors which control the corrosion of depleted uranium and transport of corrosion products through the environment. The dominant factors of corrosion processes are pH and redox potential, geomorphological structure of soil concentration and types of inorganic and organic compounds in soils, soil temperature, pressure, moisture content, microbial and fungicidal activity, micro soil fauna, salinity. The same factors also influence the dissolution of corrosion products. The conclusion is that each contaminated site specific to itself and requires extensive monitoring and multidisciplinary approach to rehabilitation.In the

belief that the topic of protection against ionizing radiation never said too much, exposed material is a kind of technological declaration of repentance, confession that the development path threatened serious unintended effects and also appeal to the attitude towards the environment and the population returns from abuse in the area reasonable use. Our mission is to minimize the detrimental effect of depleted uranium and prevent its penetration into the food chain, otherwise "invisible threat" will operate indefinitely with all its disastrous consequences on future generations.

Acknowledgement

The authors are grateful to the Serbian Ministry of Education, Science and Technological Development for the financial support of this investigation included in the project TR 31003

References:

[1] M.Rajković (2001) Osiromašeniuranijum, I-Uranijum, radioaktivnostiza konskaregulativa, Hem. Ind., 55(4) 167-182.

[2] S.Handley-Sidhua, M.Keith-Roach, R.Loyd, J.David , A.Vaughan (2010) A review of the environmental corrosion, fate and bioavailability of munitions grade depleted uranium. Sci Total Environ, 408(23) 5690–5700.

[3] UNEP ,Depleted uranium in Kosovo, post-conflict environmental assessment. United Nations Environment Programme, Switzerland. (2001)http://postconflict.unep.ch/publications/uranium.pdf

[4] M. Stojanović, Č. Lačnjevac, M. Mihajlović, M. Petrović, T. Šoštarić, J. Petrović, Z. Lopičić (2014) Ekološko i koroziono ponašanje osiromašenog uranijuma, Hem.Ind., doi:10.2298/hemind131025024s

[5] C.Papastefanou(2002) Depleted uranium in military conflicts and the impact on the environment, Health Phys, 83, 280–282.

[6] UNEP, Depleted Uranium in Serbia and Montenegro—Post Conflict Environmental Assessment, Geneva, 2002 http://postconflict.unep.ch/ publications/duserbiamont.pdf

[7] UNEP, Discussion of health issues: appendix K. In: Depleted Uranium in Serbia and Montenegro,Post Conflict Environmental Assessment.,Geneva,2002, pp.179–183.

[8] S.Petković, M.Zarić, Z.Dević (2001)Upotrebamunicijesaosiromasenim uranom u agresiji NATO nasaveznurepublikuJugoslaviju,Hemijskaindustrija, 55(7-8) 318-324.

[9] M.Radenković, S.Cupac, J.Joksić, D.Todorović (2008) Depleted Uranium mobility and fractionation in contaminated soil(Southern Serbia). EnvSciPollut Res, 15,61-67.

[10] C.A.Laue, D.Gates-Anderson, T.E.Fitch (2004) Dissolution of metallic uranium and its alloys.JRadioanalNuclChem, 261, 709–717.

[11] M.J.M. Pourbaix, Atlas of Electrochemical Equilibria in Aqueous Solutions, (Eds.), National Association of Corrosion Engineers (NACE), Texas, 1974.

[12] J.F Mcintyre, E.P.Lefeave, K.A.Musselman (1988) Galvanic corrosion behaviour of depleted uranium in synthetic seawater coupled to aluminium,

magnesium, and mild steal, CorrosSci, 44, 502–510.
[13] P.P.Trzaskoma (1982) Corrosion rates and electrochemical studies of depleted uranium alloy tungsten fiber metal matrix composite. J Electrochem Soc,1398–1402.
[14] C.C.Toque, A.C.Baker, MOD DU program: The corrosion of depleted uranium in the Kirkcudbright and Eskmeals terrestrial environments. DSTL/CR10978 V2.0, Alverstoke,2006.
[15] S.Handley-Sidhu, N.Bryan, P.J.Worsfold, D.J.Vaughan,F.R.Livens, M.J.Keith-Roach (2009) Corrosion and transport of DU in sand-rich environments, Chemosphere, 77, 1434–1439.
[16] W.Schimmack, U.Gerstmann, W.Schultz, G.Geipel (2007) Long-term corrosion and leaching of depleted uranium (DU) in soil. Radiat Environ Biophys, 46 221–227.
[17] D.J.Edmands, J.D.Brabander, D.S.Coleman (2001) Uptake and mobility of uranium in black oaks: Implications for biomonitoring DU-contaminated groundwater,Chemosphere, 44, 789–795.
[18] H.Tunney, M.Stojanović, J.Mrdaković Popić, D.McGrath,' C. Zhang (2009) Relationship of soil phosphorus with uranium in grassland mineral soils in Ireland using soils from a long-term phosphorus experiment and a National soil database,J Plant Nutr Soil Sci, 172,346 – 352
[19] A.DiLella, L.Frati, G.Protano, F.Riccobono (2003) Lichens as biomonitors of uranium and other trace elements in an area of Kosovo heavily shelled with DU rounds, Atmos Environ,37, 5445–5449.

MECHANISM OF COPPER (I) SULPHIDE LEACHING IN OXIDATIVE HYDROCHLORIC ACID SOLUTION

Branislav R. Marković[1*], Miroslav D. Sokić[1], Željko J. Kamberović[2], Dragana T. Živković[3], Nada D. Štrbac[3], Vaso D. Manojlović[1]

[1] *Institute for Technology of Nuclear and Other Mineral Raw Materials, Belgrade, Serbia*
[2] *University of Belgrade, Faculty of Technology and Metallurgy, Belgrade, Serbia*
[3] *University of Belgrade, Technical Faculty, Bor, Serbia*
**Corresponding author: b.markovic@itnms.ac.rs*

Abstract

The mechanism of the leaching process of finely grained samples of copper (I) sulphide with sodium chloride in hydrochloric acid solution and the introduction of gaseous oxygen were studied and discussed. The occurrence probability of chemical reactions were analysed based on literature data and products which were formed during the process and the overall leaching reaction was defined. Experimental data, chemical analysis, XRD, and microstructural analyses of initial sample and the leach residues, were performed to develop a better understanding of the chemical reactions that took place in the system. The role of chloride ions is to disrupt the passivating sulphur layer on the particle surface, by promoting the formation of crystalline sulphur rather than a crypto-crystalline or amorphous product.

Key words: copper (I) sulphide; hydrochloric acid; sodium chloride; leaching mechanism

Introduction

Hydrometallurgical processes provide an efficient method for processing of low-grade complex ores. In spite of the fact that in pyrometallurgical processes, the sulphide sulphur is used as fuel, hydrometallurgical processes are increasingly popular because of environmental protection. Concerns over air pollution and the environmental problem of acid rain have made governments all over the world tighten their regulations regarding the emission of sulphur dioxide. The focus is on the production of elemental sulphur and soluble copper sulphate [1].

Leaching of copper (I) sulphide has been the subject of many investigations [2–6], including leaching under high pressure and atmospheric pressure. The process of copper matte leaching under high pressure conditions, in both acidic and alkaline solutions, necessitates high capital and operation costs.

As early as 1933, Sullivan [2] showed that, in an acidified ferric sulphate leachant, chalcocite (Cu_2S) dissolved in a two-stage process with covellite (CuS) as the solid product formed at the end of the first stage. In the second stage, the process occurs through the formation of elemental sulphur. Fisher and Roman [5] reported that oxygenated sulphuric acid solutions containing halogen anions (Cl^- or Br^-) were very effective in the leaching of chalcocite. Subsequently, Roman and

Benner [7] put forward the proposal that sulphuric acid containing chloride ions could be a useful leachant for copper sulphides and the advantages of using mixed chloride-sulphate acid leachants for chalcocite-type minerals were recognised. Cho [8] investigated leaching of chalcocite in hypochlorous acid and found that the leaching rate was pH dependent. The Broken Hill Associated Smelters (BHAS) in Port Pirie, South Australia [9], developed a process for treating a lead-refining by-product, copper–lead sulphide matte, using an oxygenated acid solution containing both sulphate and chloride ions. The leaching process with oxygen takes place at 85^{o}C, while copper dissolves and lead remains in the solid residue as lead sulphate together with elemental sulphur. The cupric ions are subsequently transferred into an electrolyte sulphate solution. Cheng and Lawson [10] investigated the kinetics of leaching chalcocite in acidic oxygenated sulphate-chloride solutions and found that the process occurred in two stages, which was very similar to the conclusions of Sullivan [2]. The same authors Cheng and Lawson [11] have leached white metal (containing Cu_2S) and reported the same results as in the previous investigation [10]. This proves that the process occurs through the formation of CuS and elemental sulphur, and that the role of chloride ions is to prevent the formation of a coherent, passivating sulphur layer on the particle surface.

The results of copper (I) sulphide leaching in a solution of NaCl in the presence of oxygen and HCl are shown in this paper.

Leaching mechanism

Many research results [10–13] show that the leaching of copper-containing minerals occurs in two stages. In the first leaching stage, as the cuprous ions diffuse to the particle surface, a series of intermediate solid products are formed before 'stable' covellite is produced. During the second leaching stage, covellite reacts, leaving a shell of elemental sulphur surrounding a reducing core of unreacted covellite [11].

In chloride solutions, additional reactions of complexation are very important [15]. In cupric chloride solutions, Cu^{2+}, $CuCl^{+}$ or $CuCl_2^{-}$ are observed, and the last is predominant at high chloride ion concentrations [16]. The distribution is somewhat controversial: other authors suppose also the presence of $CuCl_3^{-}$ and $CuCl_4^{-}$ [17]. The increased solubility of cuprous chloride when chloride ions are added is explained by the successive formation of $CuCl_2^{-}$, $CuCl_3^{2-}$, and finally, $CuCl_4^{3-}$. In the conditions of high oxygen potentials and low pH values, Cu^{2+} ions will be stable.

On the basis of literature data [10–17] and the products in the solution, as well as in the solid residue of leaching, determined by X-ray analysis (Figure 3), and having in mind that all reactions occurring in electrolyte solution are electrochemical, the reaction in the first leaching stage in the Cu_2S–NaCl–HCl–O_2–H_2O system can be presented as follows:

Anodic reaction:

$$Cu_2S = Cu^{2+} + CuS + 2e^{-} \quad (1)$$

Cathodic reaction:

$$2H^+ + 1/2O_2 + 2e^- = H_2O \quad (2)$$

Overall reaction:

$$Cu_2S + 2H^+ + 1/2O_2 = Cu^{2+} + CuS + H_2O \quad (3)$$

The reaction in the second leaching stage is also electrochemical:
Anodic reaction:

$$CuS = Cu^{2+}\ S^0 + 2e^- \quad (4)$$

Cathodic reaction:

$$2H^+ + 1/2O_2 + 2e^- = H_2O \quad (5)$$

Overall reaction:

$$CuS + 2H^+\ 1/2O_2 = Cu^{2+}\ S^0 + H_2O \quad (6)$$

The overall reaction for the first and the second stage is derived from the above reactions:

$$Cu_2S + 4H^+\ O_2 = 2Cu^{2+} + S^0 + 2H_2O \quad (7)$$

Experiments

All leaching experiments were carried out in a glass reactor equipped with a teflon stirrer, condenser, thermometer, glass funnel for adding the solid sample and a sampling device (Figure 1).

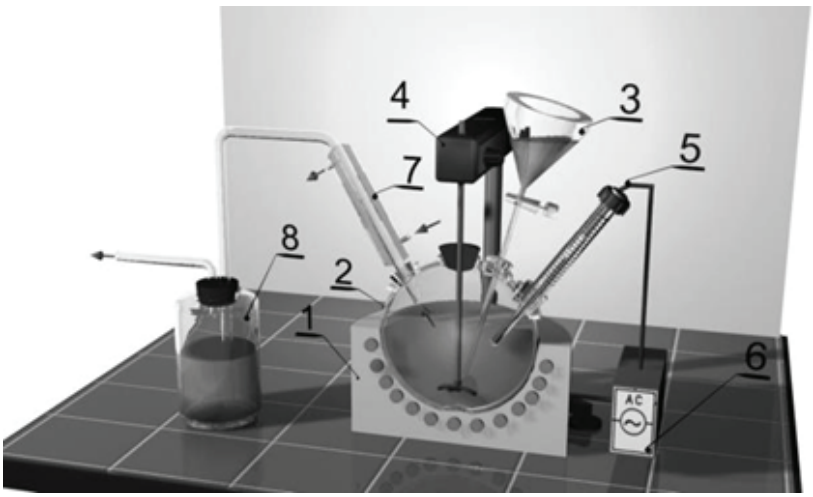

Fig. 1. Experimental set-up for the leaching process at atmospheric pressure: 1-electro-resistant callote, 2-glass reactor, 3-glass funnel, 4-electro-powered stirrer, 5-mercury contact thermometer, 6-cut off relay, 7-condenser, 8-absorber

This set-up provides stable hermetic conditions and allows heating at constant temperature. Before leaching was started, the solution of NaCl and HCl was oxygenated for 30 min at the selected temperature, then, the solid sulphide was added. From the moment of adding the solid sample, reaction time was calculated, with solution sample being withdrawn at regular intervals for chemical analysis. The amount of leaching copper was determined by AAS (Perkin Elmer). The solid residues were filtered, washed with distilled water, dried and their phase content was determined by X-ray analysis using diffractometer (PHILIPS PW-1710).

The following parameters were studied: temperature (^oC): 55-95; stirring speed (min^{-1}): 200-550; concentrations of NaCl and HCl (mol/dm^3): 0.2-0.75; concentration of total chloride ions (mol/dm^3): 0.25-0.75; and phase ratio (S:L): 10-30 g Cu_2S in 1,2 L of the solution. Leaching times were in the range of 5 to 240 min. Previous investigations [12] show that oxygen flow rate has no important influence on degree of copper leaching in acidic oxygenated chloride solutions, if the initial sample is finely sized. For that reason, in all leaching experiments, oxygen flow was 0.60 L/min.

Experimental results and discussion

Cu (I) sulphide with 80.42% of Cu and 18.64% of S and the density of 5040 kg/m^3 was used in the investigation. The sample's specific surface was S_o = 7481 m^2/m^3, S_w = 1385 m^2/g, where S_o and S_w refer to external and internal porosity, respectively. Sodium chloride of 99.5% purity and 36.2% solution of HCl were used.

Figure 2 shows the temperature dependence of Cu (I) sulphide leaching in an oxidised, acidic 0.5 M HCl/0.5 M NaCl solution, when the stirring speed was $400min^{-1}$ and phase ratio was 1200 mL:20 g Cu_2S.

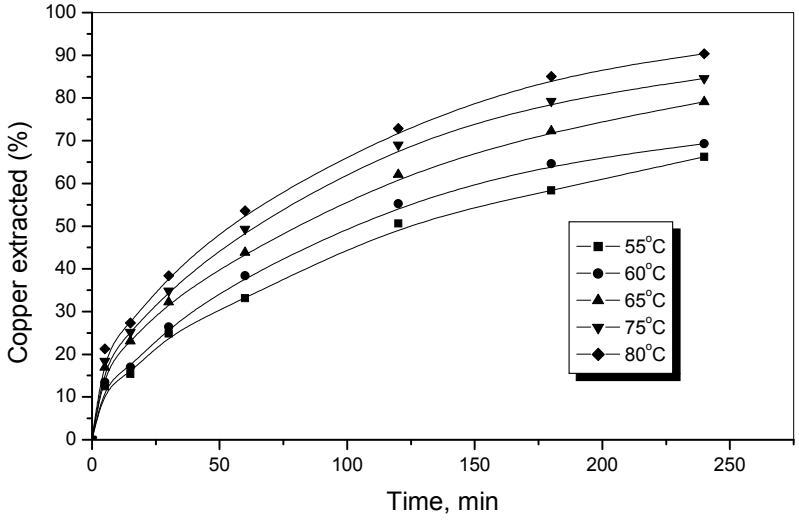

Fig. 2. Temperature dependence during Cu (I) sulphide leaching

Leaching is strongly influenced by temperature. A slower increase in the leaching degree is noticeable after 120 min. This is probably due to the surface of Cu (I) sulphide particles being blocked by the reaction's solid products; therefore it resulted in a more difficult penetration of the reaction area into the centre of the grain of Cu_2S. The maximum leaching degree was 90% Cu, after 240 min at 80°C.

The X-ray diffraction analysis of obtained solid residue, was carried out (Figure 3) in order to investigate the products and the form they occur in during leaching, particularly sulphur, which is responsible for process mechanism. It revealed the presence of clearly formed crystals of elementary sulphur. Besides sulphur, the solid residue contains $Cu_2Cl(OH)_3$. These products form a solid layer on the reaction surface, which makes the diffusion within the leaching reagents more difficult.

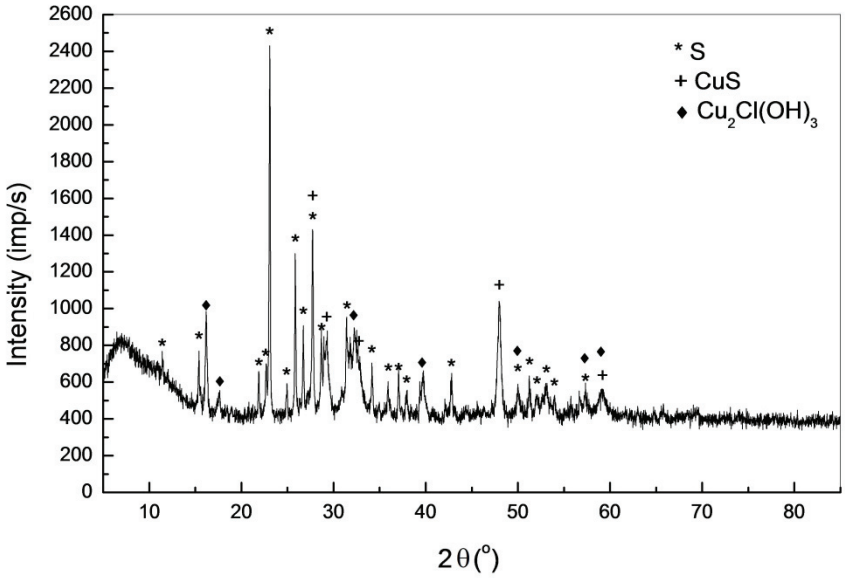

Fig. 3. X-ray of solid residue of leaching at 80°C, stirring speed 400 min^{-1} in 0.5 mol/dm^3 HCl/0.5 mol/dm^3 NaCl solution.

Conclusion

From the results obtained in the study of copper (I) sulphide leaching by NaCl and HCl solution in the presence of gaseous oxygen, the following conclusions can be made.

(1) On the basis of literature data and the products formed during leaching and X-ray analysis, it can be concluded that its chemistry mechanism is determined by the following overall reactions:

The first leaching stage: see Eq. (3)

The second leaching stage: see Eq. (6)

Overall reaction for both first and second leaching stage: see Eq. (7)

(2) The experimental study showed that high degree of leaching of copper could be achieved (90%). The increase of temperature increases the degree of leaching of copper.

Acknowledgment

The authors wish to acknowledge the financial support from the Ministry of Education, Science and Technological Development of the Republic of Serbia through the project TR34023.

References

[1] J.I. Jones, The Leaching of Chalcopyrite, PhD Thesis, Department of Metallurgy, University of British Columbia, May, 1974.
[2] J.D. Sullivan, Chemical and physical features of copper leaching, Trans. Am. Inst. Min. Metall. 106 (1933) 515–547.
[3] I.H. Warren, A study of the acid pressure leaching of chalcopyrite, chalcocite and covellite, Aust. J. Appl. Sci. 9 (1958) 36–51.
[4] W. Mulak, J. Niemiec, Kinetics of Cu_2S dissolution in acidic solution of ferric sulphate, Rocz. Chem. 43 (1969) 1387– 1394.
[5] W.W. Fisher, R.J. Roman, The dissolution of chalcocite in oxygenated sulphuric acid solution, Circ. 112 State Bur. Mines Resources, New Mexico Inst. Min. Technol., 1971.
[6] J.A. King, A.R. Burkin, R.C.H. Ferreira, Leaching of chalcocite by acidic chloride solutions, in: A.R. Burkin (Ed)., Leaching and Reduction in Hydrometallurgy, Inst. Min. Metall., London, (1975) 36–45.
[7] R.J. Roman, B.R. Benner, The dissolution of copper concentrates, Miner. Sci. Eng. 5 (1973) 3–24.
[8] E.H. Cho, Hypochlorous acid leaching of sulfide minerals, J. Met. (1987) 18–20.
[9] R. Lal, J.H. McNicol, The BHAS copper leach plant. Techn. Pap. A87-1, Metall. Soc. AIME., Warrendale, PA, 1987.
[10] Y.C. Cheng, F. Lawson, The kinetics of leaching chalcocite in acidic oxygenated sulphate–chloride solutions, Hydrometallurgy 27 (1991) 249–268.
[11] Y.C. Cheng, F. Lawson, Leaching copper matte and white metal in acidic oxygenated sulphate–chloride solutions, ICHM 1992, Changsha, China, October 23–26, vol. 1.
[12] M.H. Mao, E. Peters, Acid pressure leaching of chalcocite, in: K. Osseo-Asare, J.D. Miller (Eds.), Hydrometallurgy: Research, Development and Plant Practice, Metall. Soc. AIME, Warrendale, PA, (1983) 243–260.
[13] N.E. Meadows, N.J. Ricketts, G.D.J. Smith, Oxygen leaching of copper–lead matte in acidic chloride / sulphate solutions, Research and Development in Extractive Metallurgy, Aust. Inst. Min. Metall., Adelaide Branch, (1987) 115–120.
[14] R.Ž. Vračar, I.S. Parezanović, K.P. Cerović, Leaching of copper(I) sulfide in calcium chloride solution, Hydrometallurgy 58 (2000) 261–267.
[15] K.G. Ashurst, The thermodynamics of the formation of chlorocomplexes of

nickel and copper(II) in perchlorate medium. Nat. Inst. Metall., Johannesburg, S. Africa, Rep. 1712 (1975).

[16] M.J. Schwing-Weil, Etude des complexes chlores de cuivre (II) en solution aqueuse, Bull. Soc. Chim. Fr. 3 (1973) 823–830.

[17] A. Fontana, J. Van Muylder, R. Winand, Etude spectrophotome´trique de solutions aqueuses chlorure´es de chlorure cuivreux, a` concentrations e´leve´es, Hydrometallurgy 11 (1983) 297–314.

INTERPHASE PROCESSES BETWEEN LIQUID METAL AND SILICONE MOULD

Zoran Janjušević[1], Zvonko Gulišija[1], Marija Mihailović[1], Aleksandra Patarić[1]
Zoran Karastojković[2], N. Bajic[3]

[1]*Institute for Technology of Nuclear and Other Mineral Raw Materials, Franchet d' Esperey St.86, Belgrade, Serbia*
[2]*Technical College, Blvd. Dr Zorana Đinđića 152a, 11070 New Belgrade. Serbia*
[3]*Techno-experts d.o.o – Research and Development Center, Serbia*
z.janjusevic@itnms.ac.rs

Abstract

Processes and interactions between molten liquid metal and mould material during metal pouring and solidification, as a part of complex solidification processes, are presented in this paper. The processes on the contact surface molten metal – silicone mould, are responsible for the quality of castings surface, the castings dimensions or ingot quality, and may influence the appearance of casting faults (gas holes, cracks, etc.). These processes, according to the rate of heat outflow from the solidified metal, have also an influence on the formation of desired structures and/or casting properties.
Keywords: contact surface, metal, sand mould, steel

Introduction

This paper discusses principal processes at the interphase metal – mould, namely formation of the diffusive layer and its influence on improvement of the surface quality of castings.

The great influence on the formation of a diffusive layer has the character of gaseous environment, which is formed just at the boundary contact surface metal - mould. The degree of adhesion of a diffusive layer with casting surface depends on the properties or structure of the silicates, which are formed as result of mutual action between a mould material and a molten metal.

It becomes clear that for preventing formation of the diffusion zone, it is necessary to break the penetration of a molten metal into the sand mould pores, but also to prevent an oxidation of the first solidified metal layer, that is formed at the contact of metal surface and a mould material. However, in real circumstances it is quite impossible to stop the penetration of a molten metal in to the sand mould pore, or formation of the iron oxide(s) at mentioned interface molten metal - sand mould. From that point of view, it is reasonable to investigate mechanism and kinetics of the diffusion layer removal.

According to the literature data [1], the most desired path for further investigation is intensification of oxidizing processes, and than the formation of silicates at the contact surface molten metal - sand mould. By providing the mentioned processes, the depth of a diffusion layer might be markedly reduced, while an oxidation of penetrated metal is fully achieved, and at the same time, the

bond between the solidified metal and a mould material will be seriously weakened.

In contact of a molten metal mould material a chemical reactions will take place, and reaction products are spreading out at both sides, according to the conditions in the mould. The chemical potential also influence the chemical reactions at the contact surface, and the reactivity is increasing with temperature.

These processes at contact surface a molten metal – mould material may be of mechanical, physical, and chemical nature. These chemical reactions are insufficiently investigated, although their importance is markedly large. The chemical reactions of a molten metal with mould material could be considered as:

a) reaction of a metal with evaporative products from the mould material, which are formed from moisture or by dissociation of the mould mixture components,
b) reaction of a metal with nonevaporative products of the mould mixture.

The intensity and, generally, development of particular processes at the boundary surface metal – mould material, markedly depend on the kind of binder or additive into the mould mixture, and their behaviour in contact with a molten metal.

Experiments

Experiments were performed in moulds made by using a CO_2 method. Mould mixture is composed as follows: 90% sand (quartz); 6% water-glass; 0.1% sodium-sulphate and other active components up to 100%.

The experimental castings were cylinder-shaped of dimensions 0.038 x 0.060 m. Cast steel from a regular production programme from foundry „Ivo Lola Ribar“ Železnik-Belgrade as a pouring metal was used. Here used steels corresponded to the classes: Č 3132, Č 4733 and Č 3460, assigned by SRPS.

The pouring temperatures were in the range 1580-1605 ^{0}C, and the starting temperature of the mould was 20°C.

The investigations of processes that take place at the contact surface were performed using following methods: visual inspection of castings surface quality, light microscopy.

Results and discussion

The results of visual monitoring of castings surface are shown in Fig. 1. It can be seen that after the molten metal has penetrated into the pores of mould mixture and then undergone solidification, a strong and hardly removable oxide layer is formed in those mould mixtures where the additives where not used. The surfaces of castings, where the additives were used, are relatively clean.

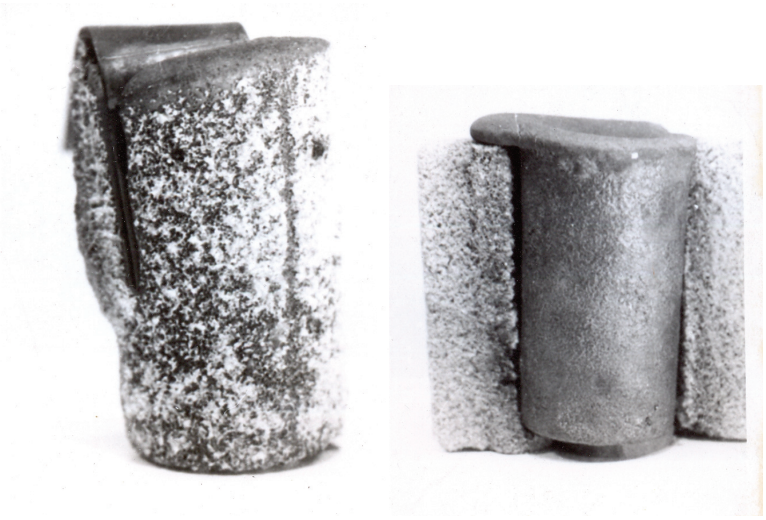

Fig. 1. Visual monitoring of castings surface.

Analysis of the products which were made in the contact molten metal – mould material, zone 1 is shown in Fig. 2, visual inspection shows a dark layer, what implies that some chemical reactions take place.

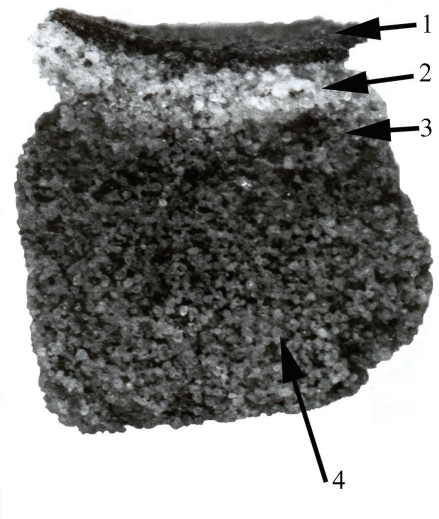

Fig. 2. Segment of the mould with zone of reactions

At Fig. 1 the first zone is shown, also it can be seen that near the castings surface the structure become homogenized because of disintegration of the SiO_2 particles. Quartz grains are almost cataclysed, partially enveloped by high temperature modifications with appearance of a glassy phase.

It is stated that the characteristic appearance of a glass is in a nest shape. Particles of quartz are frequently separated from matrix in the shape of irregular forms or cracks. In zones of castings where glassy phase is dominant, the cracks are of a channel type. Different iron oxides, as fine grains, frequently are developed in the shape of a crystal skeletons, which are characteristic for magnesite – when rapid crystallization take place after fast cooling of a viscous silicate phase.

The results of phase analysis of dark layer from zone 1, which is located at the contact surface, indicate that formed phases from dark layer correspond to tac mixture of metal and mould material. The trapped metal appear because the molten metal penetrate into the mould material, which is a porous capillary body.

An intensive heating up of a contact zone, from the first contact between the liquid metal and mould material up to the finish of solidification process and following continuously cooling of metal, has an incremental influence on a diffusion process. As a result of diffusion process the iron oxide layer becomes thicker, but also it may react with SiO_2, so the new minerals on the silicate basis are formed: fayalite – $2FeO{\cdot}SiO_2$, pyroxene – $NaFeSiO_6$, leucite – $KAlSiO_6$, plagioclase – $NaAlSi_3O_8$ and glass, Fig. 3.

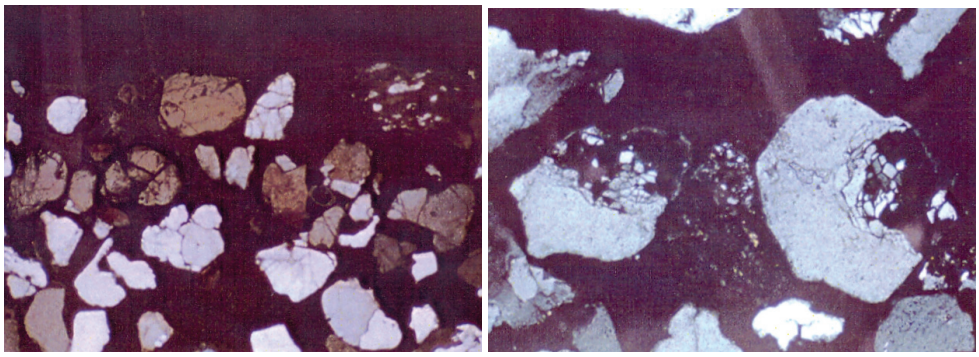

Fig. 3. New minerals on the silicate

The low-melting silicates are formed when basic oxides, which contain Mg^{2+}, Mn^{2+}, Ca^{2+} and Fe^{2+} ions react with complex ions on SiO_2 basis from the mould mixture.

Acknowledgement

These investigations were conducted under the Project 34002 funded by the Ministry of Education, Science and Technological Development of the Republic of Serbia.

References

[1] Smirnov N.S.,Prostakov M.E.,“Očistka poverhnostey otlivok”,Moskva, Metallurgia, (1985) 65-84.

[2] Kuznecov D.A., Malahov A.I., “Prigar na čugunnih otlivkah i rol kremnia čuguna v ego obrazovani”, Trudi ,D.I.Mendeleva, Moskva, (1964), 126-138.

[3] Allmond T.R, Microscopie identification in steel, Bisra, London, 1962.
[4] Bence A.E, Albee A.L, Empirical Corection Factors for the electron microanalysis of silicate and oxides, The journal of Geology, 76, 1968
[5] Albee A.L, Ray L, Corection Factors for Electron Probe Microanalysis of Silicate, Oxides, Carbonates, Anal.Chemistry, 42, 1970.
[6] Janjušević Z, Gulišija Z, Radosavljević S., Mihailović M., Influence of metal-mould interface phenomena on qualiti of casting surface, Scienci of sintering, 32, 2, (2000), 81-90.
[7] Janjušević Z, Gulišija Z, Radosavljević S., Aćimović Z., A contribution to studi of processes on the steel cast-sand mould contact surface during casting, Materials Letters, (2000), 235-241.
[8] Z.Janjušević, Z.Gulišija, M.Mihailović, A.Patarić, M.Sokić, V.Matković, B. Marković, Chemical Thermodynamic Processes at Metal-Mould Interface, Materials Transactions, Vol 54 No.10 (2013), 1925-1929, ISSN 1345-9678.
[9] Z.Janjušević, Z.Gulišija, M.Mihailović, A.Patarić, Processes at the Interface Molten Metal-Sand Mold, Metalurgija, 53, 2, (2014), 197-200, ISSN 0543-5846.

CALCULATION OF LOCAL CLEAVAGE FRACTURE STRESS IN A MEDIUM-CARBON V-MICROALLOYED STEEL USING FINITE ELEMENT ANALYSIS

G. Jovanović[1], D. Glišić[1], N. Radović[1], M. Rakin[1]

[1] *University of Belgrade, Faculty of Technology and Metallurgy, Karnegijeva 4, 11120 Belgrade, Serbia*

Abstract

Cleavage fracture of commercial medium-carbon V-microalloyed forging steel with predominantly acicular ferrite structure was studied by means of four-point bending testing at liquid nitrogen temperature in conjunction with finite element analysis. Both two-dimensional and three-dimensional finite element models were used for the purpose of comparison. Cleavage fracture was initiated by high plastic strains in the vicinity of notch tip. Strains calculated by three-dimensional modeling were higher up to 80% than for two-dimensional model. Calculated local cleavage fracture stresses rendered effective surface energy values of 49J/m^2 and 60J/m^2, for two-dimensional and three-dimensional numerical model, respectively. Both results are in good agreement with previously published data for medium carbon microalloyed steels.

Keywords: medium carbon V-microalloyed steel, acicular ferrite, critical fracture stress, finite element model.

Introduction

It was established that cleavage fracture of the microalloyed forging steels with ferrite-pearlite, bainite or martensite structure initiates by fracture of coarse second phase particles, commonly TiN particles [1–3], in the region of high stress intensification, such as peak stress in front of the notch on bend test samples. However, in microalloyed steels with acicular ferrite structure, cleavage fracture initiation is associated with plastic deformation at the notch tip, where stresses are relatively low [4–6]. Some authors proposed that, in addition to critical stress, critical plastic strain and critical stress triaxiality should be considered as additional criterions for cleavage fracture [4].

Critical parameters for cleavage fracture are determined by using finite element models (FEM) in conjunction with fractographic examinations of the notched samples tested by three- or four-point bending. Two-dimensional (2D) FEM with plane strain assumption are commonly used [1–3,7]. The question of validity of 2D FEM assuming plane strain condition arises in the case of strain induced cleavage fracture.

The aim of this investigation is to determine critical parameters of cleavage fracture by using three-dimensional (3D) FEM and to compare the results with plane strain 2D FEM, for medium carbon microalloyed steel with the structure of acicular ferrite.

Experimental Procedure

A commercial V-microalloyed medium carbon steel containing: 0.256%C, 0.416%Si, 1.451%Mn, 0.0113%P, 0.0112%S, 0.201%Cr, 0.149%Ni, 0.023%Mo, 0.099%V, 0.002%Ti, 0.038%Al, 0.183%Cu, 0.002%Nb, 0.0229%N, was tested in this work. As received hot rolled bars, 19mm in diameter, were given homogenization treatment at 1250°C for 4h followed by oil quenching. The samples were afterwards austenitized at 1250°C for 30 min and cooled at still air. In all heat treatments, argon was used as a protective atmosphere. Microstructure of the air cooled samples was revealed by polishing and etching in 2% nital solution and examined using optical microscopy.

Fracture stress was determined by four-point bending (4PB) testing in liquid nitrogen bath (-196°C) and at constant crosshead speed of 0.1mm/min, using notched Griffiths-Owen's specimens (12.7×12.7×80mm) with 45° notch angle and 0.25mm notch tip radius [8,9].

Scanning electron microscope (SEM) equipped with energy dispersive X-ray spectrometer (EDS) was used to examine fracture surface of the fractured 4PB specimens. Distance of the cleavage origin from the notch tip and cleavage facets diameters were measured from the SEM micrographs.

In order to provide data representing plastic response of the material at -196°C for FEM, uniaxial tension testing in liquid nitrogen bath was performed. Cylindrical specimens 5mm in diameter and with 30mm gauge length were used. The specimens were tested at constant crosshead speed of 0.1mm/min, giving the same order of magnitude of the true strain rate as in 4PB testing. True stress-true strain curve was plotted by non-linear polynomial regression of experimental data.

Elastic properties of the material were represented by Young's modulus of E=210GPa and Poisson's ratio of v=0.28.

Finite element analysis was performed using ABAQUS software package. Stress and strain distribution along the distance from the notch tip of the 4PB specimen was calculated using both 2D and 3D FEM, for the purpose of comparison.

Due to symmetry, only half of the 4PB specimen was modeled in the case of 2D FEM. Plane strain conditions were assumed. Quadratic eight node plane strain element type with full integration was used (CPEG8). Mesh was most refined along the notch tip, with minimal element size of $2 \cdot 10^{-3}$mm. Largest element size was 2mm. Total number of elements was 21746. 2D model assembly with meshed part is shown in Figure 1.

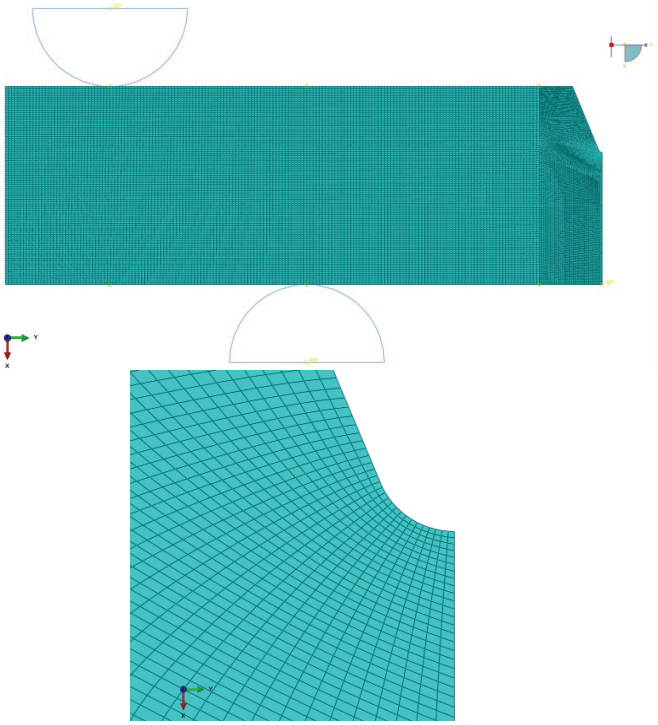

Fig. 1. 2D FEM assembly with the meshed 4PB specimen model part (left). Detail of the mesh at the notch tip of the specimen model (right).

In 3D FEM one quarter of the 4PB sample's geometry was analysed. Hexagonal eight-node element type with reduced integration was used (C3D8R). General element size was defined as 1. Mesh was gradually refined at the notch tip, down to 0.05 and at the supports to 0.2. Details of the meshed 3D model part are shown in Figure 2.

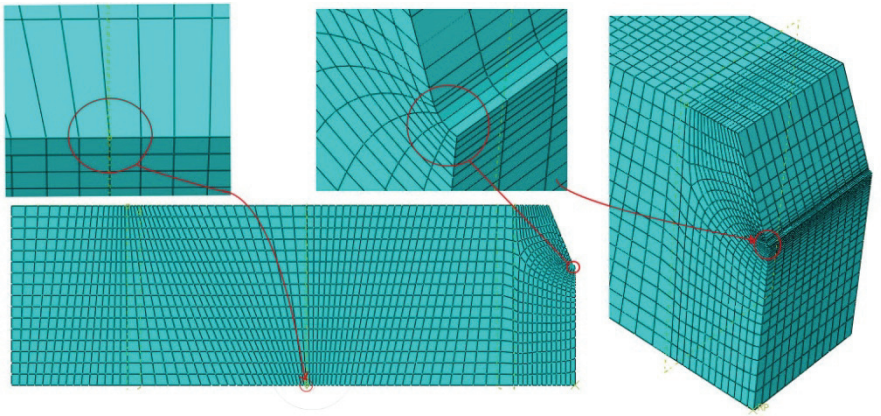

Fig. 2. Details of the 4PB specimen 3D model mesh.

In both models loading of the specimen was simulated by incremental translation of cylindrical supports that were defined as analytical rigid body in surface-to-surface contact with the part. Position of the supports is indicated in Figure 1.

Local cleavage fracture stresses and strains were determined from the stress and strain distribution curves at the distance of the cleavage origin from the notch tip. Effective surface energy was calculated according to Griffith's equation:

$$\sigma_F^* = \sqrt{\frac{\pi \cdot E \cdot \gamma}{(1-\nu^2) \cdot D}} \tag{1}$$

where σ_F^* is local cleavage fracture stress, γ – effective surface energy, *D* – diameter of the microcrack, *E* – modulus of elasticity and *v* – Poisson's coefficient.

Results

Typical microstructure of the steel shown in Figure 3 consists of proeutectoid ferrite along former austenite grain boundaries, acicular ferrite that occupies most of the former austenite grain interiors and pearlite placed as a layer between them. An example of allotriomorphic ferrite with Widmanstätten ferrite side plates is also marked at micrograph, Figure 3.

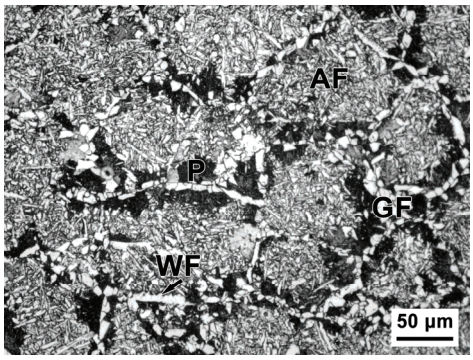

Fig. 3. Microstructure of the steel: AF–acicular ferrite, GF–grain boundary ferrite, P–pearlite and WF–Widmanstätten ferrite plates.

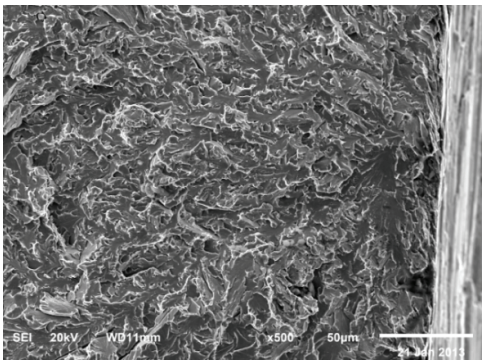

Fig. 4. SEM micrograph of the cleavage origin in 4PB specimen.

Fracture surface in the region of cleavage origin, near the notch tip is shown at SEM micrograph in Figure 4. Chevron shaped traces are clearly visible and could be easily traced back to the cleavage initiation site very close to the notch tip.

Stress and plastic strains distributions in front of the notch tip calculated by 2D and 3D FEM are compared in Figure 5.

Values of peak stresses, σ_{1max}, local cleavage fracture stress, σ_F^*, normalized by yield stress of the steel at -196°C, σ_0=775MPa, and critical plastic strains at the point of cleavage origin are summarized in Table 1, alongside with maximum bending load, F_{max}, and nominal bending stress at fracture, σ_{nom}. In

addition, distance of the cleavage origin sites from the notch tip and effective diameters of the initial cleavage facet are given.

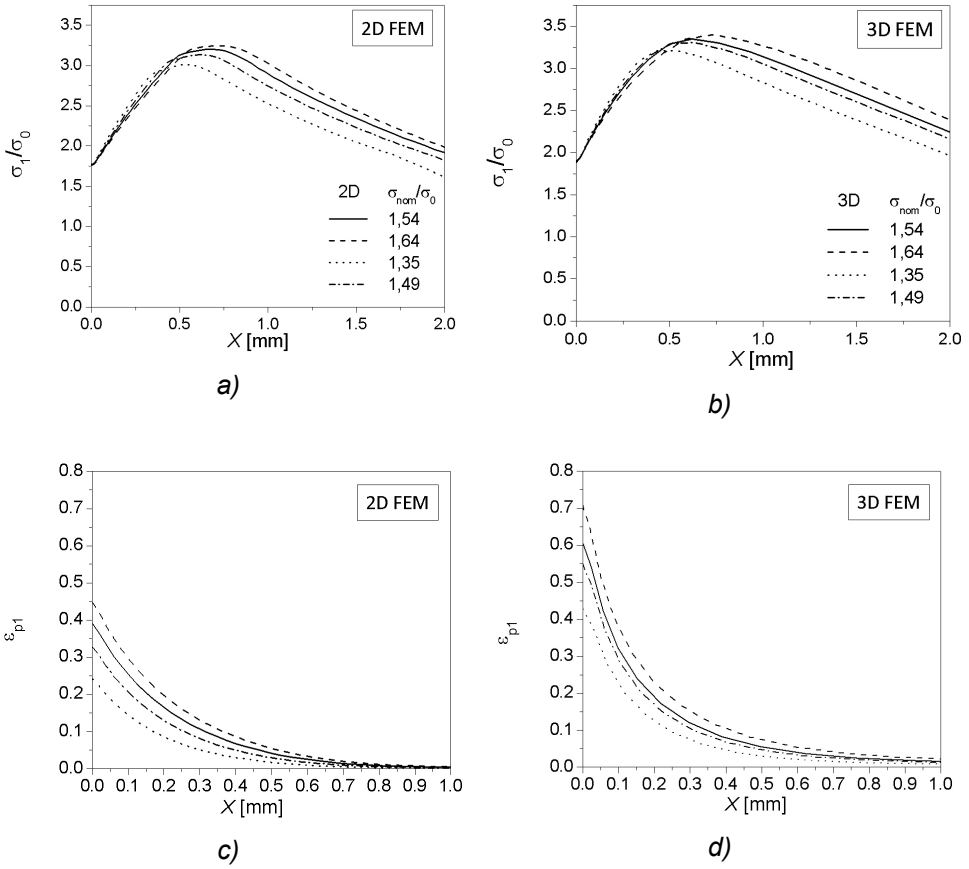

Fig. 5. Comparison of stress and strain distribution in front of the notch tip for 2D FEM (a, c) and 3D FEM (b, d).

Table 1. Fracture load, nominal fracture stress, peak stress and critical values of stress and plastic strain at the cleavage initiation site, determined by 2D and 3D FEM.

$F_{max.}$ [KN]	σ_{nom} [MPa]	σ_{1max}/σ_0 2D	σ_{1max}/σ_0 3D	X_0 [μm]	D_{eff}	σ_F^*/σ_0 2D	σ_F^*/σ_0 3D	ε_{pc} 2D	ε_{pc} 3D
28.5	1193	3.20	3.35	41.1	11.3	1.87	2.02	0.331	0.480
30.3	1268	3.25	3.40	12.2	27.0	1.77	1.87	0.431	0.670
25.1	1049	3.01	3.21	19.4	18.8	1.81	1.94	0.219	0.394
27.6	1152	3.14	3.31	54.0	21.2	1.92	2.08	0.258	0.397

Discussion

The values of maximal principal stress along the distance from the notch tip are somewhat higher in the case of 3D FEM than for the 2D FEM for all tested samples (Figures 5a and 5b). Considering higher stress intensification in the case of plane strain conditions, higher stress in 2D FEM is to be expected [4].

The difference of the peak stress values between 2D and 3D model ranges from 4.7% to 6.5%, what is in good agreement with previously reported values of 3.5%–7.5% [4]. Such relatively small discrepancies could be ascribed to the variations in adopted FEM parameters, such as meshing the part, applied load history, number of increments, geometry nonlinearity etc. In that manner, smallest finite element in front notch tip in this paper is 50μm, in referent work of Wang and coworkers it is 70μm [4]. Total number of finite elements is significantly higher in present work. It should be kept in mind, however, that no other details of FEM used were revealed by the authors. Thus, a general conclusion is that the selection of modeling process could affect the value of calculated stresses. In addition, in both cases parabolic work hardening behavior of the material at -196°C was modeled. Thus, it could be concluded that the aforementioned discrepancies are not a consequence of the method that plastic response of the material was incorporated in the model.

Differences in critical fracture stresses, σ_F^*, calculated using 2D and 3D FEM, given in Table 1, range from 5.6% to 9.0%. Those variations render the values of the effective surface energy, γ, of 49J/m^2 and 60J/m^2, for the 2D and 3D FEM respectively. Those values are in accordance to the results found in literature for medium carbon microalloyed steels [10,11]. It could be concluded that regarding stress calculation, plane strain 2D FEM could be considered as valid.

In the case of 3D model, lateral deformation takes place in narrow zone at the notch tip. The values of the true plastic strain in 3D FEM at the notch tip (distance X=0) are up to 0.71, while in the 2D FEM does not exceed 0.45 (Figures 5c and 5d). With increasing the distance from the notch tip, the plastic deformation is reduced as stress triaxiality increases and differences between values calculated by 2D and 3D FEM are diminishing.

The values of the critical plastic strain, ε_{pc}, i.e. plastic strain at the site of cleavage origin, determined using 3D FEM are by as much as 80% higher than for the 2D FEM. According to the results from the literature, in case of strain induced cleavage fracture, critical value of plastic strain, ε_{pc}, in circumstances of critical stresses triaxiality, should be considered in addition to the critical stress, σ_F^* [4]. In that case, application of 2D FEM with plane strain assumption seems unjustified and plastic strains should be calculated using 3D FEM.

Conclusions

- Stresses in front of the notch tip calculated by 3D modeling are somewhat higher than for 2D FEM.
- The values of maximal principal strain in front of the notch tip calculated by 3D FEM are considerably higher than for 2D FEM. Therefore, in the case of strain induced cleavage fracture, it is necessary to determine the value of critical strain by using 3D FEM.

- The values of critical stress for cleavage fracture calculated by 2D FEM render the value of effective surface energy of 49J/m^2, whereas in the case of 3D FEM, this value is 60J/m^2.

Acknowledgements

The authors are indebted to Ministry of Education and Science of Serbia for financial support (Project OI174004) and Serbian Oil Company for supplying experimental material.

Literature

[1] M.A. Linaza, J.L. Romero, J.M. Rodriguez-Ibabe, J.J. Urcola, Improvement of Fracture Toughness of Forging Steels Microalloyed with Titanium by Accelerated Cooling After Hot Working, Scripta Metall. Mater., 29 (1993) 1217.

[2] M.A. Linaza, J.L. Romero, J. M. Rodriguez-Ibabe and J.J. Urcola, cleavage fracture ofmicroalloyed forging steels, Scripta Metall. Mater., 32 (1995) 395.

[3] A. Echeverria, J.M. Rodriguez-Ibabe, Cleavage micromechanisms on microalloyed steels. Evolution with temperature of some critical parameters, Scripta. Mater., 50 (2004) 307.

[4] J.H. Chen, G.Z. Wang, Q. Wang, Change of Critical Events of Cleavage Fracture with Variation of Microscopic Features of Low-Alloy Steels, Metall. Mater. Trans. A, 33A (2002) 3393.

[5] Dragomir Glišić, Nenad Radović, Djordje Drobnjak, Abdunnaser Fadel, Critical stress for cleavage fracture in continuously cooled medium carbon V-microalloyed steel, Procedia Mater. Sci., 3 (2014) 1226.

[6] A. Echeverria, J.M. Rodriguez-Ibabe, The Role of Grain Size in Brittle Particle Induced Fracture of Steels, Mater. Sci. Eng. A, A346, (2003) 149.

[7] D. Glišić, Structure and Fracture of Medium Carbon Microalloyed Steels, PhD dissertation, Faculty of Technology and Metallurgy, 2013.

[8] J.R. Griffiths, D.R. Owen, An Elastic-Plastic Stress Analysis for a Notched Bar in Plane Strain Bending, J. Mech. Phys. Solids, 19 (1971) 419.

[9] D. Glisic, A. Fadel, N. Radovic, D. Drobnjak, M. Zrilic, Hem. Ind., 67 (2013) 981.

[10] M.A. Linaza, J.M. Rodriguez-Ibabe, J.J. Urcola, Determination of the Energetic Parameters Controlling Cleavage Fracture Initiation in Steels, Fatigue Fract. Eng. Mater. Struct., 20 (1997) 619.

[11] J.M. Rodriguez-Ibabe, The Role of Microstructure in Toughness Behaviour of Microalloyed Steels, Mater. Sci. Forum, 284-286 (1998) 51.

THE EFFECT OF MICROALLOYING PLATINUM WITH ZIRCONIUM AND TITANIUM ON ITS MECHANICAL CHARACTERISTICS

Biserka T. Trumic[1], Aleksandra T. Ivanovic[1], Sasa R. Marjanovic[2], Silvana B. Dimitrijevic[1], Stevan P. Dimitrijevic[3], Radoica V. Djalovic[1], Drasko S. Stankovic[1]

[1] Mining and Metallurgy Institute Bor, Zeleni bulevar 35, 19210 Bor, Serbia
[2]University of Belgrade, Technical Faculty, VJ 12, 19210 Bor, Serbia
[3]University of Belgrade, Innovation center of the Faculty of Technology and Metallurgy, Karnegijeva 4, 11000 Belgrade, Serbia

The paper presents the results of the investigations of mechanical characteristics of platinum microalloyed with zirconium, titanium and aluminum, as well as a comparative analysis in relation to pure platinum. It was investigated the effect of the addition of the above mentioned elements on the tensile strength (Rm), yield strength ($R_{p0.2}$), relative elongation (A) and the rupture time (t), both at room temperature and 1300 °C. There is a conclusion that microalloying platinum with Zr and Ti generally leads to a significant improvement of the mechanical characteristics of platinum on both the room and high temperatures.
Keywords: Pt-alloys, zirconium, titanium, mechanical properties

Introduction

Platinum and platinum metals are the elements of the eighth group of the periodic table of elements and belong to the so-called transition metals with partially filled d-4 (ruthenium, rhodium, palladium) and 5-d (osmium, iridium, platinum) electron orbital [1-5]. The consequence of such electronic configuration is a set of characteristic properties: increased corrosion resistance, fire resistance, a number of favorable physical-mechanical properties of platinum group elements. Due to the high cost of platinum and platinum metals researches in the world are very expensive and limited [6]. The subject of numerous studies were the stability of the platinum films and coatings at high temperatures [7-12]. Examination of the crystal structure and electrical properties of the platinum coating with Ti and Ta was the subject of the research of group of authors [13,14]. Special metallographic procedures for etching of samples on the basis of platinum and platinum group metals have been presented, as well [15]. The influence of plastic deformation and tempering on the mechanical properties of NiPt has been investigated [16]. The phase diagram of the system Pt-Zr has been studied and designed to Zr content of 50% (at). It has been found the presence of broad area of solid solutions with Pt base, which are formed directly from the melt by a peritectic reaction at 1780 ^{o}C. The maximum solubility of zirconium in platinum is around 1 % (at). Forming of several intermetallic compounds has been discovered in the system. Phase diagram of Pt-Ti

system is under development. Interaction character of the components in the system is complex. It has been found the presence of a range of chemical compounds, wherein some of them (TiPt) have the polymorphic character. The solubility of titanium in the platinum is around 18 % (at.), and the solubility of the platinum in the titanium at 840 ^{o}C is less than 5 % (at.).

Experimental techniques

Platinum for making alloys was obtained as a by-product in the production of electrolytic copper RTB, Serbia. By additional refinement it was achieved the necessary purity (99.95%). Impurities in the tested samples were characteristic for the raw material of Bor sites - Pd, Ag, Au, Bi, Sb, As, Cu. Melting of samples was carried out in the medium-frequency induction furnace. Annealing of samples was carried out in an electric furnace type LP08. To test the mechanical characteristics the device Mayes MK2 TC/10 was used. Chemical analysis of the material for samples was performed in atomic absorption spectrophotometer. Changes in microstructure were observed in the optical microscope.

Results and Discussion

Platinum - zirconium (Pt-Zr)

This paper investigates the mechanical properties of platinum alloy with Zr content of 0.2 to 1 %, both at room temperature and at high temperatures.

Tests were conducted on recrystallized samples in form of wire with a diameter of 0.5 mm and a length of 500 mm. The results are shown in Table 1. For comparison purposes the mechanical properties of pure platinum are given, as well.

Table 1. Properties of platinum alloy with zirconium

Composition of alloys, %	**Recrystallization temperature, °C**	**R_m, MPa, at t°C**		**$R_{p0.2}$,MPa**
		20	1300	
Pt	700	191	21	187
Pt-0,27%Zr	800	360	48	278
Pt-0,57%Zr	1.050	429	53	288
Pt-1,07%Zr	1.100	480	62	306

Alloying with small quantities of zirconium strengthens pure platinum 2-3 times both at room temperature and at high temperatures. The increase of the recrystallization temperature is noticeable, too. At the same time, with an increase in strength of platinum plasticity increases, too, which is typical for alloys with titanium.

The oxidation was carried out on wire samples, as well as on the plate measuring 10x7x0,5 mm by the method of periodic weight measurements. The total duration of each experiment was 100 h.

In the process of oxidation of the platinum it was noticed decrease in mass, which is explained by evaporation of its oxides at the given temperatures.

With increasing content of alloying element mass loss is reduced, so that in the alloy with 1% Zr mass increase is already observed.

Alloy surface after oxidation was subjected to x-ray analysis. In the roentgenogram of alloys with 0.2 % Zr lines of ZrO_2 oxide are visible, which are more pronounced in the alloy with 1 % Zr. As in the case with titanium, zirconium has a higher affinity for oxygen in comparison to pure platinum.

This feature of zirconium is used for strengthening platinum by internal oxidation. Samples of Pt alloys with 0.2 and 0.75 % (at.) Zr in the form of tiles measuring 10x7x0,5 mm were subjected to oxidation in air at 1000 ^{o}C for a period of 48 h.

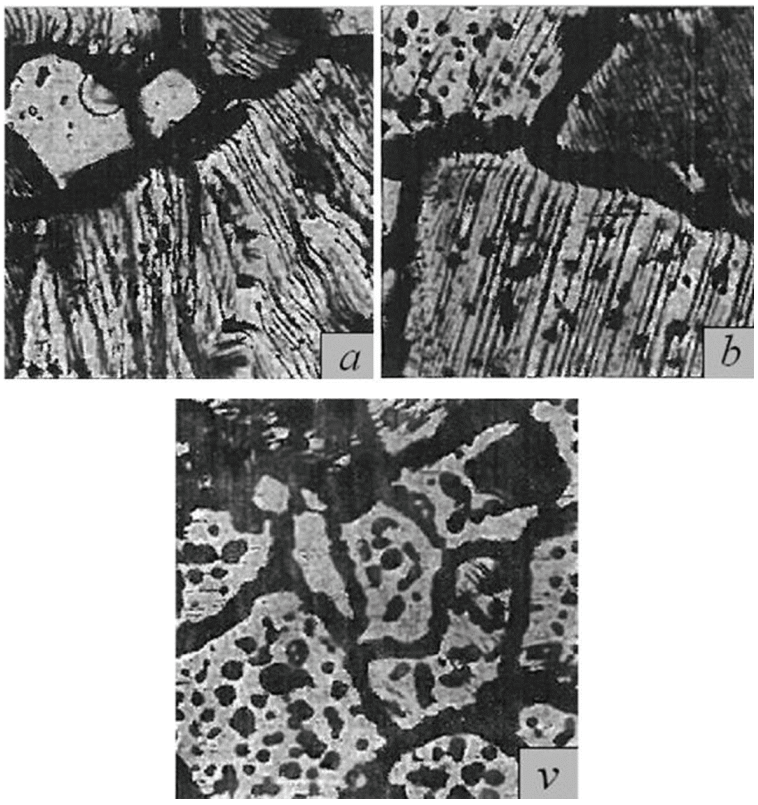

Fig. 1. The microstructure of the surface of the Pt sample (a) and its alloys with 0.2 % Zr (b) and 0.75 % Zr (v), after oxidation in air at 1000 ^{o}C during 48 h (magnification 450x)

The microstructure of the surface of samples of platinum and alloys after the specified treatment (1000 ^{o}C, 48 h) is presented in Figure 1. On the platinum surface it is noticeable characteristic relief appeared as a result of platinum oxide vapors when heated. The presence of oxides was noted on the surface of the alloys, while at alloys with 0.2 % Zr the evaporation of platinum can still be observed (which coincides with the character of the kinetic curves of oxidation). At the alloy with Zr content of 0.75 % it was observed the presence of zirconium oxide, while there is no evaporation of platinum, at all.

Platinum – titanium (Pt-Ti)

This research investigates the properties of alloys containing 0.05; 0.25 and 1.3 % Ti. Technical grade platinum was used to obtain these alloys . The properties of alloys were investigated on recrystallized wire with diameter of 0.5 mm and a length of 500 mm. The obtained results are shown in Table 2.

Table 2. Characteristics of platinum and its alloys with titanium

Composition of alloys, %	**Recrystall. temp., °C**	**HV**	**Hμ**	**$R_{m\ 20}$, MPa**	**A_{20}, %**	**R_m, MPa, at t, °C**		**Time to destruction, h**
						1300	1500	
Pt, technical grade	800	53,1	82,0	255	6,4	274	1,7	0,5
PtTi0,05	800	60,3	90,0	317	6,4	291	-	0,72
PtTi0,25	800	100,3	127,0	367	7,7	327	-	1,0
PtTi1,3	1000	250,1	286,0	564	9,0	453	275	5,6

Titanium significantly strengthens platinum both at room and high temperatures, where the strengthening effect is greater with a higher concentration of alloying element in the alloy. Simultaneously, with the strengthening of platinum the plasticity of the alloy increases.

It was also investigated the resistance of platinum alloys at high temperatures, in the air, with 0.2; 0.5; 2; 3 and 5 % (at.) Ti. The tests were performed at 1300 ^{o}C on the samples in the form of wire with diameter of 0.5 mm and a length of 500 mm. The samples were placed in a silicate furnace and after a specified time drawn out from it and weighed on an analytical balance. The total duration of each experiment was 100 h. The obtained results in the form of the kinetic curves of oxidation are shown in Figure 2.

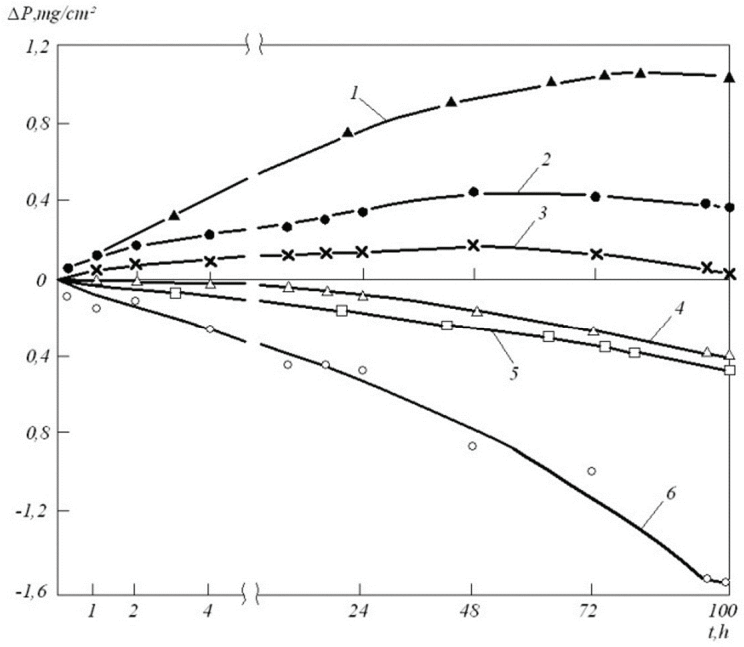

Fig. 2. Kinetic curves of oxidation of Pt-Ti alloys at 1300 °C:
1 - 5 % Ti; 2 - 3 % Ti; 3 - 2 % Ti; 4 - 0.5 % Ti; 5 - 0.2 % Ti; 6 - pure Pt

In the initial stage of the process (at annealing of 1 h) the ability to increase the mass is attributed to the oxidation of the titanium due to its higher affinity to oxygen as compared to platinum. At the same time evaporation of platinum occures. In a further short period it comes to an equilibrium between the processes of mass increase and the evaporation of platinum oxides.

By further extending the annealing time, up to 4 h, in alloys with a low content of titanium (0.2 and 0.5 % (at.)) evaporation of platinum predominates. In titanium alloys containing 2 and 3 % (at.) it was observed linear increase in mass to 48 h while in the alloy with 5 % Ti same phenomenon goes up to 100 h of oxidation.

Investigations of surface of oxidized samples by x-ray method showed the presence of titanium oxide, TiO_2, due to higher affinity of alloying element to oxygen compared to platinum.

Conclusion

Microalloying platinum with zirconium strengthens pure platinum 2-3 times, both at room temperature and at high temperatures. There is also an increase in recrystallization temperature. At the same time, with an increase in strength of platinum plasticity of platinum increases, too.

In the process of oxidation of the platinum it has been noticed a decrease in mass, which is explained by evaporation of its oxides at the tested temperatures.

With increasing content of alloying element mass loss is reduced, so that in the alloy with 1 % Zr mass increase is already observed.

Titan significantly strengthens platinum both at room and high temperatures, where the strengthening effect is greater with a higher concentration of alloying element in the alloy. Simultaneously, with the strengthening of platinum the plasticity of the alloy increases, as noted by microalloying with zirconium.

Acknowledgement

The research results presented in this paper are the result of technological development project TR 34029 "Development of production technology of Pd catalyst-catchers to reduce losses of platinum in high temperature catalysis processes", funded by the Ministry of Education, Science and Technological Development.

References

[1] H. Gavin, Platinum Met. Rev. 54 (2010) 166.
[2] E. Preston, Platinum Met. Rev.4 (1960) 48
[3] D.F. Lupton, J. Merker, B. Fischer, R. Völkl, Platinum Materials for the glass industry, 24th International Precious Metals Cconference, Williamsburg, Virginia, USA, 1–14 June 2000.
[4] Y. Ning, Z. Yang, H. Zhao, Platinum Met. Rev.4 (1996) 80.
[5] N. Yuantao, Y. Zhengfen, Platinum Met. Rev. 43 (1999) 62.
[6] B. Trumić, D. Stanković, V. Trujić, J. Min. Metall. Sect. B, 45 (1) (2009) 79.
[7] B. Wu, G. Liu, Platinum Met. Rev. 41 (1997) 81.
[8] M. Funabikia, T. Yamadaa, K. Kayanoa, Catal. Today 10 (1991) 33.
[9] B. Trumić, D. Stanković, N. Tomić, S. Šojić Danilović, Platinum based materials for jewellery manifacture, Copper, vol.33, 2 (2008) 35
[10] T. Biggs, S.S. Taylor, E. Van der Lingen, Platinum Met. Rev. 49 (2005) 2.
[11] John C. Wright, Platinum Metals Rev., 46 (2) (2002) 66.
[12] F. Xiao, F. Zhao, D. Mei, Z. Mo, B. Zeng, Biosens. Bioelectron. 24 (2009) 3481
[13] I. R. McGill, Platinum Metals Rev., 31 (2) (1987) 74.
[14] J. Luyten, J. De Keyzer, P. Wollants, C. Creemers, Calphad 33 (2009) 370.
[15] J. Luyten, C. Creemers, Surf. Sci. 602 (2008) 2491.
[16] Y. Chen, S. Liao, H. Deng, Appl. Surf. Sci. 253 (2007) 6074.

SLOW COOLING OF FLASH FURNACE AND CONVERTER SLAG-MICROSTRUCTURAL INVESTIGATIONS

Aleksandar Mihajlović[1], Milorad Gavrilovski[1], Željko Kamberović[2], Marija Korać[2], Nikola Jovanović[1]

[1]*Innovation Center of the Faculty of Technology and Metallurgy, University of Belgrade, Karnegijeva 4, Belgrade, Serbia*
[2]*Faculty of Technology and Metallurgy, University of Belgrade, Karnegijeva 4, Belgrade, Serbia*

Abstract

Technological procedure of slow cooling of smelting and converter slags is applied in order to increase overall copper recovery to the levels of 98.5% to blister copper. Presented research shows microstructural investigations on slowly cooled synthetic slags, and evaluation of following flotation possibilities. Achieved structure in both investigated samples presents fayalite and magnetite base with locally concentrated copper minerals of different composition, easily floatable. Additional benefit of converter slag slow cooling is separation of metallic copper at the bottom of ladle, which could be valorized through converter processing.
Keywords: slag, copper, slow cooling, microstructure

Introduction

In the primary copper production process, during technological operations of melting and converting, liquid slags are obtained. They represent molten oxide with small amounts of sulfides and metallic copper.

Slag from smelting contains significantly greater amount of copper than expected in an equilibrium state. Slag from converting, especially from the period of copper blowing, is typically inhomogeneous with significant amounts of suspended matte and metallic copper [1].

To achieve the technological exploitation of copper in the level of 98.5% to blister from concentrate using autogenous flash smelting technology, it is necessary to process the slag generated in the process both smelting and converting. Processing of smelting slag in the purpose of its "impoverishment" or better valorization of copper can be done in several ways [2]: by flotation or by smelting in electric-arc furnace.

Processing the slag by the scheme of slow cooling-crushing-grinding-flotation in order to obtain flotation concentrate rich in copper is recommended by BAT documents [3], if there is enough space and where there are conditions for adequate treatment of tailings.

Mineral composition and morphology of copper phases in slag have significant influence on further flotation process and are directly dependent on cooling method.

By using the flotation process, the best technological exploitation of copper is achieved, which is very important because the slag contains up to 6 to 7% of

mobile copper. Also, slow cooling on air or/and by water coagulation of dispersed copper and copper sulfide particles is promoted, additionally increasing overall copper efficiency.

The cooling metode of slag before flotation may have a significant impact on the achievement of flotation performance. Therefore, it is important to make the proper selection of cooling method of slag.

Experimental

Slag slow cooling simulation was performed experimentally as follows:

- melting of synthetic sample of flash furnace slag in electroresistant furnace and controlled cooling by defined regime,
- melting of synthetic sample of converter slag in electric arc furnace and controlled cooling by defined regime.

Synthetic samples used in the experiments were obtained by mixing the appropriate amounts of the starting components. In Table 1 and 2 are shown the amount and chemical composition of the starting components and the final chemical composition of the synthetic samples of flash furnace and converter slags.

Table 1. The amounts and chemical composition of components and synthetic sample of flash furnace slag

	weight, kg	Cu %	Fe%	SiO_2 %	Al_2O_3 %	CaO %	S %
reverberatory furnace slag 1	**16.90**	0.57	40.65	33.07	3.66	5.11	2.03
reverberatory furnace slag 2	**9.12**	0.62	40.98	32.7	3.95	4.94	2.1
quartz	**0.13**			100.00			
copper	**0.27**	100.00					
cast iron	**3.58**		100.00				
total	**30.00**	**1.40**	**47.30**	**29.00**	**3.26**	**4.38**	**1.78**

Table 2. The amounts and chemical composition of components and synthetic sample of converter slag

	weight, kg	Cu %	Fe %	SiO_2 %	Al_2O_3 %	CaO %	S %
slag from the converter, current	**25.00**	2.78	51.95	25.03	1.11	0.23	1.86
quartz	**1.02**			100.00			
copper	**0.92**	100.00					
cast iron	**0.56**		46.55				53.45
total	**27.50**	**5.87**	**48.18**	**26.46**	**1.00**	**0.21**	**2.78**

The first experiment was performed with the synthetic sample of flash furnace slag. The experiment was performed in electric arc furnaces. The furnace was loaded with the reverberatory furnace slag 1 and 2 whose quantity and composition are shown in Table 1. When slag was melted, other components shown in Table 1 were loaded into the furnace. When all of the components were melted and a homogenous melt was created, the content of the furnace was poured into the crucible. The slag obtained in this way represents synthetically generated sample of slag which, by its composition corresponds to the slag from the flash furnace. After pouring, slag was left in the pot to cool for 24 hours. The crucible was previously isolated with thermal wool in order to achive slow cooling of slag.

The second experiment was performed with the synthetic sample of converter slag. The experiment was performed in electoresistant furnace. The converter slag (Table 2) has been loaded in a furnace crucible. The furnace was heated up to 1250 °C and the temperature was maintained until all of the slag was melted. Other components, shown in Table 2, were charged in the molten slag and the temperature is maintained on 1250 °C until melting of all the components and creating a homogenous melt. Thereafter, the furnace was programmed to slowly cool new synthetically generated slag, which in its composition corresponds to the converter slag, to room temperature for 24 hours.

Samples of slag from the flash furnace the converter after melting according to specified regime, are shown in Figures 1 and 2. As shown in Figure 2, after cooling the converter slag, it was noticed separation of metal bottom plate at the bottom of the crucible. In order to determine the chemical composition of obtained slag sampling was performed at predefined locations, as presented in Figures 1 and 2.

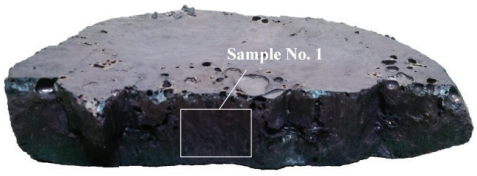

Fig. 1. The cooled slag from the flash furnace with marked location of sampling

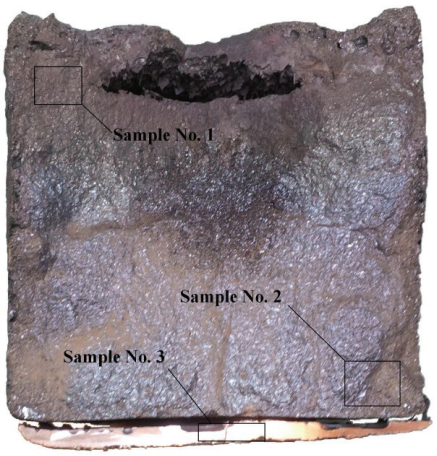

Fig. 2. The cooled slag from the converter with marked locations of sampling

The chemical composition of samples, determined by XRF method, is shown in Table 3.

Table 3. The chemical composition of samples

Element		FSF slag no. 1	PSC slag no. 1	PSC slag no. 2	PSC slag no. 3
Fe	%	49.54	52.45	52.84	1.80
Mn	%	0.27	0.17	0.16	*n.d.*
Cu	%	0.81	0.42	0.68	89.89
Zn	%	1.11	2.23	3.16	3.16
Pb	%	0.16	0.15	0.35	3.20
Ni	%	0.02	0.02	0.02	0.53
Sb	%	*n.d.*	*n.d.*	*n.d.*	0.29
Sn	%	*n.d.*	*n.d.*	*n.d.*	0.85
Rb	ppm	26	12	49	
Sr	ppm	104	20	49	
Zr	ppm	66	24	90	
Mo	ppm	627	130	289	
Hg	ppm	*n.d.*	116	169	
As	ppm	127	*n.d.*	235	
Se	ppm	37	*n.d.*	43	

The phase composition and morphological characterization of samples of slag from the flash furnace and converter was performed by optical microscopy. Some typical fragments of the samples are shown in Figures 3, 4 and 5.

Mineralogical composition of slowly cooled slag is the same as in slags that are disposed to the tailings. But, structural and textural characteristics, as well as level of crystallized minerals without glass phase mark it as entirely different.

Base of mineral composition are idiomorphic fayalite and magnetite particles and pronounced concentration of copper minerals (halcopyrite, bornite, metallic copper and rare pyrite, chalcosine, and covellite).

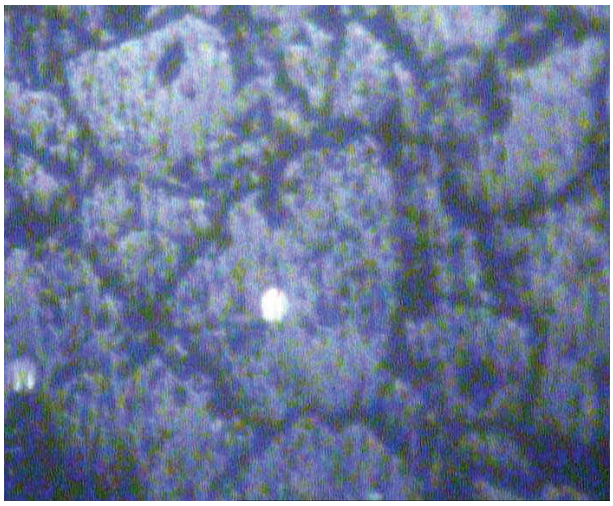

Fig. 3. Optical microscopy, FSF slag no 1

In Figure 3 crystallization of magnetite could be seen with separation of metallic copper after controlled cooling of slag.

Fig. 4. Optical microscopy, converter slag no 1

From Figure 4 fayalite crystallized in dendritic form is observed with separated copper minerals.

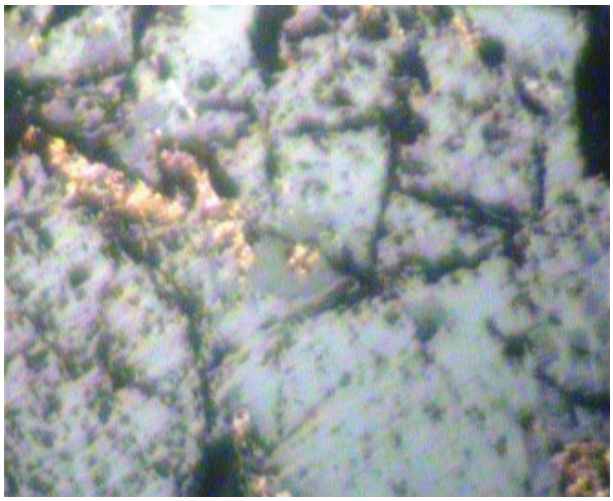

Fig. 5. Optical microscopy, converter slag no 2

In Figure 5, octahedral magnetite base could be noticed with locally concentrated copper minerals of different composition on periphery of magnetite particles.

Conclusion

By slow cooling of both FSF and converter slag in ladles, increase of mineral phases crystallization occur, which leads to increased copper yield during flotation process. During slow cooling of converter slag, due to the higher copper content, copper is collected at the bottom of the ladle and could be valorized through converting process, additionally increasing overall process copper efficiency. Fayalite and magnetite base of both slags are easily milled, increasing the flotation process productivity.

Acknowledgements

This work was financially supported by the Ministry of Education, Science and Technological Development of the Republic of Serbia and is a result of projects No. 34033.

References

[1] Heikki Jalkanen, Jouni Vehvilainen, Jaakko Poijarvi,Copper in solidified copper smelter slags, Scandinavian Journal of Metallurgy, 32 (2003), 65-70

[2] X. Wang, D. Geysen, S.V. Padilla T., N. D'Hoker, S. Huang, P.T. Jones, T. Van Gerven, B. Blanpain, Fayalite Based Slags: Metal Recovery and Utilization, 2nd International slag valorization symposium, Leuven, Belgija, 18-20 april, 2011

[3] Integrated Pollution Prevention and Control Reference Document on Best Available Techniques for the Non-Ferrous Metals Industries, Final Draft (October 2014)

ELECTROCHEMICAL SYNTHESIS OF PROTECTIVE POLYANILINE COATING ON ALUMINUM

Waleed Omymen, Ayad Salem, Milica Gvozdenović,
Branimir Grgur, Branimir Jugović[1]

Faculty of Technology and Metallurgy, University of Belgrade, Karnegijeva 4, 11120 Belgrade, Serbia
[1]Institutr of Technical Science, SASA, Knez Mihajlova 35/IV, 11000 Beograd, Serbia

Abstract

Electrochemical synthesis of polyaniline (PANI) film on aluminum electrode from aqueous solution of 0.20 mol dm^{-3} sodium benzoate containing 0.25 mol dm^{-3} aniline were investigated under potentiodynamic and galvanostatic conditions. Initial corrosion behavior of aluminum and PANI coated aluminum electrode exposed to 3% NaCl were investigated using electrochemical potentiodynamic and impedance spectroscopy technique (EIS). It was shown that PANI coating had provided corrosion protection of aluminum, decreasing the corrosion current density at least 15 times.
Key words: polyaniline, electrochemical synthesis, corrosion, aluminum

Introduction

In the last decade research in the area of electroconducting polymers (ECP) has been attracting considerable attention. Unique properties of ECP make them useful in the wide range of possible applications: microelectronic, optoelectronic, rechargeable batteries, and active corrosion protection as well [1,2]. Strategy of corrosion protection of construction metals is related to formation of coating systems in which chromium contained primers and pretreatment, as a source of both environmental and health threats could be replaced using ECP. ECP can be obtained by both chemical and electrochemical oxidative polymerization. However, electrochemical synthesis is favorable, permitting synthesis without oxidizing agent followed by doping with organic and inorganic ions in one step. Also, electrochemical technique, by setting the conditions, can produce both powders and films. CP can easily be electrosynthesized on inert anodes such as platinum, gold or glassy carbon, but this procedure is more difficult at common metals. The basic problem related to electrochemical synthesis of ECP on aluminum is connected to the fact that during the polymerization two simultaneous processes occur on the anode: electrochemical polymerization and deposition of CP and passivation of the electrode by stable protective oxide [3]. Among large number of CP, polypyrrole (PPY) and polyaniline (PANI) are the most studied for the purpose of the corrosion protection in general. There are reports on successful electrochemical synthesis of PPY on aluminum and its alloys [4-8]. There are also lot of studies concerning the use of PANI for the corrosion protection of aluminum and aluminum alloys. Most of the studies are dealing with PANI coatings obtained

by casting the polymer from the solution. Different forms of PANI were used. For example, PANI in the form of emeraldine salt was investigated for the corrosion protection of Al 3003, Al 2024-T3 alloys [1,9,10]. Emeraldine base was also used on Al 3003 and Al 2024-T3 [9,11] and AA 5182 alloys [12]. Racocot at al. reported corrosion protection of aluminum alloys by double-stranded PANI coating [13]. There are fewer studies dedicated to direct electrochemical synthesis of PANI on aluminum. Eftekary reported electrochemical synthesis of PANI from sulfuric acid and aniline solution on enzyme modified aluminum electrode [14]. Conroy and Breslin electrodeposited PANI on pure aluminum electrode using tosylic acid solution containing aniline, they pointed out strong dependence of applied potential and monomer concentration on electrodosition process [15]. Huerta-Vilca et al. investigated conditions for PANI deposition on aluminum from sulfuric acid solution pretreated with alizarin [16]. Wang and Tan studied electrodeposition process of PANI from tosilyc acid solution on chatodically pretreated AA 1100 alloy, using wire beam electrode [17]. Kaprpagam at al. electrodeposited PANI coating on Al 2024 T6 alloy from oxalic and aniline solution [18]. It can be concluded that there is a growing interest in investigation of PANI for the purpose of corrosion protection of aluminum and aluminum alloys. The protection of PANI is evident although the role of PANI is still under investigation [1]. Bearing in mind that PANI can exist in different forms, both potential and pH dependent various factors including the nature of PANI and corrosion environment are shown to be important. The aim of this paper is to present some new findings about electrochemical polymerization of aniline from sodium-benzoate solution containing aniline, for the purpose of corrosion protection.

Experimental

Polyaniline (PANI) film on aluminum electrode was obtained by electrochemical synthesis from aqueous solution of 0.25 mol dm^{-3} aniline and 0.2 mol dm^{-3} sodium-benzoate under galvanostatic conditions in the current range of 0.5 - 2.0 mA cm^{-2}. Prior to use aniline (Aldrich) was distilled under argon atmosphere. Electrolyte was prepared using bi-distilled water. Aluminum sheet served as working electrode. Before all experiments aluminum electrode was first mechanically polished with fine emery papers (2/0, 3/0 and 4/0) and then with polishing alumina (1 μm, Banner Scientific Ltd.) on polishing cloths (Buehler Ltd.). The exposed surface area of aluminum electrode during electropolymerization was 2 cm^2. Corrosion behavior of aluminum electrode and PANI coated aluminum electrode exposed to 0.5 mol dm^{-3} NaCl were investigated using electrochemical impedance spectroscopy technique (EIS). While corrosion current density of aluminum and PANI coated aluminum in 0.5 mol dm^{-3} NaCl of were determined using potentiodynamic measurements. The working surface area of electrodes in EIS experiments was reduce to 1 cm^2 using Teflon holder in order to avoid the edge effects. The reference electrode was saturated calomel electrode (SCE), while platinum wire served as counter electrode. All measurements were carried out at the open circuit potential in the frequency range 50 mHz to 100 kHz. EIS instrumentation consisted of PAR263A potentiostat connected to PAR frequency response detector FRD100.

Results and discussion

Fig. 1 shows anodic polarization curves of aluminum electrode in 0.2 mol dm^{-3} Na-benzoate and with addition of 0.25 mol dm^{-3} aniline. In the pure sodium benzoate solution corrosion potential of ~ – 0.65 V was observed. After narrow region of active aluminum dissolution, region of passivity expends up to ~1.25 V, with the average passivity current density of ~ 40 μA cm^{-2}. At the potentials more positive than 1.25 V transpassive region probably connected with transformation in Al_2O_3 film together with oxygen evolution reaction was observed. In the presence of aniline in the solution, corrosion potential was shifted for ~ 0.22 V in negative direction. This result could be explained by inhibition effect of adsorbed aniline monomer on aluminum. The aniline polymerization starts at potentials more positive than ~ 0.6 V, and proceeded up to the potential of 3.5 V. Above potential of ~2 V slow oxygen evolution reaction was observed.

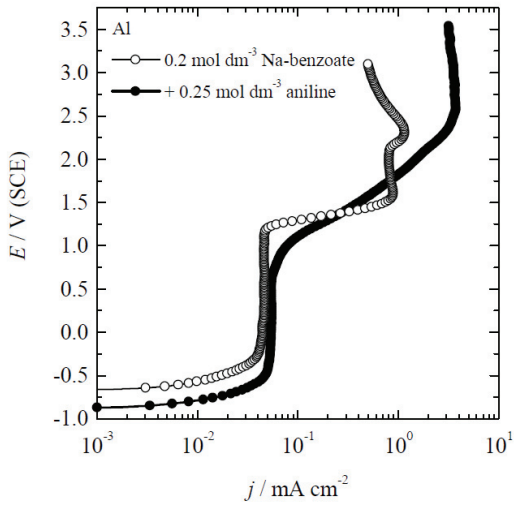

Fig. 1. Anodic polarization curves (v = 1 mV s^{-1}) of Al electrode in: (○) - 0.20 mol dm^{-3} Na-benzoate and (●) - 0.20 mol dm^{-3} Na-benzoate with 0.25 mol dm^{-3} aniline.

Galvanostatic curves of aluminum electrode in 0.2 mol dm^{-3} sodium benzoate and with addition of 0.25 mol dm^{-3} aniline for different current densities are shown on Fig. 2.

Without aniline in the solution, fast increase of the potential over time could be connected with formation of passive oxide layer and oxygen evolution reaction. With aniline in the solution, all curves have relatively stable potential plateau connected with polymerization and grow of the polyaniline. Since, only for the current densities of 1.5 and 2.0 mA cm^{-2}, PANI film was uniformly deposited on electrode, in order to avoid greater extent of degradation products and to achieve higher polymerization efficiency, for the further investigation PANI film obtained during 2400 s with current density of 1.5 mA cm^{-2} was used. The corresponding thickens of PANI film, assuming that density of benzoate doped PANI was similar

to sulfate doped PANI, ~1.5 g cm^{-3} [23] were estimated to be ~10 μm. On Fig. 3 Niquist complex plane spectra of aluminum and PANI coated aluminum electrode after 10 h of immersion in 3 % NaCl. It should be noted that after immersion in corrosion media, open circuit potential of PANI coated aluminum immediately drop near value of pure aluminum.

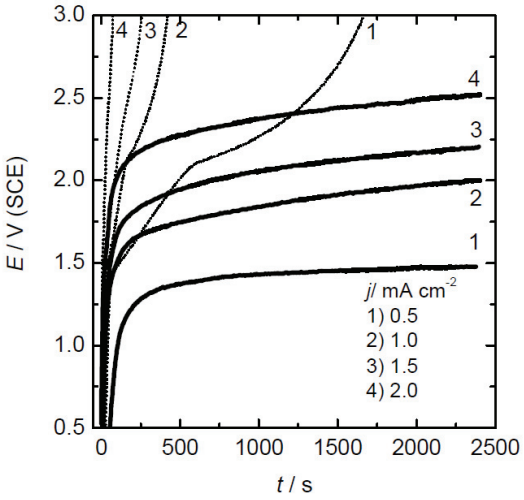

Fig. 2. Galvanostatic curves of Al electrode in: (…) - 0.2 mol dm^{-3} Na-benzoate and (Q) - 0.20 mol dm^{-3} Na-benzoate with 0.25 mol dm^{-3} aniline.

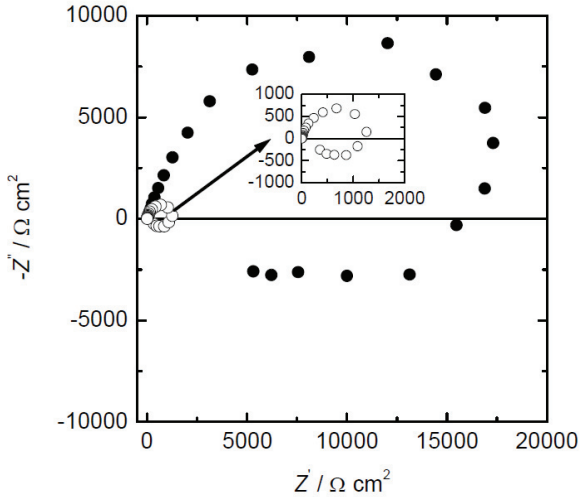

Fig. 3. Niquist complex plane spectra of: (○) - aluminum and (●) - PANI coated aluminum after 10 h of immersion in 3 % NaCl.

As it can be seen from Fig. 3, impedance spectra consist of one well defined depressed semicircle at high frequencies, while pseudo-inductive semicircle appeared at low frequency region. Similar corrosion behavior for aluminum alloys was observed in the literature, and could be connected to absorption of chloride ions [24]. Without further analysis of the data with equivalent circuit, it could be concluded that the value of the overall impedance for PANI coated aluminum was approximately 15 times greater than for the pure aluminum. Fig. 4 shows slow potentiodynamic (v = 1 mV s^{-1}) polarization curves of aluminum and PANI coated aluminum after 10 h of immersion in 3 % NaCl. Anodic polarization curves for pure aluminum and PANI coated aluminum are characterized by Tafel slopes of around 30 mV dec^{-1} and ~65 mV dec^{-1}, connected to anodic dissolution of aluminum, while chatodic polarization curves are under dominant mixed activation-diffusion control of oxygen reduction reaction. Corrosion current densities were estimated from the intercept of anodic Tafel lines with corrosion potential. For pure aluminum and PANI coated aluminum values of corrosion current density were 7.3 μA cm^{-2} and 0.35 μA cm^{-2} respectively, meaning that corrosion current density of pure aluminum electrode was decreased for more than twenty times in the presence of PANI coating.

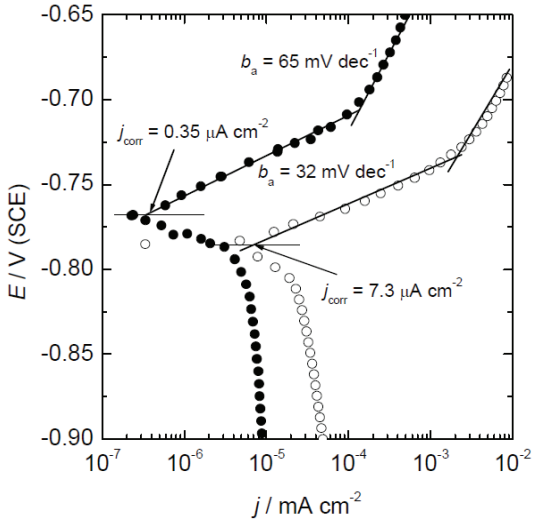

Fig. 4. Potentiodynamic polarization curves (v = 1 mV s^{-1}) (○) - aluminum and (●) - PANI coated aluminum after 10 h of immersion in 3 % NaCl.

Acknowledgment

This study was supported by the Ministry of Education, Science and Technological Development of the Republic of Serbia under the research project ON172046.

References

[1] D. E. Tallman, G. Sprinks, A. Dominis, G. G. Wallace, J. Solid State Electrochem. 6 (2002) 73.
[2] D. E. Tallman, G. Sprinks, A. Dominis, G. G. Wallace, J. Solid State Electrochem. 6(2002) 85.
[3] A. Malinauskas, J Malinauskien÷, A Ramanavičius, Nanotechnology 16 (2005) R51.
[4] S. Biallozor, A. Kupniewska, Synth. Met. 155 (2005) 443.
[5] P. Husler, F. Beck, J. Appl. Electrochem. 20 (1990) 596.
[6] F. Beck, P. Husler, J. Electroanal. Chem. 280 (1990) 159.
[7] D.E. Tallman, C. Vang, G.G. Wallace, G.P. Bierwagen, J. Electrochem. Soc. 149 (2002) C 173.
[8] S.B. Saidman, J.B. Bessone, J. Electroanal. Chem. 51 (2002) 87.
[9] K. Naoi, M. Takeda, H. Kanno, M. Sakakura, A. Shimada, Electrochim. Acta 45 (2000) 3413.
[10] D. E. Tallman, Y. Pae, G. P. Bierwagen, Corrosion 56 (2000) 401.
[11] N. A. Ogurstov, A. A. Pud, P. Kamarchik, G.S. Shapoval, Synth. Met. 143 (2004) 43.
[12] A. J. Epstein, J. A. O. Smallfield, H. Guan, M. Fahlman, Synth. Met. 102 (1999) 1374.
[13] L. Cecchetto, D. Delabouglise, J-P. Petit, Electrochim. Acta 52 (2007) 3485.
[14] R. Racicot, R. Brown, S. C. Yang, Synth. Met, 85 (1997) 1263.

CORROSION OF STEEL WITH COMPOSITE POLYANILINE COATINGS

Ayad Salem, Waleed Omymen, Branimir Jugović[1],
Milica Gvozdenović, Branimir Grgur

Faculty of Technology and Metallurgy, University of Belgrade, Karnegijeva 4, 11120 Belgrade, Serbia
[1]Institutr of Technical Science, SASA, Knez Mihajlova 35/IV, 11000 Beograd, Serbia

Abstract

The protective abilities of composite coatings based on chemically formed polyaniline-benzoate powder against the corrosion of mild steel were investigated. A polyaniline powder was prepared in the form of an emeraldine benzoate salt through chemical doping. The corrosion was investigated using an electrochemical impedance technique in 3% NaCl. Upon comparison between the corrosion behavior in 3% NaCl with commercial primer paint for iron and that with a paint containing 5 wt.% PANI, it was found that the composite coating has superior anticorrosion characteristics.
Keywords: Corrosion, Polyaniline, Composites, Benzoate.

Introduction

Polyaniline blends (composite coatings) are usually considered to be the best choices for protecting metals from corrosion. In these blends, polyaniline is highly dispersed in a classical polymer binder and can provide many advantages [1,2].

The emeraldine form of polyaniline has been the most thoroughly investigated. Emeraldine polyaniline occurs in two forms: doped (salt) and dedoped (base). Recently, it was reported that electrochemically synthesized polyaniline-benzoate thin films can protect mild steel from corrosion in different environments [14], and by Kamaraj et al. [15] found that vinyl paint-coated steel could be protected using one-percent polyaniline-benzoate. The conductivity of the benzoate-doped polyaniline was 0.155 S cm^{-1}. This study investigates composite coatings based on differently prepared polyaniline powders to assess the effects of the oligomeric structure content when protecting mild steel from corrosion. Based on these findings, the composite coating formulation was further optimized.

Experimental

The chemical synthesis of polyaniline was carried out at room temperature in 50 ml of 0.1 M H_2SO_4 with 1.86 g of aniline monomer. After stirring, 50 ml of 0.1 M H_2SO_4 containing 5.71 g of $(NH_4)_2S_2O_7$ was added dropwise. After 24 h of stirring, the green powder was filtered, washed several times with distilled water and acetone, and dried overnight. Synthesized PANI powder was treated with 1 M NH_4OH for 24 hours to obtain the emeraldine base. After washing with distilled

water and drying, the emeraldine base powders were treated with 0.1 M benzoic acid (pK_a=4.202, pH~2.6) at 70^{o}C due to its low solubility at room temperature for 12 hours to produce the polyaniline-benzoate doped emeraldine salt. The less corrosion-resistant paint (~3 g) was mixed with 1-10 wt.% of the ground polyaniline powders and applied onto a clean mild steel sample (MS, AISI 1212), 2×2, using a scalpel-based method. The coatings were 30±3 μm thick after drying. Those samples were used for impedance measuremants. A composite coating was prepared using the commercial TESSAROL®-Helios, Slovenia, which is a primer for iron based on an alkyd binder and red pigments in organic solvents, after diluting to 30 wt.% of solids using TESSAROL® thinner, The base primer and base primer modified with 5 wt.% polyaniline was applied using a scalpel-based method on both sides of a clean mild steel (12x5 cm) sample. The coatings were 60±5 μm thick after drying in the air for 24 h. The electrochemical impedance was measured using a PAR M273 potentiostat connected to a PAR 5301 lock-in amplifier; controlled by a computer through a GPBI PC2A interface. The impedance was measured at open circuit potentials from 10 mHz to 100 kHz. The UV-vis spectra of the samples dispersed in water were recorded using a LLG uniSPEC 2 spectrophotometer.

Results and Discussion

The UV-visible spectra of the different PANI samples in water from 190 to 1100 nm are shown in Fig. 1. The absorption peak at ~325 nm is assigned to the π–π* transition within the benzenoid ring, while the peak at ~700 nm is attributed to the molecular excitation associated with the quinoid-imine (Q) structure [3]. The strong sharp peak at 273 nm of chemically doped sample corresponds to the absorption of benzoic acid, and is ascribed to the π–π* transition in the benzoates, suggesting successful doping of emeraldine base. The strong peak at 388 nm is generated by the π–π* transition in the PANI chains [4]. Broad tail above at ~500 nm is associated with polaronic structures in the polyaniline [5, 6].

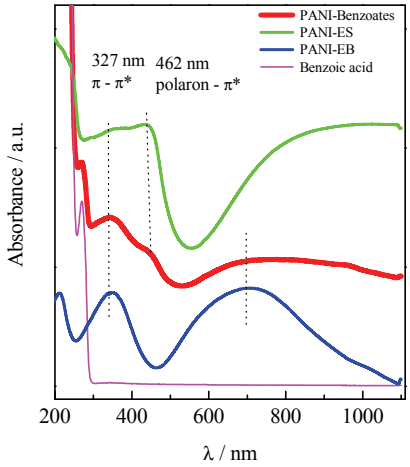

Fig. 1. UV-vis spectra of different PANI samples dispersed in water.

In order to optimize composite coatings the influence of ESC content was investigated. Base coating was mixed with 1, 3, 5 and 10 wt.% of ESC and electrochemical impedance measurements wre performed during the immersion in 3% NaCl corrosion solution. Figs 2a-c show development of the impedance spectra of different composite coatings during the immersion in 3% NaCl solution. It can be seen that impedance spectra are very complex, consisting of tree-overlapped semi-cycles. Overall impedance decreased with decrease of the polyaniline content in the composite coatings.

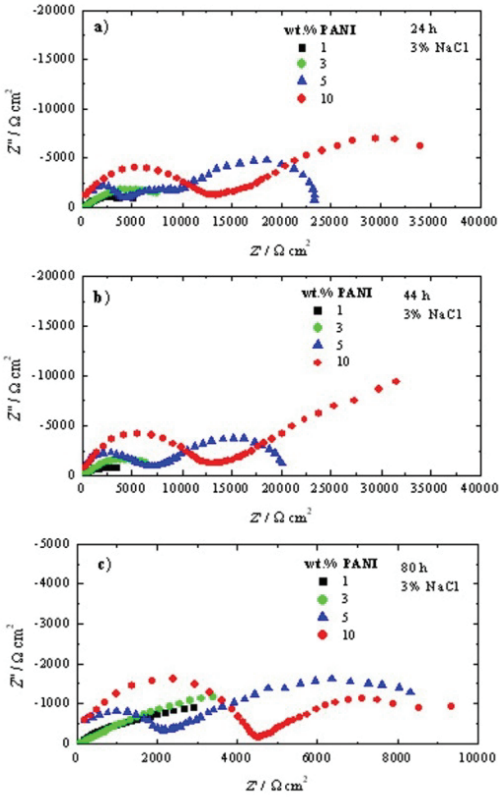

Fig. 2. Nyquist plots of the mild steel covered with 30 μm of the composite coatings after different times of immersion in 3% NaCl.

In order to obtain quantitative data for the corrosion protection processes, the impedance data were fitted with an electrical equivalent circuit, as presented in Fig. 3, with the corresponding physical model. Specifically, the corrosion of mild steel characterized using R_{corr} occurred in the bottom of the pores in the coatings (represented with R_p and C_p). The coating/solution interface can be described by the constant phase element (CPE_c), and the properties of the coating are associated with the film resistance (R_f). The film capacitance is represented by the constant phase element (CPE_f).

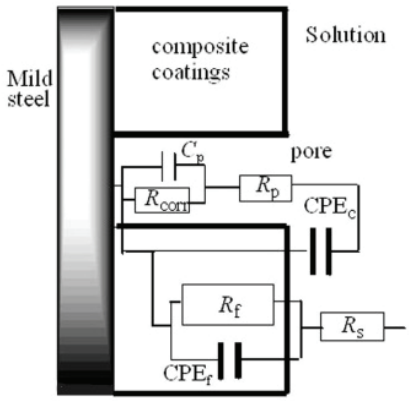

Fig. 3. Physical model of the proposed electrical equivalent circuit for corrosion processes of the composite coatings. R_s – solution resistance; R_f – coatings film resistance; CPE_f – coating constant phase element; CPE_c – coating/solution interface constant phase element; R_p – pore resistance; C_p – capacity of the pores; R_{corr} – corrosion resistance.

For the samples immersed for 48 h in 3% NaCl solution the dependence of the R_p and R_{corr} parameters are shown in Fig. 4. It can be seen that practically linear dependence was obtained. In the insert of Fig. 4 the calculated corrosion current density was shown, indicating that increase of PANI in the composite coatings increase the anticorrosion ability.

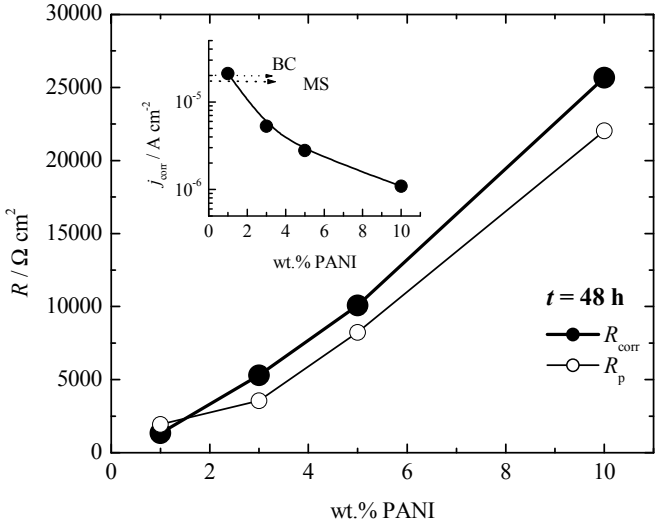

Fig. 4. Dependence of the R_p and R_{corr} for composite coatings with 1, 3, 5 and 10 wt.% of polyaniline after 48 h of immersion in 3% NaCl. Insert: Dependence of calculated current density on PANI content.

The composite coatings containing 5 wt.% of polyaniline and commercial TESSAROL®-Helios primer for iron paint were prepared and tested over 336 h in a 3% NaCl solution. An image of the samples after the corrosion test is shown in Fig. 5. The primer paint corroded and blistered, while the coatings delaminated. However, the primer paint with 5 wt.% of polyaniline remained practically unchanged.

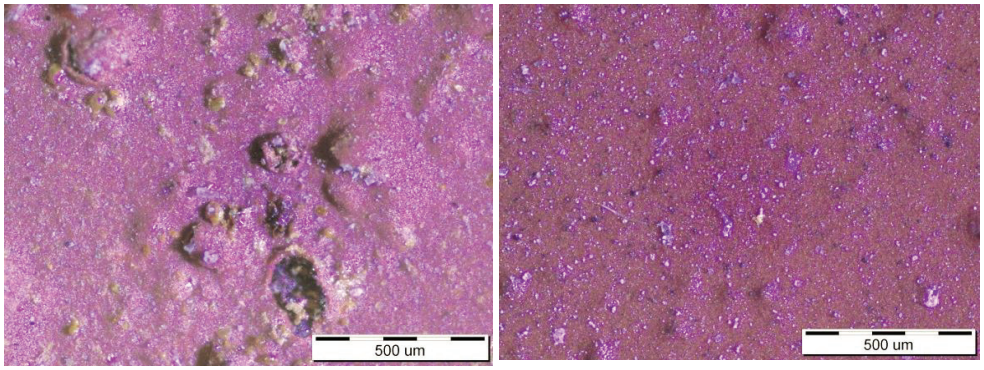

Fig. 5. Optical images of the samples after 336 h of corrosion in 3% NaCl. left: TESSAROL®-Helios primer for iron paint; right: primer for iron + 5 wt% polyaniline (based on dry paint).

Acknowledgment

This study was supported by the Ministry of Education, Science and Technological Development of the Republic of Serbia under the research project ON172046.

References

[1] J. Anand, S. Palaniappan, D. N Sathyanarayana, Conducting polyaniline blends and composites, Prog. Polym. Sci. 23 (1998) 993–1018.

[2] S. de Souza, Smart coating based on polyaniline acrylic blend for corrosion protection of different metals, Surf. Coat. Technol. 201 (2007) 7574–7581.

[3] A.R. Elkais, M. M. Gvozdenović, B. Z. Jugović, B.N. Grgur, The influence of thin benzoate-doped polyaniline coatings on corrosion protection of mild steel in different environments, Prog. Org. Coat. 76 (2013) 670– 676.

[4] K. Kamaraj, S. Sathiyanarayanan, S. Muthukrishnan, G. Venkatachari, Corrosion protection of iron by benzoate doped polyaniline containing coatings, Prog. Org. Coat. 64 (2009) 460–465.

[5] J.E. de Albuquerque L.H.C. Mattoso, R.M. Faria, J.G. Masters, A.G. MacDiarmid, Study of the interconversion of polyaniline oxidation states by optical absorption spectroscopy, Synth. Met. 146 (2004) 1–10.

[6] E. Jin, N. Liu, X. Lu,W. Zhang, Novel micro/nanostructures of polyaniline in the presence of different amino acids via a self-assembly process, Chem. Lett. 36 (2007) 1288-1289.

MICROSTRUCTURAL ANALYSIS OF CARBON STEEL AFTER SHIELDED METAL ARC WELDING PROCESS

Stjepan Kožuh[a], Mirko Gojić[a], Borut Kosec[b], Davor Lukač[c]

[a]*University of Zagreb Faculty of Metallurgy, Aleja narodnih heroja 3, 44103 Sisak, Croatia*
[b]*University of Ljubljana, Faculty of Natural Sciences and Engineering, Aškerčeva 12, 1000 Ljubljana, Slovenia*
[c]*PLINACRO d.o.o., Savska cesta 88a, 10 000 Zagreb, Croatia*

Abstract:

The aim of this paper was to determine the microstructure and hardness of welded joint of carbon steel API 5L X52. The pipe dimension ϕ219.1 x 5.6 mm is welded to the abutting V-joint. The root and filling passes as V-joint was performed by shielded metal arc welding (SMAW) process with electrodes type Boehler FOX CEL Mo with diameter of 2.5 and 3.2 mm. Analysis of the microstructure of welded joint was carried out by optical and scanning electron microscopy (SEM), respectively. The obtained microstructure was ferrite with less portion of pearlite. In microstructure of the weld metal regions with Widmanstatten`s ferrite was observed. The energy dispersive spectrometry (EDS) analysis showed sporadically presence of slag inclusions in the weld metal. The microhardness was measured in the base material, heat affected zone and weld metal. The hardness values of weld metal and heat affected zone were less than the base material.
Keywords: welding, carbon steel, microstructure, hardness

Introduction

The API 5L X52 steel (according to American Petroleum Institute specification) include seamless and welded steel line pipe. Mostly, this is steel for pipeline transportation systems in the oil industry (e.g. suitable for natural gas, water and oil). It is micro-alloyed steel (with elements Ti, Nb and V) which has satisfactory fine grains ferrite microstructure and mechanical properties (tensile strength, hardness, ductility and toughness) [1, 2]. Good weldability of these steels also contributes to their wide range of applications. Welding technology is particularly important in the construction of steel pipeline. Considering to the conditions under which welding can be performed (weather, atmospheric and field conditions) by shielded manual arc welding (SMAW) procedure emerged as a cost-effective, reliable and high-quality solution.

Because of the high heat input during welding in carbon steel a change of matrix may occur. By selecting of welding parameters and appropriate electrodes microstructural changes in the welded joint can be reduced.

In this paper the analysis of microstructure and hardness of the base material (BM), heat affected zone (HAZ) and weld metal (WM) of the welded carbon steel API 5L X52 was performed.

Experimental

The tested pipe was from API 5L X52 steel and it`s intended to be used for building the pipeline. Dimensions of the investigated pipe were ϕ 219.1 x 5.6 mm and length of 500 mm. The chemical composition of investigated steel is given in Table 1. The pipe is welded by shielded manual arc welding procedure of abutting V-joint. The electrodes used for welding procedure were electrodes type Boehler FOX CEL Mo with 2.5 and 3.2 mm in diameter. The chemical composition of electrodes was 0.1 %C, 0.14 %Si, 0.4 %Mn, and 0.5 %Mo (in wt.%) [3].

Table 1. The chemical composition of investigated steel, wt.%

	C	Mn	Si	Cu	V	Mo	Cr	Ni	Ti	Nb	Fe
BM	0.09	0.97	0.14	0.03	0.004	0.004	0.02	0.04	0.002	0.032	rest
WM	0.11	0.49	0.22	0.07	0.005	0.37	0.03	0.05	0.013	0.003	rest

The samples of dimensions 20x50 mm were cut for metallographic investigation. Sample preparation for metallographic analysis consisted of grinding and polishing. Grinding of samples was carried out with abrasive grit from 120 to 800 for a period of 5 minutes for each gradation. After grinding samples were polished with the addition of aqueous alumina Al_2O_3 (0,3 μm). Polishing time was 5 minutes. For revealing of microstructure of the samples etching in 5% solution of Nital (alcoholic solution of nitric acid) was used in the duration of 12 seconds. Microstructural analysis was carried out with an optical microscope (digital camera Olympus GX 51) and scanning electron microscope equipped with a system for EDS analysis (Tescan Vega 5136 MM). Vickers microhardness testing longitudinally across the sample was carried out on the LEICA VMHT device with indentation force of 9.804 N and duration for 10 sec.

Results and Discussion

Shielded metal arc welding (SMAW) process with coated electrode belongs to a group of fusion welding processes. Coated electrode provides good protection of weld metal and the good quality of the welded joint. Also, the thermal energy from the electric arc is used to melt additional material (electrode) and the base material. Fig. 1 shows a macrostructure of the welded joint of investigated steel on which can be clearly observed individual passes in filling of joints and difference in structure of the base material, weld metal and heat input zone.

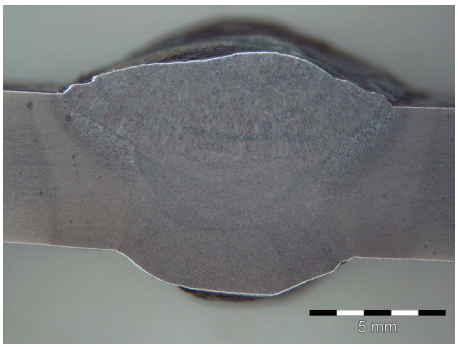

Fig. 1. Macrostructure of welded joint of API 5L X52 steel

In the weld metal, which is consisted from base and filler material, all metallurgical reactions take place. Cooling of such melt starts the solidification process of the weld metal and the formation of crystals. Figs. 2 and 3 shows microstructure of the base material, heat input zone and weld metal obtained by optical and scanning electron microscopes. The obtained microstructure is ferritic with some portion of pearlite. Also, in the microstructure of the weld metal sporadically forming regions of Widmanstatten`s ferrite are observed.

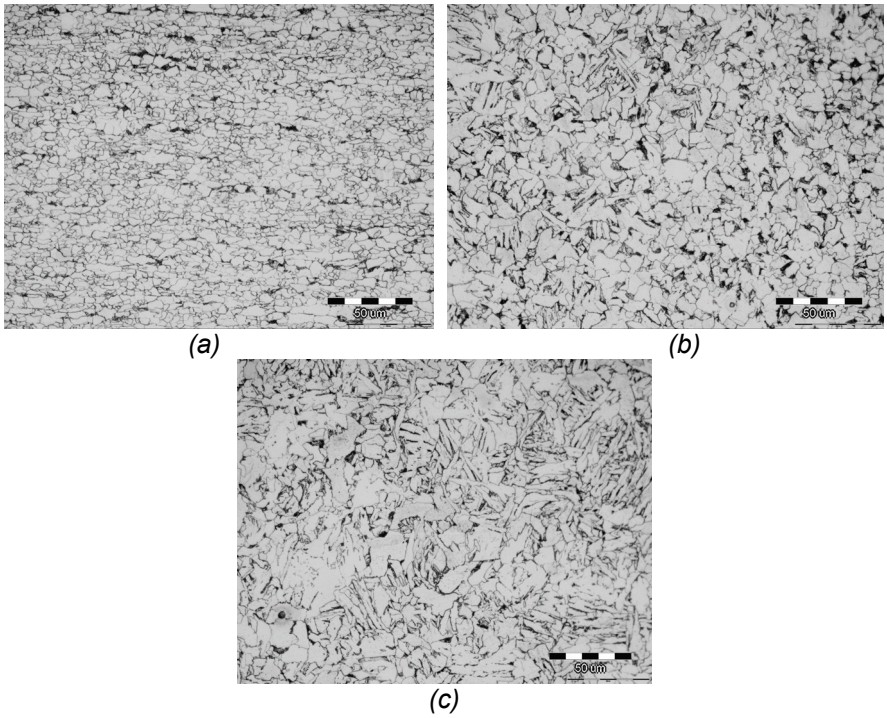

(a) *(b)*

(c)

Fig. 2. Optical micrographs of base material (a), heat affected zone (b) and weld metal (c) of the API 5L X52 steel

From the literature [4] is known that at higher cooling rates and smaller heat input the microstructure of weld metal can be consisted of proeutectoid ferrite, acicular ferrite and Widmanstatten`s ferrite. The increase in the heat input amount and decrease of cooling rate influence by appearance of higher portion of the proeutectoid and Widmanstatten`s ferrite in the microstructure on account of reducing the acicular ferrite. The crystal structure of weld metal is significantly different from the structure of base material, which is clearly visible on micrographs (Figs. 2 and 3). In the heat affected zone coarse grains can be observed. Also, detail EDS analysis showed sporadically presence of slag inclusions in the weld metal (Fig. 4). This complex inclusions contains about 73.3 %Fe, 11.3 %O, 8.9 %Si, 5.0 %Mn and 1.6 %Ti (in wt.%).

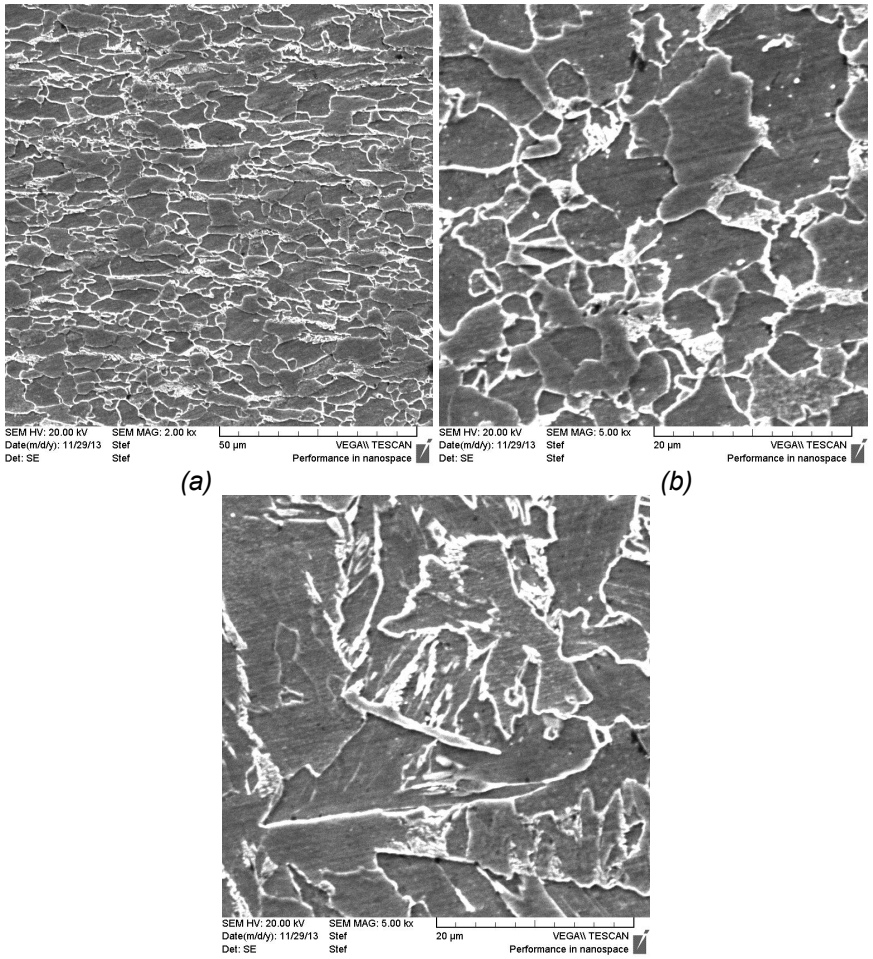

Fig. 3. SEM micrographs of base material (a), heat affected zone (b) and weld metal (c) of the API 5L X52 steel

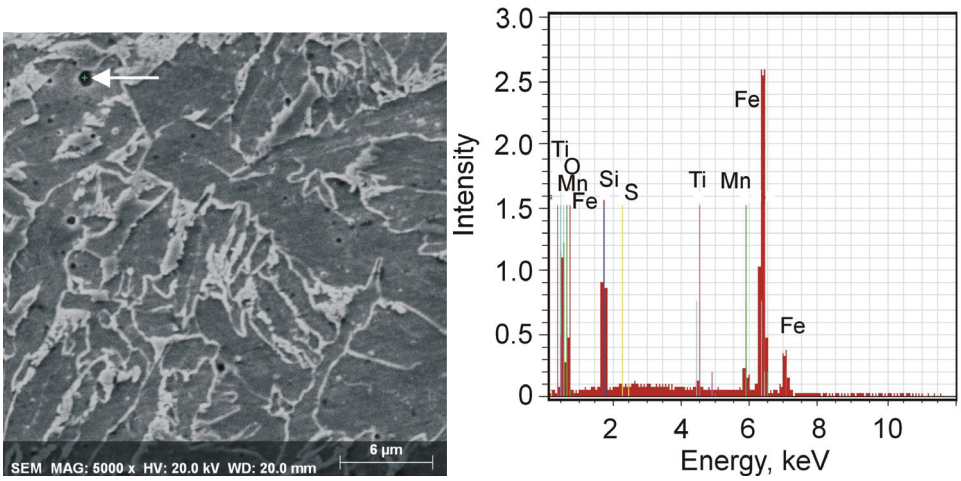

Fig. 4. The EDS analysis of inclusion in weld metal of the API 5L X52 steel

Certain heat input during welding process lead to a decrease in the microhardness of the HAZ, Fig. 5. Average values of microhardness were 199.8 HV for BM, 174.3 HV for HAZ and 188.8 HV for WM.

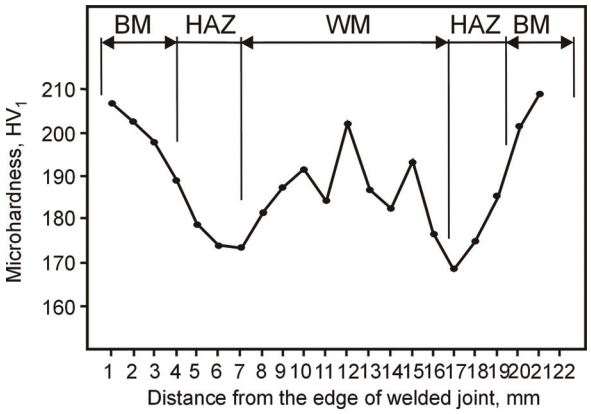

Fig. 5. Vickers microhardness distribution across the welded joint

Conclusions

On the basis of microstructure and hardness analyzes of welded steel API 5l X52 can be preformed following conclusions:

- Analyzed steel is most commonly used in the industry for construction building, pipeline etc., where welding procedure is a very important part of the process.

- Microstructural analysis of the welded joint showed the presence of ferrite and less portion of pearlite. In microstructure of the weld metal sporadically were observed regions with Widmanstatten`s ferrite.

- Also, the EDS analysis showed the presence of complex slag inclusion in the weld metal. This inclusions contains 73.3 %Fe, 11.3 %O, 8.9 %Si, 5.0 %Mn and 1.6 %Ti (in wt.%).

- Microhardness values of weld metal and heat affected zone are less than the microhardness of base material. The average microhardness of weld metal is lower about 11 HV and the heat affected zone about 25 HV in regard to base material (199.8 HV).

References

[1] B. Vargas-Arista, A. Balvantin, A. Baltazar, F. Garcia-Vasquez, On the use of ultrasonic spectral analysis for the characterization of artificially degraded API 5L X52 steel pipeline welded joints, Materials Science and Engineering A, **550** (2012) 227-234.

[2] B. Vargas-Arista, A. Albiter, C. Angles-Chavez, J.M. Hallen, Effect of Artificial Aging Time on the Mechanical Properties of Weldment on API 5L X-52 Line Pipe Steel, Metallurgical and Materials Transactions A, **37A** (2006) 2683-2670.

[3] Böhler Welding – welding guide, Böhler Schweiβtechnik Austria GmbH, 2001.

[4] R. Prokić-Cvetković, A. Milosavljević, O. Popović, Uticaj količine unete toplote na modifikacije ferita u metalu šava niskougljičnih čelika, Zavarivanje i zavarene Konstrukcije, **50** (2005) 2, 73-77.

EFFECT OF MERCAPTO SILANE CONCENTRATION ON CdS NANOPARTICLES STABILIZATION

Andjelika Bjelajac[1] , Rada Petrović[2], Jovan M. Nedeljković[3], Veljko Djokić[2], Tamara Radetić[2], Jovana Ćirković[4], Djordje Janaćković[2]

[1]*University of Belgrade, Innovation Center of Faculty of Technology and Metallurgy, Karnegijeva 4, 11120 Belgrade, Serbia*
[2]*University of Belgrade, Faculty of Technology and Metallurgy, Karnegijeva 4, 11120 Belgrade, Serbia*
[3]*Vinča Institute of Nuclear Sciences, University of Belgrade, P.O. Box 522, 11001 Belgrade, Serbia*
[4]*Institute for Multidisciplinary Research, University of Belgrade, Kneza Viseslava 1, 11030 Belgrade, Serbia*

Abstract

Cadmium sulfide (CdS) nanoparticles have wide application ranging from sensing to solar cells. Therefore it has been a challenge to control the synthesis parameters to obtain the CdS nanoparticles of desired characteristics. Within this study the stabilization of CdS nanoparticles was optimized by varying the concentration of mercapto silane (MS), used as a surfactant. The long term stable dispersions were obtained with 2 and 4 x 10^{-5} vol% of MS. Both the colloids showed the absorption onset around 485 nm. More detailed structural observation was employed via transmission electron microscopy with selected area electron diffraction detector. The results indicated that CdS nanoparticles are quasi-spherical with a mean diameter of 3.12 nm and the cubic structure for the nanoparticles stabilized with 2 x 10^{-5} vol% of MS, whereas the nanoparticles stabilized with 4 x 10^{-5} vol% of MS had a mean diameter of 4.15 nm and a mixed phase with a hexagonal predominate.

Keywords: Nanoparticles, Quantum Dots, Spectrophotometry, Electron microscopy

Introduction

Nanoparticles composed of hundreds up to few thousand atoms that show quantization of the energy levels to discrete values are called quantum dots (QDs) [1]. The quantum confinement effect results in an expansion of the band gap, thus shifting the absorption onset to lower value wavelenght. The strong enhancement of the Coulomb interaction between the charge carrriers arises the direct generation of multiexcitons by single photons. Such phenomena is known as carrier multiplication and it provides a remarkable variety of application [2]. Many studies in the field of sensing [3] and solar cells [4,5] are focused on selective size and morphology control of cadmium sulfide (CdS) quantum dots [6]. To insure the long term stability of the synthesized CdS colloids it is important to find an adequate stablization molecule that can also enable future application. The aim of this study was to analyze the effectiveness of the use of (3-mercaptopropyl)trimethoxysilane, $(OCH_3)_3Si\text{-}(CH_2)_3\text{-}SH$ (MS), which not only binds

to the CdS nanoparticle surface, controls growth and provides the stability against aggregation, but also acts as a linker to TiO_2 surface due to the bifunctional nature [7,8]. As reported in [9] the deposition of CdS onto TiO_2 leads to the enhancement of visible light absorption of TiO_2 photoanode in quantum dots sensitized solar cells. The goal of this study was also to investigate the effect of MS concentration on CdS nanoparticles phase composition.

The quantum effect was confirmed by measuring the apsorption of obtained colloids by UV-Vis spectrophotometer and the effective mass model (EMM) was employed for calculating the QDs size. To compare the estimated QDs size, transmission electron microscopy (TEM) analysis was done, whereas the phase detection was provided via selected area electron diffraction (SAED).

Experimental

To prepare the colloidal CdS QDs, similarly as in [10], 100 mL of $CdSO_4$ (0.2 mM) aqueous solution with 2 µl of MS, was put in a 3-neck 250 mL round-bottom flask that was placed in an ice bath on a stir plate while purging the solution with nitrogen gas. After 20 min of stirring and purging, the system was closed to the atmosphere and Na_2S aqueous solution was rapidly injected to a reaction mixture that instantly became pale yellow. The observed color corresponded to a CdS formation. A particular attention had to be taken in order to avoid the agglomeration and precipitation of CdS. Hence, the optimization of the capping agent quantity was made by repeating the procedure with 4 µl and 8 µl of MS. After the reactions, the solutions were observed and only those that stayed clear without any precipitates were further analyzed and used for sensitization. Herein, the stabilized CdS colloids were obtained with 2 and 4 µl of MS, whereas with 8 µl of MS the precipitation occured indicating the excess of MS. Therefore only the CdS colloids synthesized with 2 and 4 µl of MS were analyzed.

The absorbance of the colloidal CdS QDs was measured via Shimadzu 1800 UV-Vis spectrophotometer. The transmission electron micrographs and SAED patterns were obtained with the use of Jeol 3010, operating at 300 kV.

Results and discussion

The aim of this work was to obtain the stabilized CdS QDs colloids. It was primary to find an optimized quantity of MS for stabilization of colloid, since the increase of MS concentration results in increase in functionality to attach to TiO_2 surface, but the additional amount of MS in CdS synthesis causes the thickness of adsorbed MS layer onto CdS to increase and consequently the interparticle distance is decreasing while the silanol dangling groups react with the silanol groups from the neighbor particle resulting in Si-O-Si bonds that further has a flocculation of the suspension as a consequence [11].

Fig. 1 presents the absorption spectrum of the CdS colloid prepared with: a) 2 µl and b) 4 µl of MS. With respect to the absorption edge of the CdS in bulk (517 nm), the absorption shift towards the shorter wavelenght, which is due to quantum confinement effect, can be observed for both colloids. The absorption shifting is a result of electron confinement in all three dimensions of space that causes the band edges of nanoparticles whose crystallite is smaller than Bohr radius to break

up into discrete levels. Quantum confinement is responsible for the increase of energy difference between energy states and band gap. The size of CdS nanoparticles synthesized herein was calculated using EMM [12, 13] with the experimentally determined absorption onset: a) 486 nm and b) 482 nm taken as the intersection of the tangents with the wavelength axis in Fig. 1. The calculated size of CdS QDs are: a) 5.86 nm and b) 5.42 nm.

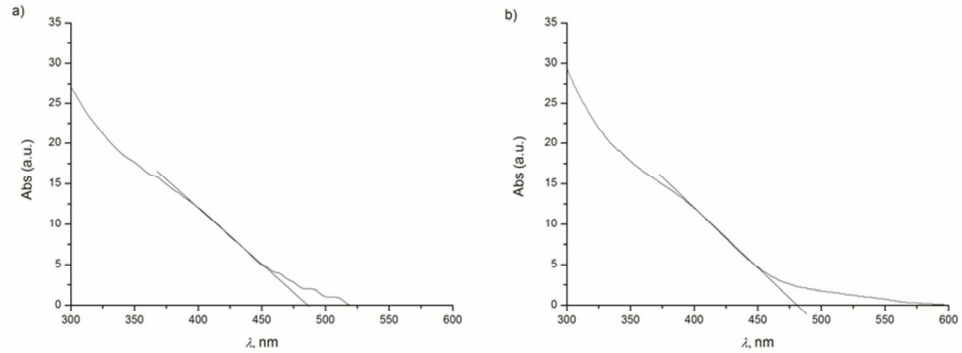

Fig. 1. Absorbance spectra of colloidal CdS QDs synthesized with: a) 2 µl of MS, b) 4 µl of MS

The calculated values using EMM are highly estimated due to possible experimental error in absorption onset reading. Therefore, the TEM analyzes were employed in order to obtained the QDs size more accurately.

Fig. 2 depicts the Dark Field TEM (DFTEM) micrographs of CdS nanoparticles, synthesized with: a) 2 µl and b) 4 µl of MS. The figure indicates that CdS nanopaticles are quasi-spherical and they are well dispersed. The size distribution of CdS nanoparticles was measured by manual counting from a population of about 120 particles per sample. Next to the DFTEM micrographs, the corresponding size distribution histograms are given. As seen from the histogram presented in Fig. 2a), the CdS QDs synthesized with 2 µl MS have a narrow size distribution with the diameter in the range of 2.03 – 4.39 nm with a mean diameter 3.12 nm, whereas histogram of the CdS QDs synthesized with 4 µl shows that the diameters are in range of 2.13 – 6.57 nm with a mean diameter of 4.15 nm. These results are in accordance with the experimental parameters taking into account that with the increase of MS concentration the thickness of adsorbed layer increases and thus, the size of nanoparticle also increases [14].

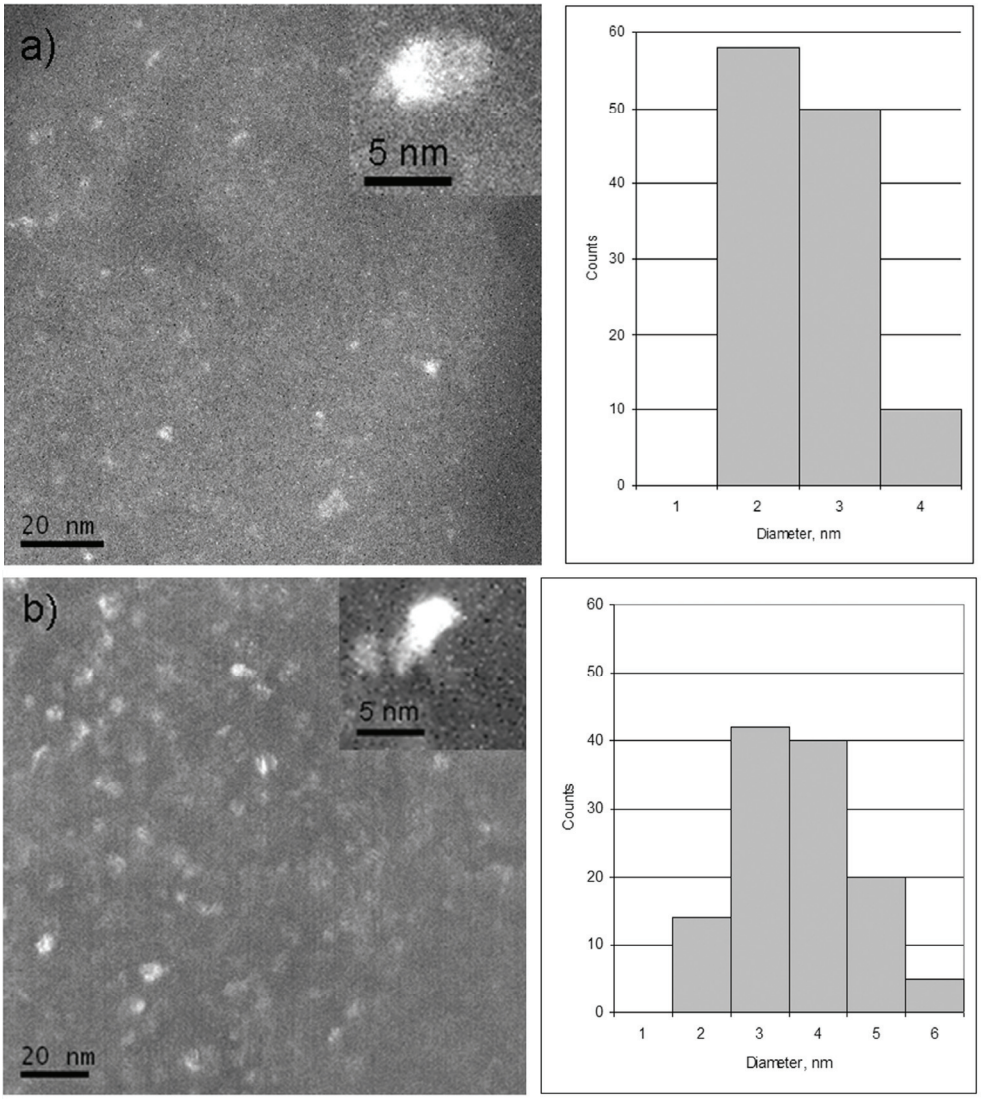

Fig. 2. The DFTEM micrographs with the corresponding histogram of size distribution of CdS QDs synthesized with: a) 2 µl and b) 4 µl of MS

The crystallographic information about the CdS colloids was obtained by interpreting the SAED patterns presented in Fig. 3. Firstly noticed from the patterns is that the CdS for both colloids is polycrystalline. Further, the measured interplanar distance ratios were compared with the standard values given in JCPDS card no. 80-0019 for cubic and JCPDS card no. 65-3414 for hexagonal structure. It can be concluded that the CdS synthesized with 2 µl of MS whose SAED pattern is given in Fig. 3a) has a cubic structure, whereas the CdS synthesized with 4 µl of MS whose SAED pattern is given in Fig. 3b) has a mixed

phase. The intensive rings characteristic for cubic phase are clearly visible in SAED pattern given in Fig. 3a), whereas in Fig. 3b) those rings are barely visible and the rings characteristic for hexagonal phase are dominant. This partial phase transition from cubic to hexagonal might be due to the internal compressive stress in the crystallite that decreases with the increase of the particle size. Thus, a smaller particle is expected to have a cubic phase, as in the case of CdS QDs synthesized with 2 µl of MS, whose mean diameter was estimated to be 3.12 nm, but with the particle size increase as showed for the CdS QDs synthesized with 4 µl of MS having a mean diameter of 4.15 nm, a hexagonal phase is predominat.

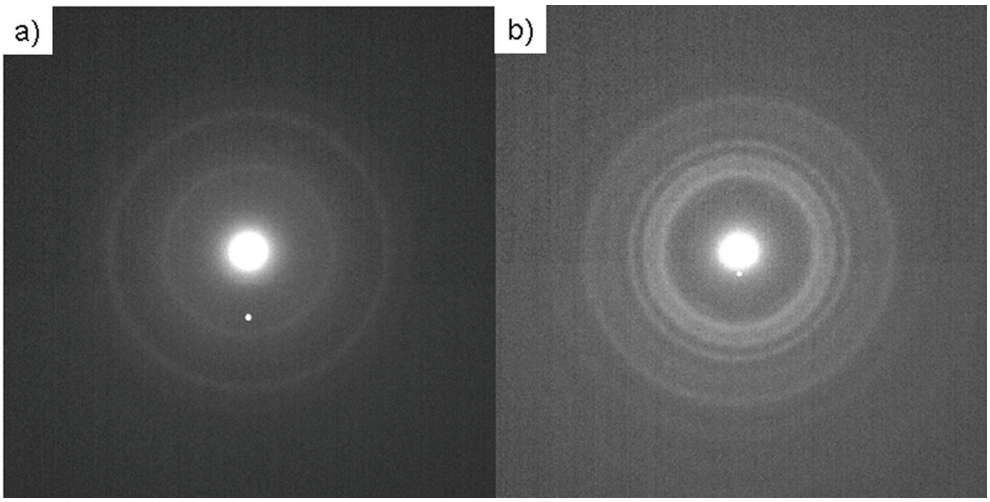

Fig. 3. SAED pattern of CdS QDs synthesized with: a) 2 µl and b) 4 µl of MS

These results illustrate the importance of the MS quantity in the synthesis of CdS QDs colloids, since it affects not only the CdS nanoparticles size but also to their phase structure.

Conclusions

In summary, the CdS quantum dots colloids were synthesized with (2 and 4) x 10^{-5} vol% of mercapto-silane (MS) which can acted as bifunctional linker for ex-situ sensitization of TiO_2. The absorption spectra of the obtained colloids confirmed the quantum confinement effect of CdS nanoparticles. The TEM and SAED analyzes provided the estimation of the QDs size to be ~ 3 nm for CdS QDs synthesized with 2 x 10^{-5} vol% of MS showing the cubic structure, whereas the CdS QDs synthesized with 4 x 10^{-5} vol% of MS were ~ 4 nm sized having the mixed phase with hexagonal dominant. This study showed that even that slight change of MS concentration can affect the CdS QDs size and what is more, it influences the phase composition.

Acknowledgements

The authors acknowledge with thanks the financial support of the Ministry of Education, Science and Technological Development, Republic of Serbia through the Projects III 45019.

References

[1] W. Russ Algar, Anthony J. Tavares, Ulrich J. Krull, Anal. Chim. Acta 673 (2010) 1–25
[2] A. J. Nozik, Chem Phys. Lett. 457 (2008) 3–11
[3] B. Fabbria, A. Gaiardoa, V. Guidia, C. Malagùa, A. Giberti, Procedia Engineering 87 (2014) 140–143
[4] W. Sun, Y. Yu, H. Pan, X. Gao, Q. Chen, L. Peng, J. Am. Chem. Soc. 130 (2008) 1124-1125
[5] P. V. Kamat, J. Phys. Chem. C 112 (2008) 18737–18753
[6] S. K. Haram, B. M. Quinn, A. J. BardJ. Am. Chem. Soc. 123 (2001) 8860-8861
[7] L. Spanhel, E. Arpac, H. Schmidt, J. Non-Cryst. Solids 147-148 (1992) 657-662
[8] S. Qian, C. Wang, W. Liu, Y. Zhu, W. Yao, X. Lu, J. Mater. Chem. 21 (2011) 4945-4952
[9] A. Bjelajac, R. Petrović, J. M. Nedeljković, V. Djokić, T. Radetić, J. Ćirković, Dj. Janaćković, Ceram. Int. 41 (2015) 7048–7053
[10]]J. M. Nedeljkovic, R. C. Patel, P. Kaufman, C. Joyce-Pruden, N. O'Leary, J. Chem. Educ. 70 (1993) 342-345
[11] M. Rahaman, Ceramic processing and sintering, Marcel Dekker Inc, NJ, 2003
[12] L. E. Brus, J. Chem. Phys. 80 (1984) 4403-4409]
[13] L. E. Brus, J.Chem. Phys. 79 (1983) 5566-5571
[14] C. J. Lin, Y. H. Yu, Y. H. Liou, Appl. Catal. B: Environ. 93 (2009) 119–125

ANALYSIS OF THE MICROSTRUCTURAL CONSTITUENTS OF ALUMINUM ALLOY Al-Mg IN CAST AND HOMOGENIZED STATE

Natalija Dolić, Karlo Štengl

University of Zagreb Faculty of Metallurgy

Within this work the effect of homogenization of samples taken from the end of aluminium alloy EN AW-5083 slab, cast by semi-continuous, vertical process with the direct water cooling (VDC process) on the development of the microstructure has been determined. In the experimental part the presence of precipitated phases on cast and homogenized samples were examined. By the quantitative analysis trough energy dispersive spectrometer (EDS) the following microstructural constituents have been determined: intermetallic phases Al_6(Fe, Mn) and Mg_2Si. Its results were compared with the thermodynamically calculated equilibrium phases obtained on the basis of the Thermo-Calc software. Also, the presence of pores has been determined. Distributions of some intermetallic phases and pores in dependence on homogenization time have been examined by light and scanning electron microscopy (SEM).
Key words: Al – Mg alloy, „Direct Chill process“, cast state, homogenization, microstructural characteristics

Introduction

The physical and mechanical properties of the material are determined by the microstructure developed during casting and the further steps in the processing, such as heat treatment and deformation or thermomechanical treatment [1]. A cast structure may have a very heterogeneous microstructure with mechanical properties that can be crucial in subsequent deformation processes.

Homogenization treatments **are** aim**ed** at the elimination of microsegregations as well as achieving favorable distribution and morphology of intermetallic precipitates formed during solidification and subsequent heat treatment [2]. The precipitate distribution, size and morphology are of a particular importance since they have significant effect on a formability and recrystallization of the alloys. However, understanding of microstructure evolution during the different stages of homogenization treatment is quite limited.

The most widely used aluminium alloys belong to the aluminium corner of the AlMgSiFeMn(+Cu) phase diagram, where there are a limited number of stable intermetallic phases. The commonly occurring particles at high temperatures are given in literature [3, 4].

Experimental

Tests were carried out on a sample of **a** slab cast by semi-continuous vertical direct water cooling process (“Direct Chill”), of dimensions: 520x1680x4809 mm, produced from charge 3121 of EN AW-5083 (EN AW-AlMg4,5Mn0,7) alloy [5, 6]. From the slab cast in this way, an about 30 mm thick transversally cut plate was

taken out from its front part, after having disposed of the technological waste of about 200 mm at the beginning of the casting.

Homogenization of the samples was carried out at a temperature of 520 °C in duration of: 1 hour (sample U1), 3 hours (sample U9), 4 hours (sample U14), 5 hours (sample U4), 7 hours (sample U12), 8 hours (sample U11) and 18 hours (sample U5) in the salt bath AVS250 Durferrit. The specimens were quenched in water at 20 °C after treatment. Samples SSU1 and SSU2 were in cast state. Figure 1 is a schematic representation of sampling.

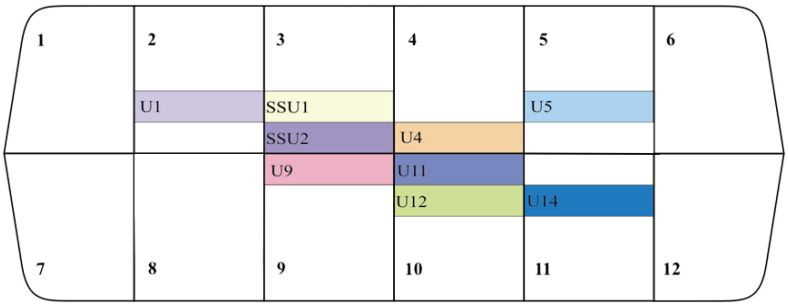

Fig. 1. Sampling from EN AW-5083 slab

For metallographic and microstructural investigation, a single specimen was taken from each designated location. They were prepared by standard procedure of grinding and polishing and afterwards etching in 0.5 % HF. Samples for the microstructural investigation were examined on the scanning electron microscope (SEM) TESCAN VEGA TS5136LS with the phase recognition on the base of chemical composition analysis by the energy dispersive spectrometer (EDS).

Thermodynamical calculation of phase equilibrium of EN AW-5083 charge 3121 alloy was preliminary performed by “Thermo-Calc” (TCW 5.0) software.

Results and discussion

The chemical composition of the investigated charge is presented in Table 1.

Table 1. Chemical composition of EN AW-5083 alloy

Chemical composition, mass %									
Si	Fe	Cu	Mn	Mg	Cr	Zn	Ti	Be	Na
0.13	0.38	0.01	0.43	4.37	0.10	0.006	0.0295	0.0045	0.003

Thermodynamical calculation of particular phases stability along with initial condition of temperature 20°C, pressure 10^5 MPa as well as specific chemical composition **(in mass.%)** of examined alloys (4.37 Mg, 0.43 Mn, 0.38 Fe and 0.13 Si) resulted in isoplete phase diagram (Figure 2a) and area of the temperature stability of each phase (Figure 2b) [6].

The equilibrium solidification of the EN AW-5083 alloy proceeds as follows (Figure 2): primary crystals of α_{Al}, Al_6Mn and Mg_2Si. Under the solidus, the Al_3Mg_2 (in the literature known as Al_8Mg_5) and Al_3Fe phases have also precipitated.

It has been determined that the primary crystals of α_{Al} at 635°C are the first to **form**, which corresponds to liquidus temperature [6]. Shortly after the **formation** of α_{Al} crystals at 625°C the first eutectic phase Al_6Mn was **solidified**, due to the relatively high content of manganese in this alloy. Beginning of secondary eutectic solidification (Mg_2Si + α_{Al}) could be predicted at 581°C. From the diagram in Figure 2a the solidus temperature at 578°C was determined, which is associated with the maximum contribution of primary dendrites of aluminum at this temperature. A precipitation of the first phase Al_8Mg_5 starts at 235°C in the solid state. Finally follows the precipitation of iron phase Al_3Fe at 115°C. Interpretation of those diagrams indicates complex solidification sequence with the series of interconnected reactions. The melt is stable from the initial calculation temperature of 650 to 578°C.

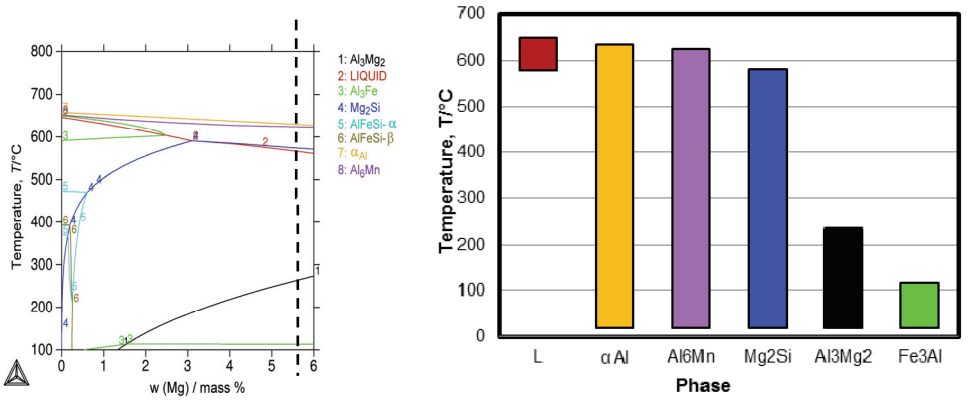

a) *b)*

Fig. 2. Thermodynamical calculation of equilibrium phase diagram of investigated EN AW-5083 alloy: polythermal section of the equilibrium phase diagram (a), areas of temperature stability for particular phases (b) [6]

Qualitative analysis of the microstructural constituents of the samples in cast state (SSU1, SSU2) EN AW-5083 alloy were performed in order to determine and/or confirm presumed stoichiometry by EDS and they are given in literature [6]. The analysis of the cast sample [6] confirms the presence of phase based on magnesium and silicon, which corresponds to the stoichiometry Mg_2Si phase, which is defined as the second eutectic phase (α_{Al} + Mg_2Si) by the "Thermo-Calc". Mg_2Si phase is shown in the images as a black irregular branched - shaped phase.

The presence of phase based on manganese (Al_6Mn) was not established although its presence as a primary eutectic phase was assumed by thermodynamic modeling of the solidification (TCW 5.0). However, the presence of phases containing aluminum, manganese and iron was determined and it seems that they correspond to Al_6(Fe, Mn) phase. Those are the white phases in the

structure which appear in various forms, such as needles [6], “Chinese script” morphology, or irregular rounded shapes. From the obtained results it could be concluded that the mentioned primary eutectic (α_{Al} + Al_6Mn), because of non-equilibrium solidification, corresponded to eutectic (α_{Al} + Al_6(Fe, Mn)). Metal base containing aluminum and magnesium could be seen as a gray background where all of the mentioned phases are different.

The presence of phases Al_8Mg_5 and Al_3Fe which should be separated in solid state was not established although their presence was assumed by thermodynamic modeling of solidification. Together with the mentioned phases present in the investigated sample, the shrinkage porosity in small quantity in microstructure also appears [6]. It appears in black color as irregularly shaped phase, formed in dendritic mushy zones where feeding is not possible.

Quantitative analysis of the microstructural constituents of all samples in homogenized state were established the presence of equal intermetallic phases as well as cast sample. An example of quantitative analysis of the sample U1A (homogenized 1 hour) is shown in Figure 3.

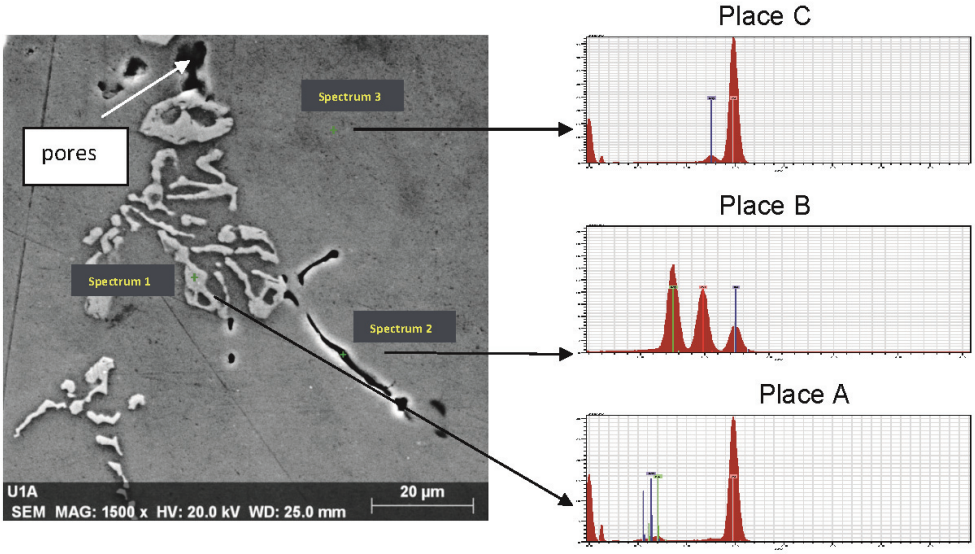

Place	Mg		Al		Si		Mn		Fe	
	w./%	at./%	w./%	at./%	w./%	at./%	w./%	at./%	w./%	at./%
A	-	-	75,30	86,28	-	-	5,54	3,11	19,16	10,61
B	36,58	39,62	42,71	41,36	20,44	19,02	-	-	-	-
C	5,53	6,10	94,47	93,90						

Fig. 3. Microstructure of the sample U1 obtained on SEM with the marked places of quantitative analysis performed by EDS, their particular spectrums and quantitative analysis (place A - white phase: Al, Fe, Mn; stoichiometry Al_6(Fe, Mn); place B - black phase: Mg, Si; stoichiometry Mg_2Si; place C - matrix: α_{Al})

These results have been confirmed by line analysis by EDS (Figure 4) from which it could be seen increased concentration of magnesium and silicon in place of black phase (Mg_2Si), and increased content of iron and manganese in locations which correspond to the phase $Al_6(Fe, Mn)$.

Visual examination of microstructural images of all homogenized samples obtained by SEM it is possible to determine the presence of equal intermetallic phases to the metal base containing aluminum and magnesium and pores as well as sample U1, Figure 5 a-d. One cannot reveal differences in the size and morphology of individual microstructural constituents on a single sample. Intermetallic phases are evenly spaced, uniform in morphology and can be identified by comparing the microstructures of the atlas and microstructure of previously conducted EDS analysis.

By visual comparison of metallographic images of different samples made by SEM, in equal increments, a certain change in the size of the investigated intermetallic phases and pores and their total surface area could be seen. Also, their different size and total surface area in relation to the cast state could be seen, which will be quantified in the following examinations.

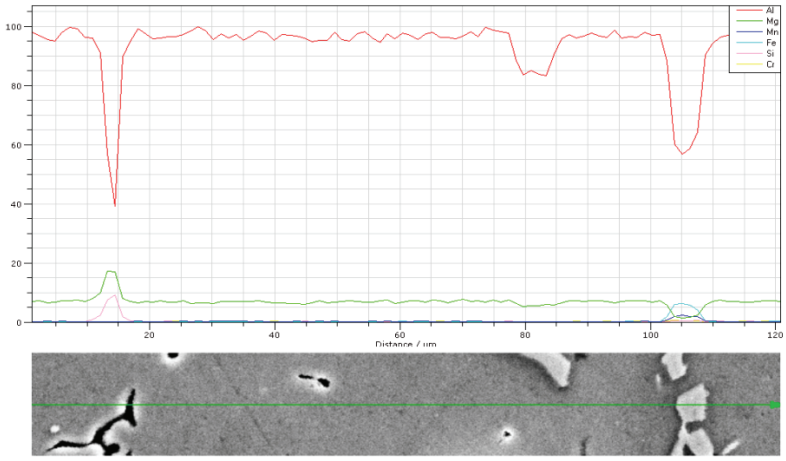

Fig. 4. Microstructure of the sample U1 obtained by SEM with the marked places of line analysis performed by EDS

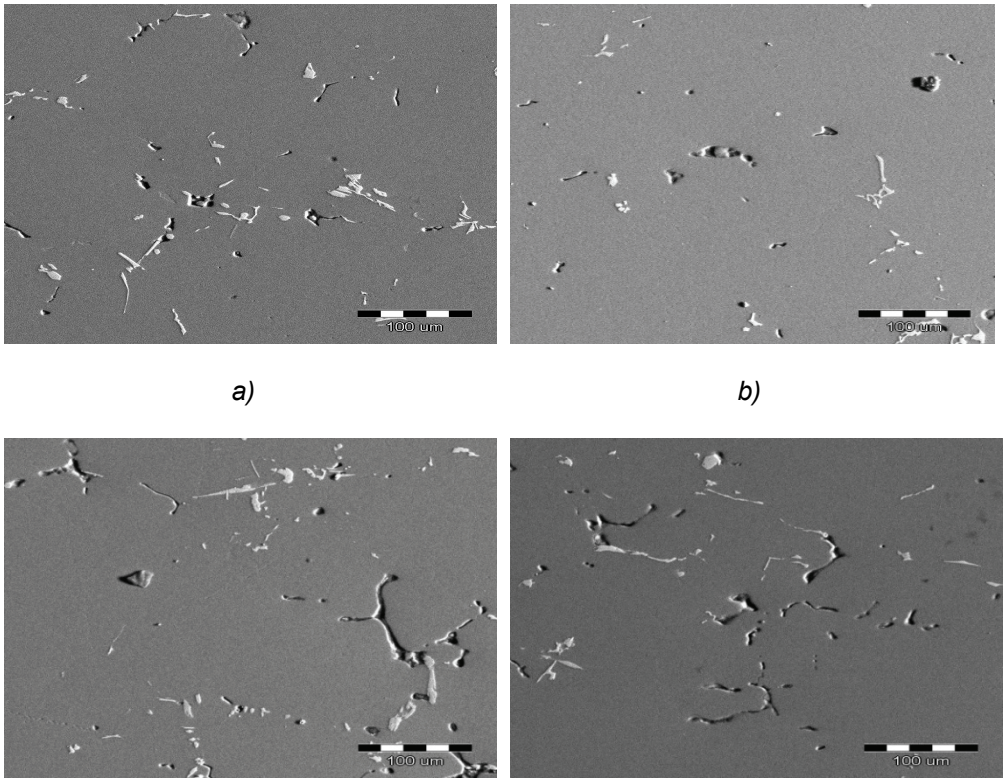

a) *b)*

c) *d)*

Fig. 5. The images of microstructures of one detail samples: a) SSU1a; b) U4; c) U11; d) U5

The most obvious change is the size and number of pores. It is possible to determine that by increase of homogenization time (from sample U1 to sample U5) occurs an increase in pore size, which is the highest after 18 hour duration at temperatures of homogenization of 520°C. With increase of homogenization time it is possible to conclude that there is a decrease of particle size of intermetallic phase Mg_2Si, while it is difficult to conclude whether the particle size of intermetallic phases $Al_6(Fe, Mn)$ changes with the change of homogenization duration.

Conclusion

By the quantitative analysis through energy dispersive spectrometer (EDS) the following microstructural constituents have been determined: intermetallic phase $Al_6(Fe, Mn)$, which, due to the unequilibrium evaluation, corresponds the first eutectic (α_{Al} + $Al_6(Fe, Mn)$ and the Mg_2Si intermetallic phase, as other eutectic phase (α_{Al} + Mg_2Si). Also, the presence of pores has been observed.

The greatest effect of homogenization duration at 520°C is on the change of total surface area and medium particle surface pores and intermetallic phase Mg_2Si (which is attributed to the melting of phase Mg_2Si and its diffusion in the solid solution):

- increasing time of homogenization leads to reduction in the total surface area of the Mg_2Si phase and the medium surface of its particles;
- increasing time of homogenization leads to increase in the share of the total surface pore, as well as the middle surface of its particles.

Mean particle surface of intermetallic phase Al_6(Fe, Mn) changes the least by changing of the length of homogenization duration, which results from its stability in the applied temperature homogenization (520°C).

Results of this study not only allow a new knowledge about impact of homogenization duration on the microstructure of aluminum alloy EN AW-5083, but also indicate the possibility of effect of homogenization time on the important factors that determine the quality of the finished product (e.g., mechanical properties, size or number of grains, etc.).

References

[1] A. Johansen, Ph. D. Thesis, Microstructures and Properties of Aluminium-Magnesium Alloys with Additions of Manganese, Zirconium and Scandium, The Norwegian University of Science and Technology, Trondheim, 2000.

[2] A. Halap, T. Radetić, M. Popović, E. Romhanji, Study of Homogenization Treatments of Cast 5xxx Series Al-Mg-Mn Alloy Modified with Zn, Light Metals, 2012, ed. C. Suarez, The Minerals, Metals & Materials Society, 387-392.

[3] A. L. Dons, The Alstruc Homogenization Model for Industrial Aluminum Alloys, Journal of Light Metals, 1 (2001) 2, 133-149.

[4] Y. J. Li, L. Arnberg, A Eutectoid Phase Transformation for the Primary Intermetallic Particle from Al_m(Fe, Mn) to Al_3(Fe, Mn) in AA5182 Alloy, Acta Materialia, 52 (2004), str. 2945-2952.

[5] EN 573-3: 2002, Aluminium and Aluminium Alloys - Chemical Composition and Form of Wrought Products - Part 3: Chemical Composition, European Comittee for Standardization (CEN), Brussels, 2002.

[6] N. Dolić, J. Medved, P. Mrvar, F. Unkić, Influence of the Cooling Rate on the Microstructure Development of the EN AW-AlMg4.5Mn0.7 Alloy, Materiali in Tehnologije, 46 (2012) 6, 563-571.

USING MAGMA^5 TO OPTIMIZE THE PARAMETERS OF CASTING AN EXCAVATOR TOOTH HOLDER

Radomir Radiša[1], Srećko Manasijević[1], Janez Pristavec[2], Vesna Mandić[3], Velimir Komadinić[1]

[1]LOLA Institute, Kneza Višeslava 70a, 11000 Belgrade, Serbia, www.li.rs
[2]Exoterm-it, Struževo 66, 4000 Kranj, Slovenia, www.exoterm.si
[3]Faculty of Engineering, University of Kragujevac, Sestre Janić 6, 34 000 Kragujevac, Serbia

Abstract

This paper describes the use of modern information technology to optimize the relevant technological parameters of casting an excavator tooth holder using the MAGMA^5 software package. From the obtained results, potential problems can be easily identified and eliminated at the design stage of castings and casting tools. This concept substantially reduces the time and costs of developing new types of castings, which definitely contributes to an increase in the competitiveness and technical competence of toolshops and foundries.
Keywords: MAGMA^5, Simulation, excavator tooth holder

Introduction

The metal casting is always somewhere in between technology and art. The essential problem is in understanding what is happening with the liquid metal which fills the mould cavity in a few tens of seconds during the cooling and solidification. A mechanism of process itself is not simple, non-available and is subjected to the abstract laws. If the mould cavity could be filled out instantaneous and then melted metal solidified equally on overall volume, we would not have a problem. However, a reality implies something very different. A slight fault in design or construction of gating system can cause series of cause-related problems (nonuniform metal flow, subcooling,...), subsequently causing series of problems (cavities emerges, porosity, residual tensions that may burst a cast by the unequal cooling, as well as the series of other faults that make a cast useless). This competition between the foundrymen skills and a hardly predictable nature of melted metal is like walking over the thin line which distinguishes success from failure, i.e. a good cast from the one that should be put into the furnace once again.

All this has until recently been based on traditional casting technology, informal skills and intuition metal casters, only to become the subject of exact calculation that with high probability predict the final result. Today, there are several software packages for the simulation of casting and solidification (MAGMA^5, Procast, Access etc...). They read graphic formats such as .stll and *.step*. Creating 3D geometry models (piston cast molding and tooling) is done with the help of CAD software packages, which export these formats [3,5].

Modern computer tools such as MAGMA[5], a package for the simulation of metal casting processes, enable the relatively fast attainment of optimized solutions for casting technology [6,7]. MAGMA[5] allows different technological parameters of a casting process to be tested. Based on the results of experimental investigations, the optimization of relevant technological parameters and their implementation under industrial conditions showed that the properties of a casting can, in practice, be significantly improved. The results show that MAGMA[5] provides satisfactory solutions in a short period, starting virtually from scratch, under industrial conditions. It was shown that the employment of these software packages brings great advantages compared to the conventional manner of adopting new products. For instance, the results obtained in a rapid generation of model elements significantly accelerated the work and improved the productivity of engineers, reduced the time for adopting new products, reduced the scope of traditional prototype testing (creating prototypes and their testing), which is expensive and time consuming, causing standstills in manufacture, and reduced expenditures for development new products.

The main goal of these software packages is the optimization of the relevant technological parameters of the casting process, increase process efficiency and quality of the castings.

Experimental

The MAGMA[5] is a software package, i.e. the computerized tool for simulation of the casting and solidification processes. This software allows the testing of different technological solutions. For the optimization of technological parameters it is necessary to determine: 3D geometric model of the casts and other components (moulds for casting, gating system, cooling media, etc.), parameters like temperature and time of casting, alloy composition, and so on. This enables the using of pre-designed 3D models (some CAD software, Fig. 1) as the inputs in an original graphic station, as well as the direct designing of simple 3D geometric models.

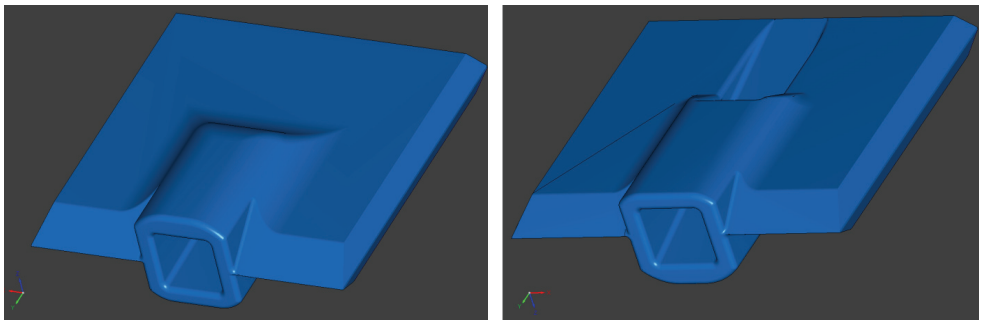

Fig 1. 3D geometric model

In the next phase, all geometric assemblies are divided into partial elements (Version V07, Fig 2). The MAGMA[5] package itself automatically generates a mesh. The fineness of the mesh, i.e., the number of mesh elements can be set by the software user by defining the minimum size of the desired elements in all three

directions of the coordinate system. The finer the mesh, i.e., the more elements it has, the more accurate the calculation of the simulation is, but the simulation time is longer. The prepared mesh is used for further calculation. For each element, i.e., part of the mesh, differential equations are used to calculate its physical and thermal parameters and the results obtained are boundary conditions for the calculation of the parameters in the neighboring element. Thus, the computer calculates element by element in 3D coordinates and finally integrates all the partial results for the overall geometry.

After defining the classes and types of material in the casting system of the MAGMA[5] software package, heat transfer coefficients were defined for the pairs of materials that are in contact. For the purpose of casting the excavator tooth holder in a molding sand mixture, the mold and core surfaces were covered with appropriate coatings to influence the thermal behavior of the mold (to reduce the heat transfer coefficient and obtain a high-quality casting surface) and the core in the casting process.

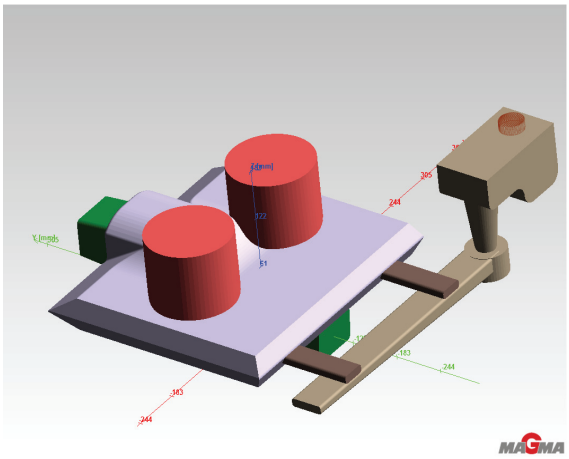

Fig 2. MAGMA[5] software package, Version V07

Material for producing the cast excavator tooth holder is within the standards GS42CrMo4V. The mold of core is made of furan. Gravity casting was done in 8 sec duration with an initial temperature of 1590 °C casting.

Results and Discussion

The results of simulation are given in 3D color diagram, wherein the colors vary with the selected criteria. The paper presents a few criteria that indicate the typical situation. For example, the *FillTemp,* showing the arrangement of metal temperature during mould filling. Using this criterion, it is immediately visible that the design of the gating system and feeder is not good (Version V02, Fig 3a). An adjustment to the gating system and feeder resulted in a better arrangement of temperature during pouring (Version V07, Fig. 3b). Instead of a single feeder, two feeders with insulating bushings were used, and the gating system dimensions were changed.

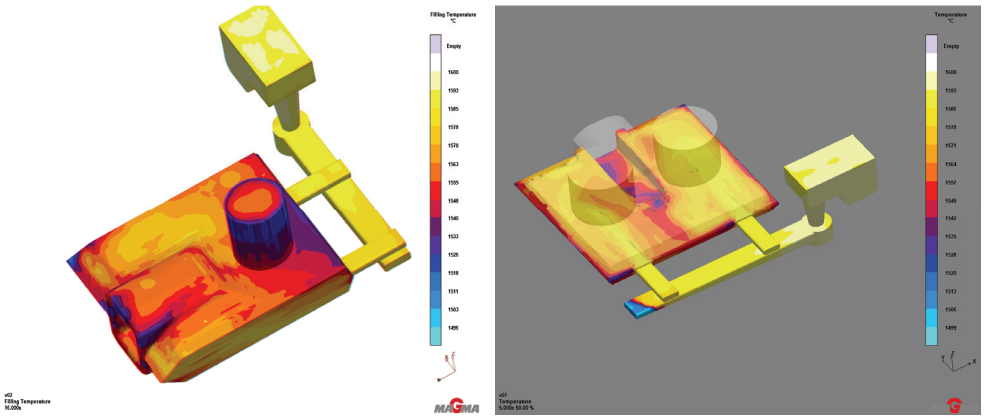

a) *b)*

Fig. 3. The FillTemp criterion: a) V02 and b) V07

Fig. 4 shows the results for the FillVelocity criterion in Version V07.

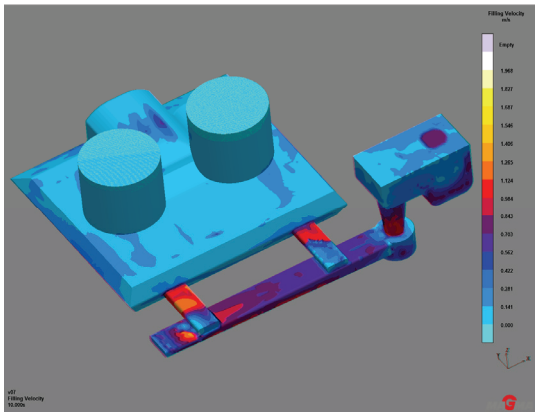

Fig. 4. The FillVelocity criterion, V07

Using the Solidification Criteria Results after the simulation is terminated, the program automatically calculated several criteria that can be selected at each point. Displaying the criteria results helps find defects in the casting and analyze the solidification behavior. Fig 5a shows the presence of porosity by applying the *TotalPorosity* criterion in Version V02, which was shown as such in practice. Figs. 5b, 5c and 5d show the results of the *Porosity* criterion in Version V07.

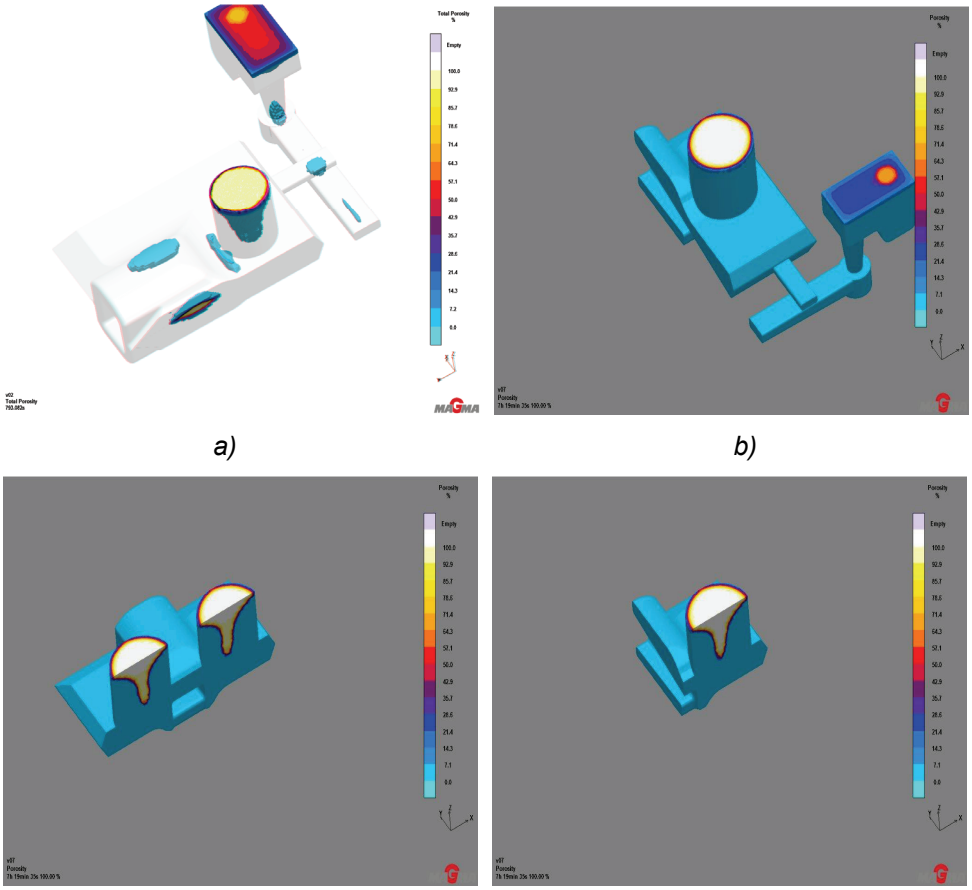

a) *b)*

c) *d)*

Fig. 5. An analysis of critical areas of the Porosity criterion: a) V02 and b), c) and d) V07

It can be seen that there is no porosity in the cast in Version V07. It was demonstrated that a "healthy cast" was obtained using such gating system in practice.

Conclusions

The paper shows that the use of virtual information technologies (in this case MAGMA[5] software package) reduce the product development time and cost, allowing a company to master the production of the large and complex castings with high quality in the first attempt.

Acknowledgements

The research presented in this paper was funded by the Ministry of Education and Science of the Republic of Serbia.

References

[1] Manasijević S., Radiša R., Petrović P.B., Skill and intuition of foundrymen or computer assisted casting. Livarstvo 47(1) (2008) pp. 10–11.
[2] Manasijevic S, Radisa R, Acimovic-Pavlovic Z, Raic K, Markovic S., Software packages for simulation and visualization of a piston casting process. Livarstvo, 48(1) (2009) pp. 14–20.
[3] Radiša R., Marković S., Pristavec J., Kvrgić V., Manasijević S., Use of CAE Techniques in Virtual design of Metalcasting technology-saving in Serbian Foundries. Livarstvo 47(1) (2008) pp. 12–24.
[4] Die casting technologie-Bühler Training programe, Bühler Druckguss AG, Uzwil, 1995.
[5] www.diecasting.org (NADCA-The North American Die Casting Association).
[6] Lola Institut, Internal Documentation, 2013.
[7] www.magmasoft.com.

SX-EW TREATMENT OF THE SOLUTION OBTAINED AFTER ACID LEACHING RTB BOR FLOTATION TAILING

Vesna Conić[1*], Ljiljana Avramović[1], Radojka Jonović[1], Radmila Marković[1], Mile Bugarin[1]

[1.] *Mining and Metallurgy Institute Bor, Zeleni bulevar 35, 19210 Bor*
vesna.conic@irmbor.co.rs

Abstract

The off-balance raw materials present important economic resource for obtaining metals if valorization performs adequately using appropriate technology. For the treatment of off-balance raw materials with low content of metals in the countries (USA, Chile and South Africa) where it is available is applied hydrometallurgical process. In almost all hydrometallurgical processes metal is obtained by using the so-called SX-EW process, i.e. using solvent extraction followed by electrolytic obtaining. The possibility of treatment of leach solution obtained after acid leaching flotation tailings by solvent extraction is shown in this paper. The percentage of copper leaching of the RTB Bor flotation tailings was 60%, where the copper content in the solution was ≈1.5 g / L.
Key words: copper, flotation tailing, acid leaching, SX-EW

Introduction

Bor City is located in eastern Serbia, near the border with Bulgaria. Copper mine Bor is located on the northeastern part of the city so that the open pit and the old Bor flotation tailing present a border of urban and industrial zones. Exploitation and processing of copper ore at Bor area has led to the degradation and pollution of land due to deposition of large amounts of mining waste (mine gangue, tailings and flotation tailings) [1]. In Bor, there are two flotation tailings: Bor and V. Krivelj and two in Majdanpek: Valja Fundata and Saski potok. Flotation tailings Bor occupies an area of 84 h and was built in the open pit and expanded on the new field of Bor River. Flotation tailing V. Krivelj is located in the valley V. Krivelj river, and was obtained by damming the valley (tunnel and collector) downstream and upstream. Old flotation tailing Field1 and Field2 Mining and Smelting Basin Bor contains about 20 million tons of tailings with about 0.3% Cu, that means that this material contains about 60,000 tons of copper (Figure 1). Negative impacts flotation tailings on the environment include: land degradation, loss and soil pollution, pollution of surface and groundwater, air and soil by heavy metals (lead, zinc, copper, arsenic), high concentrations of contaminated dust in the air and others. By hydrometallurgical treatment of these raw materials are obtained solutions that can be treated by solvent extraction and electrowinning [2]. Using MEUM software program it is possible to determine the optimal concentration of extractant and selecting the optimum operating parameters of the plant in order to achieve the best metallurgical results [3]. By construction of isotherms can be

determined technological criteria and options processing of leach solution by solvent extraction [4-10].

Fig. 1 The old Bor flotation tailing Field1 and Field2

Experimental parts

For the leaching of flotation tailings sample was used a glass reactor of volume 10 L which is shown in Figure 2. The reactor was made of stainless boron silicate glass. The reactor has a device for automatically control of temperature and stirring speed. It is also equipped with a condenser, for re-use condensate.

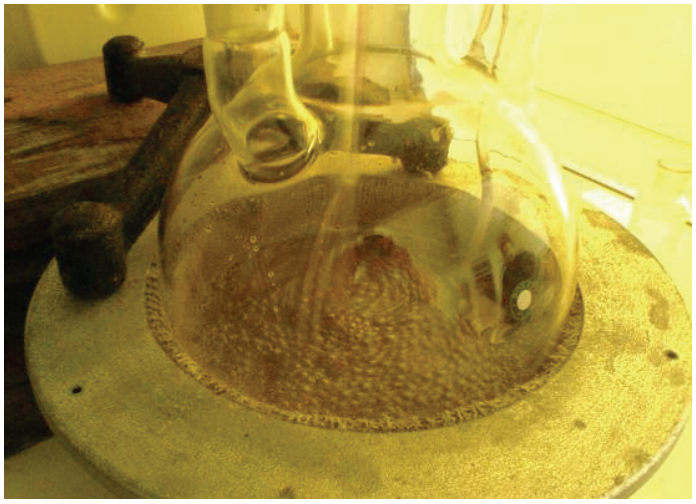

Fig. 2 The glass reactor to leach

MEUM-Acorga software program is utilized for quickly determine the number of circulating SX circuit according of the initial parameters such as: Cu concentration in the aqueous phase, acidity/pH in the aqueus phase, choice of extractant and extractant concentration.

Results and discussion

Samples from flotation tailing dump were treated by the agitation leaching method. The mine water from the accumulation Robule (mine waste water) was used as leaching solution with the following chemical composition: Cu-69,10 mg/dm^3; Pb <0.05 mg/dm^3; Zn-26.30 mg/dm^3; Cd-0.12 mg/dm^3; Ni- 0.34 mg/dm^3; Cr<0.02 mg/dm^3; Se<0.020 mg/dm^3; As<0.010 mg/dm^3; Fe-739.00 mg/dm^3; suspended matters -12.0 mg/dm^3; $SO4^{2-}$ -8243,10 mg/dm^3. A sample of tailings was used for experimental testing. Chemical content of a composite sample of tailings is shown in Table 1. [1].

Table 1. Chemical content of a composite sample of flotation tailings from depth of 17m

Element	Content, %	Element	Content %
Cu, total	0.43	Au, g/t	<0.05
Cu, ox	0.18	Ag, g/t	0.8
Fe	16.56	Hg, g/t	0.2
Cd	<0.0004	Pb	0.073
S	18.15	Zn	0.017
As	0.022	Mn	0.005
Cr	<0.001		

The results of experimental laboratory tests leaching of the flotation tailings showed that the highest level of copper leaching are achieved at the following process parameters: leaching time 4 h, temperature 80 ° C, the ratio of solid: liquid = 1: 2.5 and the pH=1. Water from the Robule lakes is used for the correction of pH and also for the leaching process which represents a special contribution to solving the problem of waste water [1]. After the leaching solution contained 1.5 g / L of copper. This solution is suitable for SX - EW process.

Models MEUM program are used for the determination of the applicability SX - EW process.In the models is varied configurations as follows 2 stages of extraction and 1 stripping stage or 2 stages of extraction and 2 stripping stage. The initial pH value of the copper solution is also varied at that pH 1.1 or pH 1.8. It is planned to using extractant Acorga M5640 with volumetric concentration of 8% in the solvent. This extractant is a strong aldoxime which consist ester as a modifier. It can be used at high concentrations PLS, low and medium pH and a high selectivity of Cu / Fe.

When the initial pH of the solution PLS is pH = 1.1 (model No 1 and No 2) presented in Figure 3 and Figure 4 by applying another one level of stripping recovery of copper growing from 78.8% to 87.7%. Constructed structure MIMIC

diagrams can define the technological parameters of operation of a solvent extraction and electrolwinning (Figure 3(c)).

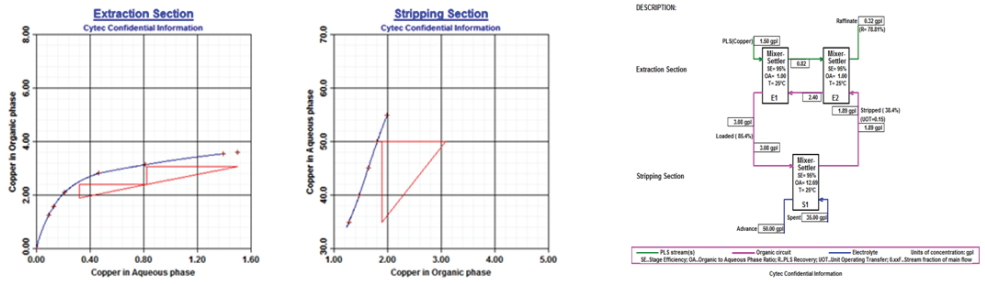

(a) (b) (c)

Figure 3 Model No 1 McCabe-Thiele diagrams for (a) extraction and (b) stripping and MIMIC diagram (c)

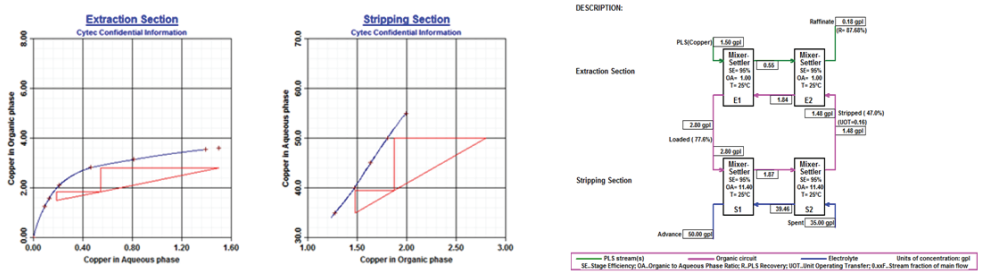

(a) (b) (c)

Fig. 4 Model No 2 McCabe-Thiele diagrams for (a) extraction and (b) stripping and MIMIC diagram (c)

Comparing model No 1 and No 2 when the pH value of solution is pH = 1.1, the recovery of the Cu would significantly when the concentration of Acorga exstractant is 8% vol., and in this case recommended configuration is 2 stages of extraction and 2 stripping stage -model No 2.

However at pH 1.8 using 8% vol. Acorga M5640, there is no reason for another level of extraction, which is indicated models No 3 and No 4 (Figure 5 and Figure 6), since the pH and concentrations of extractant Acorga are too high to enable acceptable recovery of Cu 97.04% and 98.24%.

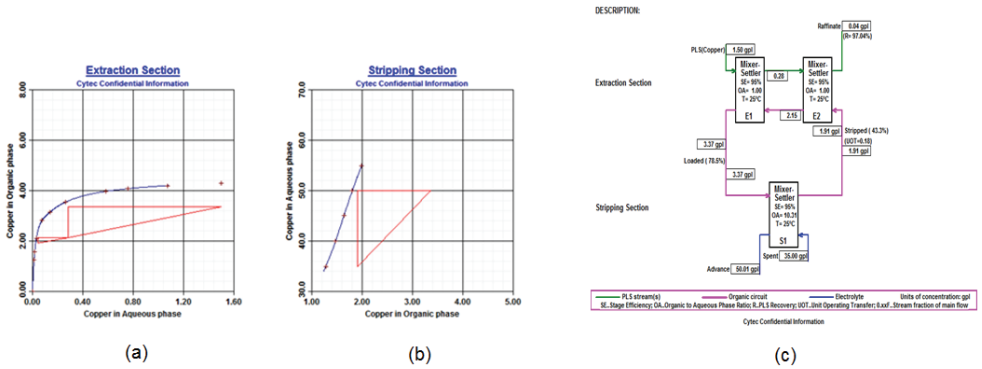

(a) (b) (c)

Fig. 5 Model No 3 McCabe-Thiele diagrams for (a) extraction and (b) stripping and MIMIC diagram (c)

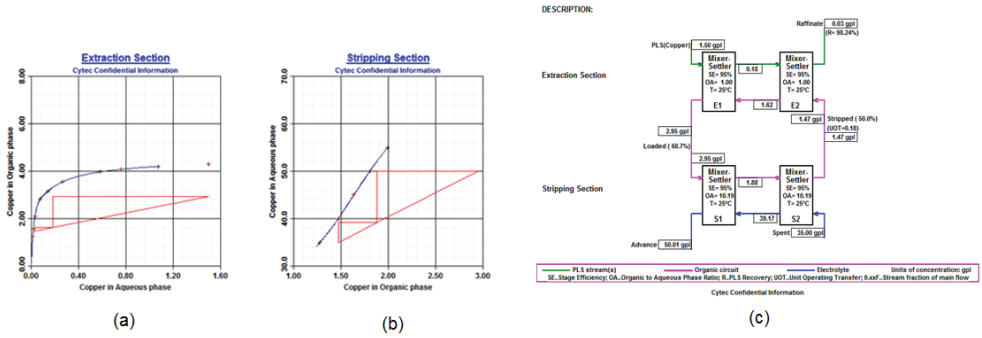

(a) (b) (c)

Fig.6 Model No 4 McCabe-Thiele diagrams for (a) extraction and (b) stripping and MIMIC diagram (c)

These models No 3 and No 4, indicating significantly less restrictions to achieve the sufficiently good recovery of Cu at configuration of 2 stages of extraction and 1 stage of stripping when 8%vol. Acorga solution using. Model No 3 indicates significant recovery of Cu and even the possibility of applying on an industrial plant.

Conclusion

The most efficient extraction is usually achieved by connecting several mikser settlers units in the series. The number of stages and how to configure will depend on the type of solution, selection of reagents and aims of the operation. Isotherms and McCabe-Thiele techniques are used to determine the optimum number of extraction and stripping for different initial conditions. Choosening of the optimal configuration and concentration of extractant is sometimes real and quick response and requires in-depth assessment of capital and operating costs.

If we choose a closed cycle in which a raffinate can be re-used for dissolution, it is possible to achieve very high efficiency of over 98%. In order to

achieve these values it is necessary when working with low pH value, provide a sufficiently high concentration exstractant.

Total we can conclude that at low pH values and relatively high content of Fe approximately 4 g/L in the PLC solution, is recommended using Acorga M5640 exstractant as the best choice.

Acknowledgement

The authors are grateful to the Ministry of Education and Science for the financial support Projects TR 37001 and TR 34004. The authors are also grateful to the Cytec Ind Acorga Technical service Fr/Sr.

References

[1] Ljiljana Avramović, Radojka Jonović, Mile Bugarin, Radmila Marković, Leaching of flotation tailings, 18th International Research/Expert Conference ”Trends in the Development of Machinery and Associated Technology”TMT 2014, Budapest, Hungary 10-12 September, 2014, pp.481-484

[2] Banza N., Gock E., Kongolo K., Base metals recovery from copper smelter slag by oxidizing, leaching and solvent extraction, Hydrometallurgy, 67, (2002)l, pp.63–69

[3] Mining chemical handbook, Edition 2010 version 2, Cytec, Chief editor Willard Thomas, Chapter 9 Solvent extraction, pp. 322-385

[4] V.Cvetkovski, V.Conić, M.Vuković, G.Stojanovski, M.Cvetkovska, Konstrukcija izotermi u solventnoj ekstrakciji bakra, Hemijska industrija 63(4), (2009), pp.309-312

[5] Stevanovic, Z., Antonijevic, M., Jonovic, R., Avramovic, L., Markovic, R., Bugarin, M., Trujic, V.,. Leach–SX–EW copper revalorization from overburden of abandoned copper mine Cerovo, Eastern Serbia. J. Min. Metall. Sect. B. 45, 2009, pp.45–57

[6] K.C. Sole, Solvent extraction and ion exchange, in: Short Course:Hydrometallurgy HYDRO 2003, 2003 International Symposium on Hydrometallurgy, 22–24 August 2003, Vancouver, Canada, 2003

[7] H.R. Watling, F.A. Perrot, D.W. Shiers, A. Grosheva, T.N. Richards, Impact of the copper solvent extraction reagent LIX 984N on the growth and activity of selected acidophiles, Hydrometallurgy 95, (2009), pp.302–307

[8] S. Panda, P.K. Parhi, N. Pradhan, U.B. Mohapatra, L.B. Sukla, K.H. Park, Extraction of copper from bacterial leach liquor of a low grade chalcopyrite test heap using LIX 984N-C, Hydrometallurgy 121-124, (2012), pp.116–119

[9] A.N. Banza, E. Gock, K. Kongolo, Base metals recovery from copper smelter slag by oxidizing, leaching and solvent extraction, Hydrometallurgy 67, (2002), pp.63–69

[10] S.K. Sahu, A. Agrawal, B.D. Pandey, V. Kumar, Recovery of copper, nickel and cobalt from the leach liquor of a sulphide concentrate by solvent extraction, Minerals Engineering 17, (2004), pp.949–951

Book of abstract

RESEARCH OF IMPACT OF METALLIC COATINGS ON MECHANICAL PROPERTIES OF SUPERALLOY BASED ON IRON A286

Mirsada Oruč[1], Milenko Rimac[2], Sulejman Muhamedagić[1], Jusuf Duraković[1], Strain Posavljak[3]

1 University of Zenica, Faculty of Metallurgy and Materials Science,BiH
2 University of Zenica, Metallurgical Institute „Kemal Kapetanović“, BiH
3 University of Banja Luka, Faculty of Mechanical Engineering, BiH
Corresponding E-mail: mirsada.oruc@unze.ba

Abstract

Superalloy based on iron marked A286 according to UNS S66 286 standard is in fact austenitic stainless steel with intermetallic strengthening. It is used for various structural parts working at temperatures above 740°C.

This paper presents the research of impacts caused by metallic coatings NiCrAlY on samples of the superalloy.

Metallic coatings were applied by HVOF method (High velocity oxyfuel) Diamond Jet procedure on samples prepared for mechanical testing. On the samples were carried out tensile testing at room and elevated temperature and hardness section.

After examination of the microstructure on the optical and scanning electron microscope was found influence of metallic coatings on mechanical properties in order to obtain products with better properties in operation.

Keywords: superalloy A286, metal coatings, mechanical properties, microstructure

CHEMICAL FUNCTIONALIZATION OF CNTS FOR GAS SENSOR APPLICATION

Ana Tomova, Aleksandar Petrovski, Anita Grozdanov, Beti Andonović, Perica Paunović, and A. T. Dimitrov

Abstract

The subject of this study is chemical functionalization as means of structural modification of multiwalled carbon nanotubes (MWCNTs). The main goal of the experiments was to create highest density of carboxyl groups on MWCNTs surface, necessary for further nanocomposite application. Two different types of MWCNTs (I: d=50÷100 nm, purity ~ 84%, synthesized by pyrolysis and II: d=10÷40 nm, purity ~ 94% , synthesized by CVD) were treated by concentrated nitritic acid (HNO_3) and by alkaline mixture ($NH_4OH+H_2O_2$). The alkaline medium as 'milder' and less aggressive than nitric acid, was expected to be less destructive and cause minimal structural damage on the MWCNTs surface. Structural changes due to oxidation were observed by Raman analysis, while the ratio of the intensities of the D and G peak was used to estimate the concentration of defects. Pristine and functionalized MWCNTs were then characterized by Thermogravimetric analysis (TGA), Scanning Electron Microscopy (SEM), Ultraviolet–visible spectroscopy (UV-Vis) and ZETA potential measurements. The results presented in this paper, show that functionalization initiates changes in CNTs structure as well as in their density of states (DOS). Functionalization of CNTs facilitates shortening and exfoliation of CNTs and decreases their agglomeration tendency. CNTs functionalized by both acid and alkaline treatment can successfully replace conventional carbon fibers as fillers in polymer composites for sensing application.

Keywords: MWCNTs, oxidation, carboxyl groups, functionalization.

CONTROLLED SYNTHESIS OF GOLD NANOPARTICLES WITH USP

Peter Majerič[1], Darja Jenko[2], Bojan Budič[3], Bernd Friedrich[4], Rebeka Rudolf[1,5]

1 University of Maribor, Faculty of Mechanical Engineering, Slovenia
2 Institute for Metallic Materials and Technologies, Ljubljana, Slovenia
3 National Institute of Chemistry, Ljubljana, Slovenia
4 RWTH Aachen, IME Institute of Process Metallurgy and Metal Recycling, Germany
5 Zlatarna Celje d.d., Celje, Slovenia
Corresponding E-mail: peter.majeric@um.si

Abstract

In the research to produce gold nanoparticles for medical purposes, an effort was made to control the synthesis process of Ultrasonic Spray Pyrolysis. The nanoparticles were created from a precursor solution of diluted $HAuCl_4$ with varying concentrations. Utilizing a separate heating zone in the process, the generated aerosol droplets first underwent an evaporation stage in order to produce dried particles of gold chloride. In the second heating zone, at a higher temperature, thermal decomposition was carried out and hydrogen gas was introduced into the system for chloride reduction. The final produced nanoparticles were collected in collection bottles with water. The nanoparticles were characterized with TEM microscopy and ICP analysis. Growth of nanocrystal types was determined by electron diffraction. Bimodal size and shape distribution was observed in the produced nanoparticles.

Keywords: Ultrasonic Spray Pyrolysis, gold nanoparticles, TEM microscopy, electron diffraction

EFFECT OF SENSITIZATION ON PITTING CORROSION RESISTANCE OF LASER MELTING 304 STAINLESS STEEL

Mohammed Jasim Kadhim, Sami I. J. Al-rubaiey & Zaman Abdalrazaq

Production Eng. and Metallurgy, University of Technology, Baghdad, Iraq

Abstract

The present paper presents an attempt to improve the corrosion resistance of sensitized 304 stainless steel by pulsed laser surface melting. Tafel extrapolation technique was used to determine the corrosion rates in 3.5% NaCl in four conditions. These conditions are as-received, sensitized, laser treatment for as received stainless steel and laser treatments after sensitization. The results obtained are expressed in terms of corrosion parameters through electrochemical behavior namely, E^{o}, I^{o}, $E_{Corr.}$, E_{P}, I_{P}, $E_{Pit.}$ And I_{Pit}. Detailed analysis found that these parameters are strongly dependent on the microstructures of the stainless steel. The results reveal when the potentials increase means the microstructure becomes thermodynamically more stable and has good corrosion resistance. The above electrochemical parameters for sensitized 304 stainless steel show that the localized corrosion rate increases which affected the phases. The laser surface melting treatment shifts the potential toward noble direction. The corrosion current densities values shift to lower values. The comparison of anodic polarization curves indicates that the corrosion rates for laser treated samples are reduced. Increasing the corrosion resistance means that the most inclusions at the surface have been dissolved in the structure due to melting. An interesting feature is the systematic shift of the pitting potential in the noble region with a laser melting. This results confirms that the laser treatment can be used successfully to improve the localized corrosion resistance.

SYNTHESIS AND CHARACTERIZATION OF SILVER NANO-POWDER

Jelena Pantić, Branko Matović

Vinča Institute of Nuclear Sciences, University of Belgrade, P. O. Box 522, Belgrade, Serbia
jelena.pantic@vinca.rs

Abstract:

Nano silver powder is obtained by oxidation reduction reaction under aqueous condition using $AgNO_3$ as silver precursor and $NaBH_4$ as reducing agent:

$AgNO_3 + NaBH_4 \rightarrow Ag + NaNO_3 + BH_3 + 1/2H_2$

The reaction product mixture was separated by centrifuging at 3500 rpm. Powder properties such as lattice parameters, crystallite and particle size were studied. X-ray diffraction analysis (XRD) was used to characterize the samples at room temperature. Calculation of the average crystallite size (D) was performed on the basis of the full width at half maximum intensity (FWHM) of the XRD peaks. Williamson-Hall plots were used to separate the effect of the size and strain in the nanocrystals. The morphologies and texture of powder was followed by Scanning electron microscopy (SEM) as well as by Atomic Force Microscopy (AFM).

TESTING OF THE ADHESION EFFECTS OF EPOXY AND ACRYLIC ADHESIVES ON OPTICAL FIBERS

Nataša Z. Tomić, Bojan I. Međo, Kata Trifković, Vesna J. Radojević, Marko P. Rakin, Radmila M. Jančić-Heinemann, Radoslav R. Aleksić†

University of Belgrade, Faculty of Technology and Metallurgy, Karnegijeva 4, 11120 Belgrade, Serbia
Corresponding author: ntomic@tmf.bg.ac.rs, tel: +381113303602, cell phone: +381 60 6356514, fax: +38111337038

Abstract

Optical fibers are transported on a drum and on some occasions it is essential to fix them and to keep them fixed to the drum. Adhesives are used in those situations to obtain the best and durable fixation. This research shows a new approach for the examination of adhesion effects and forces between the optical fibers and the adhesive during a tensile test. Two types of adhesives were tested: epoxy and acrylic adhesive. A solution of ethylene–vinyl acetate **(**EVA) copolymer in toluene was used as an epoxy adhesive for optical fibers. Polymer blends based on methacrylic acid, dissolved in toluene, were used as acrylic adhesives. The testing procedure consisted of optical fiber characterization using optical microscopy, tensile test, SEM, and FTIR analysis. A sample of two fibers connected with an adhesive was subjected to tensile test to examine the adhesion forces. Finite element modeling was used to simulate the behavior and stress distribution of the adhesion layer. This mathematical model can be used to visualize the stress distribution during the testing and to serve as a base for the development of the stress distribution during the real process of fiber unwindng from the drum. The proposed method could assist in reaching a conclusion about the quality of adhesion obtained in an experimental procedure.

Keywords: fibers; mechanical properties of adhesives; finite element stress analysis

Abbreviations: EVA – ethylene–vinyl acetate copolymer, FEM – finite element modeling, SEM – Scanning electron microscopy, FTIR – Fourier transform of infrared light